Radiative charge transfer in $He^+ + H_2$ collisions in the milli- to nano-electron-volt range: A theoretical study within state-to-state and optical potential approaches

Felicja Mrugała[1,a)] and Wolfgang P. Kraemer[2]
[1]*Institute of Physics, Faculty of Physics, Astronomy and Informatics, Nicolaus Copernicus University, Grudziadzka 5, PL 87-100 Torun, Poland*
[2]*Max-Planck-Institute of Astrophysics, Postfach 1317, D-85741 Garching, Germany*

(Received 4 October 2012; accepted 17 February 2013; published online 13 March 2013)

The paper presents a theoretical study of the low-energy dynamics of the radiative charge transfer (RCT) reaction $He^+(^2S) + H_2(X\,^1\Sigma_g^+) \rightarrow He(^1S) + H_2^+(X\,^2\Sigma_g^+) + h\nu$ extending our previous studies on radiative association of HeH_2^+ [F. Mrugała, V. Špirko, and W. P. Kraemer, J. Chem. Phys. **118**, 10547 (2003); F. Mrugała and W. P. Kraemer, *ibid.* **122**, 224321 (2005)]. The calculations account for the vibrational and rotational motions of the H_2/H_2^+ diatomics and for the atom-diatom complex formation in the reactant and the product channels of the RCT reaction. Continuum states of $He^+ + H_2(v = 0, j = 0)$ in the collision energy range $\sim 10^{-7}$–18.6 meV and all quasi-bound states of the $He^+ - H_2(para; v = 0)$ complex formed in this range are taken into account. Close-coupling calculations are performed to determine rates of radiative transitions from these states to the continuum and quasi-bound states of the $He + H_2^+$ system in the energy range extending up to ~0.16 eV above the opening of the $HeH^+ + H$ arrangement channel. From the detailed state-to-state calculated characteristics global functions of the RCT reaction, such as cross-section $\sigma(E)$, emission intensity $I(v, T)$, and rate constant $k(T)$ are derived, and are presented together with their counterparts for the radiative association (RA) reaction $He^+(^2S) + H_2(X\,^1\Sigma_g^+) \rightarrow HeH_2^+(X\,^2A') + h\nu$. The rate constant k^{RCT} is approximately 20 times larger than k^{RA} at the considered temperatures, 0.1 μK–50 K. Formation of rotational Feshbach resonances in the reactant channel plays an important role in both reactions. Transitions mediated by these resonances contribute more than 70% to the respective rates. An extension of the one-dimensional optical potential model is developed to allow inclusion of all three vibrational modes in the atom-diatom system. This three-dimensional optical potential model is used to check to which extent the state-to-state RCT rate constant is influenced by the possibility to access ground state continuum levels well above the opening of the $HeH^+ + H$ arrangement channel. The results indicate that these transitions contribute about 30% to the "true" rate constant k^{RCT} whereas their impact on the populations of the vibration-rotational states of the product H_2^+ ion is only minor. Present theoretical rate constant functions $k^{RCT}(T)$ obtained at different approximation levels are compared to experimental data: $1–1.1 \times 10^{-14}$ s^{-1} cm^3 at $T = 15$–35 K and $\sim 7.5 \times 10^{-15}$ s^{-1} cm^3 at 40 K [M. M. Schauer, S. R. Jefferts, S. E. Barlow, and G. H. Dunn, J. Chem. Phys. **91**, 4593 (1989)]. The most reliable theoretical values of k^{RCT}, obtained by combining results from the state-to-state and the optical potential calculations, are between 2.5 and 3.5 times larger than these experimental numbers. Possible sources for discrepancies are discussed.
 [http://dx.doi.org/10.1063/1.4793986]

I. INTRODUCTION

The reaction of He^+ ions with H_2 has attracted interest of experimenters and theoreticians since many decades.[1] Earlier experiments have favored dissociative charge transfer (DCT) to be the predominant reaction channel in low-energy collisions

$$He^+(^2S) + H_2(X\,^1\Sigma_g^+) \rightarrow He(^1S) + H(^2S) + H^+, \quad (1)$$

and effective rate coefficients for this binary reaction in the range 10^{-13}–10^{-14} cm^3 s^{-1} were obtained experimentally[2–4] and theoretically.[5]

However, after detecting from theoretical calculations[6] a shallow He^+–H_2 ion-molecule polarization well on the potential energy surface (PES) of the first excited electronic state of the HeH_2^+ ion and due to experimental observation[7] of H_2^+ ions in thermal collisions of He^+ with H_2, Hopper postulated[8] that radiative charge transfer (RCT) occurs as alternative reaction in these collisions

$$He^+(^2S) + H_2(X\,^1\Sigma_g^+) \rightarrow He(^1S) + H_2^+(X\,^2\Sigma_g^+) + h\nu. \quad (2)$$

He actually suggested that the reaction proceeds via a three-step collision-radiative mechanism where the first step (2a) is the formation of the polarization state[6,8]

$$He^+(^2S) + H_2(X\,^1\Sigma_g^+) \rightarrow He^+ - H_2(A\,^2A'), \quad (2a)$$

a)Electronic mail: felicja@phys.uni.torun.pl.

$$He^+ - H_2(A\,^2A') \rightarrow He - H_2^+(X\,^2A') + h\nu, \qquad (2b)$$

$$He - H_2^+(X\,^2A') \rightarrow He(^1S) + H_2^+(X\,^2\Sigma_g^+) + KE. \qquad (2c)$$

The second step (2b) in this scheme consists in radiative transitions from the initially formed polarization state He^+–H_2 on the excited state potential to levels on the ground state potential. At geometries close to the C_{2v} minimum of the upper state with $R_{He-H_2} \simeq 5$ a.u. and $R_{HH} \simeq 1.4$ a.u., the potential energy of the lower state is ∼0.8 eV above its lowest dissociation asymptote $He(1^1S) + H_2^+(X\,^2\Sigma_g^+, v' = 0)$, but ∼0.1 eV below the other higher dissociation asymptote $HeH^+(X\,^1\Sigma^+, v'' = 0) + H(1^2S)$. Therefore, the radiative mechanism was expected to lead exclusively to $He(^1S) + H_2^+(X\,^2\Sigma_g^+, v')$.

The third step (2c) finally consists in the decay of the ground state complex. For this step Hopper argued that, due to the large difference between the initial $R_{HH} \simeq 1.4$ a.u. and the HH bond length of 2.00 a.u. in the H_2^+ ion, the partitioning of the available 0.8 eV of potential energy is expected to be to about 50% in the H_2^+ vibrational mode with a peak at $v' = 2$ and to about the other half in the product kinetic energy and a small fraction in H_2^+ rotational energy due to tendency of the He to pull H_2^+ towards a linear conformation minimizing the repulsion as the products separate.

In his study Hopper used a simple argument to derive the rate coefficient for reaction (2): Taking the experimentally determined total thermal disappearance rate for He^+ ions from Refs. 3 and 4 as $k \simeq 10^{-13}$ cm^3 s^{-1} and subtracting the value for the tunneling DCT reaction derived by Preston *et al.*[5] in their model calculations, a rate coefficient for the RCT reaction of $k^{RCT} \approx 7.5 \times 10^{-14}$ cm^3 s^{-1} was obtained. This was considered as an upper limit due to the approximations made in the calculations of Ref. 5. Apart from this theoretical estimate the rate coefficient of reaction (2) was also determined experimentally[9] employing a beam cell collision technique and measuring absolute cross sections for the appearance of H_2^+ ions in low-energy collisions. A value as large as $k^{RCT} = 1.48 \times 10^{-13}$ cm^3 s^{-1} was derived from this experiment. There has been some controversy about the reliability of these results and those obtained in previous studies and the relative importance of the DCT versus RCT reaction channels in these collisions.[10,11] An attempt to clarify the situation[12] arrived finally at the conclusion that more detailed experimental studies especially on the branching ratio between dissociative and radiative charge transfer channels and more rigorous theoretical state-to-state calculations are required.

In a more recent experiment using an ion trap technique the rate coefficients for the radiative and dissociative charge transfer reactions were measured by Schauer *et al.*[13] at temperatures below 40 K. For the RCT reaction, the rate coefficient values were measured within 1.0 to 1.1×10^{-14} cm^3 s^{-1} at temperatures between 15 and 35 K and ∼7.5×10^{-15} cm^3 s^{-1} at 40 K.

A theoretical rationale for these experimental findings was found in a study by Kimura and Lane.[14] In the model they have adopted in their calculations, the H_2 molecule was assumed to be a structureless particle and radiative transitions from the (He^+ relative to H_2) vibrational continuum of the excited state to all continuum and bound vibrational levels of the ground electronic state were accounted for by means of the one-dimensional optical potential model. Further, the assumption was made that the rate of the accompanying radiative association (RA) reaction

$$He^+(^2S) + H_2(X\,^1\Sigma_g^+) \rightarrow HeH_2^+(X\,^2A') + h\nu \qquad (3)$$

is negligibly small. Obviously, this model could not account for the rotational predissociation mechanism in the formation of the He^+–H_2 complex within the excited state potential well which is an important part of the Hopper scheme. However, since the rate coefficients for the RCT + RA reaction calculated by Kimura and Lane[14] appeared to be reasonably consistent with the experimental values measured for the RCT reaction, the agreement was used in the discussion by Schauer *et al.*[13] as an argument that initial complex formation plays only a minor role in the RCT reaction. Actually, if this would prove to be true, the reaction would be a one-step (or direct) radiative reaction rather than a three-step associative-radiative process as postulated by Hopper.

The role of states of the He^+–H_2 complex formed by inverse rotational predissociation (Feshbach resonances) as well as those formed by tunneling through centrifugal barriers (shape resonances) was in the focus of our preceding state-to-state study[15] of the RA reaction (3). It was demonstrated there that Feshbach resonances play an absolutely crucial role in the dynamics of this reaction at low temperatures. There cannot be any doubt that their contribution to the RCT reaction should be equally important.

In Hopper's scheme the second reaction step (2b) is described making use of the Franck-Condon principle. According to this approximation vertical transitions take place from the C_{2v} minimum of the excited state potential down to the so-called Franck-Condon point[16] on the ground state potential. The conclusions derived from this picture are that the $HeH^+(X\,^1\Sigma^+, v'' = 0) + H(1^2S)$ asymptotic level cannot be accessed in the radiative transitions, further that the wavelength of the emitted photons should be at maximum about 153 nm, and that the H_2^+ fragments should be vibrationally excited. These theoretical conclusions were corroborated by the experimental findings that H_2^+ ions were indeed observed in thermal collisions of He^+ with H_2 whereas HeH^+ was not found in the experimental setup used in these measurements.[7] Hopper's theoretical assumptions about the mechanism of the transition step (2b) are nevertheless essentially approximative and need therefore to be investigated in further detail. First of all, (i) what are the consequences for the RCT reaction if the restriction of applying the Franck-Condon principle for the radiative transitions is released. The further questions are: (ii) what is the role of the radiative transitions to the continuum states of the ground state complex $He - H_2^+$ as compared to transitions to the quasi-bound states; and (iii) what is the impact of interactions in the dissociation step (2c) taking place on the ground state potential on populations of the vibrational and rotational states of the product ions H_2^+. In fact, it has been demonstrated that so-called final state interactions can dramatically change predictions based on simple Franck-Condon principle considerations.[17] Concerning the question about the role of transitions to continuum versus

quasi-bound states on the ground-state potential, our detailed calculations[18] of the RA reaction

$$\mathrm{He}(^1S) + \mathrm{H}_2^+(X\,^2\Sigma_g^+) \rightarrow \mathrm{HeH}_2^+(X\,^2A') + h\nu \qquad (4)$$

(taking place entirely on the ground state potential surface) have shown that ro-vibrational resonances on this potential are in their majority short-living and can hardly be distinguished from the continuum states. Although only a small energy range of about 300 cm^{-1} above the lowest dissociation threshold $\mathrm{He} + \mathrm{H}_2^+(v' = 0, j' = 0)$ was scanned in that study, one may expect that at higher energies the distinction between resonance and continuum states will become even more problematic.

It is the intention of the present study to check and possibly verify the reaction scheme proposed by Hopper. This implies to confirm the importance of inverse rotational predissociation for the formation of the He^+–H_2 complex in the first step (2a) of the RCT reaction and to investigate critically steps (2b) and (2c) which in Hopper's version of the reaction scheme acquire a more approximate character due to the use of the Franck-Condon picture.

For this purpose extensive dynamics calculations are performed in which two kinds of approaches are exploited. First, a detailed state-to-states approach is applied. It relies essentially on the theoretical model which was used in our previous studies of the radiative association reaction (4), in Ref. 18, and of the two-state reaction (3), in Ref. 15. These studies are referred to hereafter as Papers I and II, respectively.

A detailed overview of the quantum theory of radiative association in application to atom-diatom systems was presented in Paper I. Apart from treating the association as an effect of weak interaction with the radiation field, three major assumptions are made in the theory to describe the initial and final molecular states in the process: (1) the nuclear motions take place entirely on single potential energy surfaces, i.e., tunneling and diabatic transitions to other potentials are excluded, (2) the initial scattering states lie close to the lowest atom-diatom dissociation limit of the triatomic reactant system and are therefore not affected by higher fragmentation limits on this PES, (3) spin-rotation and hyperfine interactions can be ignored.

The RA studies of Papers I and II were based on the *ab initio* electronic structure calculations.[19,20] Details of the calculations of the potential energy data of the ground and first excited states of the HeH_2^+ ion over a wide range of geometries including their respective lowest dissociation channels together with the associated electric dipole moments and the transition moments connecting the two states are given there. The potential energy functions and transition moment functions used as input in the dynamics calculations were obtained from fits of appropriate Legendre polynomial expansions to the *ab initio* calculated data points. Actually, these functions have been prepared to serve also as input for calculations undertaken here—on the state-to-state description of the RCT reaction.

Formally, the final states in the RCT, i.e., the continuum and quasi-bound states of the $\mathrm{He} + \mathrm{H}_2^+$ complex, can lie even as high as 2.65 eV above the lowest dissociation limit of the ground-state PES of HeH_2^+. So, the $\mathrm{HeH}^+ + \mathrm{H}$ fragmentation limit of this PES, which lies only 0.8 eV higher than the lowest limit, can formally affect the final states. They can be partially depopulated by the proton transfer (pT) reaction, $\mathrm{He} + \mathrm{H}_2^+ \rightarrow \mathrm{HeH}^+ + \mathrm{H}$. The production of the HeH^+ ions from the $\mathrm{He}^+ + \mathrm{H}_2$ reactant pairs on the excited-state PES via this secondary reaction on the ground-state PES is called here "indirect radiative atom transfer" (iRaT). [Direct atom transfer is known not to occur in thermal $\mathrm{He}^+ + \mathrm{H}_2$ collisions.[5,6]] The question about the consequences of going beyond the strict application of the Franck-Condon principle in step (2b) of Hopper's scheme should thus be specified to the following: (i′) how the population of the entire final-state energy range in the RCT really looks like, in particular, how far above the Franck-Condon point[16] it extends, (i″) how (im)probable the iRaT branch of the reaction can be.

Within the approach adopted from the previous RA studies, questions (i)-(iii) can be answered but not rigorously. The used ground-state PES is not sufficient for a rigorous treatment of the dynamics of the $\mathrm{He} + \mathrm{H}_2^+$ system in the high energy range, certainly not for inclusion of the rearrangement transitions. Hence, the additional assumption is necessarily made in the present state-to-state study of the RCT: (4) the $\mathrm{He} + \mathrm{H}_2^+$ product system can be treated as chemically nonreactive not only below but also in some energy range above the threshold for the pT reaction. The detailed characteristics actually calculated are the rates of radiative transitions from the continuum states of the $\mathrm{He}^+ + \mathrm{H}_2(v = 0, j = 0)$ reactant pair in the collision energy range $\sim 10^{-7}$–18.6 meV and from all quasi-bound states of the $\mathrm{He}^+ + \mathrm{H}_2(para; v = 0)$ complex formed in this range to all continuum and quasi-bound states of the $\mathrm{He} + \mathrm{H}_2^+$ charge-transferred system in the energy range extending from the $\mathrm{He} + \mathrm{H}_2^+(v' = 0, j' = 0)$ dissociation asymptote ($E' = 0$) up to ~0.16 eV above the opening of the $\mathrm{HeH}^+ + \mathrm{H}$ arrangement channel [at $E' = 0.8$ eV (6487 cm^{-1})]. Adequacy of assumption (4) in these calculations is proved using the literature information[21] on dynamics of the pT reaction.

In addition to this state-to-state treatment an attempt is also made here to investigate more explicitly how much the rate constant of the RCT process is affected by radiative transitions to ground state continuum levels well above the rearrangement threshold. For this purpose an extended version of the original one-dimensional optical potential method[22–24] widely used in calculations of atom-atom RCT + RA reactions is developed. In this generalization to the present atom-diatom system all three vibrational modes of the triatomic HeH_2^+ complex are taken into account. The extended version is thus labeled as three-dimensional optical potential (3D optical potential) model. The model rigorously treats the dynamics on the excited-state PES and requires only a part of the ground-state PES, accurately determined in Ref. 19, to account for the spontaneous emission. With this new 3D generalized optical potential concept the gross reaction rate constant for the total radiative reaction RCT + RA + iRaT can be obtained where the contribution from the RA reaction (3) is separately available from the previous calculations of Paper II. Comparison of these 3D optical potential results with those obtained from the state-to-state calculations provides an estimate to which extent transitions to the higher ground state

continuum levels and the iRaT reaction contribute to the total radiative rate. The usefulness of the 3D optical model is further demonstrated when extensions to larger temperature ranges are considered in this study.

The formulas for the RCT rate constant, the emission spectrum, and radiative widths of long-living rotation-vibration resonances are presented in Sec. II. Section III gives an overall description of the state-to-state calculations done in the course of the study. The computational approach applied in the calculations is generally the same as described in Paper I, i.e., the standard formulation of Close-Coupling equations for an atom-diatom system in a Body-Fixed reference frame using a diabatic basis set (CC-BF-diabatic) plus a Coriolis coupling reducing (CCr) approximation. In Sec. IV, the 3D generalization of the optical potential model is presented in a "complete" and a "projected" (on definite final-state subspaces) version. Especially this projected version is useful for a comparison with the state-to-state results. Some details of the calculations performed within both the state-to-state and the optical potential approaches and a short description of the accompanying extended investigations of the He^+–H_2 and He–H_2^+ complexes are given in Sec. V.

The main results of the present calculations are finally summarized and discussed in Sec. VI. This includes: an analysis of the state-to-state transition rates and the photon emission spectra, cross-section results in different energy regimes, a detailed discussion and comparison of different contributions to the rate constants, and finally an analysis of vibrational and rotational-state populations of the product H_2^+ ion. Supplementary material[25] attached to this paper provides additional detailed information. It is organized in parts: part A collecting details on the state-to-state description of the RCT, part B with details on the 3D optical potential model and results obtained with its help, and part C concerning the predissociation of the $He^+ - H_2$ complex.

Consistent with the abbreviations used in Papers I and II, the reactant and the product channels of the RCT reaction are assigned as "*A*" and "*X*" channels, respectively, throughout the present paper.

II. THEORY OUTLINE

A. Rate constant

The RCT reaction (2) is considered to take place in a gas mixture at thermal equilibrium with temperature T. It is described by the rate equation

$$\frac{d}{dt} n_{\mathrm{He}+\mathrm{H}_2^+} = k\, n_{\mathrm{H}_2}\, n_{\mathrm{He}^+} \tag{5}$$

in which n denotes the number density of the subscribed species and k is the rate constant,

$$k = \sum_{I=0,1} \sum_{vj} \sum_{v'j'} k^I_{vj\to v'j'}. \tag{6}$$

where The $k^I_{vj\to v'j'}$ gives here the rate of formation of the He + $H_2^+(I)$ pairs in states with final vibration-rotation energies $\varepsilon'_{v'j'}$ of the $H_2^+(I)$ subunit obtained in transitions from the reactant system He^++ $H_2(I)$ with the initial vibration-rotation energies ε_{vj} of the $H_2(I)$ subunit, where $I = 0$, 1 are the values for the nuclear spin. The rate constant $k^I_{vj\to v'j'}$ is obtained as function of T by Boltzmann-averaging over the initial and integrating over the final states the free-free transition rate $\frac{\partial^2}{\partial E\,\partial E'} R^I(E, vj; E', v'j')\, dE\, dE'$. This is the probability per unit of time for the formation of the pairs He + $H_2^+(I; v'j')$ under the conditions that the energy of relative translational motion of He^+ and H_2 together with the internal energy ε_{vj} yield the total energy of the reactants (in the center-of-mass system) in the range $[E, E + dE]$ and that the total energy of the products is in the range $[E', E' + dE']$. The energy of the emitted photons is $[E_{\mathrm{ph}}, E_{\mathrm{ph}} + d(E–E')]$, where $E_{\mathrm{ph}} = E–E' + \Delta E$ and ΔE is the separation between the thresholds $He^+ + H_2(v = 0, j = 0)$ and He + $H_2^+(v' = 0, j' = 0)$ (at which the energies $E = \varepsilon_{00}$ and $E' = \varepsilon'_{00}$ are set to zero). Thus

$$k^I_{vj\to v'j'}(T) = \int_{\varepsilon_{vj}}^{E_{\max}} dE\, P^I(E, T) \times \int_{\varepsilon'_{v'j'}}^{E'_{\max}} dE' \frac{\partial^2 R^I(E, vj; E', v'j')}{\partial E\, \partial E'}, \tag{7}$$

$P^I(E, T)$ denotes here the appropriate population factor of the reactant states,

$$P^I(E, T) = \frac{g^I}{Z(T)} \left(\frac{2\pi\hbar^2}{\mu k_B T}\right)^{3/2} \exp(-E/k_B T), \tag{8}$$

where $Z(T) = \sum_{v\,j} g_j (2j + 1) \exp(-\varepsilon_{vj}/k_B T)$ with $g_j = g^0 = 1$ for j even and $g_j = g^1 = 3$ for j odd, μ is the reduced mass of the $He^+ + H_2$ system, and k_B is the Boltzmann constant. The value of the first upper integration limit $E_{\max}$ in Eq. (7) depends on the factor $P^I(E, T)$. For sub-thermal collision processes with maximum temperatures of ∼50 K the population of states above threshold extends only over a very small energy range, the integration limit is thus rather small: $E_{\max} \approx 20$ meV. The second integration limit $E'_{\max}$, on the other hand, should formally be as large as the dissociation energy of the H_2^+ ion from its ground vibration-rotation state, 2.651 eV (Ref. 26). However, whereas according to Hopper's considerations a much smaller value for $E'_{\max}$ would be sufficient in practice, in the present application it is assumed that $E'_{\max}$ extends at least up to the threshold of the proton transfer reaction He + $H_2^+(v', j') \to HeH^+(v'', j'')$ + H at $E' = \varepsilon''_{00} = 0.8$ eV (6487 cm^{-1}).

B. Emission intensity

The photon emission in the RCT reaction is globally characterized by the intensity $\mathcal{I}(T)$ which is the power emitted at temperature T by unit volume of the gas when $n_{\mathrm{H}_2} = n_{\mathrm{He}^+} = 1$. A more detailed characteristics of interest here is the spectral density of emission $\mathcal{I}^I(E_{\mathrm{ph}}, T)$, the quantity appearing in the resolution $\mathcal{I}(T) = \sum_{I=0,1} \int \mathcal{I}^I(E_{\mathrm{ph}}, T)\, dE_{\mathrm{ph}}$ and obtained as

$$\mathcal{I}^I(E_{\mathrm{ph}}, T) = \int dE\, P^I(E, T)\, E_{\mathrm{ph}} \times \sum_{vj} \sum_{v'j'} \frac{\partial^2 R^I(E, vj; \widehat{E}', v'j')}{\partial E\, \partial E'}, \tag{9}$$

where $\widehat{E}' \equiv E + \Delta E - E_{\rm ph}$. In the following $\mathcal{I}^I(E_{\rm ph}, T)$ is referred to as "photon emission spectrum at temperature T."

C. Cross-sections

The quantity $\frac{\partial^2}{\partial E\,\partial E'} R^I(E, vj; E', v'j')$, multiplied by a simple kinematic factor involving the wave-number $k_{vj} = \sqrt{2\mu(E - \varepsilon_{vj})}/\hbar$, gives the photon-energy-differential cross-section for $vj \to v'j'$ transition at the reactant energy E,

$$\frac{\partial \sigma^I_{vj\to v'j'}(E, E_{\rm ph})}{\partial E_{\rm ph}} = \frac{2\pi^2\hbar}{k^2_{vj}} \frac{\partial^2 R^I(E, vj; \widehat{E}', v'j')}{\partial E\,\partial E'}. \quad (10)$$

Upon summation over the final diatomic states (v', j') or/and integration over the photon energy $E_{\rm ph}$ one gets the cross-sections $\frac{\partial}{\partial E_{\rm ph}}\sigma^I_{vj}(E, E_{\rm ph})$, $\sigma^I_{vj\to c'}(E)$, and $\sigma^I_{vj}(E)$. The first quantity is the most detailed characteristic of the photon emission spectrum in the RCT reaction which will be determined in the present calculations. The other cross-sections will be determined in order to record the populations of the product states v' and j' in the reaction.

D. Free-free transition rates

The evaluation of the introduced characteristics of the RCT reaction is obviously facilitated by applying the partial-wave expansion to the initial and final atom + diatom states.

The free-free transition rate $\frac{\partial^2}{\partial E\,\partial E'} R^I(E, vj; E', v'j')\, dE\, dE'$ becomes resolved into independent contributions of transitions between initial and final partial scattering states characterized by the total angular momentum and the spectroscopic parity quantum numbers (J, p) and (J', p'), respectively,

$$\frac{\partial^2 R^I(E, vj; E', v'j')}{\partial E\,\partial E'} = \sum_J \sum_{p=\pm 1} (2J+1) \sum_{J'=J-1}^{J+1} \frac{\partial^2 R^I(EJp, vj; E'J'p', v'j')}{\partial E\,\partial E'}, \quad (11)$$

where $p' = p(-1)^{J+J'+1}$ and $p = \pm 1$. The individual partial double-differential transition rate (per units of initial and final energies) is given by the expression

$$\frac{\partial^2 R^I(EJp, vj; E'J'p', v'j')}{\partial E\,\partial E'} = \frac{4}{3\hbar^4 c^3}(E - E' + \Delta E)^3 \sum_{l,l'} |T^I_{v'j'l';vjl}(E'J'p'; EJp)|^2, \quad (12)$$

where $T^I_{v'j'l';vjl}(E'J'p'; EJp)$ denotes the reduced matrix elements of the appropriate transition dipole moment vector $\{d_q; q = -1, 0, 1$, defined in terms of SF components d_x, d_y, and d_z (see Sec. III)$\}$

$$T^I_{v'j'l';vjl}(E'J'p'; EJp) = \sqrt{\frac{2J'+1}{2J+1}} \frac{\langle E'^- J'M'p', v'j'l'|d_q|E^+ JMp, vjl\rangle}{C(J1J', MqM')}, \quad (13)$$

$|E^+ JMp, vjl\rangle$ denotes the energy-normalized partial scattering state of the $He^+ + H_2$ system with M being the quantum number of the projection of the total angular momentum on the space-fixed z-axis; the numbers behind the comma (vjl) characterize the state before scattering, l specifies the angular momentum of the relative motion. Analogously, $|E'^- J'M'p', v'j'l'\rangle$ denotes partial scattering state of the $He + H_2^+$ system; the superscripts of E and E' are the standard notation for the outgoing- and ingoing-wave boundary conditions satisfied by the scattering states. $C(\ldots, \ldots)$ denotes the Clebsch-Gordan coefficient. c in Eq. (12) is the speed of light. Occasionally, $T^I_{v'j'l';vjl}(E'J'p'; EJp)$ is referred to as free-free phototransition amplitude.

E. Resonance-background resolution

The quantities $\frac{\partial^2}{\partial E\,\partial E'} R(EJp, vj; E'J'p', v'j')$ (the index I is omitted hereafter) are highly nonuniform functions of the energies E and E' reflecting the existence of resonances with widely varying lifetime characteristics (see Ref. 25). A special treatment is needed in cases of sharp features which appear in both the E and E' dependencies due to long-living resonances. Let us denote these resonances with the symbols $\mathcal{R}^{Jp}_n$ and $\mathcal{R}'^{J'p'}_m$, respectively. The index n (m) enumerates resonance energies $E^{Jp\,\rm res}$ $(E'^{J'p'\,\rm res})$ within a given partial state Jp $(J'p')$. The treatment consists essentially in two approximations applied successively to the initial or/and to the final partial scattering states in the phototransition amplitude $T_{v'j'l';vjl}(E'J'p'; EJp)$ when $E \approx E^{Jp\,\rm res}_n$ or/and $E' \approx E'^{J'p'\,\rm res}_m$. First, the isolated resonance approximation[27] is applied. In case of $\mathcal{R}^{Jp}_n$ it gives: $|E^+ JMp, vjl\rangle \approx |E^{B_Q}_n JMp\rangle a^{JMp}_{n,vjl}(E)$ where $|E^{B_Q}_n JMp\rangle$ is a bound state of the Hamiltonian of the reactant system within an appropriate subspace Q, chosen so that $E^{B_Q}_n \approx E^{\rm res}_n$, and the function $\sum_l |a^{Jp}_{n,vjl}(E)|^2$ is a Lorentzian with the maximum $2\Gamma^{Jp}_{n,vj}/\pi(\Gamma^{Jp}_n)^2$ at $E^{\rm res}_n$ and the width at half-maximum $\Gamma^{Jp}_n = \sum_{vj} \Gamma^{Jp}_{n,vj}$. The Γ's characterize dissociative decay of $\mathcal{R}^{Jp}_n$, caused by molecular interactions only. Next, a possibility of spontaneous emission from the resonance being competitive to the dissociative decay is taken care of by adding an appropriate imaginary part $-\frac{\imath}{2}\Gamma^{Jp\,\rm rad}_n$ to the energy $E^{\rm res}$ in the factor $a^{Jp}_{n,vjl}(E)$. The operation (termed "the implicit optical potential approach" in Ref. 28) enlarges the width of the related Lorentzian to $\Gamma^{Jp}_n + \Gamma^{Jp\,\rm rad}_n$. The broadened profile is denoted below with the symbol $p^{Jp}_{n,vj}(E)$. The arising phototransition amplitudes of bound-free, free-bound, and bound-bound types are denoted as $T_{v'j'l'}(E'J'p'; E^{B_Q}_n Jp)$, $T_{vjl}(E'^{B_{Q'}}_m J'p'; EJp)$, and $T(E'^{B_{Q'}}_m J'p'; E^{B_Q}_n Jp)$, respectively. The final result is the following approximate resolution:

$$\frac{\partial^2 R(EJp, vj; E'J'p', v'j')}{\partial E\,\partial E'} \approx \frac{\partial^2 R^{\rm RCT(res)}_{vj\to v'j'}(EJp; E'J'p')}{\partial E\,\partial E'} + \frac{\partial^2 R^{\rm RCT(bck)}_{vj\to v'j'}(EJp; E'J'p')}{\partial E\,\partial E'}, \quad (14)$$

where the parts RCT(res) and RCT(bck) accumulate contributions of RCT transitions which, respectively, do or do not proceed via the long-living resonances in the A channel. Both parts account for all resonance and continuum final states of the transitions in the X channel. Thus,

$$\frac{\partial^2 R^{\mathrm{RCT(res)}}_{vj\to v'j'}(EJp;E'J'p')}{\partial E\,\partial E'} = \sum_n p^{Jp}_{n,vj}(E)\,\frac{1}{\hbar}\,\frac{\partial \Gamma^{\mathrm{RCT}}_{n,v'j'}(Jp;E'J'p')}{\partial E'}, \tag{15}$$

where

$$\frac{\partial \Gamma^{\mathrm{RCT}}_{n,v'j'}(Jp;E'J'p')}{\partial E'} = \frac{\partial \widetilde{\Gamma}^{\mathrm{RCT}}_{n,v'j'}(Jp,E'J'p')}{\partial E'} + \sum_m \Gamma^{\mathrm{RA}}_{n,m}(Jp;J'p')\,p^{\prime J'p'}_{m,v'j'}(E'), \tag{16}$$

$$p^{Jp}_{n,vj}(E) = \frac{1}{2\pi}\,\frac{\Gamma^{Jp}_{n,vj}}{\left(E-E^{Jp\,\mathrm{res}}_n\right)^2+\frac{1}{4}\left(\Gamma^{Jp}_n+\Gamma^{Jp\,\mathrm{RCT+iRaT}}_n+\Gamma^{Jp\,\mathrm{RA}}_n\right)^2}, \tag{17}$$

$$p^{\prime J'p'}_{m,v'j'}(E') \approx \frac{\Gamma^{\prime J'p'}_{m,v'j'}}{\Gamma^{\prime J'p'}_m+\Gamma^{\prime J'p'\,\mathrm{RA}}_m}\,\delta(E'-E^{\prime J'p'\,\mathrm{res}}_m). \tag{18}$$

All Γ's labeled with RCT, RA or RCT + iRaT have the meaning of radiative widths of resonances. $\frac{\partial}{\partial E'}\widetilde{\Gamma}^{\mathrm{RCT}}_{n,v'j'}(Jp;E'J'p')dE'$ is the width of resonance $\mathcal{R}^{Jp}_n$ due to transitions to continuum and non-sharp resonance states $([E',E'+dE']J'p',v'j')$,

$$\frac{\partial \widetilde{\Gamma}^{\mathrm{RCT}}_{n,v'j'}(Jp;E'J'p')}{\partial E'} = \frac{4}{3\hbar^4c^3}\left(E^{Jp\,\mathrm{res}}_n-E'+\Delta E\right)^3 \times \sum_{l'}\left|T_{v'j'l'}\left(E'J'p';E^{B_Q}_nJp\right)\right|^2. \tag{19}$$

$\Gamma^{\mathrm{RA}}_{n,m}(Jp;J'p')$ involves the amplitude $T(E^{\prime B_{Q'}}_mJ'p';E^{B_Q}_nJp)$ and describes the association of $\mathcal{R}^{Jp}_n$ into $\mathcal{R}^{\prime J'p'}_m$. The factor $p^{\prime J'p'}_{m,v'j'}(E')$ obviously accounts for the subsequent dissociative decay of the latter resonance. $\Gamma^{Jp\,\mathrm{RCT}}_n$ is the total width of $\mathcal{R}^{Jp}_n$ due to all allowed transitions which yield free H_2^+ ions and He atoms,

$$\Gamma^{Jp\,\mathrm{RCT}}_n = \sum_{v'j'}\Gamma^{Jp\,\mathrm{RCT}}_{n,v'j'} = \sum_{v'j'}\int_{\mathcal{E}'_{v'j'}}^{E'_{\max}}\frac{\partial \Gamma^{Jp\,\mathrm{RCT}}_{n,v'j'}(E')}{\partial E'}\,dE', \tag{20}$$

and

$$\frac{\partial}{\partial E'}\Gamma^{Jp\,\mathrm{RCT}}_{n,v'j'}(E') = \sum_{J'=J-1}^{J+1}\frac{\partial}{\partial E'}\Gamma^{\mathrm{RCT}}_{n,v'j'}(Jp;E'J'p'). \tag{21}$$

$\Gamma^{Jp\,\mathrm{RCT+iRaT}}_n$ is the total width of $\mathcal{R}^{Jp}_n$ due to the transitions to all continuum states in the X channel, $0 \le E' \le 2.651$ eV. Transitions to states in the energy range above the threshold for the proton transfer reaction ($E' > 6487\ \mathrm{cm}^{-1}$) can lead to the formation of $HeH^+(v'',j'')$ ions, i.e., effectively this looks like a direct radiative atom transfer reaction. As stressed in the Introduction, the reaction actually proceeds in two steps via radiative transitions to highly lying X-state continuum levels followed by proton transfer along the rearrangement channel. The term iRaT is therefore used for this reaction path.

Finally, $\Gamma^{Jp\,\mathrm{RA}}_n$ is the total width of $\mathcal{R}^{Jp}_n$ due to transitions to (truly) bound states of the HeH_2^+ ion,

$$\Gamma^{Jp\,\mathrm{RA}}_n = \sum_{\mathcal{B}}\Gamma^{Jp\,\mathrm{RA}}_{n,\mathcal{B}} + \sum_{J'}\sum_m \Gamma^{\mathrm{RA}}_{n,m}(Jp;J'p') \times \frac{\Gamma^{\prime J'p'\,\mathrm{RA}}_m}{\Gamma^{\prime J'p'}_m+\Gamma^{\prime J'p'\,\mathrm{RA}}_m}, \tag{22}$$

$\mathcal{B}$ enumerates the states reached directly from $\mathcal{R}^{Jp}_n$ and the second term is an estimation of indirect association via the long-living X-channel resonances.

The content of the part RCT(bck) is described by the formula

$$\frac{\partial^2 R^{\mathrm{RCT(bck)}}_{vj\to v'j'}(EJp;E'J'p')}{\partial E\,\partial E'} = \frac{\partial^2 \widetilde{R}^{\mathrm{RCT}}_{vj,v'j'}(EJp;E'J'p')}{\partial E\,\partial E'} + \sum_m \frac{\partial R^{\mathrm{RA}}_{vj,m}(EJp;J'p')}{\partial E}\,p^{\prime J'p'}_{m,v'j'}(E'), \tag{23}$$

where the first term is the quantity defined in Eqs. (12) and (13) after subtraction of the sharp features attributed to resonances $\{\mathcal{R}^{Jp}_n\}$ and $\{\mathcal{R}^{\prime J'p'}_m\}$, and $\frac{\partial}{\partial E}R^{\mathrm{RA}}_{vj,m}(EJp;J'p')$ in the second term, when multiplied by dE, gives the rate of association into resonance $\mathcal{R}^{\prime J'p'}_m$ of reactants being initially in states $([E,E+dE]Jp,vj)$. This rate is defined in terms of the phototransition amplitudes $T_{vjl}(E^{\prime B_{Q'}}_mJ'p';EJp)$ (see Paper I).

The resolution (14) inserted into Eqs. (10), (9), and (7) gives the corresponding resolutions of the cross-section $\frac{\partial}{\partial E_{\mathrm{ph}}}\sigma_{vj\to v'j'}(E,E_{\mathrm{ph}})$, of the emission spectrum $\mathcal{I}(E_{\mathrm{ph}},T)$, of the rate constant $k_{vj\to v'j'}$, and of the quantities derived from these by the operations $\int dE_{\mathrm{ph}}$, $\sum_{j'}$, and $\sum_{v'}$.

III. DESCRIPTION OF RCT IN THE CC-BF-DIABATIC APPROACH

The coordinates used to describe the configurations of the nuclear centers in the reactant and products systems are r, R, and θ—the lengths and the angle between the Jacobi vectors **r** and **R** which join, respectively, the protons and the center-of-mass of the protons with the He nucleus. The orientation of the plane of the three nuclei is described by azimuthal (ϕ_R) and spherical (θ_R) angles of the vector **R** with respect to a space-fixed (SF) reference frame $Oxyz$ with the origin O at the center-of-mass of H–H–He and by angle (ψ) of rotation of the plane around **R**. Euler rotations of the SF

frame over the angles ϕ_R, θ_R, and ψ give a body-fixed (BF) reference frame $OXYZ$ with the axis Z aligned to $\mathbf{R}$ and the axis Y perpendicular the plane of the nuclei. In the coordinates r, R, $(\psi, \theta) := \widehat{\mathbf{r}}_\mathrm{B}$, and $(\phi_R, \theta_R) := \widehat{\mathbf{R}}$, the Hamiltonian H^s for vibration-rotation-translation motion of the reactant ($s = A$) and product ($s = X$) systems takes the form

$$H^\mathrm{s}(r, R, \widehat{\mathbf{r}}_\mathrm{B}, \widehat{\mathbf{R}}) = \frac{1}{2\mu}\left[p^2(R) + \frac{\mathcal{C}^2(\widehat{\mathbf{R}}, \widehat{\mathbf{r}}_\mathrm{B})}{R^2}\right] + H^\mathrm{s}_\mathrm{HH}(r, \widehat{\mathbf{r}}_\mathrm{B}) + V^\mathrm{s}(r, R, \theta) \quad (24)$$

with $H^\mathrm{s}_\mathrm{HH}(r, \widehat{\mathbf{r}}_\mathrm{B}) = \frac{1}{2\mu_\mathrm{HH}}[p^2(r) + \frac{1}{r^2}\mathbf{j}^2(\widehat{\mathbf{r}}_\mathrm{B})] + V^\mathrm{s}_\mathrm{HH}(r)$, where $p(c) = \frac{\hbar}{i}(\frac{\partial}{\partial c} + \frac{1}{c})$ for $c = R$, r are the radial momentum operators and the operator in the angular coordinates has the structure $\mathcal{C}^2 = \mathbf{J}^2 + \mathbf{j}^2 - 2\mathbf{jJ}$ in which $\mathbf{J}$ and $\mathbf{j}$ denote the total angular momentum and the rotational momentum of the HH subunit, respectively. The meaning of the operator $\mathbf{j}\,\mathbf{J}$ is precisely described in Ref. 29. The μ's denote the respective reduced masses. $V^\mathrm{s}_\mathrm{HH}(r)$ and $V^\mathrm{s}(r, R, \theta)$ for $s = A\,(X)$ denote, respectively, the potential of the H_2 molecule (H_2^+ ion) and the interaction potential with the He^+ ion (He atom). These potentials are extracted from the PESes of the ground and first excited electronic states of the HeH_2^+ ion given in Ref. 19. The interaction potentials are represented by the expansions $V^\mathrm{s}(r, R, \theta) = \sum_{L=0}^{L^\mathrm{s}_\mathrm{max}} V^\mathrm{s}_L(r, R)\, P_L(\cos\theta)$ with $L^\mathrm{s}_\mathrm{max} = 4\,(10)$ for $s = A\,(X)$, where P_L denotes the Legendre polynomial of Lth order (see Fig. 1(a) and Ref. 25, Fig. A1).

In the functions $\langle R, y|E^{s\,\pm} JMp, vjl\rangle$ of the partial scattering states of the system s, the dependence on the coordinates $y = (r, \widehat{\mathbf{r}}_\mathrm{B}, \widehat{\mathbf{R}})$ is represented by the standard diabatic basis $\mathbf{\Phi}^{s\,JMp}_{1\times N^s}(y)$; the individual basis function $\Phi^{s\,JMp}_{vj\lambda}(y)$ is an eigenfunction of the operators $\mathbf{J}^2$, J_z, $\mathcal{I}$ (spatial inversion), $J_Z^2\,(= j_Z^2)$, $\mathbf{j}^2$, and H^s_HH to eigenvalues $\hbar^2 J(J+1)$, $\hbar M$, $p(-1)^J$, $\hbar^2\lambda^2$, $\hbar^2 j(j+1)$, and ε^s_{vj}, respectively. Even (odd) j's occur in the basis for $I = 0\,(1)$, the values of λ change in step of 1 from $\frac{1+p}{2}$ ($p = \pm 1$) to $\min[\lambda^\mathrm{s}_\mathrm{max}, \min(J, j)]$, and $v = 0, 1, \ldots v^\mathrm{s}_\mathrm{max}$. The values of $v^\mathrm{s}_\mathrm{max}$, $j^\mathrm{s}_\mathrm{max}$, and $\lambda^\mathrm{s}_\mathrm{max}$ for s = A and s = X are specified in Sec. V.

Denoting with $\mathbf{\Psi}^{\mathrm{s}\,(\pm)JMp}_{1\times N^\mathrm{s}_\mathrm{o}}(E; \mathbf{r}, \mathbf{R})$ the set of functions of the states $|E^{s\,\pm} JMp, (vjl)_i\rangle$ for all open scattering channels $(vjl)_i$, $i = 1 \ldots, N^\mathrm{s}_\mathrm{o}$, one obtains

$$\mathbf{\Psi}^{\mathrm{s}\,(\pm)JMp}(E; \mathbf{r}, \mathbf{R}) = \frac{1}{R}\ \mathbf{\Phi}^{s\,JMp}_{1\times N^\mathrm{s}}(r, \widehat{\mathbf{r}}_B, \widehat{\mathbf{R}})\, \mathbf{F}^{\mathrm{s}\,(\pm)Jp}_{N^\mathrm{s}\times N^\mathrm{s}_\mathrm{o}}(E; R)\, \mathbf{U}^{\mathrm{s}\,Jp}.$$

Here $\mathbf{U}^{\mathrm{s}\,Jp}$ is the transformation from the basis $\mathbf{\Phi}^{s\,JMp}$ to its space-fixed counterpart (involving eigenfunctions of $\mathbf{l}^2$ instead of j_Z^2) and the radial functions $\mathbf{F}^{\mathrm{s}\,(\pm)Jp}(E; R)$ are determined by solving the CC-BF equations, i.e., the time-independent Schrödinger equation with the Hamiltonian matrix

$$[\mathbf{H}^{\mathrm{s}\,Jp}(R)]_{\tilde{v}\tilde{j}\tilde{\lambda};\,vj\lambda} = -\delta_{\tilde{v}\tilde{j}\tilde{\lambda};\,vj\lambda}\frac{\hbar^2}{2\mu}\frac{d^2}{dR^2} + [\mathbf{W}^{\mathrm{s}\,Jp}(R)]_{\tilde{v}\tilde{j}\tilde{\lambda};\,vj\lambda}, \quad (25)$$

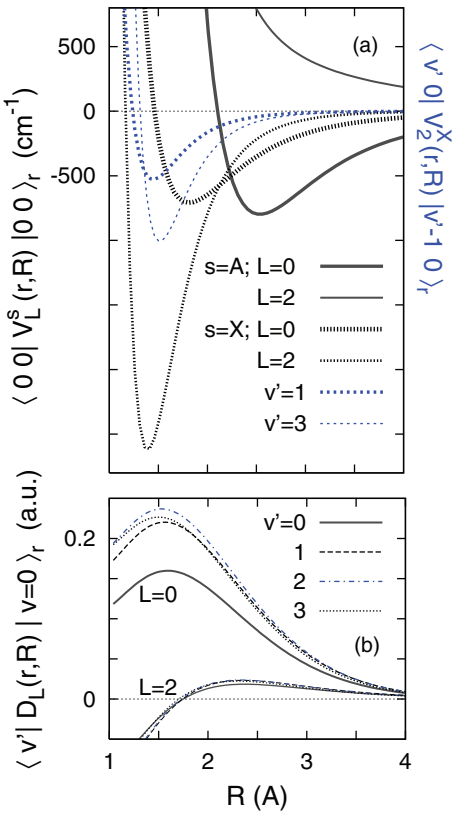

FIG. 1. Some properties of the electronic structure input. (a) Strength functions of the interaction potentials in the A and X channels from their Legendre-polynomial expansions: $V^\mathrm{s}(r, R, \theta) = \sum_{L=0}^{L^\mathrm{s}_\mathrm{max}} V^\mathrm{s}_L(r, R)\, P_L(\cos\theta)$ with $L^A_\mathrm{max} = 4\,(10)$ for $s = A\,(X)$. Shown are average values of the largest two $V^\mathrm{s}_L(r, R)$ functions in the ground ro-vibrational states of H_2^+ and H_2 for $s = X$ and A, respectively, and matrix elements of $V^X_{L=2}$ between v' and $v' - 1$ states of H_2^+ (blue lines). (b) Strength functions of the Z-component of the electric dipole vector for $A \to X$ transitions from its expansion: $d_Z(r, R, \theta) = \sum_{L=0}^{2} D_L(r, R) P_L(\cos\theta)$. Shown are matrix elements of $D_L(r, R)$ between functions of $v = 0$ $j = 0$ state of H_2 and $v' = 0 - 3$ $j' = 0$ states of H_2^+.

where

$$[\mathbf{W}^{\mathrm{s}\,Jp}(R)]_{\tilde{v}\tilde{j}\tilde{\lambda};\,vj\lambda} = \delta_{\tilde{v},v}\delta_{\tilde{j},j}\frac{\hbar^2}{2\mu R^2}[\mathbf{c}^{Jp}(j)]_{\tilde{\lambda},\lambda} + \delta_{\tilde{\lambda},\lambda}[\delta_{\tilde{v},v}\delta_{\tilde{j},j}\,\varepsilon^\mathrm{s}_{vj} + V^{\mathrm{s}\,\lambda}_{\tilde{v}\tilde{j},\,vj}(R)], \quad (26)$$

see Fig. 2 and Ref. 25, Fig. A2. The non-zero elements $[\mathbf{c}^{Jp}(j)]_{\tilde{\lambda},\lambda}$, for $\tilde{\lambda} = \lambda$ and $\tilde{\lambda} = \lambda \pm 1$, are the coefficients of the centrifugal potentials and of the Coriolis couplings, respectively, and $V^{\mathrm{s}\,\lambda}_{\tilde{v}\tilde{j},\,vj}(R)$ is the potential coupling $\sum_L \langle \tilde{v}\tilde{j}|V^\mathrm{s}_L(r, R)|vj\rangle_r\, g^\lambda_L(j, \tilde{j})$ with the rotational factor

$$g^\lambda_L(\tilde{j}, j) = (-1)^L C(\tilde{j}Lj, \lambda 0\lambda) C(jL\tilde{j}, 000). \quad (27)$$

In the following text, the subscript s is omitted when its value is A and prime is used instead of X. The symbols $|vj\rangle$ and $|\ \ \rangle'$ are used to distinguish between states of H_2 and H_2^+.

The free-free phototransition amplitude of Eq. (13) is obtained as

$$T_{v'j'l';\,vjl}(E'J'p'; EJp) = [\mathbf{U}^{J'p'\,\mathrm{T}}\langle \mathbf{F}'^{(-)J'p'}(E')| \times \mathbf{d}^{J'p'\,Jp}|\mathbf{F}^{(+)Jp}(E)\rangle_R\, \mathbf{U}^{Jp}]_{v'j'l';\,vjl}, \quad (28)$$

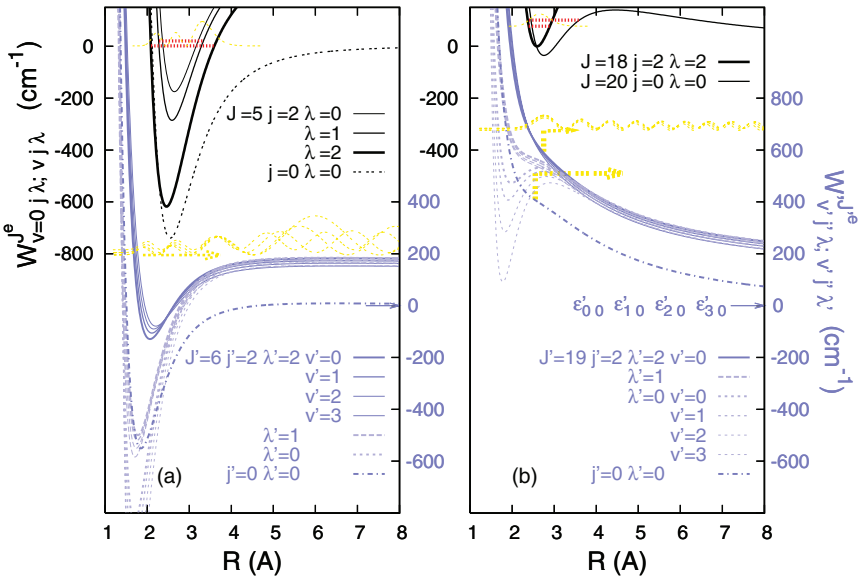

FIG. 2. Selected effective potentials $W^{J^e}_{vj\lambda;vj\lambda}(R)$ for (a) low and (b) high J values, see Eq. (26), energies of the lowest resonances supported by the potentials (red lines), and effective potentials $W'^{J'^e}_{v'j'\lambda';v'j'\lambda'}(R)$ governing dynamics of the product system in states which are accessed in radiative transitions from the resonances by virtue of the selection/propensity rules $\Delta J = \pm 1$, $\Delta j = 0$, and $\Delta\lambda = 0$. The latter potentials are shown relative to their respective asymptote $\varepsilon'_{v'j'=0}$. The yellow arrows indicate the ranges of the product continuum states which should most strongly be populated in transitions from the resonances $(b\,k\,v_R\,J) = (2\,2\,2\,5)$, $(2\,2\,0\,18)$, and $(0\,0\,1\,20)$. They are predicted by a model in which the transitions amplitudes are evaluated using only the $(v\,j\,\lambda) = (0\,b\,k)$ component of resonance function and single component continuum functions within the potentials $W'^{J'^e}_{v'bk;v'bk}(R)$ for $v' = 0 - 3$. The yellow wavy lines represent squared modula of the continuum functions.

where

$$\mathbf{d}^{J'p'\,Jp}(R) = \langle \mathbf{\Phi}'^{J'M'p'} | d_q | \mathbf{\Phi}^{JMp} \rangle_y \, \frac{\sqrt{2J'+1}}{C(J1J',Mq\,M')\sqrt{2J+1}}$$

and $d_q(R, y) = d_Z(r, R, \theta)\, D^1_{0,q}(\phi_R, \theta_R, \psi)$ with $D^1_{0,q}$ denoting element of Wigner rotation matrix.[30] It is assumed that d_X component of the dipole vector $\mathbf{d}(\mathbf{r}, \mathbf{R})$ can be totally neglected. Thus,

$$[\mathbf{d}^{J'p'\,Jp}(R)]_{v'j'\lambda';vj\lambda} = C(J1J', \lambda 0\lambda') \times \sum_{L=0,2} {}'\langle v'j'|D_L(r, R)|vj\rangle_r \, g^\lambda_L(j', j), \tag{29}$$

where the functions $D_L(r, R)$ come from the expansion of $d_Z(r, R, \theta)$ in terms of the Legendre polynomials $P_L(\cos\theta)$ (see Fig. 1(b)).

IV. 3D OPTICAL POTENTIAL MODEL

A. "Complete" version

The Hamiltonian matrices $\mathbf{H}^{Jp}(R)$ which describe in the CC-BF-diabatic representation the low-energy dynamics of the $He^+ + H_2$ system in the A channel are augmented with skew-hermitian parts $-\frac{\imath}{2}\,{}^{\rm opt}\mathbf{W}^{Jp}(R)$ whose role is to account for the total quenching of the He^+ ions due to the radiative transitions to the X channel, i.e., to all continuum and bound states, $E' \in [-1763.5, \sim 21\,400]\ \mathrm{cm}^{-1}$.

The quenching due to the joint reaction RA + RCT + iRaT (:=trad) is described by the optical potential (see Fig. B2 of Ref. 25)

$${}^{\rm opt}V(r, R, \theta) = -\frac{\imath}{2}\,\frac{4}{3c^3\hbar^3}\, d^2_Z(r, R, \theta)\, \Delta V(r, R, \theta) \tag{30}$$

in which $\Delta V = \Delta E + V^A - \overline{V}^X$ with $\overline{V}^X = V^X + V^X_{\rm HH}$ represents the average energy of emitted photons. It may be viewed as a 3D generalization of the optical potential widely used in calculations on the radiative reactions in atomic systems.[22–24,31–33] The elements of the matrix ${}^{\rm opt}\mathbf{W}^{Jp}(R) = 2\imath\langle \mathbf{\Phi}^{JMp}|\,{}^{\rm opt}V\,|\mathbf{\Phi}^{JMp}\rangle_y$ (see Fig. 3) are evaluated using the formula

$$[{}^{\rm opt}\mathbf{W}^{Jp}(R)]_{\tilde{v}\tilde{j}\tilde{\lambda};vj\lambda} = \frac{4}{3c^3\hbar^3}\,\delta_{\tilde{\lambda},\lambda}\,[[\mathbf{d}^\lambda(R)]^\dagger \times [\Delta\mathbf{V}^\lambda(R)]^3\,\mathbf{d}^\lambda(R)]_{\tilde{v}\tilde{j};vj}, \tag{31}$$

where

$$[\mathbf{d}^\lambda(R)]_{\tilde{v}\tilde{j};vj} = \sum_L \langle \tilde{v}\tilde{j}|D_L(r, R)|vj\rangle_r \, g^\lambda_L(\tilde{j}, j), \tag{32}$$

and

$$[\Delta\mathbf{V}^\lambda(R)]_{\tilde{v}\tilde{j};vj} = \sum_L \langle \tilde{v}\tilde{j}|V^A_L(r, R) - \overline{V}^X_L(r, R) \times |vj\rangle_r \, g^\lambda_L(\tilde{j}, j) + \delta_{\tilde{v},v}\delta_{\tilde{j},j}\,\Delta E. \tag{33}$$

Like in cases of molecular potentials, these elements do not depend on the quantum number J and do not mix states with different values of λ. The latter property is not an effect of the approximation $\mathbf{d}^2 \approx d^2_Z$; it would also hold true when the component d^2_X were included. (Appropriate formulas will be presented elsewhere.)

The Schrödinger equation with the non-hermitian Hamiltonian $\mathbf{H}^{Jp}(R) - \frac{\imath}{2}\,{}^{\rm opt}\mathbf{W}^{Jp}(R)$ is solved for the scattering

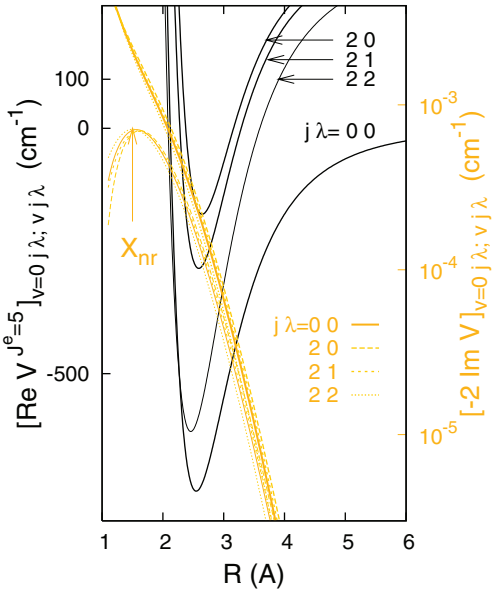

FIG. 3. Examples of complex effective potentials $V^{J^e}_{vj\lambda;\,vj\lambda}(R) = [\mathbf{W}^{J^e}(R) + i\mathrm{Im}\mathbf{V}^{J^e}(R)]_{vj\lambda;\,vj\lambda}$ that appear in the present implementation of the optical potential approach. The unlabeled yellow lines represent the matrix elements ${}^{\mathrm{opt}}W_{vj\lambda;\,vj\lambda}(R) = -2\mathrm{Im}[\mathbf{V}^{J^e}(R)]_{vj\lambda;\,vj\lambda}$ of the 3D optical potential in the BF-diabatic basis, see Eq. (31). The lines labeled with X_{nr} show the respective matrix elements ${}^{\mathrm{opt}}_{X_4}W^{J^e}_{vj\lambda;\,vj\lambda}(R)$ of the optical potential projected onto the nonreactive subspace of the X channel, see Eq. (37).

matrix $\mathbf{S}^{Jp}(E)$ and the unitarity defect of this matrix is converted to the rate $\frac{\partial}{\partial E}R^{\mathrm{trad}}_{vj}(EJp)\,dE$ of the radiative quenching from states $([E, E+dE]Jp, vj)$,

$$\frac{\partial}{\partial E}R^{\mathrm{trad}}_{vj}(EJp) = \frac{1}{2\pi\hbar}\sum_{l}[\mathbf{I} - \mathbf{S}^{Jp\,\dagger}\mathbf{S}^{Jp}(E)]_{vjl;\,vjl}. \quad (34)$$

In the vicinity of resonance $\mathcal{R}^{Jp}_n$,

$$\frac{\partial}{\partial E}R^{\mathrm{trad}}_{vj}(EJp) = \frac{\partial}{\partial E}R^{\mathrm{trad(bck)}}_{vj}(EJp) + p^{Jp}_{n,vj}(E)\,\frac{1}{\hbar}\Gamma^{Jp\,\mathrm{trad}}_n, \quad (35)$$

where the first term on rhs represents a background, a slowly varying function of the energy E, and $p^{Jp}_{n,vj}(E)$ in the second term is the Lorentzian defined in Eq. (17), having the width at half maximum determined by both the dissociative Γ^{Jp}_n and the total radiative width $\Gamma^{Jp\,\mathrm{trad}}_n = \Gamma^{Jp\,\mathrm{RCT+iRaT}}_n + \Gamma^{Jp\,\mathrm{RA}}_n$ of the resonance. It should be noted that the "broadened" Lorentzian $p^{Jp}_{n,vj}(E)$ appears here without the extra operation described in Sec. II E. This is due to the fact that the matter-radiation interaction included into the optical potential is treated on equal footing with the molecular interactions, i.e., not as a perturbation (see Table BI of Ref. 25). Practically, the widths $\Gamma^{Jp\,\mathrm{trad}}_n$ together with the other parameters ($E^{Jp\,\mathrm{res}}_n$ and $\Gamma^{J}_{n,vj}$) of the profile $p^{Jp}_{n,vj}(E)$ are extracted from the values of $\frac{\partial}{\partial E}R^{\mathrm{trad}}_{vj}(EJp)$ calculated according to Eq. (34) by a least-squares fitting to the formula (35) with the E-dependence of the background term represented by a second order polynomial (details in Eqs. (B7)–(B12) and Table BV of Ref. 25).

The rates $\frac{\partial}{\partial E}R^{\mathrm{trad}}_{vj}(EJp)$, the resonance widths $\Gamma^{Jp\,\mathrm{trad}}_n$, the related cross-sections: partial $\sigma^{\mathrm{trad}}_{vj}(EJp) = \frac{2\pi^2\hbar}{k^2_{vj}}\frac{\partial}{\partial E}R^{\mathrm{trad}}_{vj}(EJp)$ and total $\sigma^{\mathrm{trad}}_{vj} = \sum_{Jp}(2J+1) \times \sigma^{\mathrm{trad}}_{vj}(Jp)$, and the rate constant

$$k^{\mathrm{trad}}_{vj}(T) = \int_{\varepsilon_{vj}}^{E_{\max}} P^{j}(E,T)\sum_{J}\sum_{p}(2J+1)\,\frac{\partial}{\partial E}R^{\mathrm{trad}}_{vj}(EJp)\,dE \quad (36)$$

are believed to represent fully convergent characteristics of the total radiative quenching of the He^+ ions in low energy collisions with the H_2 molecules. Upon subtraction of the respective quantities for the RA reaction, determined rigorously in paper II, convergent values are obtained for the global characteristics of the RCT + iRaT reaction such as $\sigma^{\mathrm{RCT+iRaT}}_{vj}(E)$ and $k^{\mathrm{RCT+iRaT}}_{vj}(T)$.

B. $X_{N_{v'}}$ projected version

Of much help in completing the task of the present study turns out here to be a version of the 3D optical potential called "$X_{N_{v'}}$ projected." It is designated to provide an inexpensive way to monitor the convergence of the global characteristics of the radiative $A \to X$ processes with increasing size of the basis $\Phi'^{J'M'p'}$ used to describe the terminal states in the processes. Savings result from omitting the determination and the subsequent integration of the E'-resolved transition rates which would be necessary for each basis size when the state-to-state approach were exploited. In this version (see Fig. 3),

$${}^{\mathrm{opt}}_{X_{N_{v'}}}\mathbf{W}^{Jp}(R) = \frac{4}{3c^3\hbar^3}\sum_{J'=|J-1|}^{J+1}[\mathbf{d}^{J'p'\,Jp}(R)]^{\dagger} \times [\Delta\mathbf{V}^{J'p'}(R)]^3\,\mathbf{d}^{J'p'\,Jp}(R), \quad (37)$$

where $\mathbf{d}^{J'p'\,Jp}(R)$ is the transition dipole matrix defined in Eq. (29) and

$$\Delta\mathbf{V}^{J'p'}(R) = \Delta E\mathbf{I} + \langle\mathbf{\Phi}'^{J'M'p'}|V^A|\mathbf{\Phi}'^{J'M'p'}\rangle_y - \mathbf{W}'^{J'p'}(R) \quad (38)$$

represents average photon energy in transitions to the subspace of (all bound and a part of continuum) ro-vibrational states in the channel X which is spanned by the basis $\mathbf{\Phi}'^{J'M'p'}$ including $N_{v'}$ $(=v'_{\max}+1)$ lowest v' states of H^+_2, called the $X_{N_{v'}}$ subspace. The subspace X_4 is particularly important because the represented interval of the energy E', with the upper boundary $E'_{\max}(X_4) \simeq 7800\ \mathrm{cm}^{-1}$ (see Sec. V C), lies *practically* entirely below the threshold for the proton transfer reaction. The probability of the iRaT via transitions to states within the subinterval lying actually above the threshold, 6487–7800 cm^{-1}, is estimated as nearly 100 times smaller than the probability of the RCT in transitions to states in the entire 0–7800 cm^{-1} interval (details in Fig. A19). Therefore the subspace X_4 is called the 'nonreactive subspace' and is alternatively denoted with X_{nr}. The dependence of $\Delta\mathbf{V}^{J'p'}(R)$ on the quantum number J' comes from the presence of the kinetic energy term $(\sim\mathbf{c}^{J'p'}/R^2)$ in the matrix $\mathbf{W}'^{J'p'}(R)$. This term plays some role in enhancing consistency of results from the model with results from the state-to-state approach (details in Eqs. (B4)–(B6) and Figs. B3 and B4 of Ref. 25).

Instead of solving the coupled equations with the matrices $\mathbf{W}^{Jp}(R) - \frac{\imath}{2}\,{}^{\rm opt}_{X_{N_{v'}}}\mathbf{W}^{Jp}(R)$, the distorted-wave approximation is applied to account for the opt-part giving the following formulas:

- for the rate of radiative transitions from the A-channel continuum states $([E, E+dE]Jp)$ to the $X_{N_{v'}}$ subspace,

$$\frac{\partial}{\partial E} R_{(\to X_{N_{v'}})}(EJp)\,dE = \frac{1}{\hbar}\mathrm{Tr}\,\langle \mathbf{F}^{(+)Jp}(E)| \times {}^{\rm opt}_{X_{N_{v'}}}\mathbf{W}^{Jp}\,|\mathbf{F}^{(+)Jp}(E)\rangle\,dE, \tag{39}$$

  where $\mathbf{F}^{(+)Jp}(E;R)$ denotes $N \times N_{\rm o}$ matrix of radial functions of the A-channel state determined within the state-to-state approach, i.e., by solving the CC equations with the matrix $\mathbf{W}^{Jp}(R)$,
- for the width of the A-channel resonance $\mathcal{R}_n^{Jp}$ due to the radiative decay to the $X_{N_{v'}}$ subspace

$$\Gamma^{Jp}_{n\,(\to X_{N_{v'}})} = \langle \mathbf{F}_n^{B\,Jp}|\,{}^{\rm opt}_{X_{N_{v'}}}\mathbf{W}^{Jp}\,|\mathbf{F}_n^{B\,Jp}\rangle, \tag{40}$$

  where $\mathbf{F}_n^{B\,Jp}(E_n;R)$ denotes N-dim. vector of radial functions of a bound state which approximates the resonance.

V. CALCULATIONS

The calculations within the state-to-state approach of Sec. III are designed to eventually provide the temperature averaged characteristics of the RCT reaction for temperatures not substantially exceeding 40 K. As already pointed out, the range of the reactant energy $[0, E_{\rm max}]$ which is appreciably populated at such temperatures is rather small: setting $E_{\rm max} = 150$ cm^{-1} is practically sufficient. In this range, only the $v=0\,j=0$ channel of the $He^+ + H_2(I=0)$ reactants is open. At thermal equilibrium, the reaction with the ortho-hydrogen becomes possible at $E > \varepsilon_{01}(=118.4\ \mathrm{cm}^{-1})$ and therefore the contribution of the $v=0\,j=1$ channel to the rate function $k(T)$ may be expected to be totally insignificant at temperatures below 20 K. Actually, this contribution is neglected in the entire temperature range scanned which is 0.1 μK–50 K.

The calculations within the optical potential approach of Sec. IV A are designed to provide fully convergent values of the rate constant of the RCT + RA + iRaT reaction for temperatures up to 100 K. The range of the energy E covered in these calculations extends from 10^{-8} up to 354 cm^{-1} (the ε_{02} threshold).

In the whole of the calculations done in this work, three major stages can be distinguished. They are briefly described in Subsections V A–V C.

A. Dynamics in the *A* channel: $He^+ + H_2$

The dynamics was investigated in our previous work (Paper II) in the range of E up to 300 cm^{-1}. The pattern of energy levels of bound and quasi-bound states of the $He^+ - H_2$ complex found in the range is typical of weakly bound atom-diatom complexes of intermediate anisotropy strength and T-shaped equilibrium geometry. The states are fully assignable with the set of six quantum numbers v_r, b, k, v_R, J, and p. Of the four approximate numbers, v_r and b correlate with the v and j state of the H_2 subunit, respectively, k denotes the nearly preserved value of the quantum number λ, and v_R describes the atom-diatom vibrations.

In this work, the previous calculations on the $He^+ - H_2$ complex are extended to achieve the following specific goals: (i) to determine energies and dissociative widths of all quasi-bound states in the range up to the $v=0\,j=2$ threshold and of "vibrational" ($J=k$) states associated with several higher thresholds ($j=4$ and $v=1\,j=0-4$), (ii) to compare properties of rotational and vibrational predissociation of the complex, (iii) to rationalize correlations of the rotational predissociation widths with the quantum numbers assigned to the states. Calculations concerning goals (i) and (ii) are performed within the approach of Sec. III using the basis size controlling parameters: $v_{\rm max}=3$, $j_{\rm max}=13$, and $\lambda_{\rm max} = \min(3, b+1)$. To realize goal (iii), an adiabatic representation of the A-channel Hamiltonian is constructed, via diagonalization of the matrix $\mathbf{W}^{Jp}(R)$ of Eq. (26), and within this representation, the perturbative resonance theory of Fano[34] and Mies[35] is implemented. The treatment extends the popular adiabatic bender model[19,36] in that it accounts for the associated nonadiabatic bending-stretching couplings which drive the predissociation (details are given in part C of Ref. 25).

B. Dynamics in the *X* channel: $He + H_2^+$

The dynamics on the present PES was previously investigated in the following aspects. First, energies of $J'=0$–2 bound states, energies and widths of $J'=k'=0$ resonances in the range of the energy E' up to ∼2200 cm^{-1} were determined and presented together with the PES itself in Ref. 19. All bound states $[E'<0\,(58.2)$ for $I=0\,(1)]$ and all non-broad resonances ($\Gamma' < 1$ cm^{-1}) in the subrange up to 300 cm^{-1} were determined in the calculations on the RA reaction (4) in Paper I. Second, the role of the Coriolis coupling and the separability of vibrational modes of motion in the bound and long-living resonance states was tested by applying different decoupling schemes[18,19] and the natural expansion analysis.[15]

In this work, the X-channel dynamics is characterized to a much wider extent. One of the motivating facts is that knowing all sharp resonances $\mathcal{R}'^{J'p'}$ and also other, broader, structures in the energy density of continuum states $(E'J'p')$ for the E' range up to ∼6500 cm^{-1} and for J' values up to ∼20 is necessary/requisite for the evaluation of the $A \to X$ transition amplitudes according to the theory of Sec. II E. Since no approximate scheme could be devised for a reliable prediction of the structures, the most straightforward (and tedious) way is adopted. Namely, for each needed J' value (and parity p') the lifetime matrix[37] $\mathbf{Q}'^{J'p'}$, more specifically, its maximal eigenvalue $q'^{J'p'}_{\rm max}$ is determined as function of E' from the solutions $\mathbf{F}'^{J'p'}(E';R)$ of the Schrödinger equation with the Hamiltonian $\mathbf{H}'^{J'p'}(R)$ at a grid of points E'_i covering the entire range of interest with the spacing $E'_{i+1} - E'_i$ of 0.5 (1.0) cm^{-1} for $J' \le (>)10$. Peaks found in the function $q'^{J'p'}_{\rm max}(E')$, if narrower than 1 cm^{-1}, are next analyzed for the positions $E'^{J'p'{\rm res}}$ and

widths $\Gamma'^{J'p'}$ of the pertinent resonances using the procedure of Ref. 38.

The second motivation for an extended study of dynamics of the He + H_2^+ system is the need for information which can aid an analysis of the calculated final-state specific characteristics of the RCT. Accompanying goals are: (i) to identify quasi-bound states of the He–H_2^+ complex which predominantly decay by vibrational predissociation, to verify the previous predictions,[19] and (ii) to further expose the differences between this complex and its charged-transferred counterpart. For these goals, the functions $\Psi'^{(+)J'M'p'}(E'; \mathbf{r}, \mathbf{R})$ are inspected for the degree of mixing of different λ', v', and j' components at resonance energies $E' = E'^{J'p'res}$, for the nodal patterns in the θ and R dependencies within the strong-interaction region ($R \leq 4$ Å). Quantities suitable for displaying the properties are introduced by referring to the concept of the sojourn-time[39] of collision system in a confined region of the configuration space (details are given in Eqs. (A1)–(A10) of Ref. 25).

In all the lifetime and sojourn-time calculations, the basis $\Phi'^{J'M'p'}$ is built of the $(v'\ j')$ states spanning the nonreactive subspace X_4 of the X channel as defined in Sec. IV B, i.e., $v'_{max} = 3$ and $j'_{max} = 14$. The parameter λ'_{max} controlling the CCr approximation is set to 4 (adequacy of the approximation is tested in Fig. A17 of Ref. 25). This basis, also called "X_4 basis," leads to maximally $N' = 136$ coupled $(v'\ j'\lambda')$ states.

C. Radiative *A* → *X* transitions

The free-free transition amplitudes $T_{v'j'l';vjl}(E'J'p'; EJp)$, Eqs. (13) and (28), are evaluated for $v = 0$, $j = 0$, $J = 0$–20, and $J' = J \pm 1$ at sets of the energy points $\{E_i, E'_{i'}\}_{i=1,\,i'=1}^{M,\,M'}$ chosen to cover the E range of 10^{-7}–150 cm^{-1} and the E' range of 0.1–7800 cm^{-1}, in calculations for the X_4 subspace, or the range of 0.1–11 000 cm^{-1}—in calculations for the X_6 subspace (with $v'_{max} = 5$ and max $N' = 199$; see Fig. A18 of Ref. 25). Evaluation of the $J' = J$ amplitudes is skipped because they are very small. The number M of E_i points changes slightly with the value of J and is ∼15–25. The grid of $E'_{i'}$ points, adapted to the behavior of the function $q'^{J'e}_{max}(E')$, depends in turn strongly on the value of J'. On average, about 1500 points are used to cover the X_4 interval in $J' < 10$ cases. The number M' decreases to about 800 when $J' > 16$. To cover the X_6 interval, the numbers M' for the different J's are increased by about 300 to 200.

In the considered range of the energy E, there are 48 sharp resonances $\mathcal{R}_n^{Jp}$ with $n = (b\ k\ v_R)$ that pertain to quasi-bound states of the He^+–$H_2(I = 0)$ complex. Their J values range from 0 to 22, $p = 1$, and $b = 0$, 2. For transitions from these resonances, the amplitudes $T_{v'j'l'}(E'J'p'; E_n^{B_Q}Jp)$ are evaluated for all allowed final J' values. The grids of $E'_{i'}$ points are even denser than in the evaluation of the free-free amplitudes. For example, about 2000 (2300) points in the X_4 (X_6) intervals are used when $2 \leq J' \leq 5$.

The energy interval associated here with each basis (subspace) $X_{N'_v}$ is not quite arbitrary. The integrations over the energy E' of the width and rate functions determined with each basis $X_{N'_v}$ should be converged with respect to the upper integration limit $E'_{max}(X_{N'_v})$ in order to achieve consistency with results of the respective $X_{N'_v}$ projected version of the optical potential model. Because of this requirement, the limit for the X_4 subspace cannot be exactly at the threshold $\varepsilon''_{00} = 6487\ cm^{-1}$.

In the (truly) nonreactive range of E' (<6487 cm^{-1}) about 30 sharp resonances $\mathcal{R}_m'^{J'p'}$ are found with $J' = 1$–20, $p' = \pm 1$, and $k' \leq 3$. To include transitions to these resonances, the free-resonance amplitudes $T_{00J}(E'^{B_{Q'}}J'p' = 1; EJp = 1)$ at E_i points used in the respective free-free cases and all nonzero resonance-resonance amplitudes $T(E_m'^{B_{Q'}}J'p'; E_n^{E_{B_Q}}Jp)$ are evaluated.

All the transition amplitude evaluations necessary in the state-to-state part of the study as well as all the **S** matrix evaluations within the optical potential model are performed with the help of the log-derivative method[40] and its versions generalized to inhomogeneous coupled equations.[41,42]

VI. RESULTS AND DISCUSSION

The discussion focuses on results obtained at the main stage of the calculations—for the $A \rightarrow X$ transitions. Results of the calculations described in Secs. V A and V B are only quoted to support several points of the discussion. Their full presentation is enclosed in the supplementary material.[25] All results presented here in Secs. VI A–VI C, VI D 1, and VI F concern transitions from states of the $He^+ + H_2$ system below the ε_{01} threshold. Thus, always $(v\ j) = (0\,0)$ and $p = 1$; these values are omitted in most of the symbols used in these subsections.

A. State-to-state transition rates

Starting first with the A-channel continuum Fig. 4 gives examples of the calculated (J, J')- resolved doubly differential

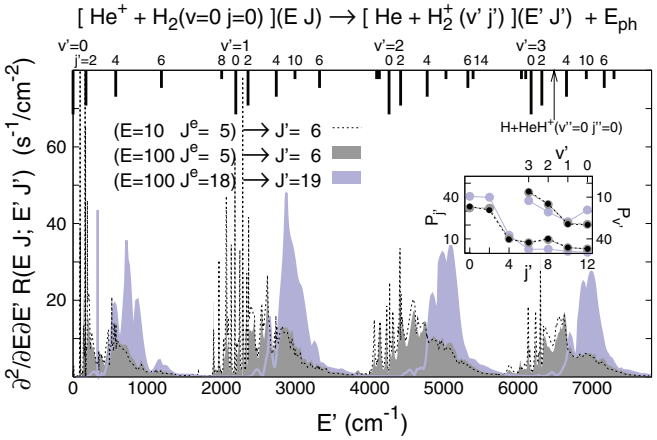

FIG. 4. Energy differential rates $\frac{\partial^2}{\partial E \partial E'} R^{RCT(bck)}(EJ; E'J')$ for free→free + resonance transitions specified in the labels. The energy E is given (in cm^{-1}) relative to the $He^+ + H_2(v = 0, j = 0)$ threshold and the energy E' is given relative to $He + H_2^+(v' = 0, j' = 0)$. The sticks in the upper part of the figure show the positions of the $v'\ j'$ thresholds and the threshold for the rearrangement $He + H_2^+ \rightarrow H + HeH^+$ reaction. In the inset are the populations $P_{c'}(EJ; J') \times 100\%$ of rotational ($c' = j'$) and vibrational ($c' = v'$) states of the H_2^+ ion resulting from the shown transitions, see Eq. (41).

rates $\frac{\partial^2}{\partial E\,\partial E'} R^{\mathrm{RCT(bck)}}(EJ;E'J')$,

$$\frac{\partial^2}{\partial E\,\partial E'} R^{\mathrm{RCT(bck)}}(EJ;E'J') = \sum_{v'}\sum_{j'} \frac{\partial^2 R^{\mathrm{RCT(bck)}}_{00\to v'j'}(EJp=1;E'J'p')}{\partial E\,\partial E'} = \sum_{v'} \frac{\partial^2}{\partial E\,\partial E'} R^{\mathrm{RCT(bck)}}_{\to v'}(EJ;E'J') = \sum_{j'} \frac{\partial^2}{\partial E\,\partial E'} R^{\mathrm{RCT(bck)}}_{\to j'}(EJ;E'J'),$$

as functions of the X-channel energy E' for two A-channel energies E and for two values of J. The low J functions display broad peaks around the v' thresholds with superimposed sharper peaks of various heights whereas for the high J value peaks are shifted considerably towards higher energies E' and the shape of the peaks is smoother. The broad features, especially their parts lying above the v' thresholds are due to free-free transitions. The sharp peaks originate from transitions to the X-channel resonances with dissociative widths Γ of the order of 0.1 cm^{-1}.

Comparing among each other the gray peak areas associated with the subsequent v' thresholds one notices that the $v'=0$ peak is smaller than the $v'=1-3$ peaks. This also holds for the high J results (light blue peaks). The sizes of the v' peaks in the rate functions directly reflect the relative magnitude of the $v=0\to v'=0,1,2,3$ matrix elements of the $A\to X$ electric dipole transition function plotted in Fig. 1. The fact that the $v=0\to v'=0$ element is smaller than the others is due to the large difference in the bond distances of H_2 compared to H_2^+.

In the inset of Fig. 4, populations $P_{c'}(EJ;J')$ of vibrational ($c'=v'$) and rotational ($c'=j'$) states of the H_2^+ ion are shown resulting from the three $(EJ)\to J'$ transitions of the figure. The populations are defined as the ratios of the E'-integrated rates in the range, i.e., in the X_{nr} subspace,

$$P_{c'}(EJ;J') = \frac{\partial}{\partial E} R^{\mathrm{RCT_{nr}(bck)}}_{\to c'}(EJ;J') \Big/ \frac{\partial}{\partial E} R^{\mathrm{RCT_{nr}(bck)}}(EJ;J') \quad \text{for} \quad c'=v',j'. \tag{41}$$

The populations are at large R distances, where the H_2^+ ion does not interact with He.

The populations of vibrational states resulting from the transitions $J=5\to J'=6$ at $E=10$ and $E=100$ cm^{-1} do not reflect the relation between the v' peaks in the respective rate functions. The values of $P_{v'=0}$ are larger than those of $P_{v'=1}$ which can be interpreted as a result of inelastic rovibrational transitions in the X channel. As shown in Fig. 1(a), the strength of the potential couplings $\langle v'|V^X_{L=2}|v'-1\rangle_r$ driving these transitions is substantial. For high J' values the region of inelasticity becomes shielded by the centrifugal potentials and the peak population is therefore not shifted to $v'=0$.

The populations of rotational states of the H_2^+ ions are also affected by the inelastic transitions in the X channel. They would be more strongly peaked at $j'=0$ if they were only determined by properties of the initial states (dominated by

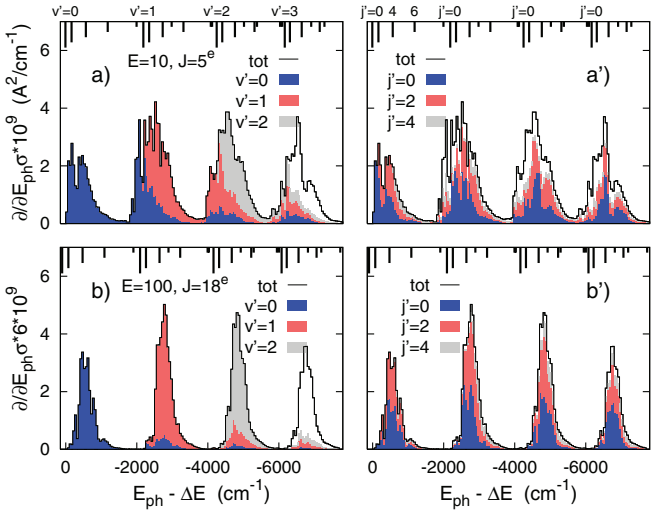

FIG. 5. (a) and (b) Partial photon-energy-differential cross-sections $\frac{\partial}{\partial E_{\mathrm{ph}}}\sigma^{\mathrm{RCT(bck)}}(EJ;E_{\mathrm{ph}})$ for two (EJ)-states of the reactant system $He^+ + H_2(v=0,j=0)$ and their resolutions into cross-sections $\frac{\partial}{\partial E_{\mathrm{ph}}}\sigma^{\mathrm{RCT(bck)}}_{\to v'}(EJ;E_{\mathrm{ph}})$ and $\frac{\partial}{\partial E_{\mathrm{ph}}}\sigma^{\mathrm{RCT(bck)}}_{\to j'}(EJ;E_{\mathrm{ph}})$ which describe transitions to specific v'- and j'-states of the product ion H_2^+. The histograms are built of average values of the cross-sections in the intervals $\Delta E_{\mathrm{ph}} = 50$ cm^{-1}. The photon energy is shown relative to the separation $\Delta E = 74\,507$ cm^{-1} between the thresholds $He^+ + H_2(v=0,j=0)$ and $He + H_2^+(v'=0,j'=0)$.

$j=0$ component) and by the propensity rules, $\Delta j=0$ and $\Delta\lambda=0$, resulting from the properties of the $A\to X$ transition dipole vector field $\mathbf{d}(r,R,\theta)$. The fact that $\mathbf{d}$ here is parallel to the body-fixed Z axis is obviously the cause of preserving λ in the transitions (see Sec. III). The tendency to preserve the rotational j state is caused by small anisotropy of $d_Z(r,R,\theta)$. It is shown in Fig. 1(b) that the $L=2$ anisotropy strength function $\langle D_{L=2}(r,R)\rangle_r$ is smaller than the $L=0$ function at R values within the well of the A-state PES by a factor ranging from ~10 at $R=2$ Å to ~2 at $R=4$ Å.

A more detailed analysis of the influence of X-channel interactions on the v'- and j'-state populations in transitions from the A-channel continuum is presented in Fig. 5. For two of the states (EJ) shown in Fig. 4, plots are shown of the photon-energy-differential cross-sections

$$\frac{\partial}{\partial E_{\mathrm{ph}}}\sigma^{\mathrm{RCT(bck)}}(EJ;E_{\mathrm{ph}}) = \frac{\pi^2\hbar^3}{\mu E}\sum_{J'=J-1}^{J+1}\frac{\partial^2}{\partial E\,\partial E'} R^{\mathrm{RCT(bck)}}(EJ;\widehat{E}'J') \tag{42}$$

and their resolutions

$$\frac{\partial}{\partial E_{\mathrm{ph}}}\sigma^{\mathrm{RCT(bck)}}(EJ;E_{\mathrm{ph}}) = \sum_{c'}\frac{\partial}{\partial E_{\mathrm{ph}}}\sigma^{\mathrm{RCT(bck)}}_{\to c'}(EJ;E_{\mathrm{ph}}) \quad \text{for} \quad c'=v',j'.$$

If vibrationally inelastic transitions did not occur in the X channel, the blue, red, and gray colored areas of the peaks in the left panels of the figure would have clear cuts at the thresholds $v'=1$, $v'=2$, and $v'=3$, respectively. The actual situation, however, is different, especially in the small J case (upper left panel). The blue areas occurring within the

peaks above the $v' = 1$ threshold added to the blue area below this threshold amount to the largest population $P_{v'}(E, J)$ of the state $v' = 0$,

$$P_{c'}(E, J) = \frac{\partial}{\partial E} R^{\mathrm{RCT_{nr}(bck)}}_{\rightarrow c'}(E, J) \Big/ \frac{\partial}{\partial E} R^{\mathrm{RCT_{nr}(bck)}}(E, J)$$
$$\text{for} \qquad c' = v', j'. \tag{43}$$

In the high $J(=18)$ case (Fig. 5(b)), the largest peaks, $v' = 1$ and $v' = 2$, become filled almost entirely with red and gray colors, respectively. Consequently, the sizes of these peaks decide on the v'-state population and the maximum population shifts to $v' = 1$.

Similarly, without rotationally inelastic transitions occurring in the X-channel, all peaks in the right panels of Fig. 5 would be nearly 100% blue which would mean an almost complete reflection of the population of $j = 0$ state of the reactant H_2 molecule into the population of $j' = 0$ state of the product H_2^+ ion. In fact, however, the peaks for the $j' = 0$ population arrive here only at ∼40%.

In analogy to the transitions from the continuum states, transitions from the A-channel resonances are characterized in Figs. 6 and 7. Figure 6 gives examples of the width functions $\frac{\partial}{\partial E'}\Gamma_n^{J\,\mathrm{RCT}}(E', J')$,

$$\frac{\partial}{\partial E'}\Gamma_n^{J\,\mathrm{RCT}}(E', J') = \sum_{v'}\sum_{j'} \frac{\partial \Gamma^{\mathrm{RCT}}_{n,v'j'}(Jp = 1; E'J'p')}{\partial E'},$$

for $J \rightarrow J' = J \pm 1$ transitions from four selected resonances $\mathcal{R}_n^J$. n denotes here the three approximate quantum numbers $(b\,k\,v_R)$. In the inset the populations of v' and j' states are shown resulting from the $(nJ) \rightarrow J'$ transitions to the entire

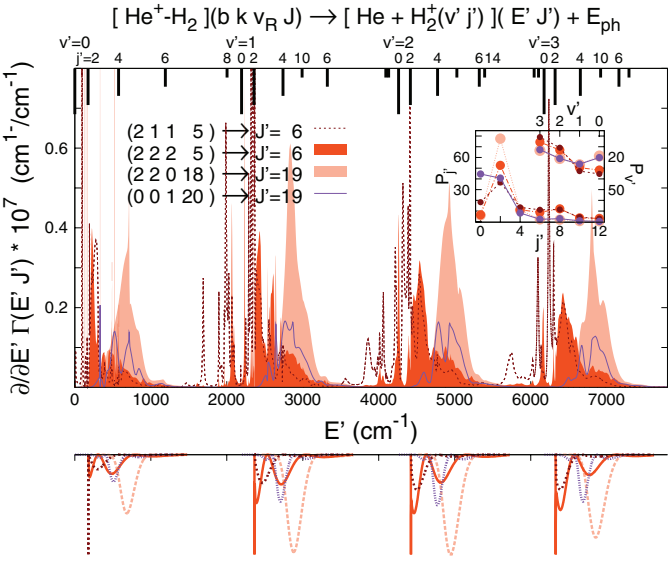

FIG. 6. Width functions $\frac{\partial}{\partial E'}\Gamma_n^{J\,\mathrm{RCT}}(E'J')$ of selected quasi-bound states of the He^+–$H_2(v = 0)$ complex. $(n\,J) = (b\,k\,v_R\,J\,p = 1)$. (Inset) The related populations (in %) of rotational and vibrational states of H_2^+ obtained from the integrated widths, $P_{c'}(nJ; J') = \Gamma^{J\,\mathrm{RCT_{nr}}}_{n,c'}(J') / \Gamma_n^{J\,\mathrm{RCT_{nr}}}(J')$ for $c' = j', v'$. (Bottom) The profiles due to resonance-free transitions obtained from the model calculations presented in Fig. 2, disregarding ro-vibrational inelasticity in the product channel.

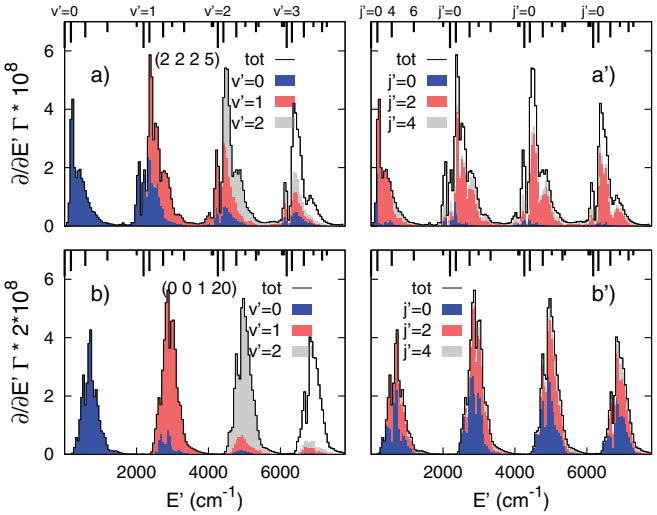

FIG. 7. (a) and (b) Widths $\frac{\partial}{\partial E'}\Gamma_n^{J\,\mathrm{RCT}}(E')$ and $\frac{\partial}{\partial E'}\Gamma^{J\,\mathrm{RCT}}_{n,c'}(E')$ for $c' = v'$ $= 0 - 3$ and $c' = j' = 0$–4 of two exemplary quasi-bound states $(n\,J)$ $= (b\,k\,v_R\,J\,p = 1)$ of the He^+–$H_2(v = 0)$ complex as functions of energy E' in the decay channel $He+H_2^+$. The histograms are built of average values of the functions in the intervals $\Delta E' = 50\ \mathrm{cm}^{-1}$.

E'-energy range displayed (the X_{nr} subspace),

$$P_{c'}(nJ; J') = \Gamma^{J\,\mathrm{RCT_{nr}}}_{n,c'}(J') \Big/ \Gamma_n^{J\,\mathrm{RCT_{nr}}}(J') \quad \text{for} \quad c' = v', j'. \tag{44}$$

Generally, the shapes of the width functions and of the corresponding populations $P_{j'}$ are more diversified compared to those in Fig. 4. This demonstrates the impact of the properties of the initial resonance state functions at R values in the range $\sim 2 - 4$ Å. Differences between the characteristics of resonances with different quantum numbers n are more pronounced compared to changes among continuum functions within the E-energy range 10–100 cm^{-1}.

The overall dependence of the width functions $\frac{\partial}{\partial E'}\Gamma_n^{J\,\mathrm{RCT}}(E', J')$ on the quantum number J is essentially the same as in Fig. 4: structures surrounding the j' $= 2$ thresholds, sharply peaked in their lower energy halves, occur in the two low $J(=5)$ cases whereas broad peaks, shifted considerably above the thresholds, occur in the two high $J(=18, 20)$ cases. This is due to the large differences in the minimum geometries of the A- and X-channel potentials $(R^A_{\mathrm{min}} - R^X_{\mathrm{min}} = 0.81$ Å and $\theta^A_{\mathrm{min}} - \theta^X_{\mathrm{min}} = \frac{\pi}{2})$. Therefore, the wells in the effective potentials $W^J_{vj\lambda=j;vjj}(R)$, which are the deepest compared to their $\lambda < j$ counterparts, fill up with growing J less quickly than the wells $W^{J'}_{v'j'\lambda'=j';v'j'j'}(R)$, the shallowest compared to the $\lambda' < j'$ wells, fill up with growing J'. If the well $W^J_{v=0bk;0bk}(R)$ supporting a given resonance $(b\,k\,v_R\,J)$ lies over the wells of the potentials $W^{J'}_{v'j'=b\lambda'=k;v'bk}(R)$ for $J' = J \pm 1, J$ (as it occurs in the cases of the $J = 5$ and $J' = 6$ potentials shown in Fig. 2(a)), the radiative transitions can terminate in the continuum states above the asymptotes of the lower potentials as well as in the resonance states lying below these asymptotes. The width functions are then combinations of resonance-resonance and resonance-free profiles. This is the case for the functions of the $J = 5$ resonances shown in Fig. 6. In the cases of high J resonances (2 2 0 18) and (0 0 1 20), the respective

effective potentials $W'^{J'}_{v'bb;v'bb}(R)$ for $b = 2$, 0 are purely repulsive as shown in Fig. 2(b). The positions and shapes of the resonance-free profiles in the width functions become essentially determined by the reflection principle.[17,43]

Obviously, the occurrence of the resonance-resonance parts in the width functions is mediated by the off-diagonal elements of the matrices $\mathbf{W}'^{J'}(R)$. Therefore, information on any details of these parts, such as positions of the sharp peaks, for example, cannot be deduced from inspection of the effective potentials. The shapes of the resonance-free parts of the width functions could, in principle, be explained with the help of a model in which the transition amplitudes were evaluated using only the largest radial component of exact resonance function, $(v\ j\ \lambda) = (0\, b\, k)$, and single component continuum functions within the potentials $W'^{J'}_{v'bk;v'bk}(R)$ for $v' = 0$–3. However, a comparison of profiles resulting from such a model, shown in the bottom of Fig. 6, with the profiles in the main panel of this figure reveals that the inelasticity in the X-channel continuum states cannot always be neglected. Inelasticity is certainly important in the case of the $b = 0$ resonance shown in the figure. The violet peaks obtained from the model are visibly shifted from the positions in the exact profile. Neglect of the rotational couplings $W'^{J'}_{v'00;v'20}(R)$ is mostly responsible for this shift. The positions of the peaks in the width functions of the (2 2 0 18) resonance are, in turn, very well reproduced by the simple model. This is because the $j' = b = 2\,\lambda' = k = 2$ state cannot directly mix with the $j' = 0$ state and the possible mixing with the $j' = 4\,\lambda' = 2$ state is much smaller.

The rotational inelasticity in the X channel manifests itself in the populations $P_{j'}(nJ; J')$ even more clearly than in the resonance width functions. The violet curve in the inset of Fig. 6 representing the populations due to transitions from the $b = 0$ resonance, (0 0 1 20), looks very much the same as the curves in the inset of Fig. 4. As already mentioned in the discussion of that figure, the tendency to preserve the $j = b = 0$ rotational state of the diatomic subunit in the radiative $A \rightarrow X$ transitions is substantially weakened by the mixing of $j' = 0$ and $j' = 2\,\lambda' = 0$ states in the X channel. The probability $P_{j'=2}$ that the product ion will be in the $j' = 2$ state becomes nearly as big as $P_{j'=0}$. All $P_{j'}(nJ; J')$ curves that pertain to $b = 2$ resonances are clearly peaked at $j' = 2$. The $\Delta j = 0$ propensity is thus generally stronger than in the cases when the initial state is a $b = 0$ resonance or a continuum state.

To describe the role of the $\Delta\lambda = 0$ rule, it is helpful to think of the radiative transitions from a given resonance $(b = 2\,k\,v_R\,J)$ as proceeding in two stages. At the first stage, the $He + H_2^+$ system is reached in the interaction region (small R's) where the $j' = 2\,\lambda' = k$ components of its continuum states are populated and then, at the stage of departure of the H_2^+ ions from the He atoms, these components are depopulated by rotational, ro-vibrational, and Coriolis interactions. The degree of this depopulation depends mainly on how effective the mixing of $j' = 2$ with $j' = 0$ state is. It is most effective when $k = 0$ and most ineffective when $k = 2$ [as indicated by the values $\frac{1}{\sqrt{5}}$ and 0 assumed for $\lambda' = 0$ and $\lambda' = 2$, respectively, by the rotational factor $g^{\lambda'}_{L=2}(0, 2)$ that enters the coupling elements $W'^{J'}_{v''0\lambda';v'2\lambda'}$, according to Eqs. (26) and (27)]. This leads to the different heights of the $P_{j'=2}$ peaks in Fig. 6 (and in Fig. 18(d)).

The populations $P_{v'}(nJ; J')$ do not exhibit any striking correlation with the quantum numbers $n = (b\,k\,v_R)$. The correlation with the number J is qualitatively the same as described above in the discussion of the populations $P_{v'}(EJ; J')$.

Figure 7 shows two examples of the width functions summed up over the final J's, $\frac{\partial}{\partial E'}\Gamma^{J\,\mathrm{RCT}}_n(E')$, and their two resolutions into parts that describe decay of the shown resonances into channels $He + H_2^+(v')$ and $He + H_2^+(j')$, respectively, cf. Eqs. (19) and (21),

$$\frac{\partial}{\partial E'}\Gamma^{J\,\mathrm{RCT}}_n(E') = \sum_{c'} \frac{\partial}{\partial E'}\Gamma^{J\,\mathrm{RCT}}_{n,c'}(E') \quad \text{for} \quad c' = v',\, j'.$$

The chosen examples, (2 2 2 5) (upper panels) and (0 0 1 20), are representative of $b = 2$ and $b = 0$ resonances and, simultaneously, of low and high J cases. The latter distinction is relevant when the resonance decay into v' channels is to be described. Actually, such description is not necessary here because it would be mostly a repetition of what was said in the comment to Fig. 5.

Comparing the resolutions presented in Figs. 7(a) and 7(b) to those in Figs. 5(a) and 5(b) (cf. also Figs. A15 and A16 in Ref. 25), one comes to the conclusion that the populations of vibrational states of the H_2^+ ion in the radiative $A \rightarrow X$ transitions are practically insensitive to the character of the initial state of the reactants, continuum or resonance state, shape ($b = 0$) or Feshbach resonance ($b = 2$). In turn, inspecting the populations of rotational states of the product ion from various states of the reactants, such as the resolutions in the right panels of Figs. 5 and 7 and the plots of $P_{j'}(nJ) = \Gamma^{J\,\mathrm{RCT_{nr}}}_{n,j'} / \Gamma^{J\,\mathrm{RCT_{nr}}}_n$ and $P_{j'}(E, J)$ in Fig. 18(b) and Fig. A15a of Ref. 25, a clear distinction between the initial $b = 2$ resonances on the one hand and the initial $b = 0$ resonances and continuum (E, J) states on the other hand is observed. The excited $j' = 2$ state is preferably populated in the former cases, $P_{j'=2} > 40\%$ and $P_{j'=2}/P_{j'\neq 2} > 2$ (when $k > 0$). In the latter cases, two states $j' = 0$ and $j' = 2$ are populated with comparable probability, $P_{j'=0} \gtrsim P_{j'=2} \approx 30\%$–$40\%$, when $J > 5$ or the state $j' = 0$ is preferred, $P_{j'=0}/P_{j'=2} \gtrsim 1.5$, when $J \leq 2$.

B. Emission spectra

Under this heading presented are quantities which involve summation/averaging of the characteristics of the individual state-to-state transitions over the initial states only.

Figure 8 shows the photon-energy-differential cross-section $\frac{\partial}{\partial E_{\mathrm{ph}}}\sigma^{\mathrm{RCT}}(E, E_{\mathrm{ph}})$ for the photon energy E_{ph}–$\Delta E \in [-7800,\ 150]\ \mathrm{cm}^{-1}$ as function of the reactant energy in the entire range considered, $E \in [0,\ 150]\ \mathrm{cm}^{-1}$. The background part of this cross-section is the sum of the partial

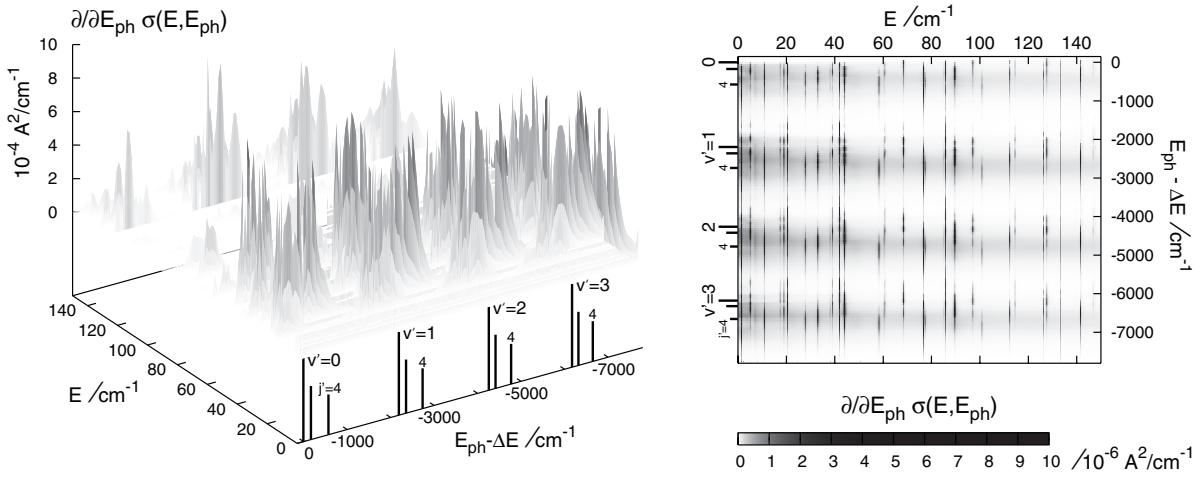

FIG. 8. Cross-section for the $\mathrm{RCT_{nr}}$ reaction $\frac{\partial}{\partial E_{\mathrm{ph}}}\sigma_{00}(E, E_{\mathrm{ph}})$ as function of reactant (E) and photon (E_{ph}) energies. $\Delta E = 74\,507\ \mathrm{cm}^{-1}$.

cross-sections of Eq. (42),

$$\frac{\partial}{\partial E_{\mathrm{ph}}}\sigma^{\mathrm{RCT(bck)}}(E, E_{\mathrm{ph}}) = \sum_{J=0}^{20}(2J+1)\frac{\partial}{\partial E_{\mathrm{ph}}}\sigma^{\mathrm{RCT(bck)}}(EJ; E_{\mathrm{ph}}),$$

and its resonance part is the sum of profiles of all 48 sharp resonances $\mathcal{R}_n^{J^e}$ which are listed in Table I, cf. Eqs. (10) and (15)–(20),

$$\frac{\partial}{\partial E_{\mathrm{ph}}}\sigma^{\mathrm{RCT(res)}}(E, E_{\mathrm{ph}}) = \frac{\pi^2\hbar^3}{\mu E}\sum_{J\,n}(2J+1)\,p^J_{n,00}(E)\,\frac{\partial}{\partial E'}\Gamma_n^{J\,\mathrm{RCT}}(\widehat{E}').$$

The two parts of the cross-section surface are exposed, respectively, in the right and left panels of Fig. 8 (note the difference in the scale factor of the third axis). The hills of the background part, the shadows parallel to the E axis, extend over the positions of the $v'\,j' = 0-4$ thresholds for $v' = 0-3$ on the E_{ph} axis. Thus, even the broad peaks of the individual rate functions $\frac{\partial^2}{\partial E\partial E'}R^{\mathrm{RCT(bck)}}(EJ; E')$ are not washed out but merely broadened by the summation over the partial states. Obviously, the sharp resonance peaks survive this operation even better. They appear in the left panel as steep "mountains" with highly irregular tops.

Integration over the energy E of the cross-section $\frac{\partial}{\partial E_{\mathrm{ph}}}\sigma^{\mathrm{RCT}}(E, E_{\mathrm{ph}})$ multiplied by $E_{\mathrm{ph}}\times\frac{\mu E}{\pi^2\hbar^3}$ and by the Boltzmann factor $P(E, T)$ gives the spectral density of photon emission from the RCT reaction at temperature T, Eq. (9). The spectrum $\mathcal{I}(E_{\mathrm{ph}}, T)$ at $T = 20$ K from the $\mathrm{RCT_{nr}}$, i.e., for E_{ph}–$\Delta E \in [-7800, 0]\ \mathrm{cm}^{-1}$, is presented together with the spectrum from the RA reaction in Fig. 9. Due to the applied averaging over the subsequent intervals $\Delta E_{\mathrm{ph}} = 50\ \mathrm{cm}^{-1}$, the spectrum has a simple appearance of broad, regularly spaced peaks, with centers at the photon energies nearly equal to the separations of the $v'\,j' = 2$ thresholds in the product channel, for $v' = 0, 1, 2, 3$, from the $v = 0\ j = 0$ threshold in the reactant channel. The highest is the $v' = 1$ peak, with top intensity at $E_{\mathrm{ph}} \approx 72\,180\ \mathrm{cm}^{-1}$. The peak near the $v' = 2$ threshold, expected by Hooper to be the highest one, is actually the second highest. Moreover, the photon-wave length corresponding to this peak—142.8 nm—is smaller than Hopper's prediction (152 nm) mostly because it also accounts for the well depth of the A-state PES relative to the $v = 0\ j = 0$ threshold which is 3351 cm^{-1} (see Fig. B2b of Ref. 25). The transitions are from the near threshold region, not from the bottom of the well.

The RA spectrum appears in the wing of the $v' = 0$ peak as two rather narrow columns of disparate heights, the higher being about 1.5 times lower than the main $v' = 0$ peak. Very similar features also appear in the wing of the $v' = 1$ peak. Their counterparts in the $v' = 2, 3$ peaks are barely discernible. This reflects the properties of the energy level structures of the He–$H_2^+(I = 0)$ complex below the subsequent v' thresholds (see Tables AI– AV and Figs. A8– A12 of Ref. 25).

All peaks in Fig. 9 are covered with two colors in the proportion which reflects the contributions of transitions from two groups of the reactant states, the continuum states and $b = 0$ resonances in one group (light blue) and the $b = 2$ resonances in the other. The contribution of the latter group is definitely larger.

The total colored area in the range of negative energies E_{ph}–ΔE gives the emission intensity $\mathcal{I}^{\mathrm{RCT_{nr}}} = 37.1\times10^{-33}$ W cm^3. The gray and blue areas at E_{ph}–$\Delta E > 0$ taken together represent the intensity $\mathcal{I}^{\mathrm{RA}} = 2.0\times10^{-33}$ W cm^3. The $b = 2$ resonance contribution to $\mathcal{I}^{\mathrm{RCT}}$+$\mathcal{I}^{\mathrm{RA}}$ is as large as 75%. Nearly 50% of this contribution is made by the two near threshold resonances (2 2 2 5) and (2 1 1 4).

C. Transition rates partially summed-up over final states

Results to be presented in this subsection concern rates of radiative transitions from individual reactant states, partial continuum or quasi-bound, to specific manifolds of product states.

TABLE I. The lowest quasi-bound states of the $He^+ - H_2(I = 0)$ complex. Energies E^{res}, dissociative widths Γ (both in cm^{-1}), and radiative widths (in 10^{-6} cm^{-1}): Γ^{RA}, $\Gamma^{RCT_{nr}}$, and $\Gamma^{RCT_{..}}$ obtained in the state-to-state approach, and $\Gamma^{RCT+RA+iRaT} := \Gamma^{trad}$—from the 3D optical potential model. Comparison of the X_4-projected version of the optical potential model with the state-to-state approach in terms of percentage deviations $\Delta = (x_{3Dopt}/x - 1) \times 100\%$ for $x = \Gamma^{RA} + \Gamma^{RCT_{nr}}$.

State				$A \to X_4$			$A \to X_6$	$A \to X$
b k v_R	J	E^{res}[a]	Γ[a]	Γ^{RA}[a]	$\Gamma^{RCT_{nr}}$[b]	Δ	$\Gamma^{RCT_{..}}$[c]	Γ^{trad}
2 0 0	6	17.61	1.2 (−2)	8.34	91.9	0.0	117.8	154.2
	7	42.19	5.8 (−2)	7.79	94.5	1.5	120.9	160.3
	8	68.51	7.7 (−2)	6.60	93.6	0.2	119.3	154.7
	9	114.6	2.2 (−2)	5.97	87.0	0.6	110.8	143.1
	10	146.96	1.2 (−2)	4.96	87.1	0.4	110.7	141.4
2 1 0	12	1.54	∼0[d]	3.70[e]	109.2	−0.2	137.6	171.5
	13	44.2	0.2	3.11	96.6	−0.6	121.6	167.8
	14	89.8	0.2	1.99	100.8	0.1	126.9	161.2
	15	137.8	2.3 (−1)	0.32	101.2	−0.9	123.2	153.9
2 1 1	4	5.25	1.7 (−2)	6.18	90.0	0.1	114.7	151.3
	5	20.66	2.4 (−2)	6.13	88.1	0.1	112.4	149.4
	6	39.18	3.0 (−2)	6.22	89.7	0.1	114.3	147.3
	7	60.89	3.2 (−2)	6.23	84.3	0.1	107.1	145.5
	8	85.95	3.0 (−2)	5.52	88.1	0.0	112.4	144.1
	9	97.2	0.1	5.10	89.4	−0.5	113.4	145.9
	10	127.8	1.3 (−1)	1.47	87.2	−0.5	109.7	136.4
2 2 0	17	15.52	∼0[d]	0.05	116.2	0.4	144.9	175.4
	18	77.55	1.3 (−2)	0.02	108.3	0.6	135.7	163.7
	19	142.3	5.5 (−1)	0.00	103.6	0.8	129.7	156.3
2 2 1	13	33.26	4.7 (−2)	0.20[f]	97.8	0.1	122.7	150.5
	14	76.92	8.9 (−2)	0.10	92.5	0.2	115.9	142.1
	15	122.8	1.3 (−1)	0.00	87.5	−0.3	109.8	134.0
2 2 2	5	1.68	2.9 (−3)	3.48	79.8	0.9	100.9	126.9
	6	19.23	3.1 (−2)	6.36	83.9	0.7	107.2	139.0
	7	38.12	1.8 (−3)	1.95	80.3	0.6	101.2	123.8
	8	60.50	8.4 (−3)	1.61	75.5	1.2	95.5	118.2
	9	85.34	1.7 (−2)	0.33	74.3	0.6	93.3	113.6
	10	112.47	2.8 (−2)	0.27	71.0	0.6	89.2	108.8
	11	141.80	4.3 (−2)	0.13	62.8	0.4	79.0	103.6
2 0 1	0	139.57	2.0 (−2)	6.98	69.8	0.5	89.8	118.5
	1	142.30	2.2 (−2)	6.89	69.2	1.1	88.7	117.3
	2	147.76	2.6 (−2)	6.53	65.4	0.9	83.2	115.0
2 2 3	2	126.46	6.9 (−5)	3.42	53.7	1.1	68.4	87.4
	3	133.51	3.4 (−4)	2.52	53.9	1.0	68.2	86.2
	4	142.84	1.0 (−3)	2.16	53.2	0.9	68.1	84.6
2 1 2	1	152.04	5.0 (−4)	5.10	60.3	0.3	77.1	100.6
0 0 7	3	0.32	9.7 (−2)		0.5		0.7	0.8
	4	1.0	0.7		[g]			
6	6	1.7	1.0 (−1)		1.2		1.9	2.4
	7	3.5	1.5		[g]			
5	8	2.16	0.7 (−3)	0.13	4.9	0.2	6.2	7.5
	9	7.2	1.1		[g]			
4	11	11.1	0.1	0.09	7.9	1.3	10.0	12.6
	12	21	4.2		[g]			
3	13	7.96	1.2 (−7)	0.15[f]	22.7	1.1	28.6	34.8
	14	29.0[h]	2.7 (−1)	0.06	14.9	1.0	18.7	22.8
	15	48.5	5.6		[g]			
2	16	24.65	3.6 (−6)	0.01	35.4	0.5	44.4	53.5
	17	58.5	0.2	0.00	25.8	0.3	32.5	39.2
	18	89.3	5.1		[g]			
1	19	50.69	2.3 (−6)	0.00	52.3	0.1	65.5	78.8
	20	101.02	4.5 (−2)	0.00	41.4	0.1	51.9	63.0

TABLE I. *(Continued.)*

State			$A \to X_4$			$A \to X_6$	$A \to X$
$b\ k\ v_R\ J$	E^{res}[a]	Γ[a]	Γ^{RA}[a]	$\Gamma^{\text{RCT}_{\text{nr}}}$[b]	Δ	$\Gamma^{\text{RCT..}}$[c]	Γ^{trad}
0 21	19.72	~ 0[d]	0.00	82.1	0.5	102.2	123.5
22	89.11	3.4 (−7)	0.00	72.9	0.8	90.3	109.5

[a]Most of these results were presented graphically in Fig. 4 of Ref. 15.
[b]Accounts for transitions to the nonreactive subrange of the X-channel continuum, more specifically, to $E' \in [0, 7800]$ cm^{-1}. The contribution of iRaT in transitions to $E' \in [6487, 7800]$ cm^{-1} is estimated to be in most cases smaller than 1%, see Fig. A19 of Ref. 25.
[c]The symbol ".." added to the label RCT marks a contribution of iRaT in transitions to $E' \in [6487, 11\,000]$ cm^{-1}. $E'_{\max} = 11\,000$ cm^{-1} is the upper limit of energies included into the subspace X_6.
[d]Denotes extremely sharp resonance, $\Gamma < 10^{-9}$ cm^{-1}.
[e]The number is nearly 1.5 times larger than that given in Ref. 15 (Table VI) because it accounts for an additional transition—to the X channel resonance $J' = 13$, $E'^{\text{res}} = 14.3$ cm^{-1} which decays almost entirely by spontaneous emission to bound states.
[f]The number is nearly two times larger than that given in Ref. 15 because it additionally accounts for transitions to the two long-living X-channel resonances: $J' = 12$, E'_{res}=10.5 cm^{-1}, and $J' = 14$, $E'^{\text{res}} = 29.1$ cm^{-1} (see Table III in Ref. 18). These resonances decay by spontaneous emission with probabilities estimated as 0.94 and 0.05, respectively. The estimates are the ratios $\Gamma'^{\text{rad}}/(\Gamma'+\Gamma'^{\text{rad}})$ obtained from the nonradiative and radiative ($X \to X$) widths listed in Table III of Ref. 18.
[g]Broad resonance included into the background in the present calculations. See Fig. 10.
[h]The position of this resonance was incorrectly listed in Table VI of Ref. 15.

1. Transitions from continuum states

Rates of transitions from the continuum states ($[E, E + dE] J$) to all continuum states in the X_4 subspace,

$$\frac{\partial}{\partial E} R^{\text{RCT}_{\text{nr}}(\text{bck})}(E, J) = \int_0^{E'_{\max}(X_4)} dE' \sum_{J'=J-1}^{J+1} \frac{\partial^2}{\partial E\, \partial E'} \times R^{\text{RCT}(\text{bck})}(EJ; E'J') \qquad (45)$$

with $E'_{\max}(X_4) = 7800$ cm^{-1}, are plotted in Fig. 10(a) as functions of the energy E for several values of J. The function for a given J first rises from zero when the energy E approaches from below the top of the centrifugal barrier (E^J_{cbr}) in the effective potential $W^J_{000;000}(R)$, then eventually has a peak if there is a shape resonance in the top region, and finally approaches a value which remains nearly constant up to the end of the E range shown. The plateau values of different J functions are nearly the same. Adding to the rate functions (45) their counterparts for transitions to the X-channel bound states[15] would not introduce any visible change to Fig. 10(a). Upon a closer inspection, the plateau values of the different J functions would be found to coincide even slightly better. Thus, apart from the peaks, the behavior of the rate functions in Fig. 10(a) can be approximated by the following formula:

$$\left[\frac{\partial}{\partial E} R^{\text{RCT}_{\text{nr}}(\text{bck})} + \frac{\partial}{\partial E} R^{\text{RA}(\text{bck})}\right](E, J) \approx \Theta\left(E - E^J_{\text{cbr}}\right) \frac{1}{2\pi\hbar}\, p^{\text{RCT}_{\text{nr}}+\text{RA}}, \qquad (46)$$

where $\Theta(..)$ denotes the Heaviside unit-step function and $p^{\text{RCT}_{\text{nr}}+\text{RA}} \approx 2.7 \times 10^{-6}$ is the probability of radiative

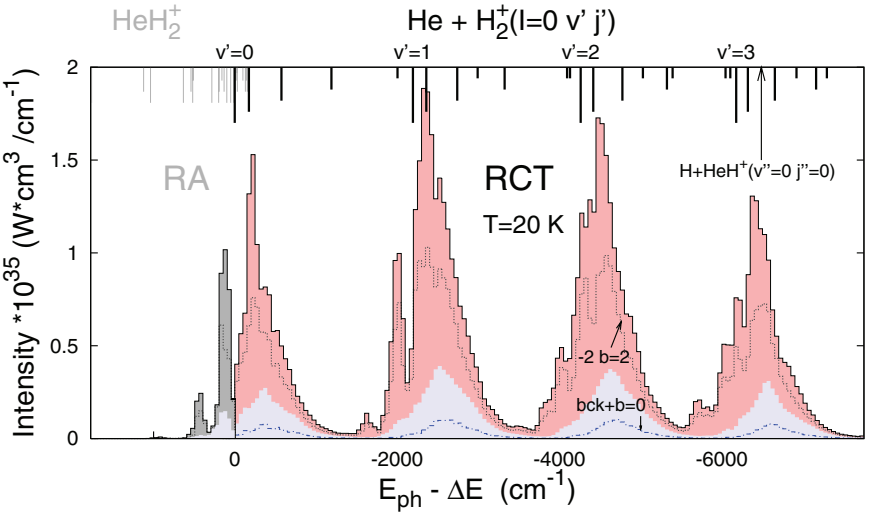

FIG. 9. Photon emission spectrum from the RCT and RA reactions at $T = 20$ K (represented by average values of the emission density $\mathcal{I}(E_{\text{ph}}, T)$ in the subsequent photon energy intervals $\Delta E_{\text{ph}} = 50$ cm^{-1}). The curve labeled "−2 b = 2," the light-blue area labeled "bckg + b = 0," and the blue "b = 0" curve show how much the spectrum would change if the following transitions, respectively, were neglected: from the two near threshold $b = 2$ resonances at E_{res} = 1.68 and 5.25 cm^{-1}, from all $b = 2$ resonances, and from all reactant states except the twelve sharp $b = 0$ resonances listed in Table I. The unlabeled sticks in the upper left part show the "vibrational" bound state energies of HeH_2^+ ($I = 0$), see Fig. 2 in Ref. 15.

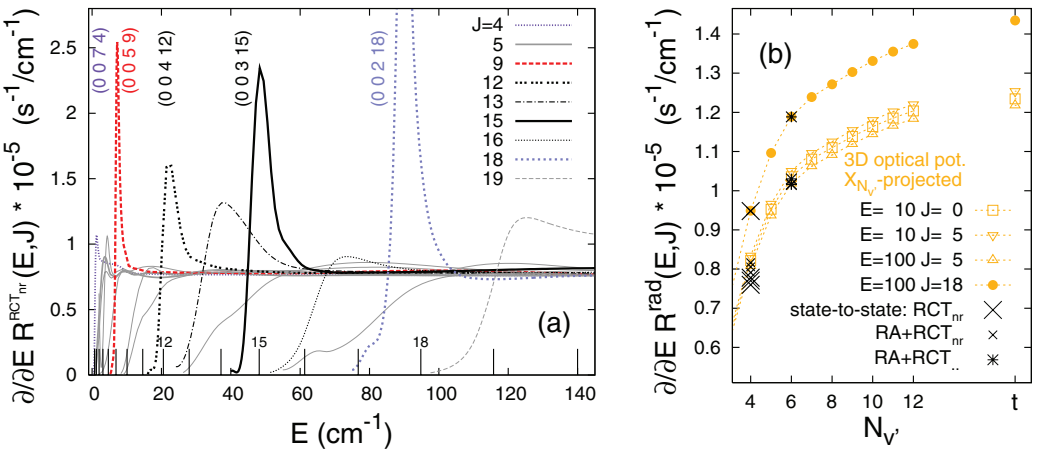

FIG. 10. (a) Rates $\frac{\partial}{\partial E} R^{\mathrm{RCT_{nr}(bck)}}(E, J)$ for $J = 4$–19 as functions of energy of the reactants $He^+ + H_2(v = 0, j = 0)$. The labels of the broad peaks are the quantum numbers $(b\, k\, v_R\, J)$ of the related short-living quasi-bound states of the reactants (see Table I). The sticks in the bottom show the heights of the centrifugal barriers in the effective potentials $W^{J^e}_{000;000}(R)$ for $J = 4$–20. (b) Values of the rates $\frac{\partial}{\partial E} R^{\mathrm{RCT_{nr}(bck)}}(E, J)$ for selected (EJ)-states plus the respective values of $\frac{\partial}{\partial E} R^{\mathrm{RA(bck)}}(E, J)$ versus the rates $\frac{\partial}{\partial E} R^{\mathrm{bck}}_{(\to X_{N_{v'}})}(E, J)$ obtained from the optical potential model, Eq. (39), for $N_{v'} = 4$ and for $N_{v'} > 4$. Symbols at the position denoted by "t" represent the total radiative rates $\frac{\partial}{\partial E} R^{\mathrm{trad(bck)}}(E, J)$ obtained from the "complete" version of the 3D optical potential, Eqs. (34) and (35).

transitions from continuum reactant states to the "nonreactive" subspace of the product continuum and bound states. The RA contribution to the probability is $p^{\mathrm{RA}} \approx 1.1 \times 10^{-7}$ for $J = 0$–6 and decreases rapidly when J grows further, assuming values of $\sim 3 \times 10^{-8}$, $\sim 8 \times 10^{-10}$, and 0 for $J = 10$, 15, and ≥ 23, respectively.

Figure 10(b) shows how the rates of radiative transitions from reactant continuum states change when the subspace $X_{N_{v'}}$ of product states enlarges from the "nonreactive" subspace X_4 up to the entire X channel, defined above as covering the E'-energy range of $[-1763.5, \sim 21\,400]$ cm^{-1}. Namely, the rates increase by a factor which is nearly independent of the energy E and the number J of the states and converges to the value of ~ 1.52. In consequence, p^{trad}—the total radiative transition probability from any continuum state (E, J) which lies above the centrifugal barrier E^J_{cbr} attains the value of $\sim 4.1 \times 10^{-6}$. A close value (of $\sim 3.95 \times 10^{-6}$) is obtained when one inspects the classical counterparts of the probabilities $p^{\mathrm{trad}}(E, J) = 2\pi\hbar \frac{\partial}{\partial E} R^{\mathrm{trad(bck)}}(E, J)$, evaluated according to the formula[44]

$$p^{\mathrm{trad}}(E, b) = 2 \int_{R_{\mathrm{trn}}}^{\infty} dR\, \frac{A(R)}{\{2[E - Eb^2/R^2 - V(R)]/\mu\}^{1/2}}, \tag{47}$$

in which the transition rate function $A(R)$ and the potential $V(R)$ are taken as $\frac{1}{\hbar}\, {}^{\mathrm{opt}}W_{000;000}(R)$ [Eq. (31)] and $W^{J=0}_{000;000}(R)$, respectively. b denotes the impact parameter, and $R_{\mathrm{trn}}(E, b)$ is the turning point at which the velocity $\{\ldots\}^{1/2}$ vanishes.

Figure 11 focuses on the behavior of the rates $\frac{\partial}{\partial E} R^{\mathrm{rad}}(E, J)$ at energies below the centrifugal barriers E^J_{cbr}, which are disregarded in the analysis of Fig. 10. The behavior is demonstrated to be consistent with Wigner's threshold laws for reaction probabilities

$$2\pi\hbar \frac{\partial}{\partial E} R^{\mathrm{rad}}(E, J) \underset{E \ll E^J_{\mathrm{cbr}}}{\sim} \mathcal{C}^{\mathrm{rad}}_J E^{J+1/2}. \tag{48}$$

The coefficients $\mathcal{C}^{\mathrm{rad}}_{J=0}$ (in units of $E^{-1/2}$ and E in cm^{-1}) are 8.65×10^{-6}, 5.45×10^{-6}, and 2.49×10^{-7} for rad = trad, RCT$_{\mathrm{nr}}$, and RA, respectively. The calculated values of $\mathcal{C}^{\mathrm{rad}}_{J>0}$ are given in Ref. 25. Obviously, there is no $E^{J=0}_{\mathrm{cbr}}$ and $E^{J=1}_{\mathrm{cbr}}$ may be used in Eq. (48) to describe the range of threshold behavior of $J = 0$ rates. The value of $E^{J=1}_{\mathrm{cbr}}$ which is 0.037 cm^{-1} serves hereafter as a rough boundary between "cold" and "subthermal" energy ranges. Using this terminology, the two other facts that emerge from Fig. 11 and Eq. (48) may be stated: (i) there is no quasi-bound state of the reactant system in the cold range, (ii) the relation between the rate functions $\frac{\partial}{\partial E} R^{\mathrm{rad}}(E, J)$ for rad=trad and rad = RCT$_{\mathrm{nr}}$ +RA remains the same as in the subthermal range, i.e., their ratio stays close to 1.52.

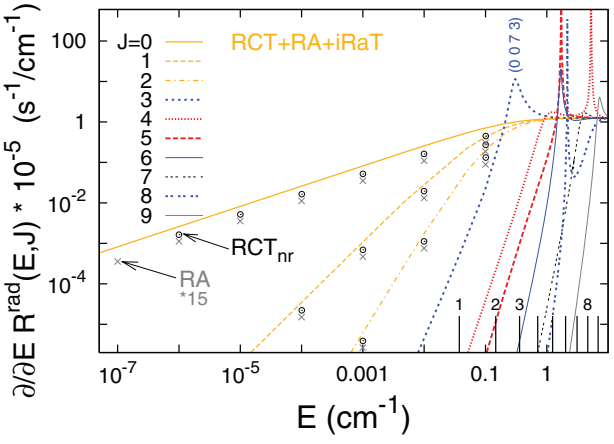

FIG. 11. Rates $\frac{\partial}{\partial E} R^{\mathrm{rad}}(E, J)$ of the reactions rad = RCT + RA + iRaT, RCT$_{\mathrm{nr}}$, RA as functions of reactants energy in the range 10^{-7}–10 cm^{-1}. The sticks in the lower right corner show the heights of the centrifugal barriers in the effective potentials $W^{J^e}_{000;000}(R)$ for $J = 1, \ldots, 9$. The sharp peaks in the red lines are the lowest $b = 2$ resonances, the other peaks are $b = 0$ resonances, see Table I.

2. Transitions from quasi-bound states

Consistent with Eq. (15), counterparts of functions (45) for radiative transitions from long-living resonances $\mathcal{R}_n^J$ are the sums of Lorentzians

$$\frac{\partial}{\partial E} R^{\mathrm{rad(res)}}(E, J) = \frac{1}{2\pi\hbar} \sum_n \frac{\Gamma_n^J \, \Gamma_n^{J\,\mathrm{rad}}}{(E - E_n^{J\,\mathrm{res}})^2 + \frac{1}{4}(\Gamma_n^J + \Gamma_n^{J\,\mathrm{trad}})^2}, \tag{49}$$

where rad = $\mathrm{RCT_{nr}}$, RA, RCT + iRaT indicates the considered subspace of final states of the transitions. Table I gives a list of parameters of these functions for sharp resonances $(b\,k\,v_R\,J) := (n\,J)$ that are most important in the present simulations ($b = 0, 2$ resonances in the $[0, E_{\max}]$ range). Together with the energies E^{res} and the dissociative widths Γ four sets of radiative widths Γ^{rad}: for rad = RA, $\mathrm{RCT_{nr}}$, RCT.. and trad are listed. All these widths except Γ^{trad} were obtained within the state-to-state approach, i.e., via prior determination of the functions $\frac{\partial}{\partial E'}\Gamma_n^{J\,\mathrm{rad}}(E')$.

The widths $\Gamma^{\mathrm{RCT..}}$ account for transitions to continuum states in the subspace X_6. The symbol ".." in the label signifies a probable admixture of the iRaT since $E'_{\max}(X_6) \approx 11\,000$ cm^{-1} lies well above the threshold for this reaction. The values of $\Gamma_n^{J\,\mathrm{RCT..}}$ together with their resolutions into $\Gamma_{n,c'}^{J\,\mathrm{RCT..}}$ for $c' = v'$, j' will be used later to assess reliability of the populations $P_{c'}(nJ)$ determined in the calculations that accounted only for transitions to the subspace X_{nr}, see Eq. (44).

The widths Γ^{trad} implicitly account for the resonance decay to the entire channel X and serve therefore here as reference to estimate the magnitude of the contribution of transitions excluded in the calculations of the widths $\Gamma^{\mathrm{RCT_{nr}}} + \Gamma^{\mathrm{RA}}$, i.e., transitions to the subspace $X \backslash X_{\mathrm{nr}}$ which represents nearly 60% of the X-channel energy range. According to Table I, the contribution is only of the size of ∼35% and is practically the same for all resonances. Of the same magnitude is also the contribution brought to the rates $\frac{\partial}{\partial E} R^{\mathrm{trad(bck)}}(E, J)$ by transitions from the initial continuum states to the subspace $X \backslash X_{\mathrm{nr}}$, as indicated by the value of $1 - p^{\mathrm{RCT_{nr}+RA}}/p^{\mathrm{trad}}$.

Comparing the widths Γ^{RA} and Γ^{trad} in Table I it becomes obvious that association into bound states of the HeH_2^+ ion contributes little to the radiative decay of the resonances (at most 5.5%–6%) in the cases of low J resonances (2 0 1 0–2) and (2 0 0 6). and the role of the RA becomes even smaller with growing J of the initial state.[15]

3. Optical-potential versus state-to-state results

The above estimates are important for conclusions of the present study. The fact that the used reference data Γ^{trad} and $\frac{\partial}{\partial E} R^{\mathrm{trad(bck)}}(E, J)$ are obtained from the optical potential model may raise some criticism. The model is applied here, probably for the first time, in the context of 3D collision dynamics. Essential to the application are the approximate formulas (33) and (38) which relate the energies of the emitted photons to the matrix elements of the potentials involved in the bases $\mathbf{\Phi}^{JMp}$ and $\mathbf{\Phi}^{\prime J'M'p'}$, respectively. Apart from noticing that the classical idea of the Mulliken difference potential[45] is exploited in this model, no rigorous theoretical justification of the formulas can be offered. It is therefore requisite to demonstrate that results from the present implementation of the optical potential model are reasonably consistent with results from the quantum-mechanical state-to-state approach. This is done by enclosing into all tables of this paper the relative percentage deviations $\Delta = (x_{\mathrm{3Dopt}}/x - 1) \times 100\%$ between values of the presented characteristics obtained from the state-to-state calculations and from the X_4 projected version of the optical potential model. Moreover, results obtained from the state-to-state and the optical potential calculations with the basis X_6 are compared graphically in several figures.

In Table I the values of the widths $\Gamma^{\mathrm{RCT_{nr}}} + \Gamma^{\mathrm{RCT}} := x$ and $\Gamma_{(\to X_4)} := x_{\mathrm{3Dopt}}$ are compared. In the majority of cases the deviations are small, $|\Delta| \lesssim 1\%$. Deviations of the same size occur between the values $\Gamma^{\mathrm{RCT..}} + \Gamma^{\mathrm{RA}}$ listed in Table I and their 3Dopt counterparts $\Gamma_{(\to X_6)}$. This is shown in Fig. 12(a).

The main purpose of Fig. 12 is to demonstrate that the widths $\Gamma_{(\to X_{N_{v'}})}$ converge with increasing $N_{v'}$ towards the values Γ^{trad} obtained by the "complete" optical potential. The rate of this convergence is practically independent of the quantum numbers $(b\,k\,v_R\,J)$ of the resonances and is actually also independent of any initial state (resonance or flat continuum). Plots of $\frac{\partial}{\partial E} R^{\mathrm{bck}}_{(\to X_{N_{v'}})}(E, J) / \frac{\partial}{\partial E} R^{\mathrm{trad(bck)}}(E, J)$ as functions of $N_{v'}$ for the (E, J) cases shown in Fig. 10(b) would be hardly distinguishable from the plots of $\Gamma_{(\to N_{v'})} / \Gamma^{\mathrm{trad}}$ in Fig. 12(b). This is because all the initial states of the radiative transitions considered here correlate with $v = 0$ state of free H_2 which is only weakly distorted by interaction with He^+ at R-distances where the transitions take place. The convergence of the transition characteristics is nearly completely determined by the same factor in all cases, which is the accuracy of approximating the $v = 0$ function of H_2 in the basis of $v' = 0, \ldots, N_{v'} - 1$ functions of H_2^+ (blue curves in Fig. 12(b)).

D. Cross-sections

1. At energies $E < \varepsilon_{01}$

The characteristics to be presented here summarize all important partial contributions to the background, $\frac{\partial}{\partial E} R^{\mathrm{rad(bck)}}(E, J)$ for $J = 0$–20, with the contributions (49) of all important sharp resonances $(b = 0, 2\,k\,v_R\,J)$, for $J = 0$–22.

The total cross-sections σ^{rad} for rad = $\mathrm{RCT_{nr}}$, RA, trad are plotted as functions of the energy E in Figs. 13 and 14 and listed for selected energies in Table II. All resonances from Table I except those with $\Gamma \ll \Gamma^{\mathrm{trad}}$ show up as peaks in the cross-section functions. In every function, the peaks grow out of a background which decreases slowly with growing E. The backgrounds of the functions $\sigma^{\mathrm{trad}}(E)$ and $\sigma^{\mathrm{RCT_{nr}}}(E)$ are seen to decrease with nearly the same rate whereas the background of the function $\sigma^{\mathrm{RA}}(E)$ decreases evidently faster.

Figure 14 more clearly displays this difference. The energy dependence of the cross-sections $\sigma^{\mathrm{rad(bck)}}$ for rad = $\mathrm{RCT_{nr}}$ + RA and rad =trad is demonstrated to be well described by the formula of the Langevin capture model,[46,47] $p^{\mathrm{rad}}\,\sigma^{\mathrm{cpt}}(E)$, in which the values of p^{rad} are as estimated in the discussion of Fig. 10 and the capture cross-section $\sigma^{\mathrm{cpt}}(E)$

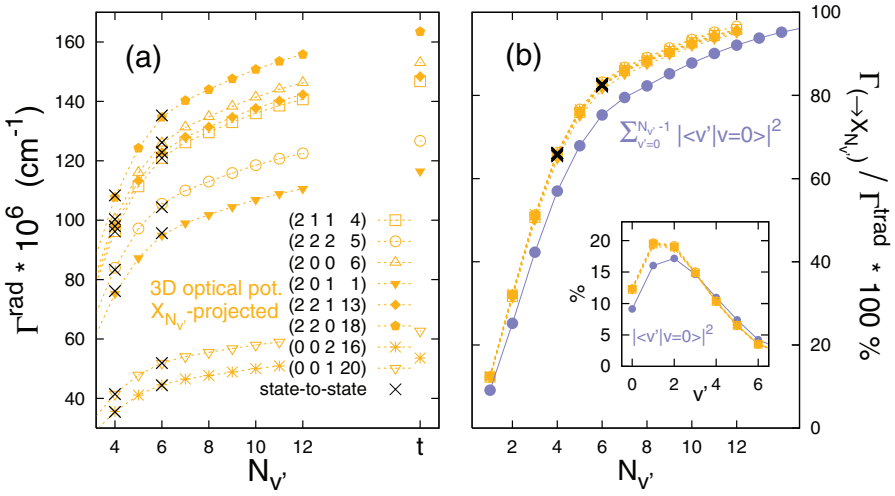

FIG. 12. (a) Radiative widths $\Gamma_{(\to X_{N_{v'}})}$ of selected A channel resonances due to transitions to X-channel subspaces enlarging from the nonreactive subspace X_4 ($E'_{max} = 7800$ cm^{-1}) to X_{12} ($E'_{max} \approx 18\,000$ cm^{-1}). Comparison of results from the $X_{N_{v'}}$-projected version of the 3D optical potential with the state-to-state results for $N_{v'} = 4$ and 6. At the position "t" shown are the total radiative widths Γ^{trad} obtained from the unprojected optical potential. (b) Some details on the convergence: $\Gamma_{(\to X_{N_{v'}})} \to \Gamma^{trad}$. Accuracy of representing the $v = 0$, $j = 0$ state of H_2 in terms of v' $j' = 0$ states of H_2^+ displayed by $\sum_{v'=0}^{N_{v'}-1} |\langle v'0|0\,0\rangle|^2$ for $N_{v'} = 1 - 12$. (Inset) Values of $\Gamma_{(\to X_1)}/\Gamma^{trad}$ and $[\Gamma_{(\to X_{v'+1})} - \Gamma_{(\to X_{v'})}]/\Gamma^{trad}$ for $v'>0$ compared to the squared overlaps $|\langle v'0|v = 0\,0\rangle|^2$ for $v' = 0 - 6$.

is obtained by interpolating between the values $\sigma(E = E^J_{cbr}) = \pi \frac{\hbar^2 J(J+1)}{2\mu E^J_{cbr}}$ that correspond to the top points (R^J_{cbr}, E^J_{cbr}) of the centrifugal barriers in the potentials $W^J_{000;000}(R)$ for $J = 4$–20. At energies larger than 7 cm^{-1}, the capture cross-section takes the form $\sigma^{cpt}(E) \approx \varsigma E^{-1/2}$ with $\varsigma = 1374$ Å$^2 \times \sqrt{\text{cm}^{-1}}$ (or $10.47\, a_0^2 \sqrt{E_H}$). The decrease with collision energy like $E^{-1/2}$ is typical of ion-molecule reactions without threshold.[47] The departure from this behavior which is seen in Fig. 14 at energies below 7 cm^{-1} is most likely an effect of improper functional representation of long-range tail of the potential V^A (see Fig. A2b of Ref. 25).

The energy dependence of the cross-section $\sigma^{RA(bck)}$ is not describable by the capture model because the probability p^{RA} cannot be treated as a constant in the summation over the partial (J) contributions. Due to the rapid decrease of this probability with increasing J from 10 to 23 the cross-section $\sigma^{RA(bck)}$ decreases faster than $E^{-1/2}$. The dependence becomes close to E^{-1} at energies above 20 cm^{-1}, $\sigma^{RA(bck)}(E) \approx c/E^{0.96}$ with $c = 4.2\times10^{-4}$ Å^2 cm$^{-0.96}$.

The light green curves in Fig. 13 represent estimates of the cross-sections for the iRaT and the "true" RCT obtained as

$$\sigma^{\sim iRaT}(E) = \overline{P^{pT}} \times [\sigma^{trad} - \sigma^{RCT_{nr}} - \sigma^{RA}](E)$$
$$\approx \overline{P^{pT}} \times \left[1 - \frac{p^{RCT_{nr}+RA}}{p^{trad}}\right] \sigma^{trad}(E) \qquad (50)$$

and as $\sigma^{\sim RCT} = \sigma^{trad} - \sigma^{RA} - \sigma^{\sim iRaT}$, respectively. The symbol $\overline{P^{pT}}$ denotes a fraction of states in the subspace $X \backslash X_{nr}$ reached in radiative transitions from the A channel that would pertain to the system $HeH^+ + H$ rather than to $He + H_2^+$

TABLE II. Cross-sections σ (in 10^{-4}Å^2) for RA, RCT_{nr}, and RA + RCT + iRaT := trad reactions at selected energies E (in cm^{-1}) below the ε_{01} threshold. Contributions to $\sigma^{RCT_{nr}}$ and σ^{trad} of transitions from continuum states of reactants (bck). Comparison of results from the state-to-state approach and from the X_4 projected version of the 3D optical potential model in terms of $\Delta = (x_{3Dopt}/x - 1) \times 100\%$ for $x = \sigma^{RCT_{nr}} + \sigma^{RA}$.

		$\sigma^{RCT_{nr}}$			σ^{trad}[a]				$\sigma^{RCT_{nr}}$			σ^{trad}[a]	
E	σ^{RA}[b]	tot	bck	Δ	tot	bck	E	σ^{RA}[b]	tot	bck	Δ	tot	bck
5	2.03	32.5	15.0	0.3	53.5	23.9	50	0.10	6.6	6.4	− 1.0	10.0	9.7[d]
7.2	0.73	20.5	20.2[d]	1.8	32.6	32.0[d]	60	0.14	5.9	4.7	0.5	9.2	7.3
10	0.41	11.9	11.2	2.8	19.1	17.8	70	0.10	4.9	4.5	0.8	7.6	6.9
						0.0[c]							+0.2[c]
15	0.30	9.5	9.2	1.5	15.0	14.6	80	0.06	4.4	4.2	1.2	6.8	6.4
25	0.19	7.8	7.5	1.7	12.2	11.8	90	0.84	57.5	6.1[d]	0.6	91.5	9.3[d]
40	0.21	7.0	6.0	0.9	11.1	9.3	100	0.05	4.2	3.8	1.0	6.5	5.9
			+0.3[e]			+0.4[c]				+0.2[e]			+0.3[c]

[a] Assuming that contribution of the iRaT can be described as $\overline{P^{pT}} \times (\sigma^{trad} - \sigma^{RCT_{nr}} - \sigma^{RA})$ with $\overline{P^{pT}} \in [0.15, 0.30]$ (see the text and Fig. A19 of Ref. 25), an estimated cross-section for the RCT is obtained as $[1 - \overline{P^{pT}} \times (1 - \frac{1}{1.52})]\sigma^{trad} - \sigma^{RA} := \sigma^{\sim RCT}$.

[b] At $E > 20$, the "bck" contribution can be described as $\sigma^{RA(bck)}(E) \approx 4.2/E^{0.96}$.

[c] Deviation of $\sigma^{trad(bck)}(E)$ from the value of the capture model, $p^{trad} \times \varsigma/E^{1/2}$ with $p^{trad}\varsigma = 56.3$ in the present units (or $42.9 \times 10^{-6}\, a_0^2 E_H^{1/2}$). See Fig. 14.

[d] Effect of non-monotonicity due to included broad resonance, see Table I and Fig. 10.

[e] Deviation of $[\sigma^{RCT_{nr}(bck)} + \sigma^{RA(bck)}](E)$ from the capture model value of $37.1/E^{1/2}$.

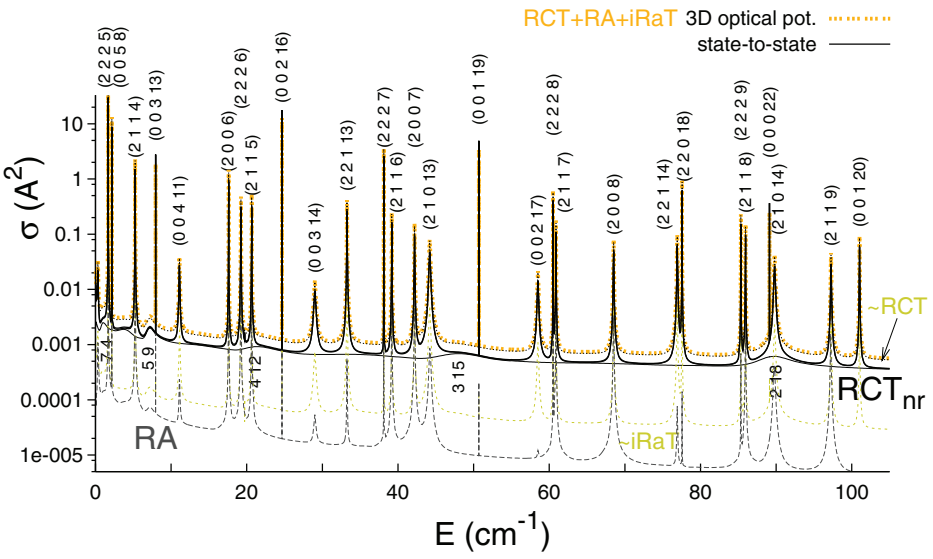

FIG. 13. Total cross-sections $\sigma^{\mathrm{rad}}(E)$ for rad = $\mathrm{RCT_{nr}}$, RA, and RCT + iRaT + RA:=trad as functions of reactant energy in the range below the ε_{01} threshold (at 118.37 $\mathrm{cm^{-1}}$). The peaks are labeled with the quantum numbers $(b\,k\,v_R\,J)$ of the corresponding quasi-bound states of the $\mathrm{He^+}$–$\mathrm{H_2}(v=0)$ complex. The tiny line in the background of the thick black curve shows the contribution of $\sigma^{\mathrm{RCT_{nr}(bck)}}$. The vertical labels below this line give the numbers v_R and J of the most pronounced shape resonances ($b = k = 0$) included into the background (see Fig. 10(a)). The tiny curve labeled ~RCT (slightly below the yellow one) shows an estimation of the cross-section for the RCT obtained as $\sigma^{\mathrm{trad}}-\sigma^{\mathrm{RA}}-\sigma^{\sim\mathrm{iRaT}}$. The assumed iRaT contribution (light-green line) is: $\sigma^{\sim\mathrm{iRaT}} = 0.15\times(\sigma^{\mathrm{trad}} - \sigma^{\mathrm{RCT_{nr}}} - \sigma^{\mathrm{RA}})$, see Table II.

if the proton transferred channel were not artificially closed on the X-state PES used (see Fig. A0 of Ref. 25). By combining the information obtained in the present study on the

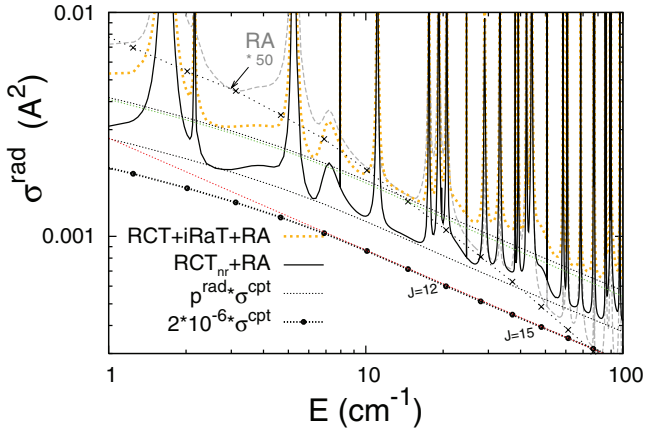

FIG. 14. Total radiative cross-sections $\sigma^{\mathrm{rad}}(E)$ for rad = $\mathrm{RCT_{nr}}$ + RA and rad = RCT + iRaT + RA:=trad as functions of reactant energy in the sub-thermal range below ε_{01} compared to the cross-section $p^{\mathrm{rad}}\sigma^{\mathrm{cpt}}(E)$ of the Langevin capture model.[46,47] Dots represent values of the capture cross-section $\sigma^{\mathrm{cpt}}(E = E^J_{\mathrm{cbr}}) = \pi\,\frac{\hbar^2\,J(J+1)}{2\mu\,E^J_{\mathrm{cbr}}}$ determined from the heights E^J_{cbr} of the centrifugal barriers in the potentials $W^J_{000;000}(R)$ for J = 5–17. The red line shows the function $\varsigma/\sqrt{E}$ with $\varsigma = 1374\ \mathrm{Å^2}\times\sqrt{\mathrm{cm^{-1}}}$ fitted to values of $\sigma^{\mathrm{cpt}}(E = E^J_{\mathrm{cbr}})$ for J = 9–20. The green line, close to the $p^{\mathrm{trad}}\sigma^{\mathrm{cpt}}(E)$ line, represents results from the classical formula $2\pi\int p^{\mathrm{trad}}(E,\,b)\,b\,db$ with $p^{\mathrm{trad}}(E,\,b)$ given by (47). Also shown is the cross-section $\sigma^{\mathrm{RA}}(E)$ to which the capture model does not apply. Crosses represent approximate values of $\sigma^{\mathrm{RA(bck)}}(E = E^J_{\mathrm{cbr}})$ evaluated as $\frac{\hbar^2\pi}{2\mu E^J_{\mathrm{cbr}}}\sum_{\tilde{J}=0}^{J}(2\tilde{J}+1)\,p^{\mathrm{RA}}(\tilde{J})$. The constant probabilities $p^{\mathrm{RCT_{nr}+RA}} = 2.7\times10^{-6}$ and $p^{\mathrm{trad}} = 4.1\times10^{-6}$, and the J-dependent p^{RA} are deduced from plateau values of the respective rate functions $\frac{\partial}{\partial E}R^{\mathrm{rad(bck)}}(E,\,J)$, see Fig. 10(a) and Eq. (46). Note that the cross-sections σ^{RA} and $\sigma^{\mathrm{RA(bck)}}$ are enlarged 50 times in the figure.

populations of the states in the subspace (Figs. 10(b) and 12) with the information available in the literature[21] on the probabilities of the proton transfer reaction the value of $\overline{P^{\mathrm{pT}}}$ is estimated as 0.15–0.3 (see Fig. A19 of Ref. 25 for details). Thus, the cross-section for the iRaT is obtained at each energy E as the fraction of ~5%–10% of the total radiative cross-section σ^{trad}. The fact that $\sigma^{\sim\mathrm{iRaT}}(E)$ is larger than $\sigma^{\mathrm{RA}}(E)$ seems realistic. The resulting estimate of the background part of $\sigma^{\sim\mathrm{RCT}}(E)$ is $p\sigma^{\mathrm{cpt}}(E)$–$\sigma^{\mathrm{RA(bck)}}(E)$ with p = 3.68–3.89 $\times\ 10^{-6}$. Using the approximate formulas from the previous paragraphs of this subsection one easily evaluates the ratio $\sigma^{\sim\mathrm{RCT(bck)}}(E)/\sigma^{\sim\mathrm{trad(bck)}}(E)$. It indicates that the RCT constitutes about 88%–94% of the total radiative reaction RCT + RA + iRaT. The final estimate, given in Sec. VI E, is only slightly lower.

The shapes of the cross-section functions $\sigma^{\mathrm{rad}}(E)$ for rad = $\mathrm{RCT_{nr}}$, RA, trad simplify enormously in the cold energy range where they are composed of a few lowest partial rates $\frac{\partial}{\partial E}R^{\mathrm{rad}}(E,\,J)$ in the form (48). At energies below 0.001 $\mathrm{cm^{-1}}$ (ultra-cold range),

$$\sigma^{\mathrm{rad}}(E) \approx \frac{\hbar^2\pi}{2\mu}\mathcal{C}^{\mathrm{rad}}_{J=0}\,E^{-1/2}. \tag{51}$$

An illustrative plot is enclosed in Ref. 25 (Fig. B6a). The plot also shows that the capture model, i.e., $p^{\mathrm{rad}}\sigma^{\mathrm{cpt}}(E)$, adequately describes the background of $\sigma^{\mathrm{rad}}(E)$ down to an energy of about 0.5 $\mathrm{cm^{-1}}$ where no less than three partial rates (J = 0–2) contribute.

2. At energies $\varepsilon_{01} < E < \varepsilon_{02}$

As mentioned in Sec. V, the majority of calculations for this energy range are done using the optical potential model. The results, describing the total radiative quenching of $\mathrm{He^+}$

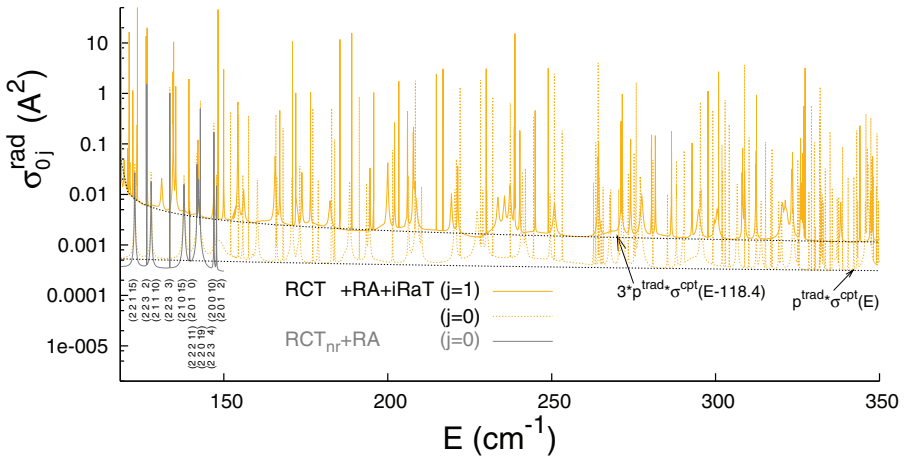

FIG. 15. Total cross-sections $\sigma_{0j}^{\mathrm{rad}}(E)$ for rad = RCT + iRaT + RA and $\mathrm{RCT_{nr}}$ + RA and for $j = 0$ and $j = 1$ as functions of reactant energy above the ε_{01} threshold. The background parts of the functions are well described by the Langevin capture model, $\sigma_{0j}^{\mathrm{rad(bck)}}(E) \approx (2j+1)\,\sigma^{\mathrm{cpt}}(E-\varepsilon_{0j})$ with $\sigma^{\mathrm{cpt}}(E_{\mathrm{coll}})$ determined as described in Fig. 14. The vertical labels are the quantum numbers $(b\,k\,v_R\,J)$ of the quasi-bound states of the $\mathrm{He^+}-\mathrm{H_2}$ complex that are included in Table I. There are above 130 peaks in the function $\sigma_{00}^{\mathrm{trad}}(E)$ in the range from 150 $\mathrm{cm^{-1}}$ up to $\varepsilon_{02} = 354$ $\mathrm{cm^{-1}}$ and about 125 peaks in the function $\sigma_{01}^{\mathrm{trad}}(E)$ in the range $\varepsilon_{01} - \varepsilon_{02}$ related to quasi-bound states of the $\mathrm{He^+}-\mathrm{H_2}$ complex, see Tables BI–BIII and Fig. B6b of Ref. 25.

in collisions with $\mathrm{H_2}(v = 0, j)$, are generated for both open channels in the collisions, $j = 0$ and $j = 1$. The main goal is to compensate for the omission of the $j = 1$ channel in the state-to-state calculations and to estimate the respective contribution to the rate constant for the "true" RCT.

Figure 15 shows the cross-sections $\sigma_{0j}^{\mathrm{trad}}(E)$ for $j = 0$, 1 as functions of $E \in [118.4, 350]$ $\mathrm{cm^{-1}}$. Details on various contributions to these quantities are provided in Fig. B7a of Ref. 25. The backgrounds of the partial cross-sections, $\sigma_{0j}^{\mathrm{trad(bck)}}(EJp) = \frac{\hbar^3\pi^2}{\mu(E-\varepsilon_{0j})}\frac{\partial}{\partial E}R_{0j}^{\mathrm{trad(bck)}}(EJp)$, are shown to behave consistently with the capture model, i.e.,

$$\frac{\partial}{\partial E}R_{0j}^{\mathrm{trad(bck)}}(EJp) \approx \sum_{\lambda=(1-p)/2}^{\min(j,J)} \Theta\big(E - E_{\mathrm{cbr}}^{J^p jl(\lambda)} - \varepsilon_{0j}\big) \times \frac{1}{2\pi\hbar}\,p^{\mathrm{trad}}. \tag{52}$$

Here $E^{J^p jl(\lambda)}$ denotes barrier top in an appropriate adiabatic potential $e_{v=0jl}^{J^p}(R)$ which correlates with the potential $W_{0j\lambda;0j\lambda}^{Jp}(R)$ through the relation $l(\lambda) = J + j + \frac{1-p}{2} - 2\lambda$. The result of the summation $\sum_{J,p}(2J+1)\sigma_{0j}^{\mathrm{trad(bck)}}(EJp)$ appears as simple as

$$\sigma_{0j}^{\mathrm{trad(bck)}}(E) \approx (2j+1)\,p^{\mathrm{trad}}\,\sigma^{\mathrm{cpt}}(E-\varepsilon_{0j}), \tag{53}$$

where σ^{cpt} is the capture cross-section introduced in Subsection VI D 1. This formula approximates well the function $\sigma_{01}^{\mathrm{trad(bck)}}(E)$ in the entire range shown in Fig. 15 except very near the threshold ε_{01}. The behavior of $\sigma_{01}^{\mathrm{trad}}(E)$ in the threshold region is analyzed in Fig. B6b of Ref. 25.

Rich structures of peaks emerge from the backgrounds of the cross-sections in Fig. 15. They represent quasi-bound states of the complexes $\mathrm{He^+} - \mathrm{H_2}(I)$ for $I = 0$, 1 that live longer than 5 ps ($\Gamma < 1$ $\mathrm{cm^{-1}}$). Altogether there are 269 such states in the range $[\varepsilon_{01}, \varepsilon_{02}]$. The characteristics of the states used as parameters of the individual Lorentzian profiles in the cross-sections, i.e., the energies E^{res} and the widths Γ and Γ^{trad}, are presented in Fig. B7b and in Tables BII–BIV of Ref. 25. The set of the widths Γ^{trad} of the quasi-bound states is completed with respective widths of all (603) bound states of the complex (Tables BV–BIX) in order to better see the correlations with the quantum numbers assigned to the states. It is found that the correlations are reasonably well represented by the formula

$$\Gamma_{b\,k\,v_R}^{J\,\mathrm{trad}} \approx \Upsilon(v_R, v_\theta) - \sum_{m=1}^{2}\gamma_m(v_R, v_\theta)\times[J(J+1) - k^2]^m,$$

where $v_\theta = b - k$. The parameter Υ assumes the value of $\sim 250 \times 10^{-6}$ $\mathrm{cm^{-1}}$ for $v_R = v_\theta = 0$, diminishes rapidly with growing v_R and much less rapidly with growing v_θ The parameter γ_1 is of the size of 2×10^{-7} $\mathrm{cm^{-1}}$ (further details are given in Fig. B8 of Ref. 25).

E. Rate constants

Upon Boltzmann averaging of the cross-sections $\sigma_{0j}^{\mathrm{trad}}(E)$ for $j = 0$, 1 and $\sigma_{00}^{\mathrm{rad}}(E)$ for rad = $\mathrm{RCT_{nr}}$, RA, the respective rate constants $k_{0j}^{\mathrm{rad}}(T)$ are obtained as functions of temperature in the range 1 μK−100 K. These functions are presented in Figs. 16 and 17 and in Table III under symbols $k_{I=0}^{\mathrm{rad}}$ and $k_{I=1}^{\mathrm{rad}}$ for $j = 0$ and $j = 1$, respectively. Additionally, the thermal averaging of the cross-sections $\sigma_{0j}^{\mathrm{trad}}(E)$ for $j = 0$, 1 is performed in a way which better conforms the conditions of the experiment of Ref. 13, namely, assuming constant 3:1 population ratio of $I = 1$ and $I = 0$ states or so called "normal" hydrogen in the gas mixture with the $\mathrm{He^+}$ ions. Appropriate counterparts of the functions $k_I^{\mathrm{trad}}(T)$ for $I = 0$, 1 are obtained as

$${}_{\mathrm{n}}k_I^{\mathrm{trad}}(T) = k_I^{\mathrm{trad}}(T)\frac{Z(T)}{4Z_I(T)}, \tag{54}$$

where $Z = \sum_I g^I Z_I$ and $\sum_I g^I = 4$, see Eq. (8). They are also presented in Fig. 16 and in Table III.

TABLE III. Rate constants k (in 10^{-15} s^{-1} cm^3) for reactions RA, RCT$_{nr}$, RCT.., and RA + RCT + iRaT(:=trad) at selected temperatures T from the range 2–50 K. Contributions of transitions from continuum states (bck) and from selected groups of resonances in reactant channel. Results from the state-to-state approach ($A \to X_4$ and $A \to X_6$) and from the 3D optical potential model. Comparison of the X_4 projected version of the model with the state-to-state approach in terms of $\Delta = (x_{3Dop}/x - 1) \times 100\%$ for $x = k^{RCT_{nr}} + k^{RA}$. Under the symbol ${}_nk^{trad}$ listed are values of the rate constant for the RA + RCT + iRaT in gas mixtures with "normal" H_2.

	$A \to X_4$						$A \to X_6$	$A \to X$						
	$k^{RA}_{I=0}$		$k^{RCT_{nr}}_{I=0}$			Δ	$k^{RCT..}_{I=0}$	$k^{RA+RCT+iRaT}_{I=0}$			$k^{trad}_{I=1}$			${}_nk^{trad}$
T	tot[a]	bck[b]	tot[c]	bck[d]	res[e] $b=0$			tot[f]	bck	res $b=0$	tot[g]	bck[h]	res[i] $b=1$	[j]
2	3.16	0.37	70.7	3.4	5.7	0.8	89.8	113.2	5.7	9.3				41.6
5	2.39	0.31	49.1	4.3	3.8	0.7	62.4	79.3	7.0	6.0				39.1
7	2.03	0.28	40.3	4.5	3.1	0.7	51.3	65.3	7.3	4.9				37.3
10	1.73	0.25	33.5	4.7	2.5	0.7	42.6	54.4	7.5	4.0				35.4
15	1.46	0.22	28.8	4.8	2.1	0.6	36.6	46.7	7.7	3.3				33.5
20	1.30	0.21	26.6	4.9	1.8	0.6	33.8	43.2	7.8	2.9	0.1			32.1
25	1.17	0.20	25.2	4.9	1.7	0.6	32.0	40.9	7.8	2.6	0.3	0.1		31.0
30	1.05	0.19	23.9	4.9	1.5	0.5	30.3	38.7	7.7	2.4	0.8	0.2	0.1	30.1
35	0.94	0.18	22.4	4.7	1.4	0.5	28.4	36.3	7.4	2.2	1.7	0.5	0.3	29.3
40	0.83	0.16	20.7	4.4	1.3	0.4	26.1	33.6	7.1	2.0	2.9	0.9	0.4	28.6
45	0.73	0.15	18.8	4.1	1.2	0.4	23.8	30.8	6.7	1.8	4.2	1.3	0.6	28.0
50	0.64	0.14	17.0	3.8	1.0	0.4	21.5	28.1	6.2	1.7	5.6	1.8	0.8	27.5

[a]The values differ slightly (by 4% at most) from those listed in Table X of Ref. 15. This is mostly because: (i) the present numbers account additionally for transitions to the six very sharp X-channel resonances which are listed in Table III of Ref. 18 (j even case), (ii) the contributions of the A-channel resonances are reevaluated using the "cutting factor" $\Gamma/(\Gamma + \Gamma^{RA+RCT+iRaT})$ in place of $\Gamma/(\Gamma + \Gamma^{RA})$.

[b]At $T > 10$ K, can be approximated by $0.374 \times T^{-0.192}/Z(T) := \overline{k^{RA(bck)}}(T)$ with $Z(T)$ defined in Eq. (8) and truncated to $1 + 9\exp(-170.31/T) + 5\exp(-509.37/T)$.

[c]Temperature dependence of resonance part ("tot"−"bck") can be described at $T > 15$ K (see Fig. 17(b)) as: $46.9 \times T^{-0.255}/Z(T) := \overline{k^{RCTnr(res)}}(T)$.

[d]Analytical representation at $T > 10$ K is: $B^{RCTnr+RA}/Z(T) - \overline{k^{RA(bck)}}(T) := \overline{k^{RCTnr(bck)}}(T)$ with $B^{RCTnr+RA} = 5.1$ matching well the value of $\sqrt{\frac{2}{\mu}}\varsigma \times p^{RCTnr+RA} = 5.0$, where ς is the parameter of the capture cross-section presented in Fig. 14.

[e]Contribution of the twelve sharp $b = 0$ resonances listed in Table I.

[f]Assuming that the iRaT contribution is $\overline{P^{pT}} \times (k^{trad} - k^{RCTnr} - k^{RA})$ with $\overline{P^{pT}} \in [0.15, 0.3]$ (see footnote a in Table II), the rate $k^{RCT}_{I=0}$ is estimated to constitute about 87%−92% of the value of $k^{trad}_{I=0}$ for a given T.

[g]About 87%−92% of the value of $k^{trad}_{I=1}$ for a given T is estimated to be the rate $k^{RCT}_{I=1}$. See footnote *f*.

[h]Added to $k^{trad(bck)}_{I=0}$ in the tenth column gives the total background part nearly constant at $T > 20$ K: $\overline{k^{trad(bck)}}(T) = B^{trad} = 7.9$. The respective value from the capture cross-section is 7.6.

[i]Contribution of about forty $b = 1$ resonances which occur in the energy range of 118.37−350 cm^{-1}. See Fig. B7b of Ref. 25.

[j] At $T > 15$ K, the contribution ${}_nk^{trad}_{I=1}(T)$ constitutes a nearly constant fraction of ∼2/3 of the values of ${}_nk^{trad}(T)$. The "bck" contribution is nearly the same as $k^{trad(bck)}$, see Fig. 16(b). More details on the function ${}_nk^{trad}(T)$ in the range $T = 5$–100 K are given in Fig. B9 and in Tables BX– BXI of Ref. 25.

Figure 16(a) shows the rate constant function of the total radiative quenching of the He^+ ions from the gas mixture with "equilibrium" hydrogen, $k^{trad}(T) = k^{trad}_{I=0}(T) + k^{trad}_{I=1}(T)$, and compares the magnitudes and shapes of its various parts in the entire temperature range considered. At temperatures below 1 mK, the function $k^{trad}(T)$ as well as its parts $k^{RCT_{nr}}(T)$ and $k^{RA}(T)$ are constant

$$k^{rad}(T) \approx \frac{\hbar^2\pi}{2\mu^{3/2}} \mathcal{C}^{rad}_{J=0};$$

the respective values are 4.56, 2.88, and 0.13×10^{-16} s^{-1} cm^3. At temperature between 1 mK and 2 K, the function $k^{trad}(T)$ rapidly grows due to increasing involvement of reactant states other than the $J = 0$ state. Transitions from $J = 1$–3 continuum states enlarge the background part of the function by a factor about 10 and transitions from the lowest resonances, in particular from the (2 2 2 5) state, build up a peak whose height at $T = 2$ K exceeds more than ten times the value of the background. At higher temperatures, $10 < T < 100$ K, transitions from all included continuum states together with transitions from the shape resonances ($b = 0$ and $b = 1$ states) produce a nearly constant "bck+shp" part of $k^{trad}(T)$ whereas the contribution of the Feshbach resonances ($b = 2$ and $b = 3$ states) decreases roughly like $T^{-2/5}$ (see Fig. B9 and Tables BX– BXI of Ref. 25 for a more detailed description).

At temperatures below 20 K, the function $k^{trad}(T)$ practically describes the quenching due to collisions with $H_2(I = 0)$ only; the constituent $k^{trad}_{I=1}$ is totally negligible (see Table III and Fig. 16(b)). One may wonder how the quenching at these low temperatures would look like if the gas mixture contained pure ortho-hydrogen. This is answered in Fig. 16(a) by showing the rate constant function ${}_ok^{trad}(T) = \frac{4}{3}{}_nk^{trad}_{I=1}(T)$. Its overall shape in the range $T < 1$ K is quite similar to the shape of the function $k^{trad}(T)$ but two significant shifts occur: the cold limit of ${}_ok^{trad}$ lies higher, at 7.54×10^{-16} s^{-1} cm^3, and the peak appears at a lower temperature, of ∼10 mK. This peak is built by transitions from $b = 1$ resonances, predominantly from the $(1\,1\,8\,2^e)$ resonance which lies only 0.008 cm^{-1} above the ε_{01} threshold (see Fig. B6b and Table BIII of Ref. 25). At temperatures around 1 K, transitions from $b = 3$ resonances (see Table BIV of Ref. 25) begin to build a second, though much lower peak in the function ${}_ok^{trad}(T)$, with maximum value of $\sim 30 \times 10^{-15}$ s^{-1} cm^3 attained near 10 K.

Figure 16(b) gives an expanded view of the function $k^{trad}(T)$ and of its parts in the temperature range 10–100 K and additionally shows two sets of curves and symbols which serve the following two purposes: (i) a comparison of $k^{trad}(T)$

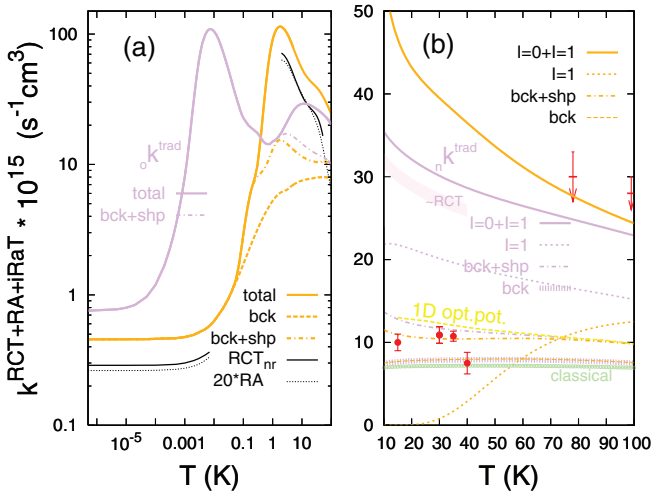

FIG. 16. (a) Rate constants of the radiative reactions RCT + RA + iRaT(:=trad), RCT_{nr}, and RA determined as functions of temperature in the present study: $k^{trad}(T)$—in the range 1μ K−100 K (from the 3D optical potential model), $k^{RCT_{nr}}(T)$ and $k^{RA}(T)$—in the subranges 1 μK−10 mK and 2−50 K (from the state-to-state approach). Note that the values of k^{RA} are enlarged 20 times in the figure. Also shown are the contributions to $k^{trad}(T)$ of transitions from the reactant continuum states (bck) and shape resonances ($b = 0$ and $b = 1$ states). The violet curves are for the RCT + RA + iRaT in gas mixtures with pure *ortho*-H2. (b) Rate constant $k^{trad}(T)$ and its various components in the range 10−100 K plus the function ${}_nk^{trad}(T)$ and its respective components describing the RCT + RA + iRaT in gas mixtures with "normal" hydrogen. "∼RCT"—an estimated contribution of RCT to ${}_nk^{trad}$ (see Fig. A19a of Ref. 25). "Classical"—obtained from the classical cross-section shown in Fig. 14. Comparison with results from the 1D optical potential model of Ref. 14 and with the available experimental data (red symbols): the values of k^{RCT} determined in Ref. 13 (dots) and the upper limits for $k^{RCT+iRaT}$ determined in Refs. 3, 4, and 12 (downward arrows).

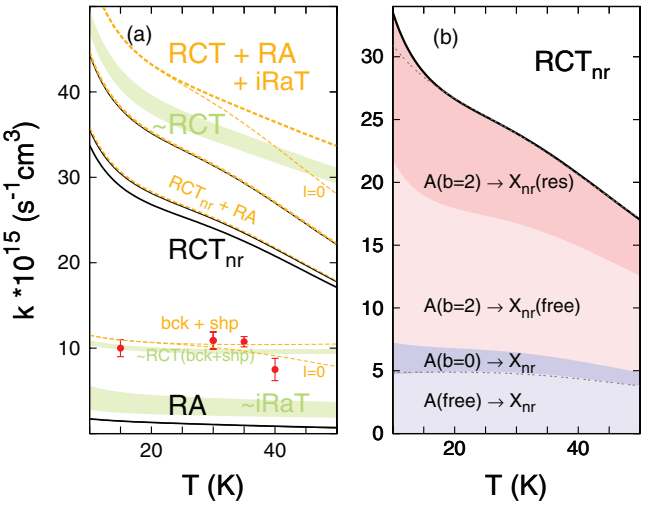

FIG. 17. (a) Rate constant $k^{RCT}(T)$ in the temperature range 10−50 K (the green area labeled ∼RCT) obtained from the calculated rate constant functions (black and yellow lines) $k^{RA}_{l=0+1}(T)$, $k^{RCT_{nr}}_{l=0}(T)$, and $k^{RCT+RA+iRaT}_{l=0+1}(T)$ under the assumption (see text and Fig. A19 of Ref. 25) that the values of $k^{iRaT}(T)$ are within the range shown by the green strip labeled ∼iRaT. Comparison of the estimated "bck + shp" part of $k^{RCT}(T)$ (excluding the Feshbach resonance contributions) with the experimental data of Ref. 13. The nearly coincident yellow and black lines show rate constants due to transitions to the X_4 and X_6 subspaces obtained from the $X_{N_{v'}}$-projected optical potential and the state-to-state approaches. (b) Rate constant of the RCT due to transitions to the nonreactive subspace of the X channel. The colored areas under the $k^{RCT_{nr}}(T)$ curve (black solid line) show contributions of transitions from the A-channel continuum (free), sharp shape ($b = 0$), and Feshbach ($b = 2$) resonances. The latter contribution is resolved into parts showing the role of two kinds of final states of the transitions: the X-channel continuum and resonance states. The gray pointed lines show the analytical fits (described in Table III): $\overline{k^{RCT_{nr}(bck)}}(T)$ and $\overline{k^{RCT_{nr}(res)}}(T) + \overline{k^{RCT_{nr}(bck)}}(T)$.

with the rate constant function for the quenching of the He^+ ions from mixtures with the "normal" hydrogen, ${}_nk^{trad}(T) = \sum_l {}_nk^{trad}_l(T)$, and (ii) a confrontation of both functions with the available experimental data[3,4,12,13] and the previous theoretical simulation.[14]

The rate constant ${}_nk^{trad}(T)$ takes a clearly smaller value than its "equilibrium" counterpart $k^{trad}(T)$, 35.4 versus 54.4 $\times 10^{-15}$ s^{-1} cm^3, at the lower border of the T interval shown in Fig. 16(b) but it decreases less rapidly inside the interval and becomes by only ∼6% smaller at the upper border, 22.9 versus 24.4 $\times 10^{-15}$ s^{-1} cm^3. Actually, the background parts of the two functions are almost identical and nearly constant within the entire interval 10–100 K,

$$ {}_nk^{trad(bck)}(T) \approx k^{trad(bck)}(T) \approx \sqrt{\frac{2}{\mu}}\, \varsigma\, p^{trad}, $$

which is a consequence of the validity of the capture model, Eq. (53). The common background is quite close to the rate constant curve which is obtained from the classical cross-section plotted in Fig. 14. Thus, the difference between the functions ${}_nk^{trad}(T)$ and $k^{trad}(T)$ appears here as a purely quantum effect since it almost entirely stems from the involvement of the A-channel resonances in the RCT + RA + iRaT reaction. The resonance parts of the functions, ${}_nk^{trad(res)}(T)$ and $k^{trad(res)}(T)$, differ in values at $T = 10$ K like 27.9 and 46.9 $\times 10^{-15}$ s^{-1} cm^3 and in shapes within the 10–100 K interval like $T^{-0.26}$ and $T^{-0.41}$.

Of particular interest in the present study are the contributions of the Feshbach versus shape resonances in the reactant channel. They can be estimated by comparing the curves labeled in Fig. 16(b) "$I = 0 + I = 1$," "bck + shp," and "bck," those drawn in yellow color—for k^{trad}, and in violet—for ${}_nk^{trad}$. The shape resonances are seen to contribute approximately one fourth to the "bck+shp" value of k^{trad} which is $\sim 10^{-14}$ cm^3 s^{-1}. The Feshbach resonances enlarge this value by a factor which varies from nearly 5 at $T = 10$ K to nearly 2.5 at 100 K. It has to be noticed, however, that at temperatures $T \lesssim 10$ K the rate constant k^{trad} sensitively depends on positions of the near threshold $b = 2$ resonances, like (2 2 2 5) and (2 1 1 4). A slight correction of the potential V^A can easily shift these resonances below the threshold. The high peak at $T = 2$ K would then disappear and the values at $T = 10 - 15$ K would diminish even by 50% (see Fig. B9d of Ref. 25). But even when taking a slight inaccuracy of the upper state potential into account, one can safely conclude that no less than 70% of the magnitude of the rate constant k^{trad} at temperatures 15−40 K are due to transitions from the Feshbach resonances. The contribution decreases from ∼70% to ∼60% with T increasing from 40 to 100 K.

A comparison of the violet and yellow "bck + shp" curves in Fig. 16(b) reveals that the shape resonances make actually a somewhat larger contribution to the rate constant ${}_nk^{trad}$ than to k^{trad}. So, the decreased values of ${}_nk^{trad}$ are just due to the involvement of the Feshbach resonances. More

precisely, the decrease is caused by the fact that the average position of $b = 3$ states relative to the threshold ε_{01} is higher than the average position of $b = 2$ states relative to ε_{00}. Further details on ${}_{\rm n}k^{\rm trad}$ versus $k^{\rm trad}$ are given in Fig. B9 and in Tables BX–BXI of Ref. 25. Here, it should be emphasized that the percentage contribution of the Feshbach resonances to the rate constant ${}_{\rm n}k^{\rm trad}$ is still large, i.e., ∼60 % in the entire 10–100 K range.

The "bck+shp" part of $k^{\rm trad}(T)$ [or ${}_{\rm n}k^{\rm trad}(T)$] is the closest counterpart of results which are obtainable for the entire rate constant function from one-dimensional optical potential models, see Figs. B1 and B2 and Table BI of Ref. 25. Indeed, this part of ${}_{\rm n}k^{\rm trad}(T)$ agrees very well with the results from the model calculations of Kimura and Lane[14] shown in the figure. The agreement is an important aspect in the present theoretical argumentation to characterize the RCT reaction.

As already indicated by the state-to-state calculations, it is especially the benefit from applying the present extended version of the optical potential model that the rate constant for the radiative quenching of the He^+ ions from the mixture with the H_2 molecules can be safely determined. This provides the basis for demonstrating the importance of the quasi-bound $b = 2$ and $b = 3$ states formed by the reactants. The large increase in the rate constant due to these resonance states is fully consistent with Hopper's hypothesis about the role of rotational predissociation as a possible initial step of the RCT reaction but it is in conflict with the experimental findings of Schauer *et al.*[13] Their values for the rate constant of the RCT reaction at temperatures in the range 15–40 K are far below the ${}_{\rm n}k^{\rm trad}(T)$ curve in Fig. 16(b). But they coincide well with the present "bck + shp" curve(s). On the background of the present results it becomes therefore evident that the conclusion by Schauer *et al.* "that radiative charge transfer does not involve complex formation" cannot be maintained. Even if inaccuracies in the potential determinations and the effects of approximations in the dynamics calculations are critically taken into account, there cannot be any doubt about the importance of Feshbach resonances in this process.

Actually, the rate constant ${}_{\rm n}k^{\sim\rm RCT}$ (see Fig. A19 of Ref. 25 and Fig. 17(a)) rather than ${}_{\rm n}k^{\rm trad}$ should be compared to the experimental results of Ref. 13 which reduces the discrepancy, however, only slightly. The relative deviations $[{}_{\rm n}k^{\sim\rm RCT}/k^{\rm RCT}_{\rm expt} - 1]\times 100\%$ are of the size of 150% –250%.

There is, on the other hand, an example for a fairly good agreement between the present results and earlier experimental findings. The values of the rate constant $k^{\rm trad}$ at temperatures in the range 80−100 K appear to be close to the upper bound for the rate of production of the H_2^+ and HeH^+ ions in $He^+ + H_2$ collisions obtained experimentally by Johnsen *et al.*[3,4] These measurements are quoted in Fig. 16(b) by the two downward arrows. The same upper bound has also been referred to by Schauer *et al.*[13] to demonstrate consistency with the earlier experiments. Surprisingly, in their Fig. 4 this bound is substantially lowered.[48]

Figure 17(a) presents a resolution of the rate constant $k^{\rm trad}(T)$ into contributions of the three participating reactions in the temperature range 10–50 K. The resolution is made using the state-to-state results for the RA and $\rm RCT_{nr}$ reactions and the estimation for the iRaT which is described in Sec. VI D 1. Translated to rate constant, Eq. (50) gives $k^{\sim\rm iRaT}(T) = f(T)k^{\rm trad}(T)$ with $f(T) = \overline{P^{\rm pT}}\times[1 - k^{\rm RCT_{nr}+RA}_{I=0}(T)/k^{\rm trad}_{I=0}(T)]$. This estimate and the corresponding estimates of the "true" RCT rate constant $k^{\sim\rm RCT} = (1 - f)k^{\rm trad} - k^{\rm RA}$, and of its "bck + shp" part are shown in the figure by the light green strips. The contributions of $k^{\sim\rm RCT}$, $k^{\sim\rm iRaT}$, and $k^{\rm RA}$ to the values of $k^{\rm trad}$ are: ∼87%−92%, ∼10%−5%, and ∼3%−2%, respectively. At $T < 40$ K, the calculated values of $k^{\rm RCT_{nr}}_{I=0}$ constitute approximately two thirds of the estimated values of $k^{\sim\rm RCT}$.

Figure 17(b) shows a resolution of the rate constant $k^{\rm RCT_{nr}}_{I=0}(T)$ for $T \in [10, 50]$ K into contributions depending on the character of individual states of the radiative $A \to X_{\rm nr}$ transitions: either resonance ($b = 2$ or $b = 0$) or continuum (free) states in the A channel and either resonance or continuum states in the $X_{\rm nr}$ subspace of the X channel. The largest contribution, of about 40%, is due to $b = 2 \to$ free transitions. Resonance-resonance transitions play a comparable role, but are definitely not as dominating as was expected by Hopper. This is due to the fact that the X-channel resonances are generally shorter-living, less discernible from continuum, than their A-channel counterparts (see Figs. A3–A13 and Tables AI–AV of Ref. 25). It should be noticed here, however, that the resolution of the entire $b = 2$ resonance contribution into the $A(b = 2) \to X$(free) and $A(b = 2) \to X$(resonance) parts presented in the figure is actually somewhat artificial. It has been obtained by dividing the range of integration over the energy E' of the respective width functions $\partial\Gamma/\partial E'$, i.e., the range $0 - E'_{\rm max}(X_4)$, into two subranges that included halves of the intervals between the subsequent $\varepsilon_{v',\,j'=2}$ thresholds lying, respectively, above and below these thresholds for $v' = 0 - 3$.

F. Populations of final states

1. As functions of energy $E < \varepsilon_{01}$

Populations of vibrational and rotational states of the H_2^+ ion produced in transitions from individual resonance and continuum states of the $He^+ + H_2(v = 0, j = 0)$ reactants (examples displayed in Figs. 4–6, and Ref. 25, Fig. A16) are discussed here in the form summarized—as the ratios of the cross-sections,

$$P_{c'}(E) = \sigma^{\rm RCT_{nr}}_{\to c'}(E)/\sigma^{\rm RCT_{nr}}(E) \qquad \text{for} \quad c' = v',\, j'.$$

In this form they are presented in Fig. 18 for four selected values of the energy E, including one from the ultra-cold range.

The populations $P_{v'}(E)$ for $v' = 0 - 3$ in Fig. 18(a) do not differ much from the "individual" populations $P_{v'}(EJ; J')$ and $P_{v'}(nJ; J')$ shown in Figs. 4 and 6. Practically independently of E, the populations are $P_{v'=0} \approx P_{v'=1} \approx 30\% - 35\%$ and $P_{v'=2} \approx 20\%$.

The maximum of $P_{v'}$ occurs at the two lowest states, not at $v' = 2$. As pointed out previously, this is an effect of vibrational inelasticity in the X channel. However, the effect is probably overestimated in the figure due to the limitation of the manifold of product states to the $X_{\rm nr}$ subspace. It can be expected that radiative transitions to the subspace $X\backslash X_{\rm nr}$ will populate also $v'>3$ states and that subsequent inelastic transitions from this subspace will enhance populations of $v' = 3, 2$

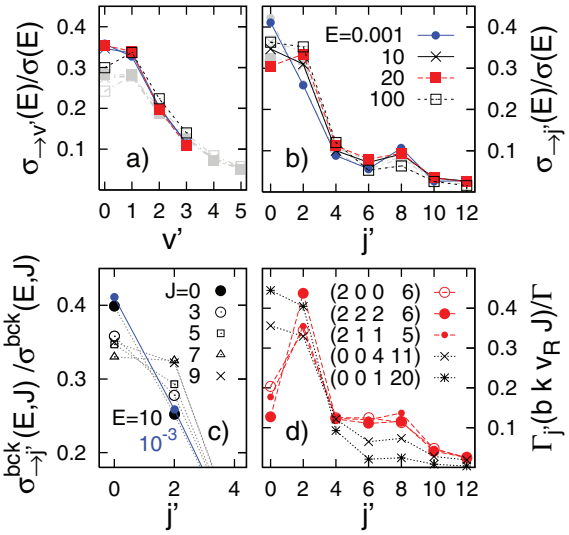

FIG. 18. Populations $P_{c'}(E) = \sigma_{\to c'}(E)/\sigma(E)$ of a) vibrational ($c' = v'$) and (b) rotational ($c' = j'$) states of the product ion H_2^+ of the RCT_{nr} reaction ($v'_{max} = 3$) for three energies E of the reactants in the subthermal range, chosen to be close (filled red squares) and far from $b = 2$ resonance positions (black symbols), and for $E = 0.001$ cm^{-1} representing the ultra-cold range. At the latter energy, the total cross-section is $\sigma^{RCT_{nr}}(E) \approx \frac{\pi\hbar^2}{2\mu} \mathcal{C}^{RCT_{nr}}_{J=0} \times E^{-1/2} \approx 2.15\times10^{-4+3/2}$ Å^2. The values of $\sigma^{RCT_{nr}}(E)$ for the other energies can be found in Table II. The gray symbols show the populations due to transitions to the X_6 subspace of the X channel ($v'_{max} = 5$). (c) Population of $j' = 0$ and $j' = 2$ states in transitions from continuum states (E, J). Dependence on the number J. (d) Comparison of j'-state populations from decay of $b = 2$ and $b = 0$ resonances. The values of the total widths Γ are listed in Table I, in the column $\Gamma^{RCT_{nr}}$. See also Figs. A16 and A18 of Ref. 25.

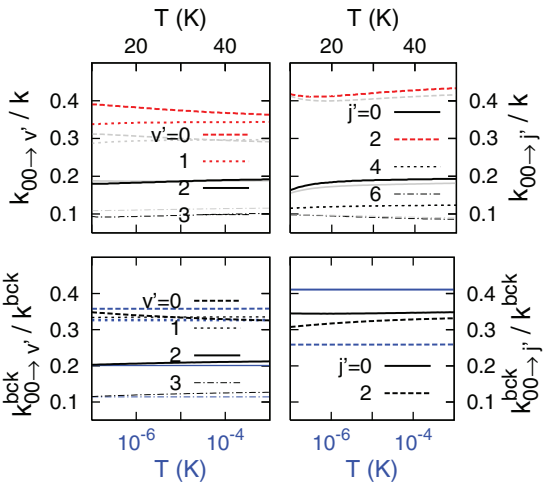

FIG. 19. (Upper) Temperature averaged populations $P_{c'}(T) = k_{00\to c'}(T)/k(T)$ of vibrational ($c' = v'$) and rotational ($c' = j'$) states of H_2^+ ions produced in the RCT_{nr} reaction at temperatures $T \in [10, 50]$ K. The values of $k(T)$ are listed in Table III (in the column "tot" of $k^{RCT_{nr}}_{I=0}$) and plotted in Fig. 17. The gray lines show populations due to transitions to the X_6 subspace of the X channel. (Lower) Populations of the product ion states in the RCT_{nr} reaction from the reactant continuum states at temperatures $T \in [10, 50]$ K (black lines, the upper T axis) compared to the populations at cold temperatures (blue lines). The values of $k^{bck}(T)$ in the subthermal range are listed in Table III (the fifth column); the values in the cold range are plotted in Fig. 16(a) (the "RCT_{nr}" line).

states in X_{nr}. In the "true" RCT the states $v' = 0 - 3$ will therefore be more evenly populated compared to what is shown with the dark symbols in Fig. 18. A shift of the maximum population to $v' = 2$, however, does not seem to be likely. This is indicated by the gray symbols in Fig. 18(a) representing populations due to transitions to the subspace X_6, which cover about 80% of all transitions contributing to the "true" RCT (according to the estimations of Ref. 25, Fig. A19a).

The populations $P_{j'}(E)$ shown in Fig. 18(b) for $E = 0.001$, 10, and 100 cm^{-1} have shapes that are characteristic of transitions from continuum states and $b = 0$ resonances. This is obvious for transitions at the energy $E = 0.001$ cm^{-1} since $P_{j'}(E) \approx P_{j'}(E, J = 0)$ in the ultra-cold range. At this energy, the j'-state population is clearly peaked at the lowest state, $P_{j'=0} \approx 40\%$ while $P_{j'=2} \approx 25\%$. The two lowest j' states dominate at the energies $E = 10$ and 100 cm^{-1}: $P_{j'=0} \approx 35\%$ and $P_{j'=2} \lesssim P_{j'=0}$. As was stated at the end of Sec. VI A and as illustrated in panel (c) of the present figure, such populations occur in transitions from partial continuum (E, J) states when $J > 5$. Indeed, the largest contributions to the total cross-sections at the two energies $E = 10$ and 100 cm^{-1} are made by the partial cross-sections for $J = 9$ and $J = 18$, respectively.

However, at energies approaching $b = 2$ resonance positions, such as $E = 20$ cm^{-1}, the relation between the two dominant populations becomes reversed: $P_{j'=2} \gtrsim P_{j'=0}$. Obviously, at energies very close to these resonances, $P_{j'=2}(E) \approx \Gamma^{RCT_{nr}}_{j'} / \Gamma^{RCT_{nr}}$ and, as shown in Fig. 18(d), the population of the state $j' = 2$ dominates over population of any other j' state.

2. *As functions of temperature T∈ [10⁻⁷ − 50] K*

The populations as functions of temperature are defined as

$$P_{c'}(T) = k^{RCT_{nr}}_{\to c'}(T)/k^{RCT_{nr}}(T) \qquad \text{for} \quad c' = v', j'$$

and are shown in Fig. 19 for the two temperature intervals: $10 - 50$ K and $10^{-7} - 10^{-3}$ K. In addition, the figure presents the populations $P^{RCT}_{c'}(T)$ which result from the $A \to X_6$ reaction (shown as gray lines in the upper panel) and the populations $P^{bck}_{c'}(T)$ obtained just from the background parts of the rate constant functions for the RCT_{nr} (black lines in lower panels). $P^{bck}_{c'} = P_{c'}$ for $T < 10^{-3}$ K. All the populations turn out to be nearly constant within the subthermal and the ultra-cold temperature intervals.

The populations $P_{v'}(T)$ in the temperature range 10–50 K are close to those in Fig. 18 represented by the functions $P_{v'}(E)$ for $E = 10$, 100 cm^{-1}, namely, $P_{v'} \approx 36\% - 39\%$, 34%, $18\% - 19\%$, and $9\% - 10\%$ for $v' = 0$, 1, 2, and 3, respectively. Only slightly different are the corresponding values of $P^{bck}_{v'}$ at temperatures in the subthermal as well as in the ultra-cold interval, $P^{bck}_{v'} \approx 35\%$, 20%, and 11% for $v' = 0 - 1$, 2, and 3, respectively. Transitions from the rotational resonances in the A channel which are accounted for by the $P_{v'}$ values but excluded from the $P^{bck}_{v'}$ values have thus rather little effect on the population of vibrational states of the product ion.

Transitions to the "reactive subspace" of the X channel can in principle change the populations $P_{v'}$ as was pointed

out previously. Comparison with the values of $P_{v'}^{\mathrm{RCT..}}$ in the upper left panel of Fig. 19 shows that the populations of the $v' = 0 - 1$ states are lowered (to ≈30%) whereas the population of $v' = 2$ state remains at the level of ≈19%. This shows that transitions to the $X\backslash X_6$ subspace in the "true" RCT can be expected to reduce the difference between the two populations by one half at most.

The populations of the j' states are shown in the right panels of Fig. 19. The values of $P_{j'}(T)$ at $T \in [10, 50]$ K are: ≈41%–43%, 16%–19%, and 12% for $j' = 2$, 0, and 4, respectively. The big population of the excited $j' = 2$ state could only be produced by transitions from the $b = 2$ resonances. This should be evident from the discussion of Sec. VI A and is, in addition, illustrated here by a comparison with the populations $P_{j'}^{\mathrm{bck}}(T)$. At temperatures in the subthermal interval $P_{j'=0}^{\mathrm{bck}} \gtrsim P_{j'=2}^{\mathrm{bck}} \approx 35\%$, i.e., these values are determined by transitions from $b = 0$ resonance and high J continuum states. At cold temperatures, when no A-channel resonance participates in the radiative transitions, the population of $j' = 0$ state becomes dominant, $P_{j'=0}^{\mathrm{bck}} (= P_0) \approx 40\%$.

The maximal populations $P_{v'=0,1}$ and $P_{j'=2}$ are identified by red lines in Fig. 19 to underline that they are at variance with Hopper's predictions (maximum at $v' = 2$ and $j' = 0$, respectively). An explanation for the present maximum population results can be obtained with the aid of the X_4 projected version of the optical potential model (details in Figs. B4c–B4e of Ref. 25). The populations extracted from the model, denoted by ${}^{\mathrm{opt}}P_{c'}$ for $c' = v', j'$, obviously disregard the impact of vibrationally and rotationally inelastic transitions in the X channel. The populations ${}^{\mathrm{opt}}P_{v'}$ nearly match Hopper's prediction. The value for $v' = 2$ state is very close to the maximal value, for $v' = 1$ state, and the value for $v' = 0$ state is the smallest.

This is in contrast to the role of the X-channel interactions in the case of rotational states. The populations ${}^{\mathrm{opt}}P_{j'}$ have an even higher maximum at $j' = 2$ state compared to the populations $P_{j'}$ which is even more inconsistent with Hopper's prediction. The fact that the population of rotational states of the H_2^+ ion has its maximum at $j' = 2$ and not at $j' = 0$ has to be attributed to the dominance of $b = 2k > 0$ resonances in the A channel and to the strong tendency to preserve the quantum number k in transitions to the X channel.

VII. CONCLUSIONS

Accurate state-to-state calculations are performed to study the radiative charge transfer process originating from subthermal collisions of He^+ with H_2 and to evaluate the reaction scheme proposed by Hopper[8] characterizing RCT as opposed to DCT.

These calculations demonstrate clearly the importance of complex formation on the A-state potential via the rotational predissociation mechanism. This is in full support of Hopper's postulate[8] about the first step (2a) in his RCT reaction scheme but disagrees with the comment in Ref. 13 that "radiative charge transfer does not involve complex formation." Actually transitions from these Feshbach resonances ($b = 2$) contribute to about 75% to the total rate constant k^{RCT} in the temperature range ~10–40 K. The remaining 25% are due to transitions from A-channel free states as well as from shape resonances ($b = 0$) which contribute only about 5%–8%. Among the transitions from Feshbach resonances it turns out that those to X-channel resonances are equally important as those to X-channel free states.

In Hopper's scheme the second reaction step (2b) is described making use of the Franck-Condon principle with the consequence that maximum photon emission is predicted to occur at 153 nm and that H_2^+ fragments should be vibrationally excited with a peak at $v' = 2$. Actually, from the state-to-state calculations the photon emission spectrum is obtained with broad peaks centered at transition energies to states of the $He + H_2^+$ system near the $v'\, j' = 2$ thresholds for $v' = 0, 1, 2, 3$, where the highest peak occurs for $v' = 1$ and the peak for $v' = 2$ is slightly smaller. The corresponding photon wave-lengths are 138.6 and 142.8 nm. The vibrational state population of the H_2^+ fragments does not reflect the relations between the peak sizes in the emission spectrum, however. The ions occur mostly in the two lowest states, with the percentage populations $P_{v'=0} \gtrsim P_{v'=1} \approx 40\% - 30\%$ while the fraction of the ions in the $v' = 2$ state is only $P_{v'} \approx 20\%$. This demonstrates the importance of vibrationally inelastic transitions in the X channel.

The rotational state population among the H_2^+ ions produced at temperatures ~10–50 K is also at variance with Hopper's expectation since $P_{j'=0} \approx 20\%$ while the maximum is $P_{j'=2} \approx 40\%$. The big population of $j' = 2$ state is caused by transitions from $b = 2k > 0$ resonances. At very low temperatures, $T < 1$ mK, when transitions from the A-channel resonances are totally unimportant, the j'-state population is different: the maximum occurs at the lowest state, as expected by Hopper, $P_{j'=0} \approx 40\%$, and $P_{j'=2} \approx 25\%$.

The rate constant determination within the present state-to-state approach suffers from the fact that transitions to high lying X-channel states cannot rigorously be taken into account[25] and limitation to a non-reactive part ($\mathrm{RCT_{nr}}$) misses their non-negligible contributions. The compromise (~RCT) introduced in this study takes advantage from the possibility to calculate the total radiative quenching rate (k^{trad}) of He^+ ions within the 3D optical potential approach. The values $k^{\sim\mathrm{RCT}}$ estimated as ~90% of the calculated k^{trad} are derived correcting this value using the known contribution from the RA reaction (3)[15] and an estimated iRaT effect. The large discrepancy, however, between these $k^{\sim\mathrm{RCT}}$ values and the experimentally determined results of Schauer *et al.*[13] cannot be attributed to inaccuracies in the basic potential calculations[19] or uncertainties in the iRaT estimate. Comparison of the various contributions to the RCT rate constant with the experimental findings[13] and the results of the model calculations[14] of Kimura and Lane demonstrates clearly that the large difference is mostly due to inclusion of the effect of rotational Feshbach resonances in the present theoretical RCT study.

It is an advantageous feature of the 3D version of the optical potential model that it can account for rotational (and vibrational) Feshbach resonances in the reactant channel, more precisely, the version can provide decay rate of any, Feshbach or shape, resonance in atom + diatom collisions due to spontaneous emission to a lower electronic state. Application of

the 3D model facilitated an extension of the temperature range scanned in the state-to-state study to higher temperatures, up to 100 K. The values of the rate constant function $k^{\text{trad}}(T)$ obtained for $T \in [80, 100]$ K, with above 60% contribution from about 240 rotational $b = 2$ and $b = 3$ resonances, are close to the experimentally derived upper bound for the rate of production of the H_2^+ and HeH^+ ions in $He^+ + H_2$ collisions.[3,4]

[1] B. H. Mahan, J. Chem. Phys. **55**, 1436 (1971).
[2] F. C. Fehsenfeld, A. L. Schmeltekopf, P. Goldan, H. I. Schiff, and E. E. Ferguson, J. Chem. Phys. **44**, 4087 (1966).
[3] R. Johnsen and M. A. Biondi, J. Chem. Phys. **61**, 2112 (1974).
[4] R. Johnsen, A. Chen, and M. A. Biondi, J. Chem. Phys. **72**, 3085 (1980).
[5] R. K. Preston, D. L. Thompson, and D. R. McLaughlin, J. Chem. Phys. **68**, 13 (1978).
[6] D. G. Hopper, Int. J. Quantum Chem. Symp. **12**, 305 (1978).
[7] E. G. Jones, L. C. Wu, B. M. Hughes, T. O. Tiernan, and D. G. Hopper, J. Chem. Phys. **73**, 5631 (1980).
[8] D. G. Hopper, J. Chem. Phys. **73**, 3289 (1980).
[9] L. C. Wu and D. G. Hopper, Chem. Phys. **57**, 385 (1981).
[10] R. Johnsen and M. A. Biondi, J. Chem. Phys. **74**, 6996 (1981).
[11] D. G. Hopper, J. Chem. Phys. **74**, 6997 (1981).
[12] H. Boehringer and F. Arnold, J. Chem. Phys. **84**, 1459 (1986).
[13] M. M. Schauer, S. R. Jefferts, S. E. Barlow, and G. H. Dunn, J. Chem. Phys. **91**, 4593 (1989).
[14] M. Kimura and N. F. Lane, Phys. Rev. A **44**, 259 (1991).
[15] F. Mrugała and W. P. Kraemer, J. Chem. Phys. **122**, 224321 (2005).
[16] The Franck-Condon point lies ∼0.66 eV above the $He(1^1S) + H_2^+(X\,^2\Sigma_g^+, v' = 0)$ asymptote. The position (∼0.8 eV) given in Ref. 8 is actually relative to the bottom of the asymtotic H_2^+ well.
[17] R. Schinke, *Photodissociation Dynamics* (Cambridge University Press, 1993), Chap. 4.
[18] F. Mrugała, V. Špirko, and W. P. Kraemer, J. Chem. Phys. **118**, 10547 (2003).
[19] W. P. Kraemer, V. Špirko, and O. Bludsky, Chem. Phys. **276**, 225 (2002).
[20] M. Šindelka, V. Špirko, and W. P. Kraemer, Theor. Chem. Acc. **110**, 170 (2003).
[21] J. D. Kress, R. B. Walker, and E. F. Hayes, J. Chem. Phys. **93**, 8085 (1990); B. Lepetit and J. M. Launay, *ibid.* **95**, 5159 (1991); V. Aquilanti, G. Capecchi, S. Cavalli, D. De Fazio, P. Palmieri, C. Puzzarini, A. Aguilar, X. Giménez, and J. M. Lucas, Chem. Phys. Lett. **318**, 619 (2000); B. Maiti, C. Kalyanaraman, A. N. Panda, and N. Sathyamurphy, J. Chem. Phys. **117**, 9719 (2002); T.-S. Chu, R.-F. Lu, K.-L. Han, X.-N. Tang, H.-F. Xu, and C. Y. Ng, *ibid.* **122**, 244322 (2005).
[22] J. S. Cohen and J. N. Bardsley, Phys. Rev. A **18**, 1004 (1978).
[23] J. N. Bardsley, J. S. Cohen, and J. M. Wadehra, Phys. Rev. A **19**, 2129 (1979).
[24] B. W. West, N. F. Lane, and J. S. Cohen, Phys. Rev. A **26**, 3164 (1982).
[25] See supplementary material at http://dx.doi.org/10.1063/1.4793986 for: (1) more results on resonances in the non-reactive $He + H_2^+$ collisions, on predissociating states of the $He^+ - H_2$ complex (widths from the generalized adiabatic-bender model), on bound states of $He^+ - H_2$ (radiative widths from the 3D optical potential model); (2) extended demonstration of propensity rules in the $A \to X$ transitions, of the impact of the X-state interactions on the product state populations; (3) demonstration of threshold laws in cross-sections and rate-constants for the radiative quenching of He^+ in collisions with *para*- and *ortho*-H_2; (4) estimation of the iRaT contribution to the calculated characteristics of the RCT + iRaT; (5) accuracy estimations of the present state-to-state calculations; (6) details on implementation of the 3D optical potential model (determination of resonance parameters, construction of projected versions).
[26] R. E. Moss, Mol. Phys. **80**, 1541 (1993).
[27] H. Feshbach, Ann. Phys. **5**, 357 (1958); **19**, 287 (1962).
[28] F. H. Mies, J. Chem. Phys. **51**, 787 (1969).
[29] G. Brocks, A. van der Avoird, B. T. Sutcliffe, and J. Tennyson, Mol. Phys. **50**, 1025 (1983).
[30] L. C. Biedenharn and J. D. Louck, *Angular Momentum in Quantum Physics* (Addison-Wesley, 1981).
[31] D. L. Cooper, K. Kirby, and A. Dalgarno, Can. J. Phys. **62**, 1622 (1984).
[32] B. Zygelman and A. Dalgarno, Phys. Rev. A **38**, 1877 (1988).
[33] B. Zygelman, A. Dalgarno, M. Kimura, and N. F. Lane, Phys. Rev. A **40**, 2340 (1989); A. Dalgarno, M. L. Du, and J. H. You, Astrophys. J. **349**, 675 (1990); P. C. Stancil and B. Zygelman, *ibid.* **472**, 102 (1996); L. B. Zhao, P. C. Stancil, J. P. Gu, H.-P. Liebermann, Y. Li, P. Funke, R. J. Bunker, B. Zygelman, M. Kimura, and A. Dalgarno, *ibid.* **615**, 1063 (2004); X. J. Liu, Y. Z. Qu, B. J. Xiao, C. H. Liu, Y. Zhou, J. G. Wang, and R. J. Buenker, Phys. Rev. **81**, 022717 (2010); M. Gustafsson, S. V. Antipov, J. Franz, and G. Nyman, J. Chem. Phys. **137**, 104301 (2012).
[34] U. Fano, Phys. Rev. **124**, 1866 (1961).
[35] F. H. Mies, Phys. Rev. **175**, 164 (1968).
[36] S. L. Holmgren, M. Waldman, and W. Klemperer, J. Chem. Phys. **67**, 4414 (1977); L. Tao and M. H. Alexander, *ibid.* **127**, 114301 (2007), and references therein.
[37] F. T. Smith, Phys. Rev. **118**, 349 (1960).
[38] F. Mrugała and R. Moszynski, J. Chem. Phys. **109**, 10823 (1998).
[39] W. Jaworski and D. M. Wardlaw, Phys. Rev. A **45**, 292 (1992).
[40] B. R. Johnson, J. Comput. Phys. **13**, 445 (1973).
[41] F. Mrugała, J. Comput. Phys. **58**, 113 (1985); J. Chem. Phys. **91**, 874 (1989).
[42] F. Mrugała, Int. Rev. Phys. Chem. **12**, 1 (1993).
[43] M. S. Child, *Semiclassical Mechanics with Molecular Applications* (Clarendon, 1991), Chaps. 5 and 9.
[44] S. E. Butler, S. L. Guberman, and A. Dalgarno, Phys. Rev. A **16**, 500 (1977).
[45] R. S. Mulliken, J. Chem. Phys. **55**, 309 (1971).
[46] G. Gioumousis and D. P. Stevenson, J. Chem. Phys. **29**, 294 (1958).
[47] R. D. Levine and R. B. Bernstein, *Molecular Reaction Dynamics and Chemical Reactivity* (Oxford University Press, New York, 1987), Chap. 2.
[48] The actual estimation of Ref. 4 is: $0.2 \times k$ where k is the rate coefficient for decay of He^+ ions in two-body collisions with H_2 due to dissociative charge transfer and reactions accompanying it, mostly RCT and iRaT (in the present notation). The values of k listed in Table I of Ref. 4 for $T = 78$ and 330 K are $(1.5 \pm 0.15) \times 10^{-13}$ and $(1.1 \pm 0.1) \times 10^{-13}$ cm^3/s, respectively.

A. SUPPLEMENTARY MATERIAL — PART A

RADIATIVE CHARGE TRANSFER

$$\mathbf{He}^{+} + \mathbf{H}_2 \longrightarrow \mathbf{He} + \mathbf{H}_2^{+} + h\nu$$

STATE-TO-STATE DESCRIPTION

ELECTRONIC STRUCTURE INPUT

to

CALCULATIONS on DYNAMICS of RCT

Fig. A0. Electronic structure input

— limitations on accuracy of state-to-state description

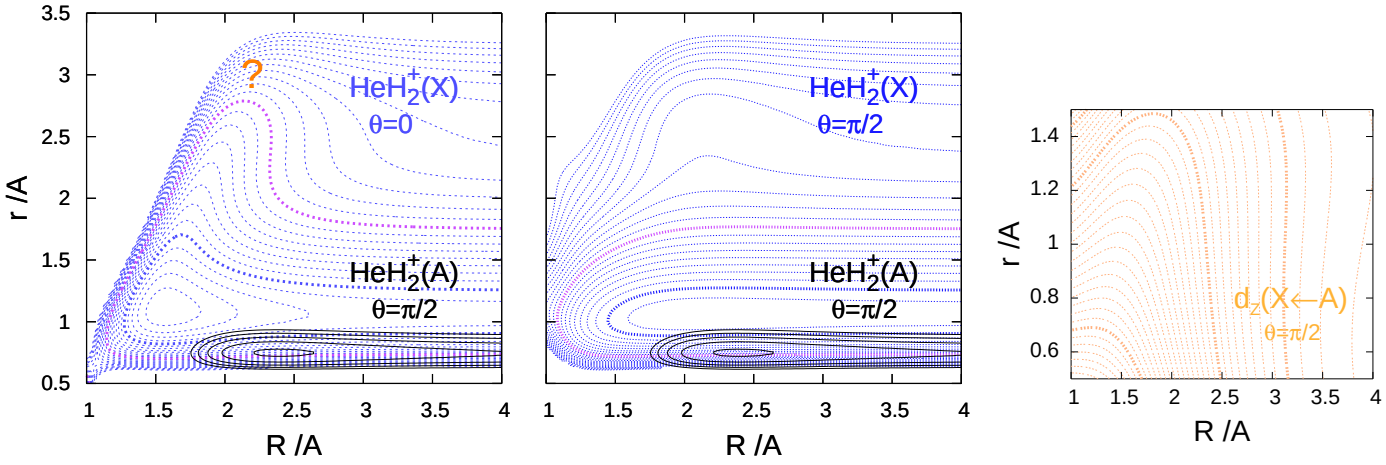

Fig. A0a. Potential energy surfaces for the ground (X) and first excited (A) electronic states of HeH_2^+ from Ref. 1 and Body-Fixed Z-component of electric dipole vector field for $A \rightarrow X$ transitions from Ref. 2, $V^A(r,R,\theta)$, $V^X(r,R,\theta)$, and $d_Z^{\rm BF}(r,R,\theta)$, respectively. r and R denote the lengths of the Jacobi vectors $\mathbf{r}$ and $\mathbf{R}$ for the He+H_2 system, with $\mathbf{r}$ joining the H-nuclei, and θ denotes the angle between the vectors. Shown are contour plots of 2D cuts of the surfaces at $\theta=\frac{\pi}{2}$ and $\theta=0$ (for V^X). The contours of V^A and V^X are drawn in step of 0.1 eV and cover the ranges -0.4 – 0 (zero at $He^+ + H_2(v=0,j=0)$) and -0.4 – 2 eV (zero at $He + H_2^+(v=0,j=0)$), respectively. The thicker blue lines show the zero-energy contours in the two cuts of V^X and the violet contours are for the energy 0.8 eV which on exact X-state PESes is nearly coincident with the position of the $H + HeH^+(v=0,j=0)$ threshold. On the present PES, the entrance to this channel is closed by an artificial wall (indicated by the red question mark). The contours of d_Z are drawn in step of 0.025 ea_0 and cover the range 0–0.85. The three thicker contours (starting from the rightmost) are for 0.1, 0.3, and 0.7 ea_0, respectively.

The zero-energy contour of V^A indicates approximately the range of the r coordinate which is occupied by the reactants at low collision energies. It also indicates the part of the lower surface which is reached by vertical transitions from the reactant states. This is the only part of V^X which is needed to evaluate the characteristics of the total radiative reaction RCT+RA+iRaT within the optical potential model. Sufficient accuracy of this part is documented in Fig. A0b.

The artificial wall arises on the surface V^X because the analytical fit of Ref. 1 is used here beyond the r-coordinate range which was sampled in the *ab initio* calculations of V^X in that work. This is made for underscoring the fact that the rearrangement scattering $He+H_2^+ \rightarrow HeH^+ + H$ is not possible on the present surface, or in other words, that the surface is insufficient for rigorous determination of continuum states of the $He+H_2^+$ system at energies at which the rearrangement in the reality occurs. Determining the states within a possibly accurate inelastic scattering approach seems the best that could be done in this situation. Moreover, when judging adequacy of the applied approach one should keep in mind that the proton transfer reaction is only a secondary process in relation to the radiative reaction which is in the focus of the study. It belongs to effects of the final-state interactions, like the vibrational and rotational de-excitation of the H_2^+ ions discussed in the paper. Even among these effects the significance of the proton transfer appears rather low (see Fig. A19b). Thus, the necessarily limited treatment of the X-state dynamics is believed to be reasonable in some energy range above the rearrangement threshold and at least tolerable in the entire range accessible in the radiative $A \rightarrow X$ transitions. To strengthen this belief one may recall the following. The main limitation of the entire state-to-state approach applied in the study is the impossibility to separate out the contribution of the iRaT process from the calculated rate constant $k^{\rm RCT+iRaT}$ (the proton transfer is a part of the iRaT). According to the theoretical estimations and the experimental evidence existing before, quoted in the Introduction, the contribution should be negligible. The estimate obtained here (see Fig. A19b) — $k^{\rm iRaT}/k^{\rm RCT+iRaT} \lesssim 10\%$ — confirms that even if the iRaT is not totally negligible its rigorous description could be skipped, at least in the first state-to-state simulations.

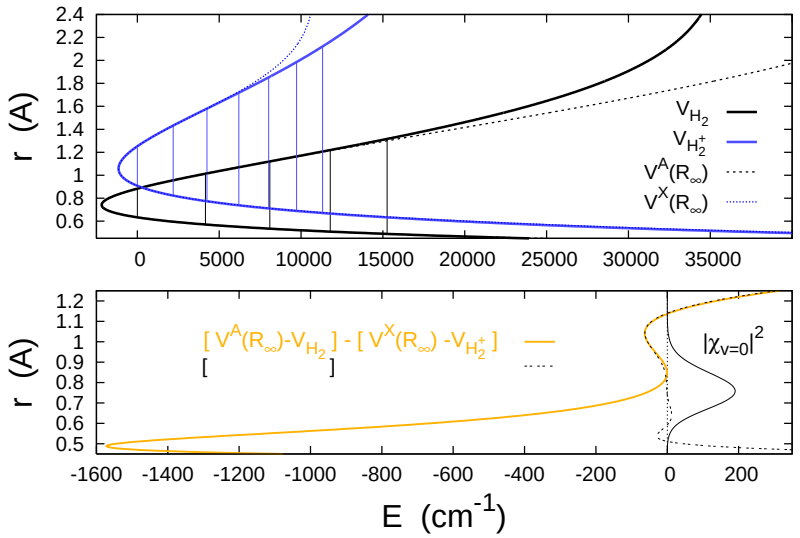

Fig. A0b. 1D cuts of the surfaces $V^A(r,R,\theta)$ and $V^X(r,R,\theta)$ at R=R_∞=40Å compared to the accurate potentials of H_2 and H_2^+, respectively, calculated in Refs. 4 and 5.

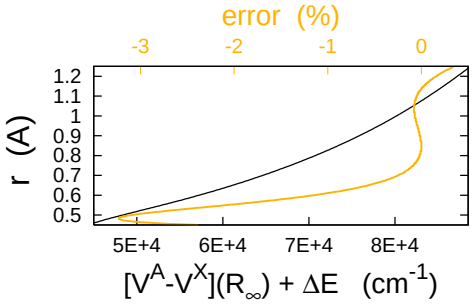

In the left panels, the potentials are shifted on the energy scale so that the lowest (v=0) vibrational levels in them coincide. The actual separation between the v=0 level in $V^A(R_\infty)$ and in $V^X(R_\infty)$, accounted for in the right panel, is ΔE=74507 cm^{-1}. $\chi_{v=0}(r)$ denotes the radial function of v=0 state of H_2. The state is only weakly disturbed by interaction with He^+, so the probability density along the r coordinate in low energy states of the reactants is well represented by $|\chi_{v=0}(r)|^2$.

The potentials extracted from the asymptotic regions of the A- and X-state PESes of $HeHH^+$ appear consistent with the accurate potentials of H_2 and H_2^+, respectively, up to energies close to the positions of v=4 levels. Substantial inaccuracies arise at higher energies, in the large r parts of the potentials: $V^A(R_\infty)$ becomes too high, and $V^X(R_\infty)$ becomes too low. The inaccuracy of V^A is obviously inconsequential to the description of the radiative reactions at collision energies of interest in the study (below ~350 cm^{-1}). The inaccuracy of V^X certainly impairs the X-state-energy resolved characteristics, like the width functions $\frac{\partial}{\partial E'}\Gamma$ shown in Fig. A18. More specifically, the peaks in these functions which are associated with the v'>4 thresholds may be shifted down, even by more than 1000 cm^{-1}, as displayed in Fig. A0c, and also the overall sizes of these peaks may be disturbed, as it follows from Fig. A0d and Fig. 12. However, despite these inaccurate shapes, the integrated values of these functions summarize to the global characteristics of the RCT+iRaT reaction which should be essentially correct. As it can be deduced from Figs. 10b and 12 of the paper (see also comments to Fig. A18), the global characteristics of the RCT+iRaT+RA depend on the potential V^X only through the difference $V^A-V^X+\Delta E$ which is involved in the construction of the optical potential and only in the short r range indicated here by the plot of $|\chi_{v=0}(r)|^2$. The right panel of Fig. A0b (the yellow curve) suggests that accuracy of the optical potential in the important range is indeed satisfactory.

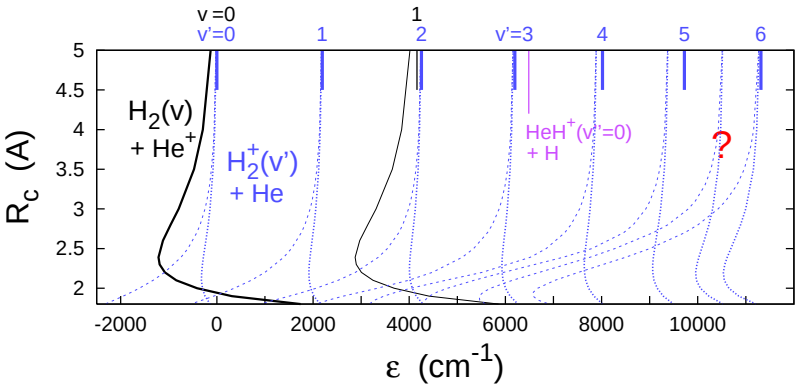

Fig. A0c. Energy levels in the potentials $V^A(r,R$=R_c,θ=$\frac{\pi}{2})$, $V^X(r,R$=R_c,θ=$\frac{\pi}{2})$, and $V^X(r,R$=R_c,θ=0), i.e. in the 1D cuts of the PESes shown in Fig. A0a, as functions of the parameter R_c. The large-R_c-limits of the functions are compared to the exact separations of vibrational energy levels in H_2^+ and in H_2 (Refs. 4–6), represented by the sticks in the upper x-axis.

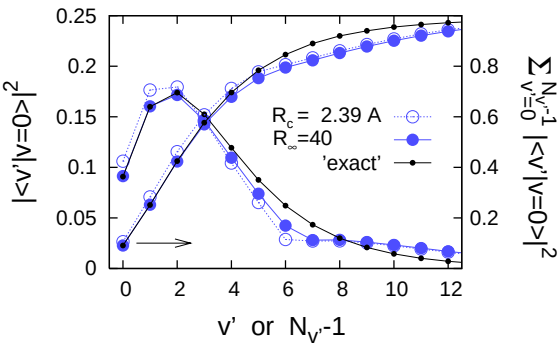

Fig. A0d. Squared overlaps between functions corresponding to the energies $\varepsilon_{v=0}(R_c)$ and $\varepsilon_{v'}(R_c)$, shown in Fig. A0c, for two values of R_c. 'exact' denotes the values obtained using the respective accurate functions of H_2 and H_2^+.

Fig. A1. Electronic structure input

Details relevant to state-to-state description of RCT

/when product states are in the non-reactive range/

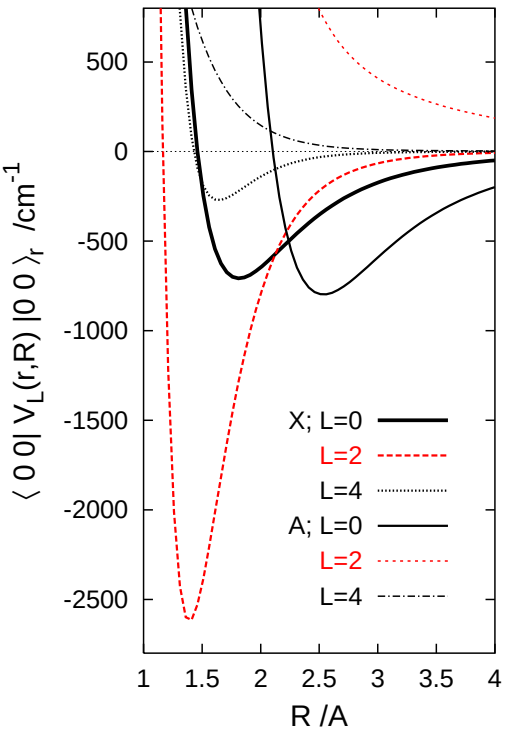

Fig. A1a. Potential energy surfaces of the X- and A states of HeH_2^+. The anisotropy strength functions $V_L^s(r,R)$ resulting from the Legendre-polynomial expansions of the interaction potentials

$$V^s(r,R,\theta) - V^s(r,R{\to}\infty) = \sum_L V_L^s(r,R)\, P_L(\cos\theta)$$

for s=X, A. Shown are the average values of the largest three of these functions in the ground ro-vibrational states of H_2^+ and H_2 for s=X and A, respectively.

The differences between the two PESes in the sign and strength of the L=2 terms exposed by the red curves and the displacement of minima of the L=0 curves play an important role in the dynamics of the RCT reaction; they influence strongly the emission spectra, the relative sizes of resonance→resonance and resonance→free contributions. See the discussion of Figs. 6, 7, and A14.

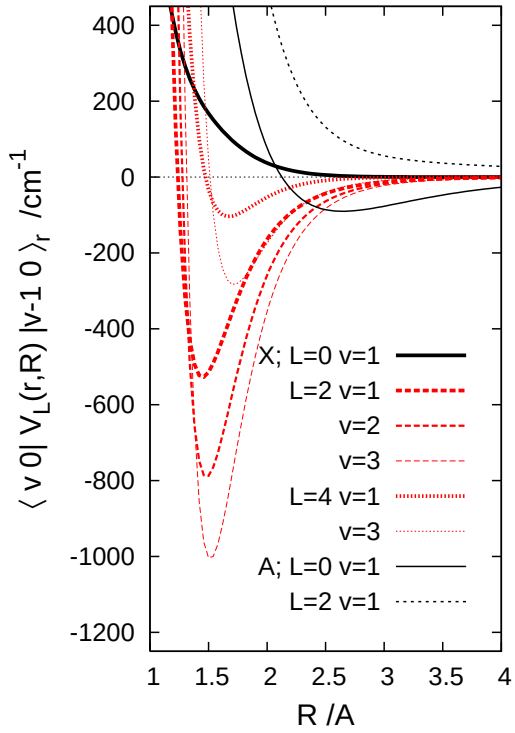

Fig. A1b. Matrix elements of the potential functions $V_L^s(r,R)$ between v and $v{-}1$ vibrational functions of H_2^+ for s=X and of H_2 for s=A.

The elements of $V_{L>0}^X$ (the red curves) cause sizeable ro-vibrational inelasticity in the product channel of the RCT reaction and have a significant impact on the population of vibrational states of the H_2^+ ions; Figs. 4, 6, A14-A16.

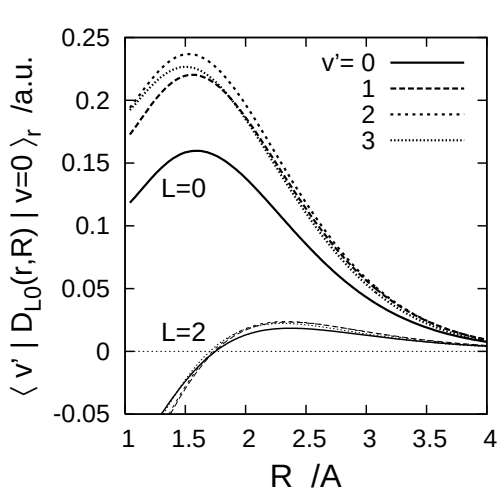

Fig. A1c. Electric dipole vector field for $A{\to}X$ transitions – the Legendre-polynomial expansion of Body-Fixed Z-component (from Ref. 2)

$$d_Z^{\rm BF}(r,R,\theta) = \sum_{L=0,2} D_{L0}(r,R) P_L(\cos\theta)\,.$$

Shown are the matrix elements $\langle v'j'|D_{L0}(r,R)|vj\rangle_r$ between functions of $v{=}0\,j{=}0$ state of H_2 and $v'{=}0{-}3\,j'{=}0$ states of H_2^+. Changes for $j{=}2$ and/or $j'{=}2$ states would hardly be visible on this plot.

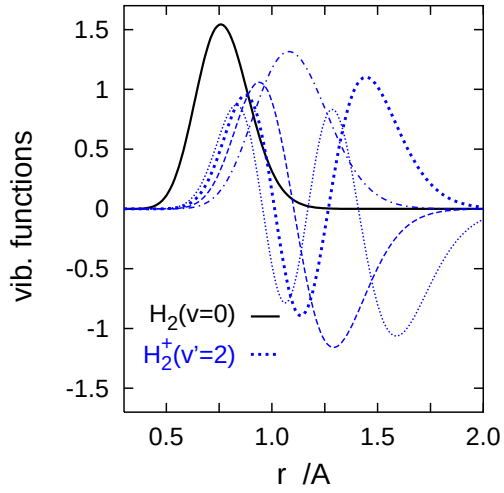

Fig. A1d. Radial functions of $v{=}0\,j{=}0$ state of H_2 and of $v'{=}0{-}3\,j'{=}0$ states of H_2^+.

The overlapping between the $v{=}0$ and v' functions,
$|\langle v'|v{=}0\rangle|{=}0.30,\ 0.40, 0.41,$ and 0.38 for $v'{=}0, 1, 2,$ and 3, respectively, is mostly responsible for the relations between the matrix elements plotted in Fig. A1c,

$$\begin{aligned}\langle v'{=}2|D_{00}|v{=}0\rangle_r \ &\sim\ \langle v'{=}1|\,\ldots\rangle_r \\ &>\ \langle v'{=}0|\,\ldots\rangle_r\,.\end{aligned}$$

Fig. A2. Hamiltonians for reactant and product systems in Close-Coupling Body-Fixed-**diabatic** representation*

$$R\left\langle {}_{\rm BF}\Phi^{JMp}_{\widetilde{\beta}}(\mathbf{r},\widehat{\mathbf{R}})\,\middle|\,{}_{\rm BF}H(\mathbf{r},\mathbf{R})\,\tfrac{1}{R}\,{}_{\rm BF}\Phi^{JMp}_{\beta}(\mathbf{r},\widehat{\mathbf{R}})\right\rangle_{\mathbf{r},\hat{\mathbf{R}}} = -\delta_{\widetilde{\beta},\beta}\,\tfrac{\hbar^2}{2\mu}\tfrac{d^2}{dR^2} + W^{Jp}_{\widetilde{\beta},\beta}(R)$$

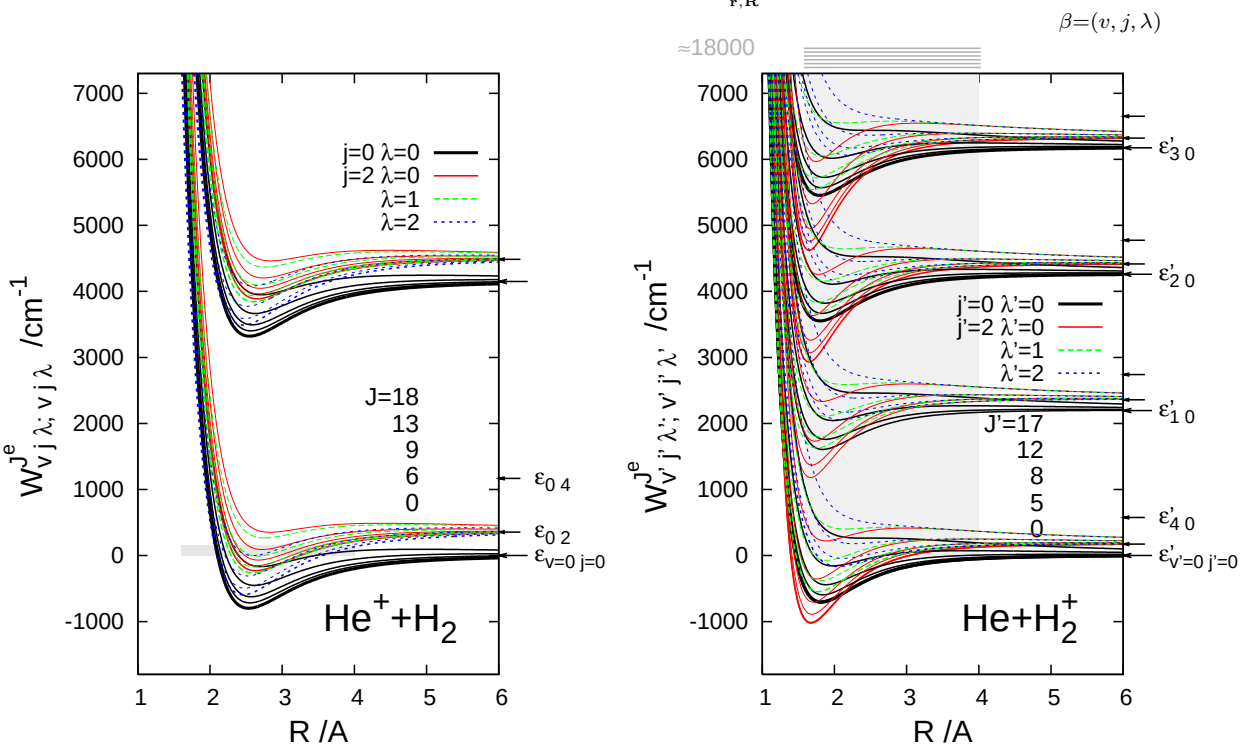

Fig. A2a. Selected effective potentials governing dynamics of the systems, i.e. averages of the PESes V^A and V^X in selected basis functions ${}_{\rm BF}\Phi^{JMp}_{vj\lambda}$ plus the respective centrifugal terms $\frac{\hbar^2}{2\mu}[J(J+1)+j(j+1)-2\lambda^2]/R^2$. The shadowed areas indicate the ranges of energy and atom-diatom distances which are important in the RCT reaction at $T\leq 50$ K.

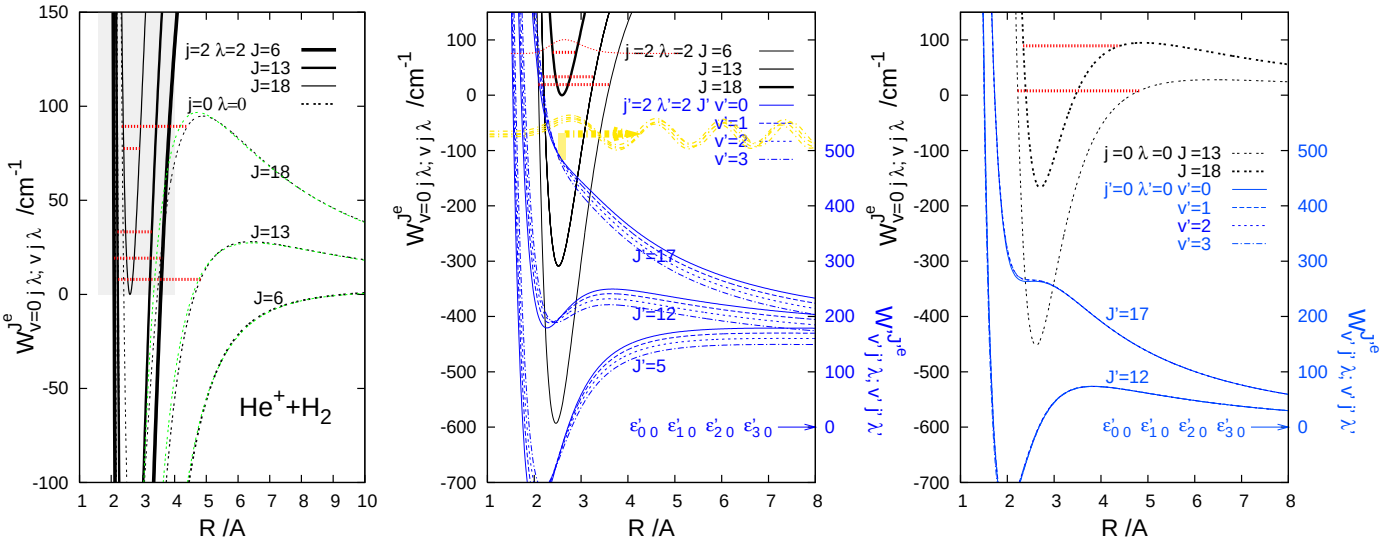

Fig. A2b. Enlarged views of some effective potentials for the reactant system (black curves), energies of resonances (b=2 k=2 and b=0 states of the He^+-H_2 complex‡) supported by the potentials (red lines), and effective potentials of the product system (blue curves) pertaining to states populated in radiative transitions from the resonances by virtue of the selection/propensity rules♯ $\Delta J=-1$ and $\Delta\lambda=0$. The yellow arrow indicates ranges of the product continuum states which (according to the reflection principle[8,9]) should most strongly be populated in transitions from the b=k=2 v_R=0 J=18 resonance (i.e. states of energies ∼530 cm^{-1} above the vibrational thresholds $\varepsilon'_{v'\,j'=0}$ for v'=0–3). The green curves in left panel show potentials $-\frac{C_4}{R^4}+\frac{\hbar^2}{2\mu}\frac{J(J+1)}{R^2}$ with C_4=2.779 a.u. The approximation $W^0_{000;000}(R)\approx-\frac{C_4}{R^4}$ does not hold beyond R=13 Å: the relative deviation rapidly reaches 50% and grows rapidly with R.

* see Ref. 3 (Sec. IV); ‡ see Table I in the paper; ♯ see Figs. A13 and A14.

NOTATION

Symbols with and without prime are used in the figure labels and captions of this material to denote the same quantities (quantum numbers) for the He^++H_2 and He+H_2^+ systems, respectively.

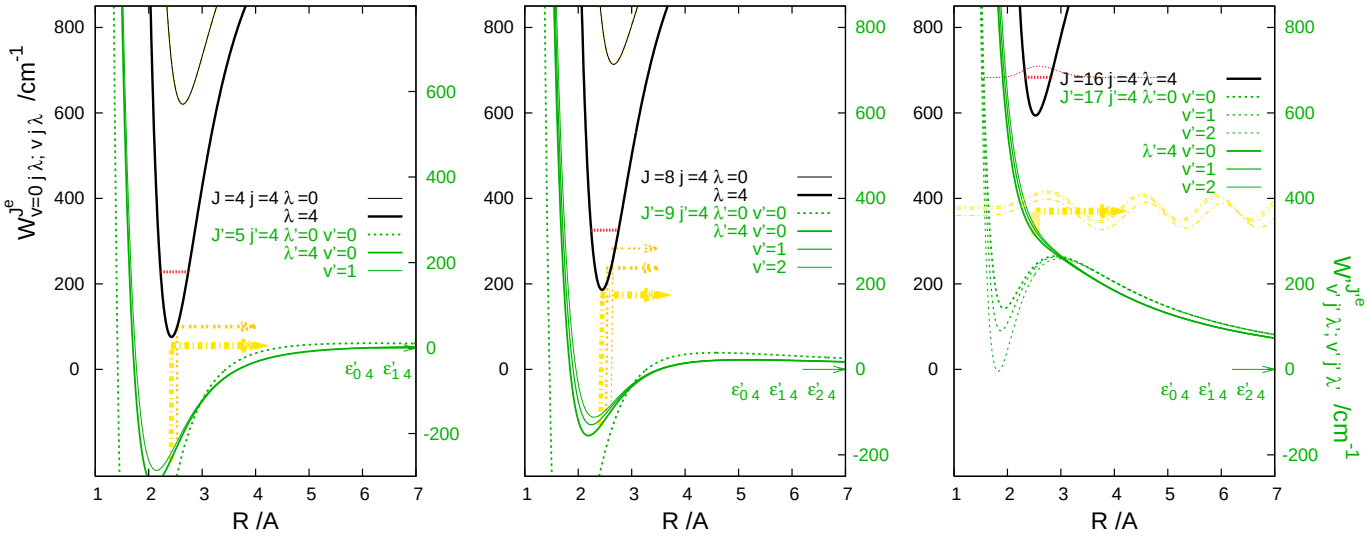

Fig. A2c. Selected effective potentials of He^++H_2 associated with the $\varepsilon_{0\,4}$ threshold (black curves), energies of the lowest (v_R=0) resonances supported by these potentials (red lines), and effective potentials of He+H_2^+ which are most important in the RCT from the resonances. Resonances supported by the potentials $W^J_{0j\lambda;\,0j\lambda}$ decay preferably to states governed by the potentials $W'^{J'}_{v'j'\lambda';\,v'j'\lambda'}$ with j'=j and λ'=λ. (Note that the latter potentials are shown relative to their respective $\varepsilon'_{v'\,j'}$ threshold). Yellow arrows indicate positions of the main resonance-free peaks in the photon emission spectra as predicted by a simple one-dimensional model which uses single potentials for the reactant and product systems, $W^J_{044;044}$ and $W'^{J+1}_{v'44;v'44}$, respectively. A confrontation of the predictions with the exact calculated spectra is given in Fig. A14.

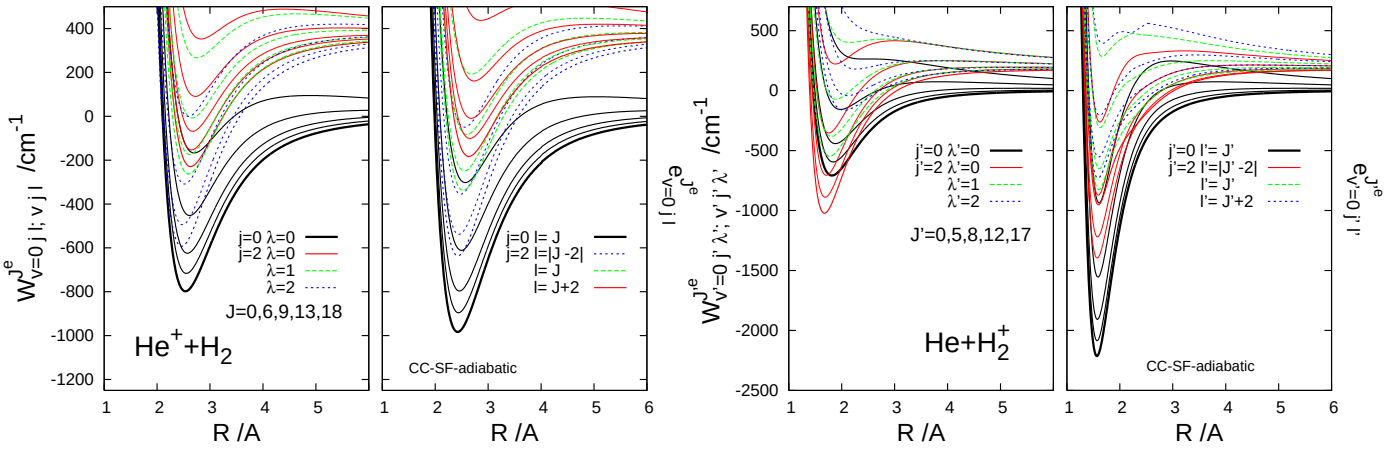

Fig. A2d. A comparison of the effective potentials in the BF-diabatic representation with the lowest adiabatic potentials $e^{J^e}_{vjl}(R)$ obtained by diagonalizing the matrix $\mathbf{W}^{J^e}(R)$=$\{W^{J^e}_{v\,j\lambda;\,\widetilde{v}\,\widetilde{j}\,\widetilde{\lambda}}(R)$; $v,\widetilde{v}$=0−3, $j,\widetilde{j}$=0, 2, …, 14; $\lambda,\widetilde{\lambda}$=0, 1, 2, 4$\}$. For $j\leq$4, $e^{J^e}_{vjl}(R)\underset{R\to\infty}{\longrightarrow}\varepsilon_{vj}+\frac{\hbar^2}{2\mu}l(l+1)$, where l is the angular momentum quantum number of relative atom-diatom motion in the space-fixed (SF) reference frame, l=$|J-j|$, $|J-j|+2$, …, $J+j$. The comparison exhibits the strength of rotational couplings in the systems. The respective adiabatic representation of the Hamiltonian (given here the acronym CC-SF-adiabatic) was exploited in perturbative calculations on rotational predissociation of the He^+-H_2 complex, see Fig. C5 (in part C).

SOJOURN-TIME ANALYSIS

— an extension of life-time matrix calculations

cf. Sec. IV of paper I (Ref. 3) and Sec. III of paper II (Ref. 7)

The notion of sojourn time of a collision system in the confined region of the configuration space (see eg. Ref. 11) is directly connected with the collision-time delay or the life-time matrix introduced by Smith, Ref. 10. The connection is exposed by the following formula for the life-time matrix

$$\frac{1}{2\pi\hbar}\,\mathbf{Q}^{Jp} = \big\langle \mathbf{\Psi}^{(+)JMp} \big|\, P_{\,[0,R_\infty]}\mathbf{\Psi}^{(+)JMp}\big\rangle - \imath\hbar\big\langle \mathbf{O}_E^- - \mathbf{O}_E^+\mathbf{S} \;\big|\; \mathbf{C}(R_\infty)\,(\mathbf{O}^- - \mathbf{O}^+\mathbf{S})\big\rangle\,, \qquad \text{(A1)}$$

in which $P_{\,[0,R_\infty]}$ denotes the projector on the interval $[0, R_\infty]$ of R-coordinate outside which the atom-diatom interaction is practically negligible, $\mathbf{C}(R_\infty)$ is the operator of the probability flux through the surface $R{=}R_\infty$,

$$\mathbf{C}(R_\infty) = \frac{1}{2\mu}\big[\delta(R{-}R_\infty)\,\mathbf{p}_R + \mathbf{p}_R\,\delta(R{-}R_\infty)\big] \qquad \text{with} \qquad \mathbf{p}_R = -\imath\hbar\mathbf{I}\frac{d}{dR}\,,$$

the symbol $\underset{1\times N_o}{\mathbf{\Psi}^{(+)JMp}}(E;\mathbf{r},\mathbf{R})$ stands for the set of the partial scattering outgoing waves which correspond to all possible initial scattering channels at the energy E, and the symbols $\mathbf{O}^{\pm Jp}$ stand for the diagonal matrices of radial functions which appear in the asymptotic form of $\mathbf{\Psi}^{(+)JMp}(E;\mathbf{r},\mathbf{R})$, see Eqs. (30)—(31) in paper I. The subscript E denotes the derivative with respect to the energy. The 'energy-normalization' of the scattering functions is assumed.
The first term in formula (A1), specifically its trace

$$t^{Jp}(E;R_\infty) = 2\pi\hbar\,\mathrm{Tr}\,\big\langle \mathbf{\Psi}^{(+)JMp}(E)\,\big|\,P_{\,[0,R_\infty]}\mathbf{\Psi}^{(+)JMp}(E)\big\rangle \qquad \text{(A2)}$$

can be interpreted as the mean total sojourn time of the collision system in the interaction region ('total' refers here to the summation over the initial channels). Sojourn time in a region confined by a surface $R{=}\overline{R}$ is obtained simply by using the respective projector $P_{\,[0,\overline{R}]}$.

Applying the CC-BF-diabatic approach of paper I to the states $\mathbf{\Psi}^{(+)JMp}(E;\mathbf{r},\mathbf{R})$, see Eqs. (20)—(32) in paper I and Eqs. (17)—(18) in paper II,

$$\begin{aligned}\mathbf{\Psi}^{(+)JMp}(E;\mathbf{r},\mathbf{R}) &= \frac{1}{R}\,{}_{\mathrm{BF}}\mathbf{\Phi}^{JMp}(r,\widehat{\mathbf{r}}_B,\widehat{\mathbf{R}})\,{}_{\mathrm{BF}}\mathbf{F}^{(+)Jp}(E;R)\,\mathbf{U}^{Jp}\\ &= \sum_\lambda \mathbf{\Psi}_\lambda^{(+)Jp}(E;r,R,\theta)\,\Theta_\lambda^{JMp}(\phi_R,\theta_R,\psi)\,, \qquad \text{(A3)}\end{aligned}$$

$$\left[\big[\mathbf{\Psi}_\lambda^{(+)Jp}(E;r,R,\theta)\big]_{v_ij_il_i} = \tfrac{\sqrt{2\pi}}{rR}\sum_v\sum_{j\ge\lambda}\chi_{vj}(r)\,Y_{j\lambda}(\theta,0)\sum_{\tilde\lambda}\big[{}_{\mathrm{BF}}\mathbf{F}^{(+)Jp}(E;R)\big]_{vj\lambda,v_ij_i\tilde\lambda}\big[\mathbf{U}^{Jp}(j_i)\big]_{\tilde\lambda,l_i}\right]$$

one can easily make the following resolutions of the total sojourn time

$$t^{Jp}(E;\overline{R}) = \sum_\lambda t_\lambda^{Jp}(E;\overline{R}) = \sum_v t_v^{Jp}(E;\overline{R}) = \sum_j t_j^{Jp}(E;\overline{R}) \qquad \text{(A4)}$$

with

$$t_{\lambda}^{Jp}(E;\overline{R}) = \int_0^{\overline{R}} dR \sum_v \sum_{j\geq\lambda} \sum_{i=1}^{N_o} \mid f_{vj\lambda}^{(+)Jp}(E,\alpha_i;R) \mid^2 , \tag{A5}$$

$$t_{j}^{Jp}(E;\overline{R}) = \int_0^{\overline{R}} dR \sum_v \sum_{\lambda}^{\lambda_{\max}} \sum_{i=1}^{N_o} \ \ldots\ldots , \tag{A6}$$

$$t_{v}^{Jp}(E;\overline{R}) = \int_0^{\overline{R}} dR \sum_j \sum_{\lambda}^{\lambda_{\max}} \sum_{i=1}^{N_o} \ \ldots\ldots , \tag{A7}$$

where

$$f_{\beta_f}^{(+)Jp}(E,\alpha_i;R) = \sqrt{2\pi\hbar} \times \left[{}_{\rm BF}\mathbf{F}^{(+)Jp}(E;R)\mathbf{U}^{Jp}\right]_{f,i} \qquad \text{for} \quad f{=}1,\ldots,N, \ \ i{=}1,\ldots,N_o ,$$

β and α denote the collections of the quantum numbers (v,j,λ) and (v,j,l), respectively. $\lambda_{\max}{=}\min(j,J,4)$. The symbol $\overline{R}$ is used hereafter to denote the confined region $[0,\overline{R}]$. All the other symbols have the same meaning as described in paper I.

The λ- components of the partial scattering states introduced in Eq. (A3) can be used to define the following local sojourn times[11] or 'sojourn-time maps'

$$t_{\lambda}^{Jp}(E;R,\theta) = 2\pi\hbar R^2 \int r^2\, dr\, \mathbf{\Psi}_{\lambda}^{(+)Jp}(E;r,R,\theta)\big[\ldots\big]^{\dagger} . \tag{A8}$$

These maps and the sojourn-time components $t_{\lambda}^{Jp}(E;\overline{R})$, $t_{v}^{Jp}(E;\overline{R})$, and $t_{j}^{Jp}(E;\overline{R})$ provide information on (stationary) scattering states within the confined region $[0,\overline{R}]$ which is analogous to the information provided on bound states by the probability densities $\rho_{\lambda}(E^B Jp;R,\theta)$ and the distributions $\rho_{\lambda}(E^B Jp)$, $\rho_{v}(E^B Jp)$, and $\rho_{j}(E^B Jp)$ defined in Sec. III.B of paper II. To make the analogy even closer, one can introduce the following 'normalized sojourn-times'

$$\rho_{\lambda}(EJp;\overline{R};R,\theta) \ = \ \frac{t_{\lambda}^{Jp}(E;R,\theta)}{t^{Jp}(E;\overline{R})} , \tag{A9}$$

$$\rho_{c}(EJp;\overline{R}) \ = \ \frac{t_{c}^{Jp}(E;\overline{R})}{t^{Jp}(E;\overline{R})} \qquad \text{for} \quad c{=}\lambda,v,j . \tag{A10}$$

These quantities are used in several plots of this material to display properties of continuum and short-living resonance states of the He $+\mathrm{H}_2^+$ system in the wide energy range that can be accessed in the studied RCT reaction.

Of some help in rationalizing the reaction outcome are the sojourn-times $t^{Jp}(E,v_i,j_i;\overline{R})$ and $t^{Jp}(E,v_i;\overline{R}){=}\sum_{j_i} t^{Jp}(E,v_i,j_i;\overline{R})$ which pertain to the collision system with specified initial rotational and/or vibrational state of diatom. These times as well as their $c{=}v,j,\lambda$ -components are obtained from Eqs. (A4)-(A7) by omitting one or two of the sums denoted by the symbol $\sum_i (=\sum_{v_i}\sum_{j_i}\sum_{l_i})$.

A practical advantage of formula (A1) over the well-known relation of the lifetime matrix to the partial scattering matrix, $\mathbf{Q}^{Jp}{=}\imath\hbar\mathbf{S}_E^{Jp\,\dagger}\mathbf{S}^{Jp}$, has previously[12] been pointed out. It stems mostly from the fact that the sojourn-time matrix $\langle\mathbf{\Psi}^{(+)JMp}(E) \mid P_{\,[0,R_\infty]}\mathbf{\Psi}^{(+)JMp}(E)\rangle$ can be evaluated easily with the help of the popular invariant-imbedding methods, in particular the log-derivative method[13], omitting the stage of explicit determination of multichannel scattering functions within the entire interaction region $[0,R_\infty]$. Obviously, this advantage can not be taken, i.e. the scattering functions have to be explicitly determined if the various resolutions of the total sojourn-time are of interest. However, these functions can be easily generated if one uses algorithms that combine the log-derivative propagator with the Riccati transformation technique, as originally proposed in Ref. 13 (Sec. 5.2.1).

A COMPARISON

of

REACTANT and PRODUCT SYSTEMS

$\mathbf{He^+ + H_2}$ and $\mathbf{He + H_2^+}$

Fig. A3. $He^+ + H_2$ and $He + H_2^+$ systems

at low energies

Properties of continuum and resonance functions

in short range of atom-diatom distances*

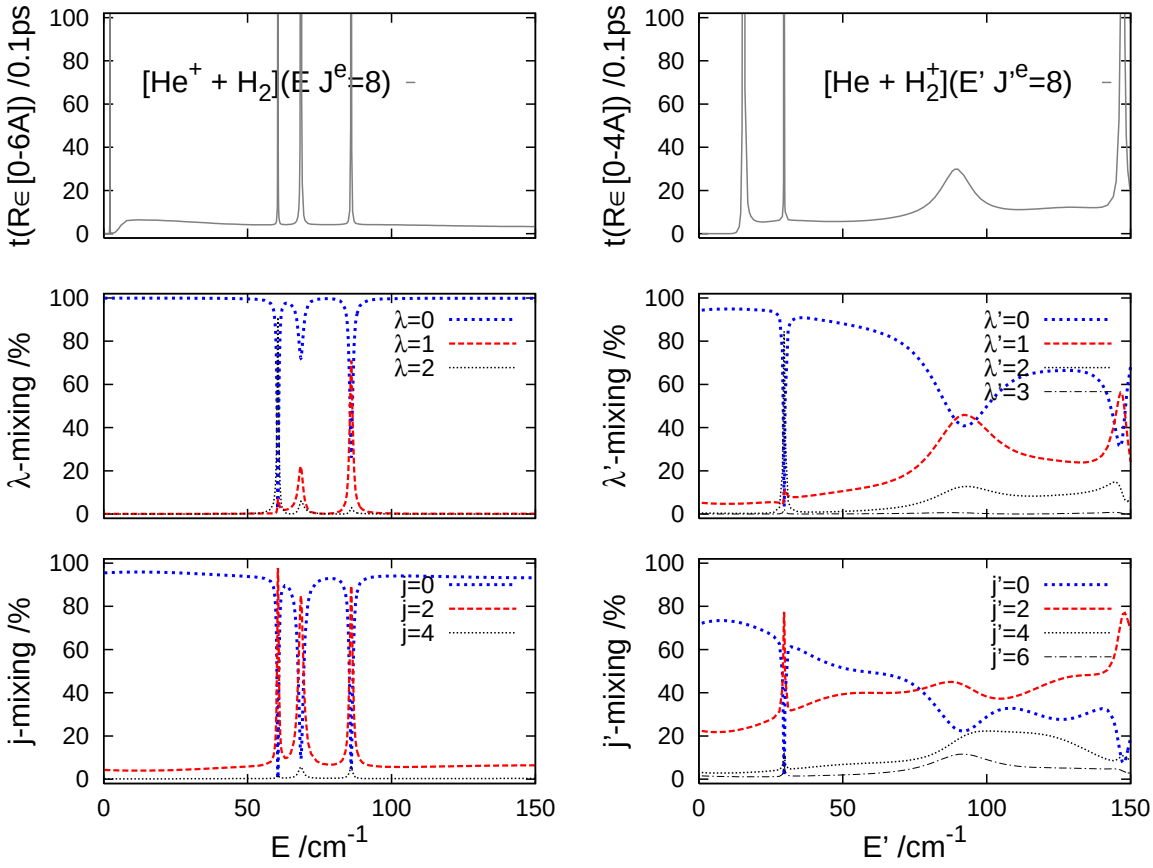

Upper panels: sojourn time $t^{Jp}(E;\overline{R})$ of the two collision systems in the regions $[0,\overline{R}]$ specified in the labels as function of collision energy, see Eq. (A2). The time is shown exemplarily for the systems being in the partial scattering states ($E\,J$=8) of e symmetry.

Lower panels: λ- and j-mixing in the ($E\,J$=8^e) states displayed by the 'normalized sojourn-times' $\rho_\lambda(EJp;\overline{R})$ and $\rho_j(EJp;\overline{R})$, respectively, see Eqs. (A10).

* $R\lesssim 4\,\AA$ is the region of atom-diatom distances where the radiative transitions between the systems are possible, i.e. the values of the electric dipole transition function are non-negligible, see Fig. A1c.

COMMENTS

The left panels illustrate the main properties of dynamics of the reactant system in the coordinate and energy ranges which are important for the RCT reaction at temperatures below 50 K: j=0 state of H_2 dominates in the functions of continuum states and of the shape resonances [the leftmost peak in $t(E)$], j=2 state dominates in the functions of Feshbach resonances [the peaks at $E\approx$60, 68, and 86 cm^{-1}].

The right panels show the product system in the analogous coordinate and energy ranges. Two or three lowest rotational states of $H_2^+(para)$ are strongly mixed in the functions of continuum states and of short-living resonances [the peak at $E'\approx$90 cm^{-1}]. The λ'-mixing is also substantial.

The range of E' shown here constitutes merely one per cent of the energy range which is accessed in the RCT reaction, see Fig. A2a. An extension of the present comparison to higher energies is given in Fig. A7.

Fig. A4. λ- and j-mixing*
in

A4a. quasi-bound states♯
of
$He^+ + H_2(v=0)$
$(b\,k\,v_R\,J)$

k — max λ; b — max j

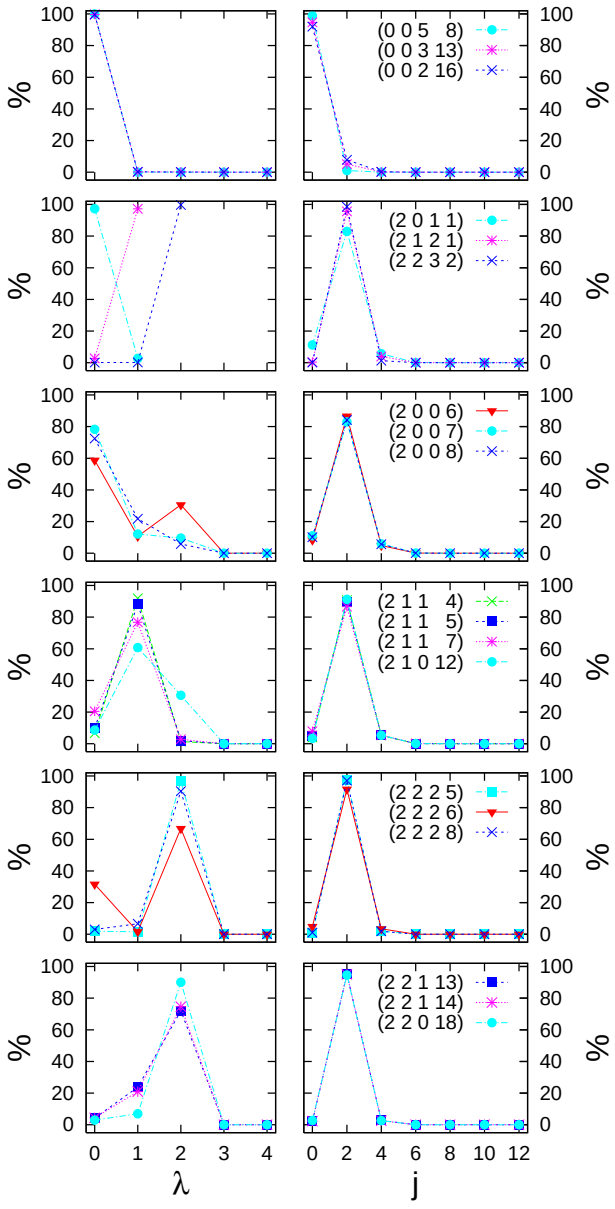

♯See Table I in the paper for information on energies, dissociative and radiative widths of these states.

A4b. long-living low energy resonances♮
in
$He + H_2^+$

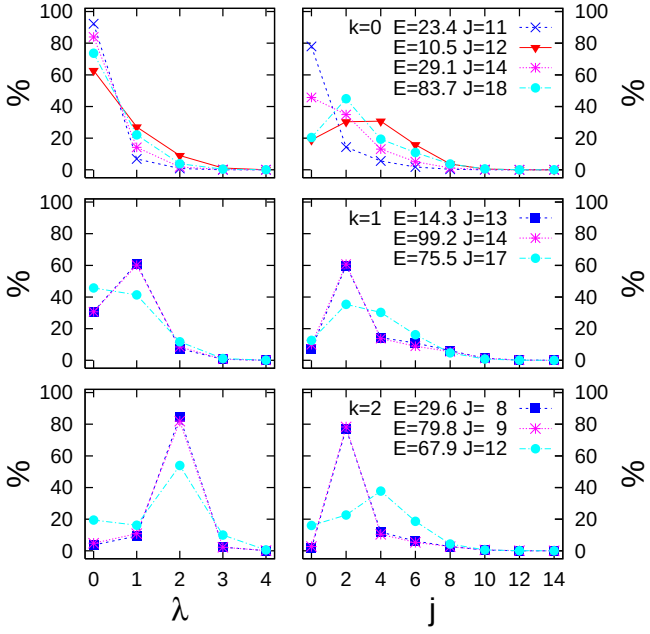

♮ Most of the resonances shown have dissociative lifetimes larger (or $\gg$) than 1 ns. See Table III in paper I and Table VII in paper II.

COMMENT

There is almost no j-mixing in the states of the $He^+ - H_2$ complex; the peaks in ρ_j reach nearly 100 % at j=2. The λ-mixing is also small, except for cases of close proximity on the energy scale of states characterized by the same J- and different k-numbers; here the states (2 0 0 6) and (2 2 2 6).

Strong perturbations in the structure of energy levels of the complex due to Coriolis coupling are displayed in Table CIV and in Fig. C3 (in part C).

Both kinds of mixing are clearly larger in states of the $He^+ - H_2$ complex. Note the comparable strength of two λ-components in the states shown in the middle right panels.

* The mixing is displayed here in terms of the probability distributions $\rho_\lambda(E^B Jp)$ and $\rho_j(E^B Jp)$ calculated from bound-state functions approximating the resonances, see paper II.

Fig. A5. Quasi-bound states of $He^+ + H_2(v=0)$ Probability densities*

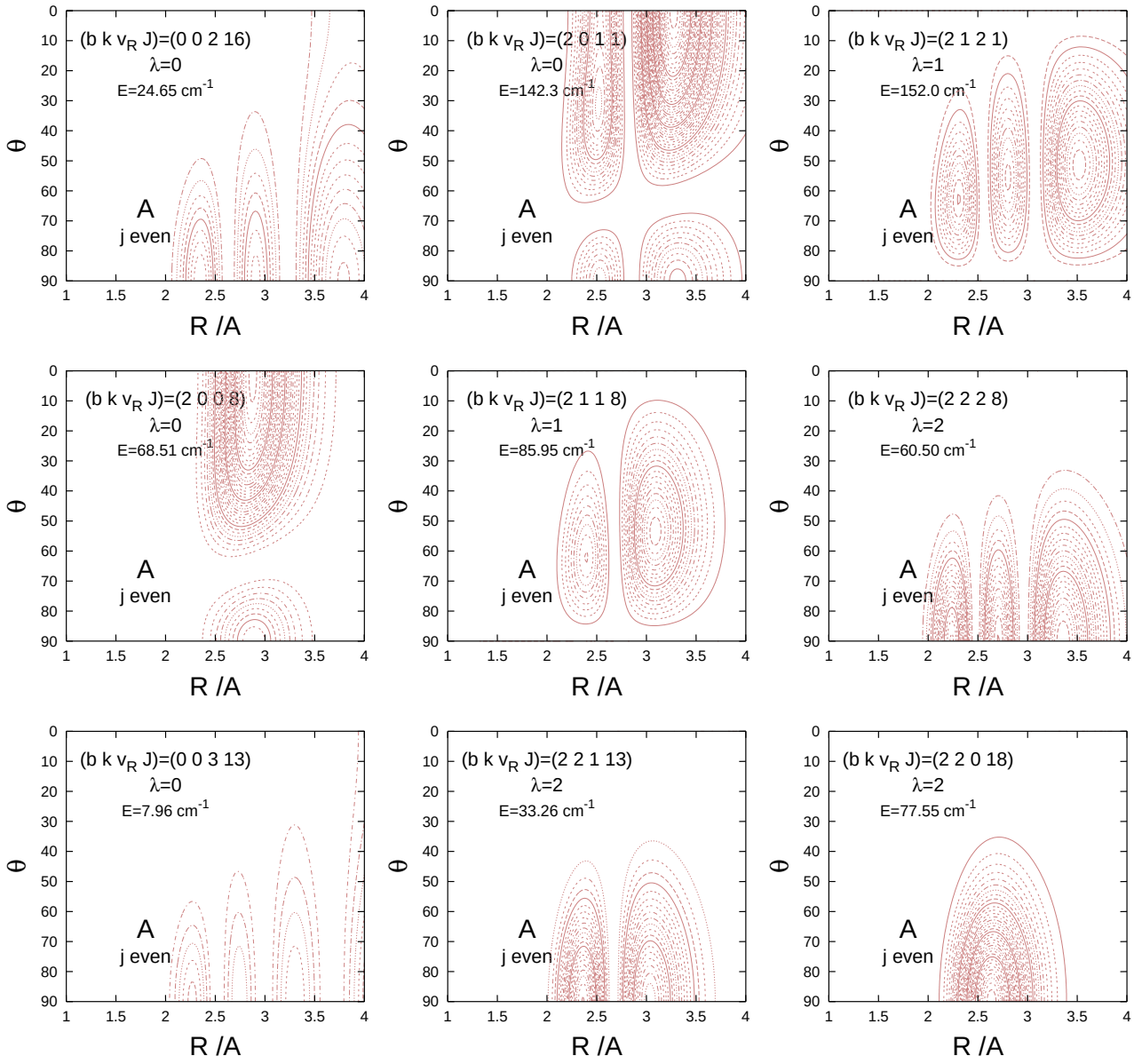

* Plotted are the leading λ-components of the probability densities $\rho(E^B Jp; R, \theta)$ calculated from bound-state functions approximating the resonances. The contours are shown in step of 0.05 in the half of the range of θ since $\rho(..., \theta) = \rho(..., 180° - \theta)$ for $\theta \in [90°, 180°]$.

Fig. A6. Long-living* low energy resonances in $He+H_2^+$ Probability densities†

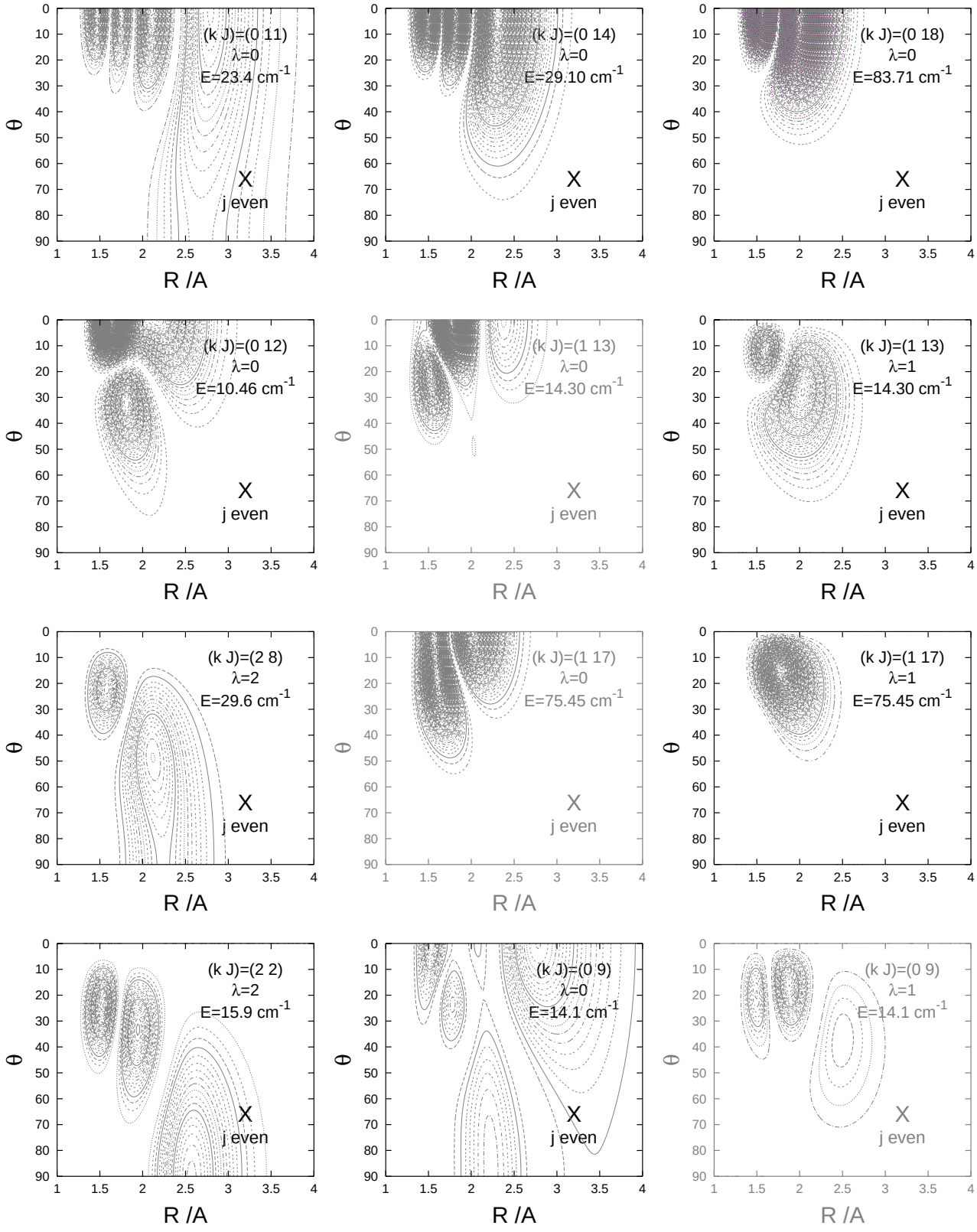

* Lifetimes larger (or ⋙) than 1 ns. See Table III in paper I.

† Plotted are the leading λ-components of the probability densities $\rho(E^B Jp; R, \theta)$ calculated from bound-state functions approximating the resonances. See Table VII in paper II for an assignment of vibrational quantum number v_θ and v_R to these functions, based on the analysis of their natural expansions.

Fig. A7. $He^+ + H_2(I=0)$ and $He + H_2^+(I=0)$ systems

at higher energies (up to $v=1\, j=4$ thresholds)

Properties* of multichannel continuum and resonance functions

in short range of atom-diatom distances

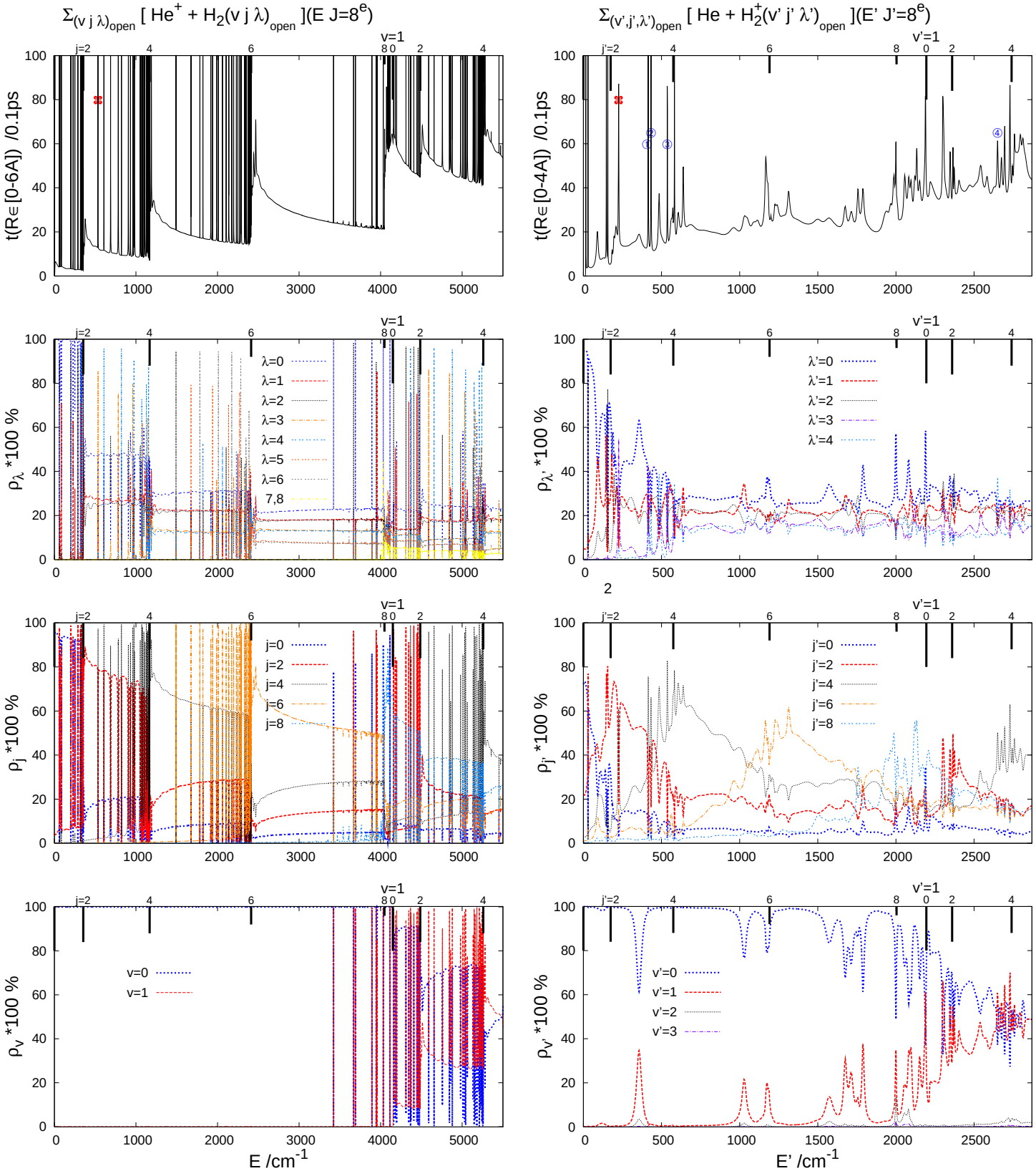

* The quantities plotted: the total sojourn times of the systems in the indicated confined regions $[0, \overline{R}]$ and the related normalized components $\rho_c(EJp; \overline{R})$ for $c=\lambda, j$, and v, all defined in Eqs. (A2) and (A10).
The results in the left panels are 'exact' — do not involve the CCr approximation, see Fig. A17.

COMMENTS

(i) The properties of the $He^+ + H_2$ system at energies E higher than 150 cm^{-1} have practically no impact on the studied RCT reaction at temperatures below 50 K. The actual purpose of enclosing here the plots for this system at higher energies is to facilitate the interpretation of the plots for $He + H_2^+$.

(ii) It should be noted that the quantities $\rho_c(EJp;\overline{R})$ for $c{=}\lambda, j$, and v are direct measures of λ- j- and v-mixing due to atom-diatom interaction at energies below the first excited threshold only (the fact exploited in Fig. A3). Above this threshold, the quantities reveal some properties which actually pertain to non-interacting subsystems [a result of the summation in Eq. (A2) over the scattering functions evolved from all possible, at a given total energy E, initial states of the subsystems, identified here by the quantum numbers $(v\,j\,\lambda)_{\rm open}$]. These are the properties displayed by the base lines of all functions plotted in the left panels:
a) the step-like behavior at the thresholds; the total sojourn time t jumps up because of the appearance of a new state with very slow translational motion of the subsystems,
b) the ordering of the components $\rho_j{>}\rho_{j-2}{>}\ldots{>}\rho_0$ taking place in the entire energy range between the j and $j{+}2$ thresholds,
c) the relations between the components ρ_λ, energy independent between the subsequent thresholds, reflecting the numbers of different $(v\,j)_{\rm open}$ states with given value of $\lambda_{\rm open}$. For example, the relations $\rho_{\lambda=0}{:}\rho_{\lambda=1}{:}\rho_{\lambda=2}{:}\rho_{\lambda=3}{:}\rho_{\lambda=4}{=}3{:}2{:}2{:}1{:}1$ which should hold at energies E between the $v{=}0\,j{=}4$ and $v{=}0\,j{=}6$ thresholds are close to these displayed in the second left panel.
Thus, only departures from the base lines in the functions $\rho_c(EJp;\overline{R})$ testify to the c-mixing of interest here.

(iii) The sharp peaks in the left panels are obviously a manifestation of quasi-bound states of the $He^+{-}H_2$ complex. The association of the peaks with the subsequent j-thresholds is clear, especially from the plots of $\rho_j(EJp;\overline{R})$. All peaks associated with the $j{=}8$ threshold are suppressed for the sake of clarity of the figure. The heights of the peaks in the functions $\rho_j(E)$ testify to a very small j-mixing in all states of the complex. Therefore all of them can be easily assigned with the approximate quantum number $b(=\max j)$. The corresponding peaks in the functions $\rho_\lambda(E)$ are also pronounced enough to allow for an un-ambiguous assignment of approximate quantum number k to the majority of states. Uncertainties due to a substantial increase of λ-mixing arise when the energy separation of the states gets small (regions close to the thresholds, cases of accidental near-degeneracy).
Further characterization of the complex is given in part C of this material.

(iv) The right panels of the figure illustrate how much different from $He^+{-}H_2$ the charge-transferred complex $He{-}H_2^+$ is. Very little regularity can be noted in the plot of the total sojourn-time (no pronounced threshold feature appears in the baseline, the positions and heights of the peaks do not correlate clearly with the positions of the subsequent j' thresholds).

(v) The plot of the functions $\rho_{j'}(E')$ shows broad maxima centered at the positions of the thresholds $v'\,j'$ for $v'{=}0, 1$. These maxima, especially their left parts ($E'{<}\varepsilon_{v'\,j'}$), may be viewed as a result of blending numerous sharp peaks which would occur in these regions if the interaction between He and H_2^+ were much less anisotropic, like the interaction between He^+ and H_2. A few sharp peaks survive only. The corresponding peaks in the functions $\rho_{\lambda'}(E')$ indicate the approximate quantum number k' to label the underlying states of $He{-}H_2^+$.

In some of these states (especially below the j'=4 threshold), one can even trace some similarity to the He^+-H_2 complex in the character of atom-diatom bending motion. An example is shown in Fig. A7a. However, in the majority of states of $He-H_2^+$ the bending and stretching motions of He relative to H_2^+ look more or less entangled (see Fig. A11); a meaningful labeling of these states with a complete set of (six) quantum numbers would not be easy (if at all possible).

(vi) The diatomic vibrational motion is relatively well-separated from other modes of motion in the $He-H_2^+$ complex, at least at energies E' below the v'=1 j'=0 threshold. Therefore the function $\rho_{v'=1}(E')$ plotted in the bottom right panel shows relatively clear peaks in this region. Using this fact, one can assign the approximate quantum number v'_r=1 to the related states of the complex. These states are counterparts of the bound states of the $HeH_2^+(I=0)$ ion; they decay by vibrational predissociation, i.e. to channels He + $H_2^+(v'\,j')$ with $v'<v'_r$.

Fig. A7a. Sojourn-time maps *

for exemplary resonances† in

$He^+ + H_2$ and $He + H_2^+$

below the v=0 j=4 and v'=0 j'=4 thresholds

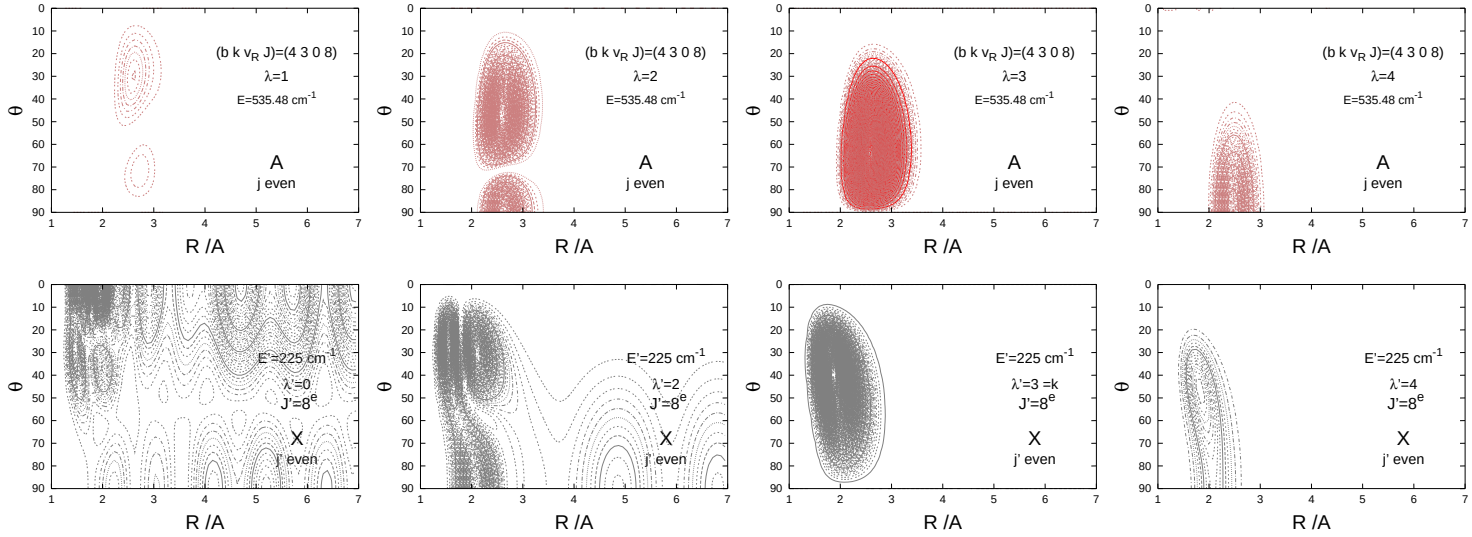

*Plotted are the 'sojourn-time densities' $\rho_\lambda(EJp;\overline{R};R,\theta)$, see Eq. (A9), normalized to give $\sum_\lambda \int_0^{\overline{R}} dR \int d\theta\, \rho_\lambda(EJp;\overline{R};R,\theta)$=1 for $\overline{R}$=17 Å . The contours are shown in step of 0.002 in the half of the range of θ since $\rho(...,\theta)=\rho(...,180°-\theta)$ for $\theta\in[90°,180°]$.

†Peaks marked with the red symbols in the upper left and right panels of Fig. A7. The lifetimes of the two resonances are 102.1 and 1.9 ps, respectively. See also Fig. C1 and Table CI (in part C).

Note the similarity between the upper and lower plots for the λ (λ')=3 and λ (λ')=4 components and the distorted structure of the λ'=2 component. Because of the shape and strength of $\rho_{\lambda'=3}(..,;R,\theta)$ and the sizes of $\rho_{j'=4}$ and $\rho_{v'=0}$ at E'=225.6 cm^{-1}, the presented quasi-bound state of $He-H_2^+$ can be given the complete label: $(v'_r\,b'\,v'_R\,k'\,J'\,p')$=(0 4 0 3 8^e).

On the same grounds, the other peaks marked in the upper right panel of Fig. A7 can be completely assigned:

	$(v'_r\,b'\,v'_R\,k')$	$E'_{\rm res}$	τ/ps
①	(0 4 1 3)	414.9	3.6
②	(0 4 0 4)	432.9	3.0
③	(0 4 2 3)	537.2	4.6
④	(1 4 0 4)	2650.2	0.6

Fig. A8. He+$H_2^+(I{=}0)$ and He+$H_2^+(I{=}1)$ systems

at energies below $v'{=}1$ threshold

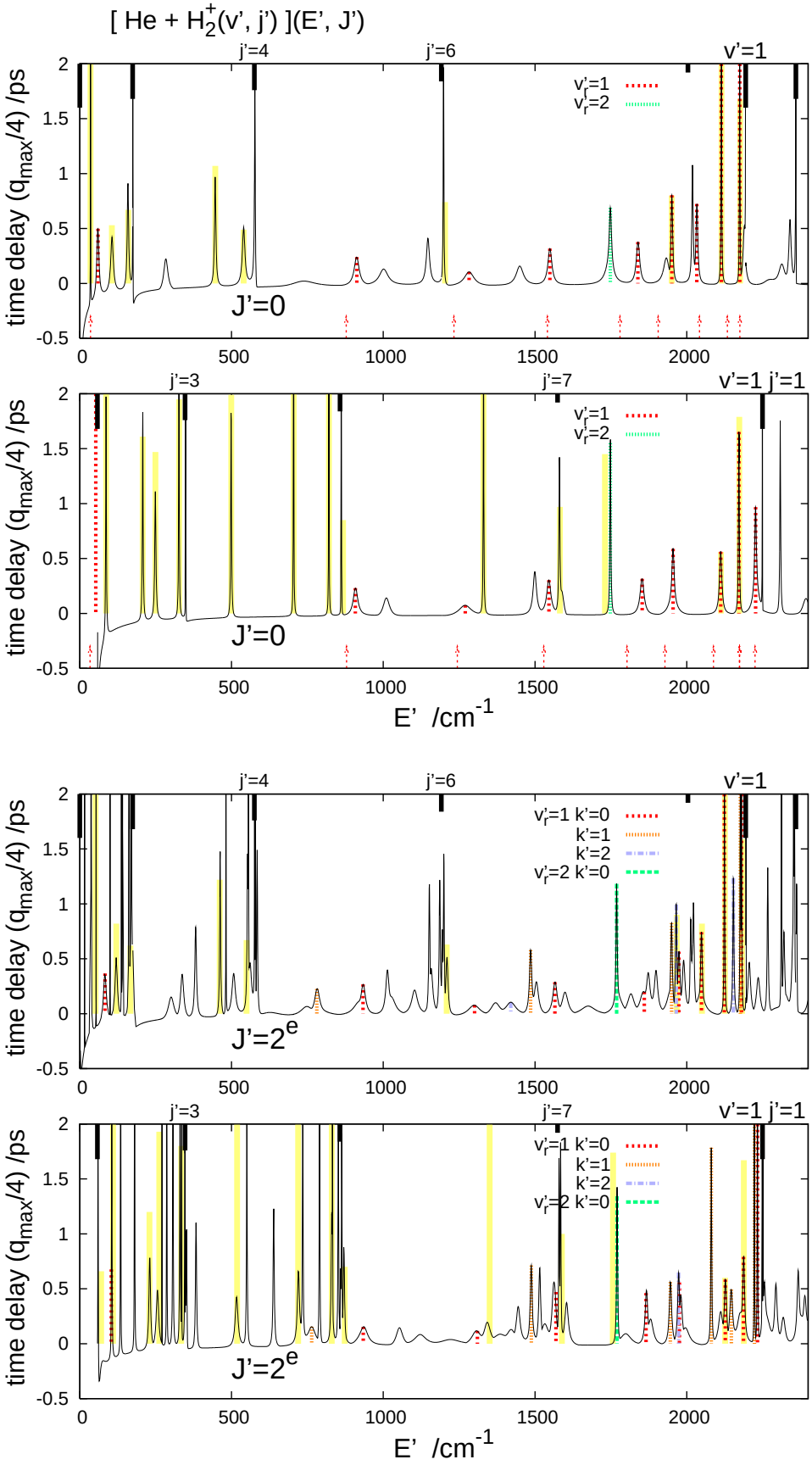

Plotted are the maximal eigenvalues $q_{\max}^{J'p'}$ (divided by 4) of the lifetime-matrix $\mathbf{Q}^{J'p'}$ for two partial waves ($J'\,p'{=}1$). The heights of the peaks give lifetimes of the corresponding quasi-bound states of the He-$H_2^+(I{=}0)$ (j' even) and He-$H_2^+(I{=}1)$ complexes. The yellow bars show results of Ref. 1 obtained with the stabilization method (for $k'{=}0$ states only). The arrows show energies of the $v_r'{=}1$ states predicted by the adiabatic separation scheme described in that work. Detailed comparison is presented in Tables AI-AIV.

TABLE AI: He−H_2^+(I=0). Energies E', widths Γ' (both in cm^{-1}), and lifetimes $\tau'=\hbar/\Gamma'$ (in ps) of quasi-bound J'=0 states below the v'=1 j'=2 threshold[a]. Listed are all states[b] in this range that live longer than 0.4 ps (Γ'<13 cm^{-1}).

Life-time matrix[c]				Stabilization[d]		Life-time matrix[c]				Stabilization[d]	
v'_r	E'	Γ'	τ'	E'	τ'	v'_r	E'	Γ'	τ'	E'	τ'
0	35.4	2.7 (−1)	19.9	35.5[e]	26.4	0	1198.5	2.2	2.4	1203.5	0.74
1	59.5	8.2	0.6			2	1748.4	8.8	0.6		
0	106.1	10.4	0.5	105.7	0.53	1	1950.9	6.5	0.8	1950.5	0.80
0	158.6	5.4	1.0	159.5	0.67		*2003.9*				
	174.2					0	2018.9	5.0	1.1		
0	446.2	5.3	1.0	446.5	1.07	1+0	2033.6	7.4	0.7		
0	539.9	10.1	0.5	540.1	0.49	1	2114.1	2.3	2.3	2114.5	2.43
	575.3					1	2174.4	1.5	3.5	2175.8	1.68
0	577.1	2.8	1.9				*2194.4*				
0	1147.2	12.6	0.4			1	2340.3	9.1	0.6		
	1191.2						*2359.5*				

[a]The threshold energies $\varepsilon'_{v'\,j'}$ for v'=0 j'=2, 4, 6, 8 and v'=1 j'=0, 2 are given in the table (italic numbers). These energies are as they result from the present PES of the X-state of HeHH$^+$. In comparison with the accurate data[6] for H_2^+, the values of $\varepsilon'_{v'=0\,j'}$ for j'=3−8 (listed here and in Tables AII-AIV) are too low by 0.1−0.2 cm^{-1} and the values of $\varepsilon'_{v'=1\,j'}$ for j'=0−2 are too high by 3.2−3.3 cm^{-1}.

[b]Generally, the states are identified with the peaks in the eigentime functions $q_{\max}^{J'p'}(E')$ plotted in Fig. A8. Several peaks lying very close to the thresholds $\varepsilon'_{v'j'}$ are discarded, however. Inspection of the corresponding functions indicates that these peaks may not correspond to resonances or that their heights substantially overestimate the real resonance lifetimes.

[c]The matrix was evaluated and analyzed as described in Ref. 12. The assignment of states with the approximate quantum numbers was based on the analysis of the sojourn times in the interaction range described earlier in this file. Specifically, the numbers v'_r and k' (for J'^e>0 and J'^f>1) were found by inspecting the components $\rho_{c'}(E'\,J'p';\overline{R}=4\mathring{A})$ for $c'=v'$ and $c'=\lambda'$, respectively, see Fig. A7. The numbers b' and v'_R, given in Tables AII and AIV, were inferred from the sojourn-time maps $\rho_{\lambda'}(E'J'p';\overline{R},R,\theta)$, see Fig. 7a.

[d]Results of Ref. 1.

[e]Assigned with v'_r=1 in Fig. 3 of Ref. 1.

TABLE AII: Same an in Table AI for J'=0 states of He−H_2^+(I=1) below the v'=1 j'=1 threshold[a].

Life-time matrix						Stabilization		Life-time matrix				Stabilization	
v'_r	b'^b	$v'_R{}^b$	E'	Γ'	τ'	E'	τ'	v'_r	E'	Γ'	τ'	E'	τ'
			58.2					0	861.7	7.4 (−1)	7.2	867.4	0.85
0			86.5	2.4	2.2	87.0	2.60	0	1330.4	2.0	2.6	1330.1	2.70
0			207.5	2.8	1.9	207.3	1.61		*1574.2*				
0			249.0	4.5	1.2	249.3	1.47	0	1580.5	3.8	1.4	1582.0	0.97
0	3	4	326.7	2.1	2.5	327.4	1.95	2	1748.3	3.3	1.6	1730.3	1.45
			347.0					1	1954.8	9.2	0.6		
0	5	1	498.7	2.8	1.9	499.0	1.99	1	2111.8	9.2	0.6	2112.7	0.56
0	5	2	704.5	1.5	3.5	704.7	3.88	1	2171.8	3.2	1.7	2173.2	1.79
0	5	3	820.8	1.2	4.5	821.0	4.55	1	2226.6	6.4	0.8		
			857.4						*2249.5*				

[a]The thresholds $\varepsilon_{v'\,j'}$ for v'=0 j'=1, 3, 5, 7 and v'=1 j'=1 are shown by the italic numbers in the table.

[b]A possibility of assigning these numbers was searched only for states below the v'=0 j'=5 threshold.

TABLE AIII: He−H_2^+(I=0). Energies E', widths Γ' (both in cm^{-1}), and lifetimes $\tau'=\hbar/\Gamma'$ (in ps) of quasi-bound $J'=1,2$ states below the $v'=1\,j'=2$ threshold. Listed are all states in this range that live longer than 0.4 ps ($\Gamma'<13$ cm^{-1}).

$J'=1^e$							$J'=1^f$			
Life-time matrix					Stabilization[a]		Life-time matrix			
v'_r	k'	E'	Γ'	τ'	E'	τ'	v'_r	E'	Γ'	τ'
0	1	31.3	3.9 (−1)	13.6						
0	0	41.9	7.0 (−2)	75.9	41.0	59.7				
1	0	67.5	11.8	0.4						
0	0	111.0	12.0	0.4	110.4	0.57				
0	1	131.5	1.0 (−1)	51.0						
0	1	154.1	8.3 (−2)	64.0						
0	0	162.0	6.1	0.9	161.9	0.66				
0	1	172.5	5.3 (−2)	100.2						
		174.2								
0	1	376.6	4.3	1.2			0	378.9	2.5	2.1
0	0	451.7	4.3	1.2	451.4	1.14				
0	1	510.1	5.8	0.9			0	514.3	3.6 (−1)	14.8
0	0	544.3	6.9	0.8	543.3	0.54				
0	1	566.2	6.0	0.9			0	570.9	1.6 (−2)	332.7
		575.3								
0	1	579.3	2.0	2.6			0	580.9	12.4	0.4
							0	608.8	5.6	1.0
							0	905.8	3.6	1.5
0	1	1092.7	11.7	0.5			0	1090.9	4.7	1.1
0	0	1147.8	7.9	0.7						
0	1	1183.8	5.5	1.0			0	1182.5	2.2	2.4
		1191.2								
0	1	1197.1	2.7	2.0			0	1201.5	8.2	0.6
0	0	1203.5	11.6	0.5	1205.3	0.70				
1	1	1472.4	7.9	0.7						
2	0	1753.9	4.1	1.3						
1	0	1837.0	12.1	0.4			0	1836.2	1.7	3.1
1	0	1850.6	7.7	0.7						
1	1+0	1947.0	5.0	1.1			0	1963.7	2.8	1.9
1	0+1	1957.0	11.0	0.5	1956.1	0.84				
0	1	1982.5	9.6	0.6						
		2003.9								
0	0	2006.8	7.5	0.7						
							0	2022.9	4.8	1.1
1	0	2038.0	7.2	0.7	2040.9	0.72				
1	0	2117.5	2.4	2.2	2118.2	2.42				
1	1	2167.9	2.9	1.8			1	2168.4	3.0	1.8
1	0	2176.4	1.5	3.6	2178.1	1.68				
		2194.4								
1	1	2309.0	1.4	3.7			1	2310.0	1.1	4.7
1	0	2343.5	9.0	0.6						
1	1	2353.4	6.3 (−1)	8.5			1	2354.0	1.6 (−1)	33.8
		2359.5								

J'=2^e							J'=2^f				
Life-time matrix					Stabilization[a]		Life-time matrix				
v'_r	k'	E'	Γ'	τ'	E'	τ'	v'_r	k'	E'	Γ'	τ'
0	2	15.9	2.9 (−3)	1836.4							
0	1	37.4	9.5 (−1)	5.6							
0	0	53.8	9.9 (−3)	537.7	52.0	-					
0	2	99.7	1.4 (−2)	379.2							
0	0	120.1	9.1	0.6	120.5	0.82					
0	1	137.0	1.3 (−1)	39.6							
0	2	140.9	2.1 (−1)	25.4							
0	1	162.2	1.6	3.4							
					166.3	0.62					
0	2	170.1	4.2 (−1)	12.8							
		174.2									
							0	1	175.3	6.1 (−1)	8.7
0	2	337.4	12.8	0.4			0	2	337.5	12.4	0.4
0	1	381.8	6.4	0.8			0	1	387.9	2.9	1.8
0	0	462.4	3.5	1.5	461.1	1.22					
0	2	481.6	3.8 (−1)	14.1			0	2	481.7	2.2 (−2)	244.5
							0	1	518.8	2.6	2.1
0	0	553.0	3.4	1.6	549.6	0.67					
0	2	555.9	1.0	5.5			0	2	555.9	1.2	4.4
							0	1	572.1	2.7	1.9
		575.3									
0	2	578.8	2.7	2.0			0	2+1	578.1	4.7	1.1
0	1+0	584.5	3.5	1.5							
							0	1	1101.8	12.3	0.4
0	0	1151.8	4.5	1.2							
0	2	1158.0	12.9	0.4			0	2	1155.0	8.1	0.7
0	1+0	1186.1	4.4	1.2			0	1	1188.9	5.9	0.9
		1191.2									
0	1+0+2	1199.7	3.7	1.4			0	1+2	1197.4	3.0	1.8
0	0+1+2	1210.0	10.4	0.5	1208.3	0.63					
1	1	1485.5	9.3	0.6			1	1	1495.3	9.2	0.6
2	0	1770.0	4.7	1.1							
							0	1	1855.5	6.5	0.8
1	1+0	1950.2	6.4	0.8							
1	2	1965.3	5.3	1.0	1966.3	0.90	1	2	1956.8	4.6	1.2
1	0+1+2	1974.5	9.4	0.6							
0	1+0	1990.6	12.0	0.4			0	1	1991.5	7.6	0.7
		2003.9									
0	1+0	2013.0	6.2	0.9			0	2+1	2009.3	6.3	0.8
0	0+2	2022.6	5.6	0.9							
1	0	2048.7	7.1	0.8	2050.2	0.82					
1	0	2124.4	2.4	2.2	2125.7	2.52					
1	2	2153.8	4.1	1.3			1	2	2153.8	4.2	1.3
1	1	2176.6	2.3	2.3			1	1	2177.9	2.5	2.1
1	0	2180.5	1.7	3.2	2182.4	1.59					
		2194.4									
1+0	0	2206.0	11.4	0.5							
							1	1	2239.7	12.8	0.4
1	2	2266.9	3.9	1.4			1	2	2267.4	3.6	1.5
1	1	2312.1	2.0	2.6			1	1	2314.5	1.4	3.8
1	2	2320.0	7.1	0.7			1	2	2321.8	7.6	0.7
1	0	2351.9	2.6	2.1			1	2	2352.0	2.2	2.4
1	0	2355.0	2.2	2.4			1	1	2356.8	5.5 (−1)	9.6
		2359.5									

[a]All states assigned with k'=0 in Ref. 1.

TABLE AIV: Same as in Table AIII for J'=1, 2 states of He−H_2^+(I=1) below the v'=1 j'=1 threshold.

J'=1[e]									J'=1[f]			
Life-time matrix							Stabilization[a]		Life-time matrix			
v'_r	k'	b'	v'_R	E'	Γ'	τ'	E'	τ'	v'_r	E'	Γ'	τ'
0+1	0			92.6	2.1	2.6	94.3	4.81				
0	1			174.0	8.5 (−1)	6.3			0	175.7	8.8 (−1)	6.0
0	0			215.5	4.0	1.3	214.3	1.36				
0	0			251.3	6.3	0.8	253.5	1.60				
0	1	3	4	297.0	1.1 (−1)	50.0			0	295.8	6.5 (−2)	81.6
0	0	3	4	327.8	2.4	2.2	329.7	1.92				
0	1			343.5	2.1 (−1)	25.5			0	343.0	8.4 (−2)	63.6
				347.0								
0	1			364.9	5.8	0.9			0	364.2	6.6	0.8
0	0	5	1	504.7	6.0	0.9	505.4	2.15				
0	1	5	2	630.0	3.5	1.5			0	630.9	4.0	1.3
0	0	5	2	709.9	4.4	1.2	709.6	4.01				
0	1	5	3	785.1	2.8	1.9			0	786.2	3.8	1.4
0	0	5	3	823.6	3.3	1.6	824.2	4.78				
0	1			852.1	7.1 (−1)	7.4			0	853.6	1.6	3.3
				857.4								
0	0			862.0	4.8	1.1	869.3	0.79				
							1336.9	3.13[b]				
1	1			1473.9	4.8	1.1			1	1475.1	3.9	1.4
0	0+1			1559.0	10.8	0.5						
				1574.2								
0	1+0			1582.9	5.8	0.9	1584.3	0.98	0	1589.0	11.9	0.4
0	0			1592.7	7.3	0.7						
2	0			1755.7	3.4	1.6	1739.4	1.52				
1+0	1			1942.0	11.3	0.5			1	1930.0	12.3	0.4
1	0			1964.0	11.2	0.5						
									0	1995.2	6.8	0.8
1	1			2073.0	2.9	1.9			1	2073.3	2.3	2.3
1	0			2116.4	8.9	0.6	2117.4	0.57				
1	1			2140.1	5.1	1.0			1	2140.5	4.2	1.3
1	0			2176.0	3.6	1.5	2178.2	1.76				
1	1			2218.2	3.0	1.8			1	2216.4	1.4	3.8
1	0			2229.6	2.3	2.3						
1	1			2247.1	2.4 (−1)	22.2			1	2246.8	3.8 (−1)	13.9
				2249.5								

J'=2[e]									J'=2[f]				
Life-time matrix							Stabilization[a]		Life-time matrix				
v'_r	k'	b'	v'_R	E'	Γ'	τ'	E'	τ'	v'_r	k'	E'	Γ'	τ'
									0	1	58.8	3.9 (−1)	13.5
0	0			60.1	3.9	1.4	70.4	0.66					
0+1	0			105.4	1.6	3.4	109.7	12.1					
0	2			134.5	1.0	5.6			0	2	134.5	1.0	5.1
0	1			180.6	1.2	4.3			0	1	184.8	1.3	4.1
0	0			230.5	6.1	0.9	229.6	1.20					
0	0			256.0	10.9	0.5	262.0	1.93					
0	2			270.7	2.6 (−2)	204.2			0	2	270.7	3.1 (−2)	169.1
0	2			286.5	1.0	5.2			0	2	285.1	2.5	2.2
0	1	3	4	306.8	2.4	2.2			0	1	304.8	3.5 (−1)	15.2
0	0	3	4	330.2	2.3	2.3	334.2	1.80					
0	2	3	4	335.6	2.6 (−1)	20.2			0	2	334.9	4.9 (−1)	10.9
0	0	3	5	346.1	8.0 (−1)	6.6							
				347.0									

0	1	5	1	382.9	4.4	1.2			0	1	379.7	5.1	1.0
0	0	5	1	516.5	11.3	0.5	518.3	2.22					
0	2	5	1	550.5	2.6	2.1			0	2	550.7	3.2	1.7
0	1	5	2	638.9	4.2	1.3			0	1	641.4	3.2	1.7
0	0	5	2	720.3	8.0	0.7	719.4	4.15					
0	2	5	2	734.6	2.2	2.4			0	2	735.0	2.7	2.0
0	1	5	3	790.0	2.2	2.4			0	1	793.7	2.6	2.0
0	2	5	3	832.5	6.2 (−1)	8.5	830.4	5.29	0	2	832.2	2.3	2.3
0	0+1			851.9	2.3	2.3							
				857.4									
0	1+0			863.1	2.7	2.0			0	1	862.3	4.7	1.1
0	1+0			872.5	8.9	0.6	872.9	0.70					
							1350.5	3.94[b]					
1	1			1487.6	7.4	0.7			1	1	1488.9	6.6	0.8
0	2			1515.4	7.5	0.7							
0	0+1			1563.0	9.4	0.6			0	1	1564.5	9.9	0.5
				1574.2									
0	0+1			1579.1	3.0	1.8							
0	2			1584.3	2.9	1.8			0	1+2	1582.9	6.2	0.9
							1588.6	1.00					
									0	2+1	1594.0	9.3	0.6
2	0			1770.4	3.7	1.4	1757.3	1.74					
0+1	0+1			1867.0	10.9	0.5							
1	1			1946.2	9.2	0.6			1+0	1+2	1957.3	8.2	0.6
1	2+0			1973.0	8.2	0.6							
1+0	2+0+1			1981.0	12.0	0.4							
1	1			2080.9	2.9	1.8			1	1	2083.8	2.6	2.0
1+0	0			2127.6	9.2	0.6	2126.7	0.60					
1+0	1			2146.0	10.8	0.5			1	1	2147.8	6.1	0.9
1	0			2187.8	7.1	0.7	2188.1	1.67					
1	1			2222.6	8.2 (−1)	6.4			1	1	2221.3	3.7	1.4
1	0			2233.0	1.4	3.9							
0+1	2			2248.6	1.3 (−1)	42.3			1	1	2248.8	2.6 (−1)	20.3
				2249.5									

[a]All states assigned with k'=0 in Ref. 1.

[b]The corresponding life-time matrix result is smaller than 0.4 ps.

COMMENTS

(i) Fig. A8 and Tables AI-AIV complete the quantitative characterization of the He-H_2^+ complex that was provided, for the same energy range and J' values, in Ref. 1. Merely three k'=0 states have been found that live longer than 5 ps. Here, it is seen that there are numerous k'>0 states living longer than the k'=0 states. Over thirty of them are characterized by τ'>5 ps.

(ii) All states are assigned with the number v_r'. States decaying by vibrational predissociation [v_r'>0 and $E'<\varepsilon_{10}'\,(\varepsilon_{11}')$ for I=0 (1)] are identified. The predictions of the adiabatic scheme of Ref. 1 for positions of the v_r'=1 states are qualitatively confirmed. Deviations are from −20 to +60 cm^{-1}. The lowest v_r'=1 states of the two (I=0 and I=1) complexes are found to lie about 20 cm^{-1} higher than previously thought. Consequently, the lowest VP state of the He-H_2^+(I=0) complex lives about 40 times shorter than previously predicted, i.e. only 0.6 ps. Many rotationally predissociating states [v_r'=0] live much longer.

(iii) Several examples of states of the He-H_2^+(I=1) complex are found in which rotations of the H_2^+ subunit are not severely hindered by interaction with the He atom so that the states can be assigned with the quantum numbers b' and v_R'.

DETAILS

on

DYNAMICS

in

THE PRODUCT CHANNEL

of

RCT

Fig. A9. $He+H_2^+(I=0)$ system

in a wide energy range. Collision-time delay

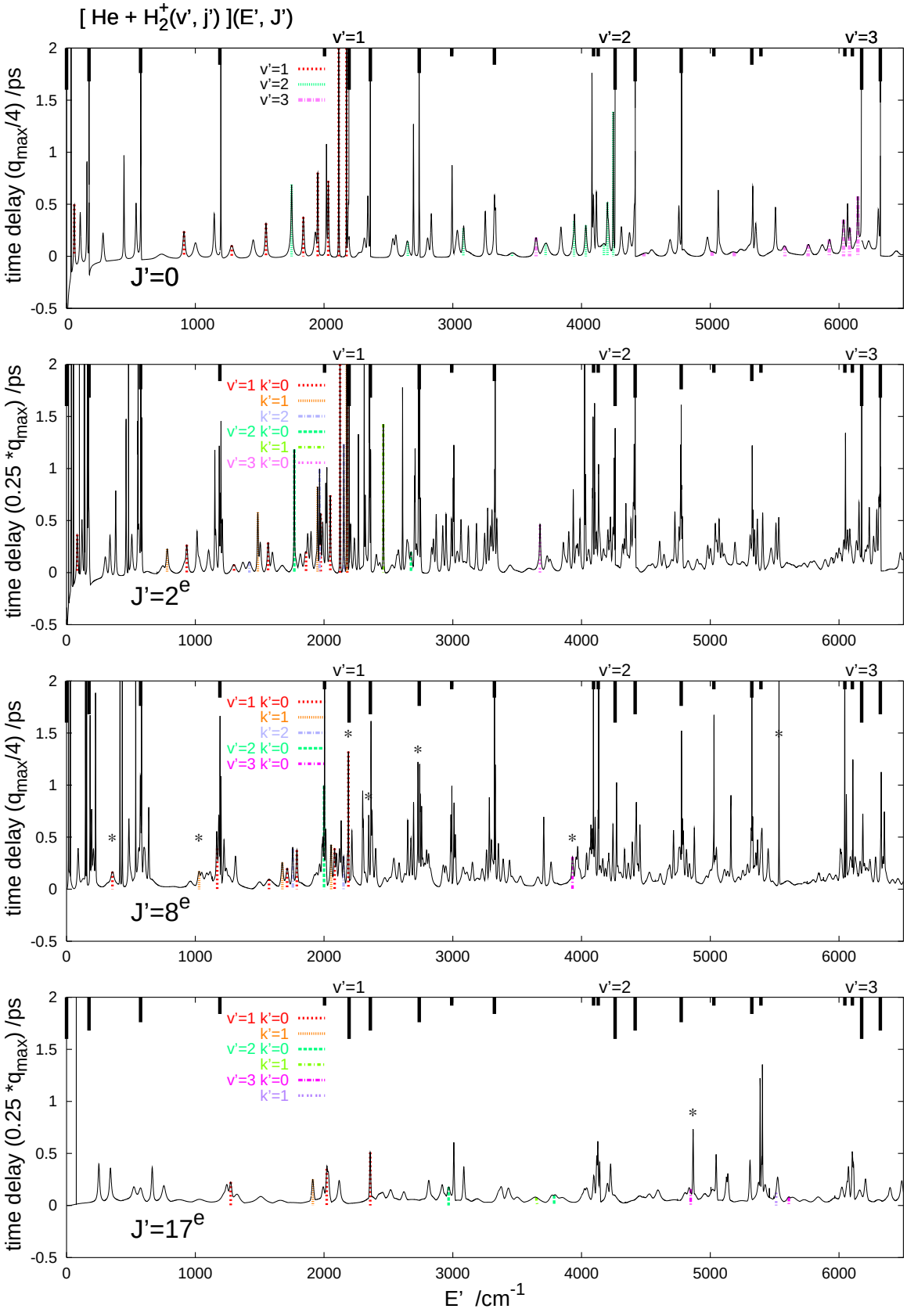

The maximal eigentimes $q_{\max}^{J'p'}/4$ for several partial waves ($J'\,p'$=1) as functions of energy E' in the range up to the opening of the HeH^++H channel. The color lines show the vibrationally predissociating (VP) states of the He-$H_2^+(I=0)$ complex detected by inspection of the related sojourn-time functions, Figs. A7 and A10.
Note that the lifetimes of VP states are generally shorter than lifetimes of most other resonances, especially in the low and medium J' cases.

Fig. A10. $He+H_2^+(I=0)$ system

Properties* of continuum and resonance functions

in short range of atom-diatom distances

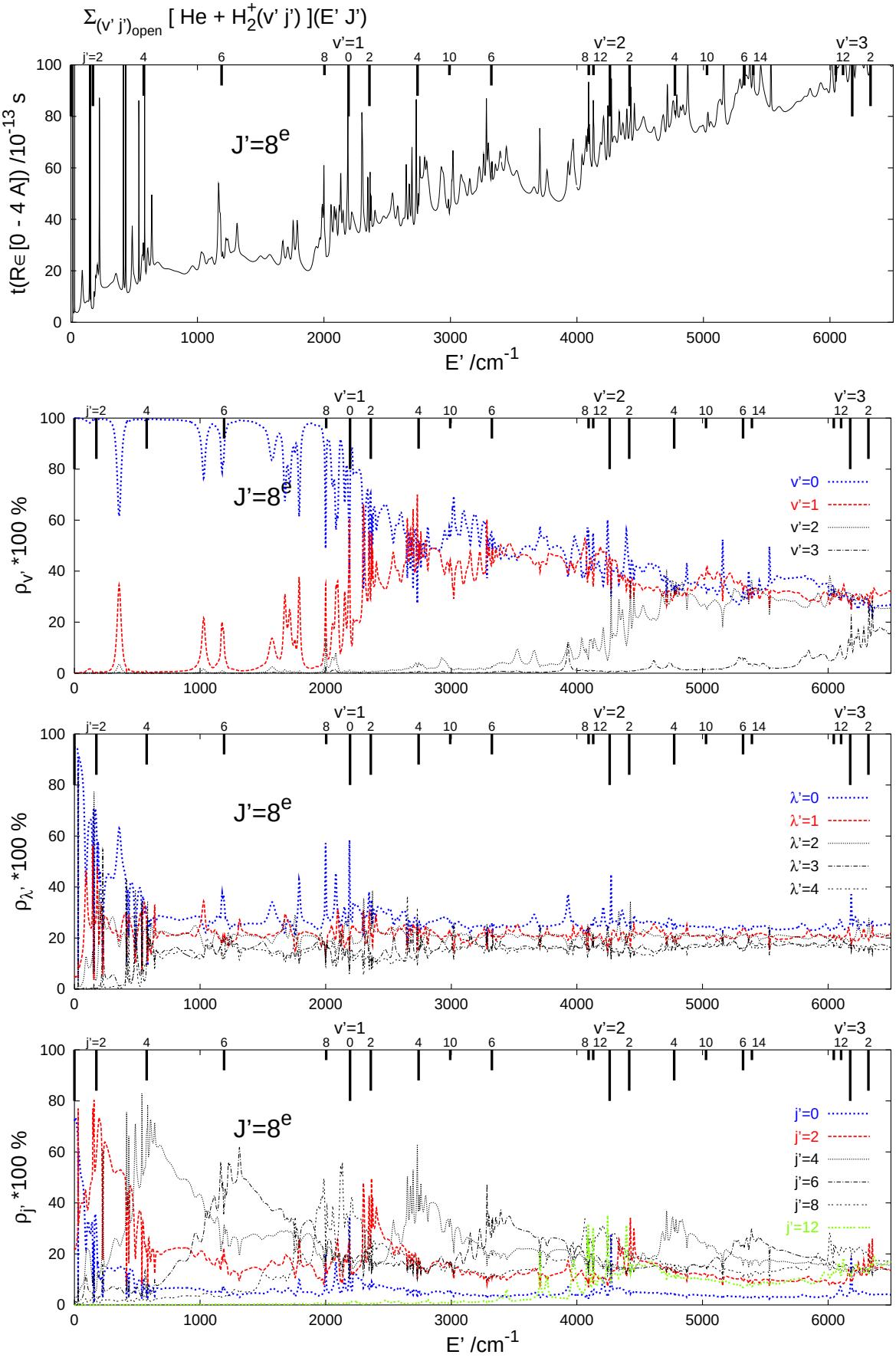

* Same as in Fig. A7 but for a larger range of E'.

Fig. A10a. Properties of continuum and resonance functions: low J' example

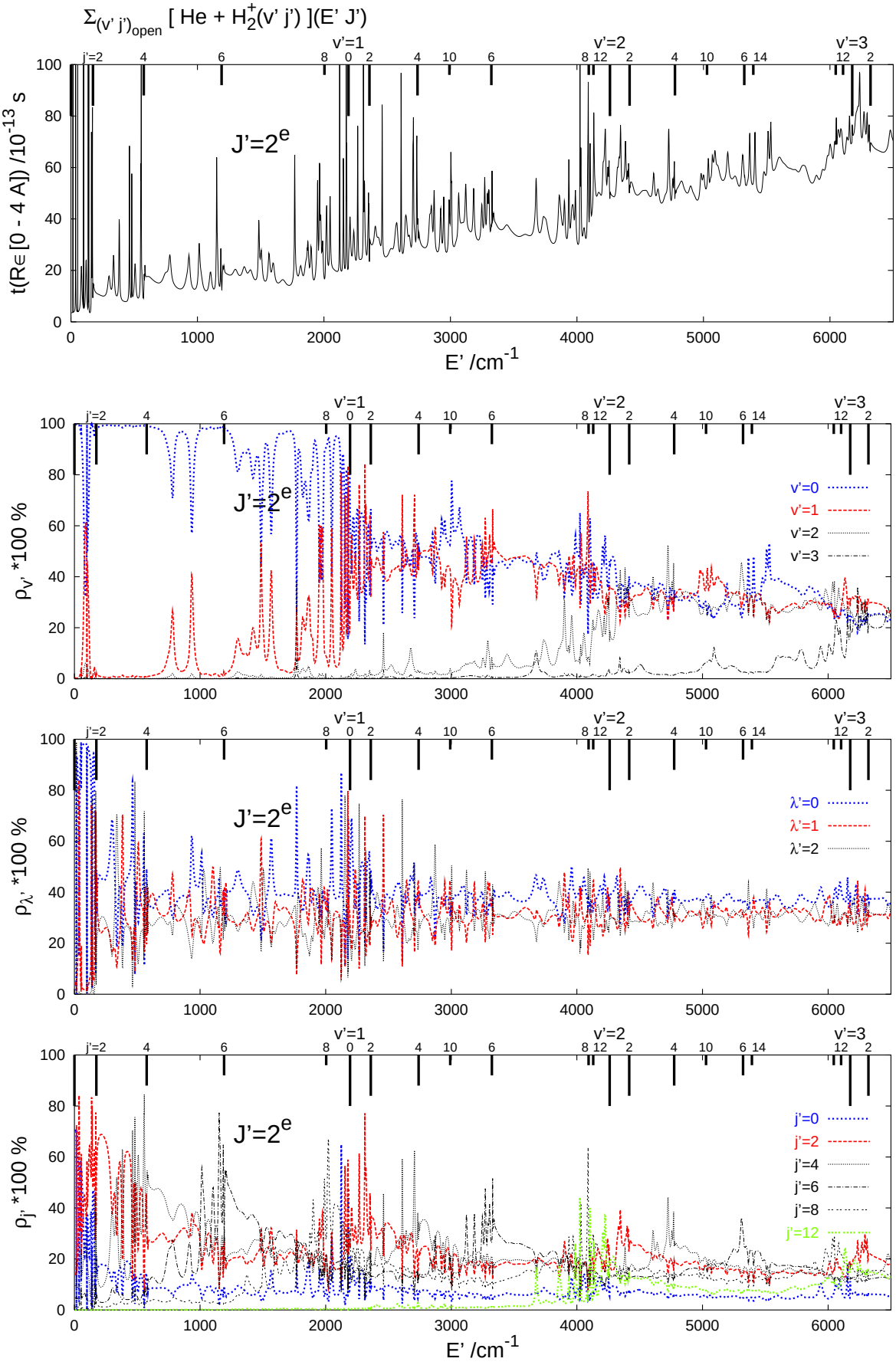

Fig. A10b. Properties of continuum and resonance functions: high J' examples

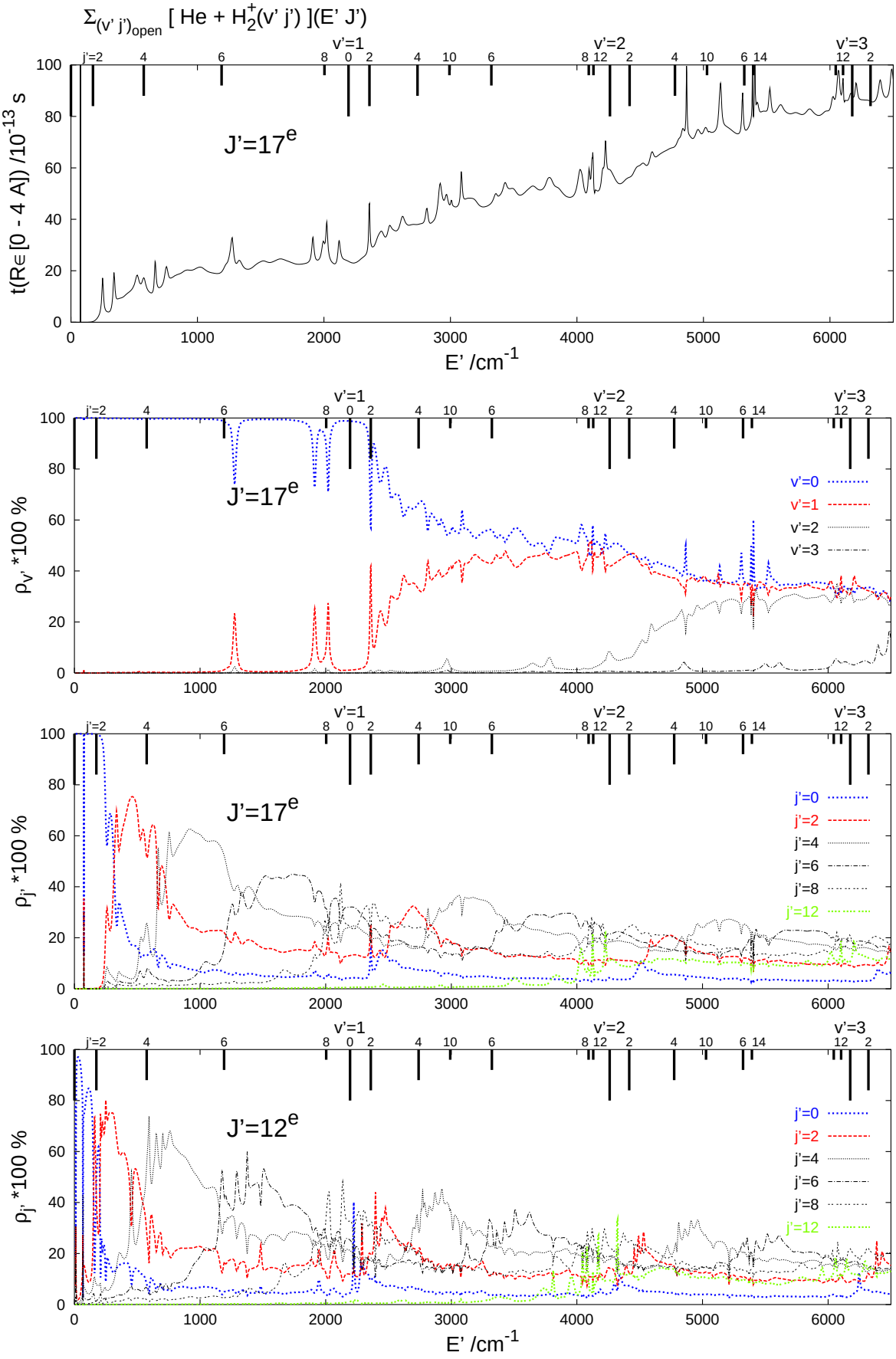

Note the shifting and smoothing of the broad peaks in the functions $\rho_{j'}(E')$ with growing J' — effects of increasing centrifugal barriers and Coriolis couplings.

Fig. A10c. Resolutions of sojourn-times into initial channel components

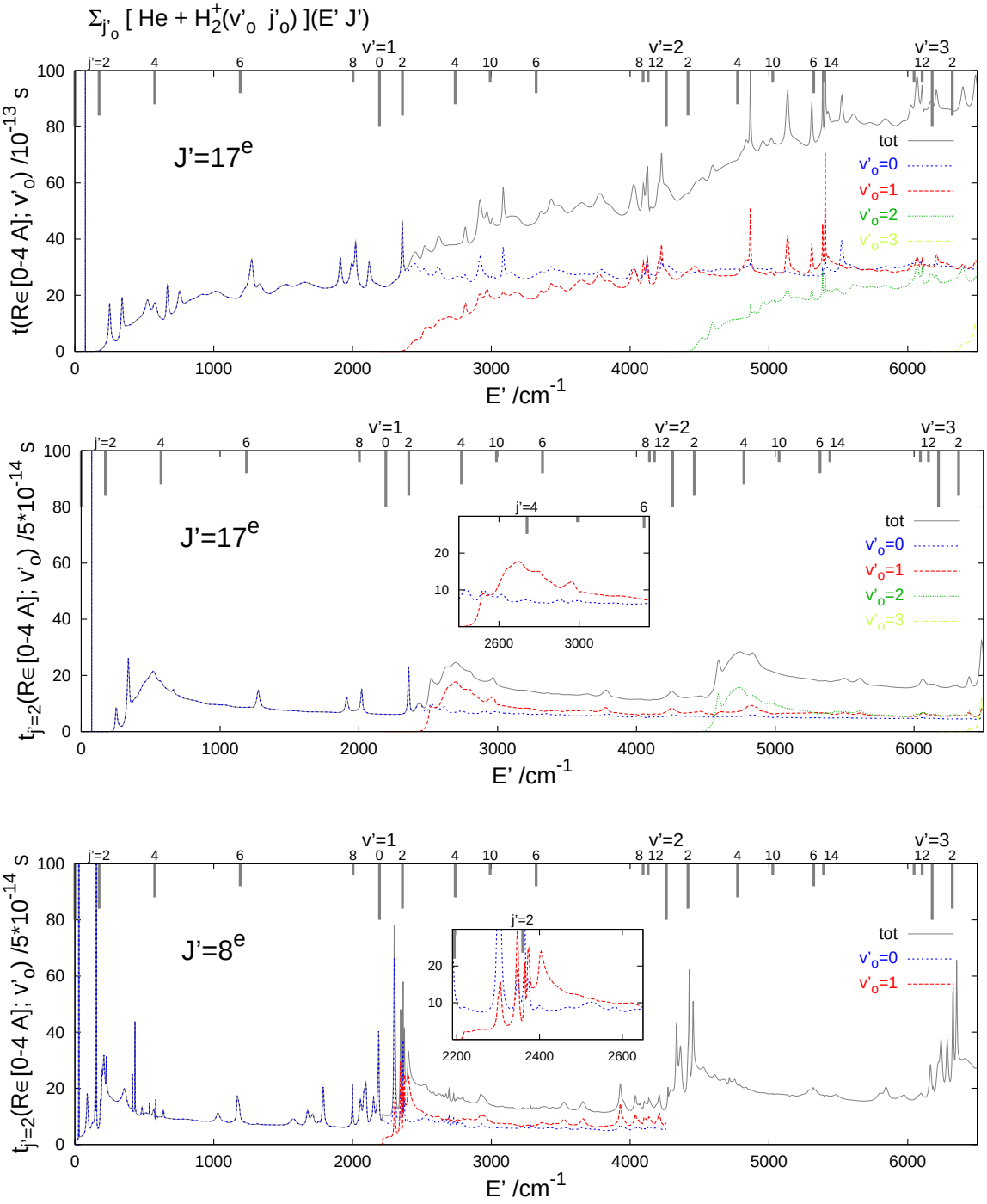

Note that tot=$\sum_{v'_o} t_{j'=2}(\ ;v'_o)$ is the product of the quantities $\rho_{j'=2}$ and t plotted in the preceding parts of the figure.

The broad peaks in the functions $t^{J'}_{j'=2}(E';\overline{R})$ indicate the regions of the product energy E' which are preferentially accessed in the radiative resonance→free transitions from the b=2=k J=J'±1 quasi-bound states lying in the considered (low) reactant energy range (E<150 cm^{-1}). The relative magnitude of different v'_o -components of these functions within the peaks indicates roughly the population of vibrational states among the H_2^+ products of the transitions. See comments to Figs. A14 and A15.

Fig A10d. (E' J'^{e}=17)-states in a range above (v' j')=(2 2) threshold

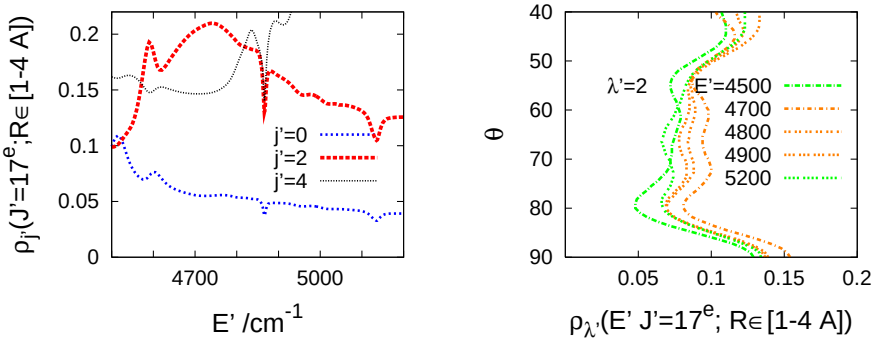

a) Left: enlarged fragment of the third panel of Fig. A10b. The energy range shown coincides with the position of the large peak in the width function $\frac{\partial}{\partial E'}\Gamma^{\rm RCT}(E'\,J'{=}17)$ of the A-channel resonance $(b\,k\,v_R\,J){=}(2\,2\,0\,18)$, displayed in Fig. A17 (in its bottom panel).

b) Right: the normalized 1-dim. sojourn-time densities $\rho_{\lambda'}(E'J'p';\overline{R};\theta){=}\int^{\overline{R}} dR\,\rho_{\lambda'}(E'J'p';\overline{R};R,\theta)$, see Eq. (A10). Shown is the range of θ where the X-channel functions can have a significant overlap with the function of the A-channel resonance (2 2 0 18), see the right bottom panel of Fig. A5.

The fact revealed by the figure on the structure of the X-channel continuum functions in the considered energy range is the relative increase of the $j'{=}2$ and $\lambda'{=}2$ components. The occurrence of the peak in the width function of the (2 2 0 18) resonance in Fig. A17 is thus fully consistent with the following two facts:

1) The function of the A-channel resonance is strongly dominated by the $(j\,\lambda){=}(2\,2)$ component, see the bottom panel of Fig. A4a.

2) The radiative $A{\to}X$ transitions preserve (exactly or approximately) the λ- and j-numbers, see Eq. (A11).

Fig. A9a. $\mathbf{He{+}H_2^+}(I{=}0)$ system

Statistics of resonances in the nonreactive range, $E'{<}6487$ cm^{-1}

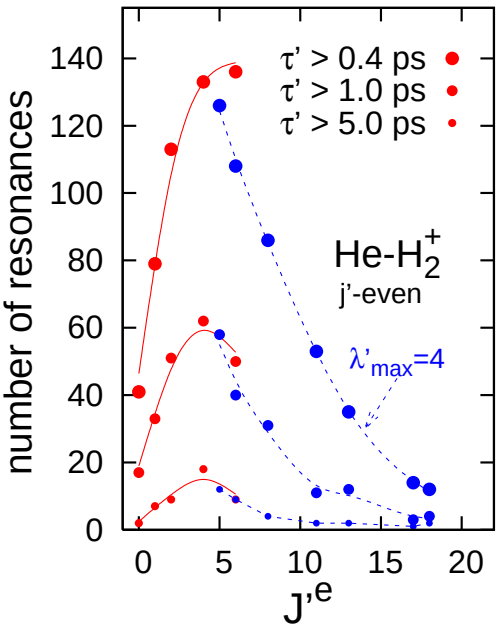

Counted here are the peaks in the eigen-lifetime functions $0.25{\times}q_{\rm max}^{J'^e}(E')$, see Fig. A9, whose heights give resonance lifetimes in three ranges: $\tau'{>}0.4$ps, $\tau'{>}1.0$ps, and $\tau'{>}5$ps. All eigen-lifetime functions were calculated with the basis X_4 ($v'{=}0{-}3$ and $j'{=}0,2..14$ states of H_2^+ included). The resonance numbers represented by the blue symbols come from calculations in which the Coriolis-Coupling-reducing (CCr) approximation ($\lambda'{\le}4$) was additionally applied.

In the overwhelming majority, the resonances live shorter than 5 ps ($\Gamma'{>}1$ cm^{-1}). These resonances were considered too broad to be separated out of the background in the calculations of the $A{\to}X$ transitions amplitudes. Altogether, in the range of $J'{=}1{-}20$, $p'{=}{\pm}1$, there are about 40 resonances living longer than 50 ps. About 30 of them (with $k'{\le}3$), were treated by the analytical approximation described in Sec. IIE.

Fig. A11. High energy resonances* in $He+H_2^+$ Sojourn-time maps**

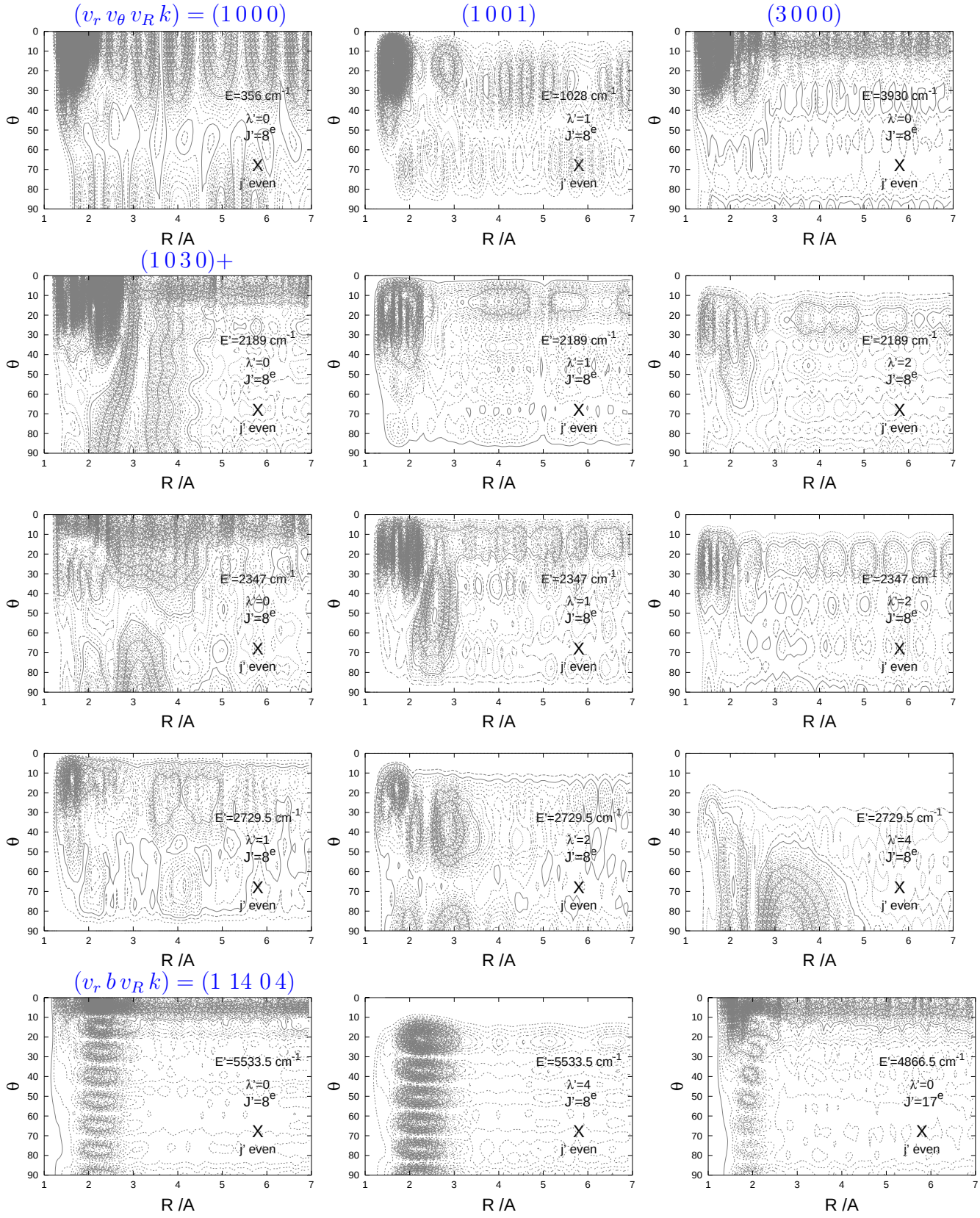

* Shown are the resonances marked with asterisks in Fig. A9. ** See the caption of Fig. A7a.

In the upper row are the lowest vibrationally predissociating J'^e=8 states associated with the v'=1 and v'=3 thresholds. The case in the second row is a mixture of vibrationally predissociating state with another resonance. The approximate quantum numbers (the blue labels) are assigned in a crude manner (see Table AV), in most evident cases only.

Fig. A11a. Sojourn-time maps for selected† $J'=6^e$ resonances near $v'=1$ threshold

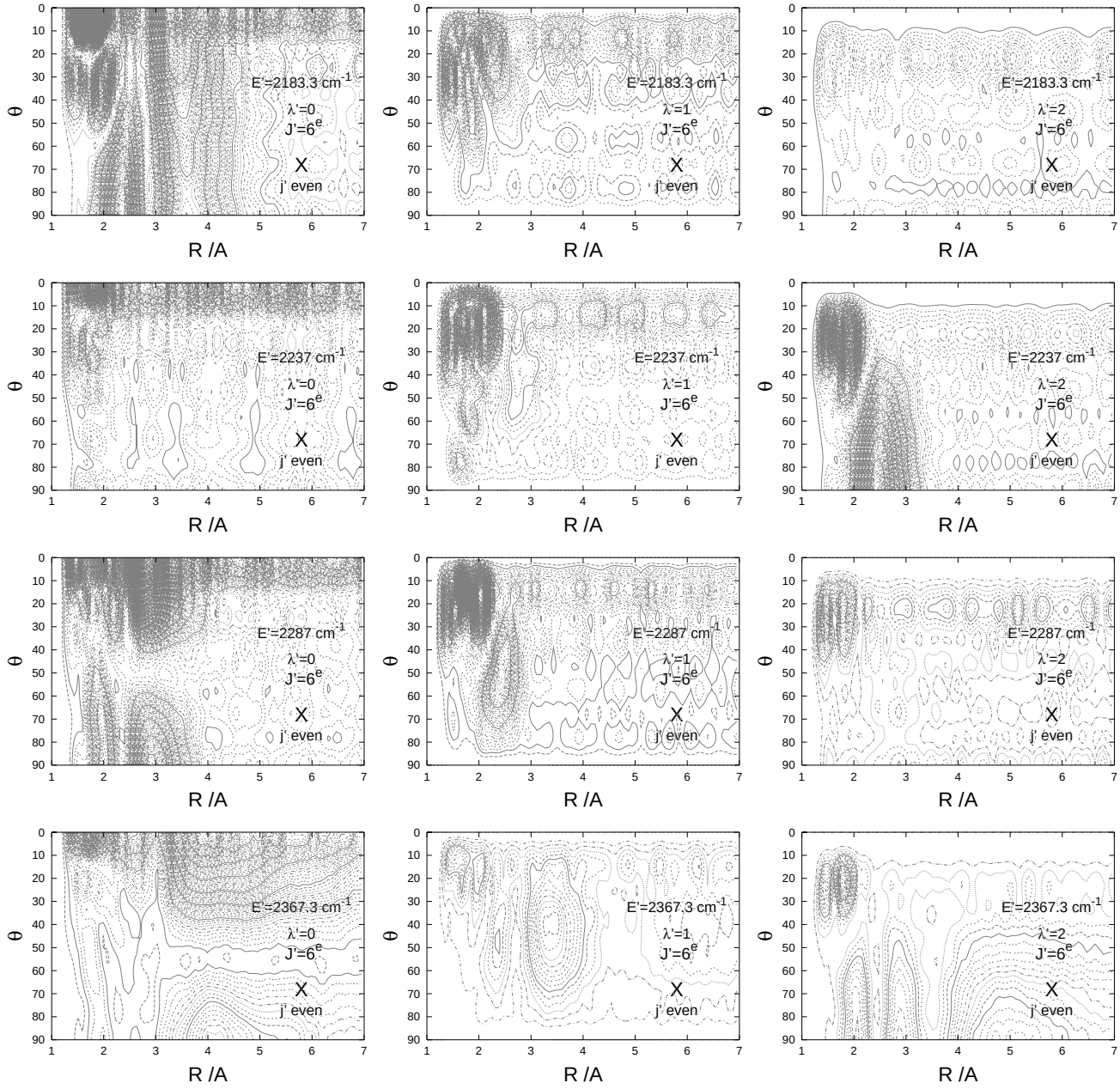

† the cases marked with asterisks in Fig. A17

Fig. A12. He-$H_2^+(I{=}0)$ complex

Energies of 'vibrational' states (v' [(∗)] $J'{=}k'$)

for $J'{=}0, 1^f, 2^f$ and $v'{=}0{-}3$

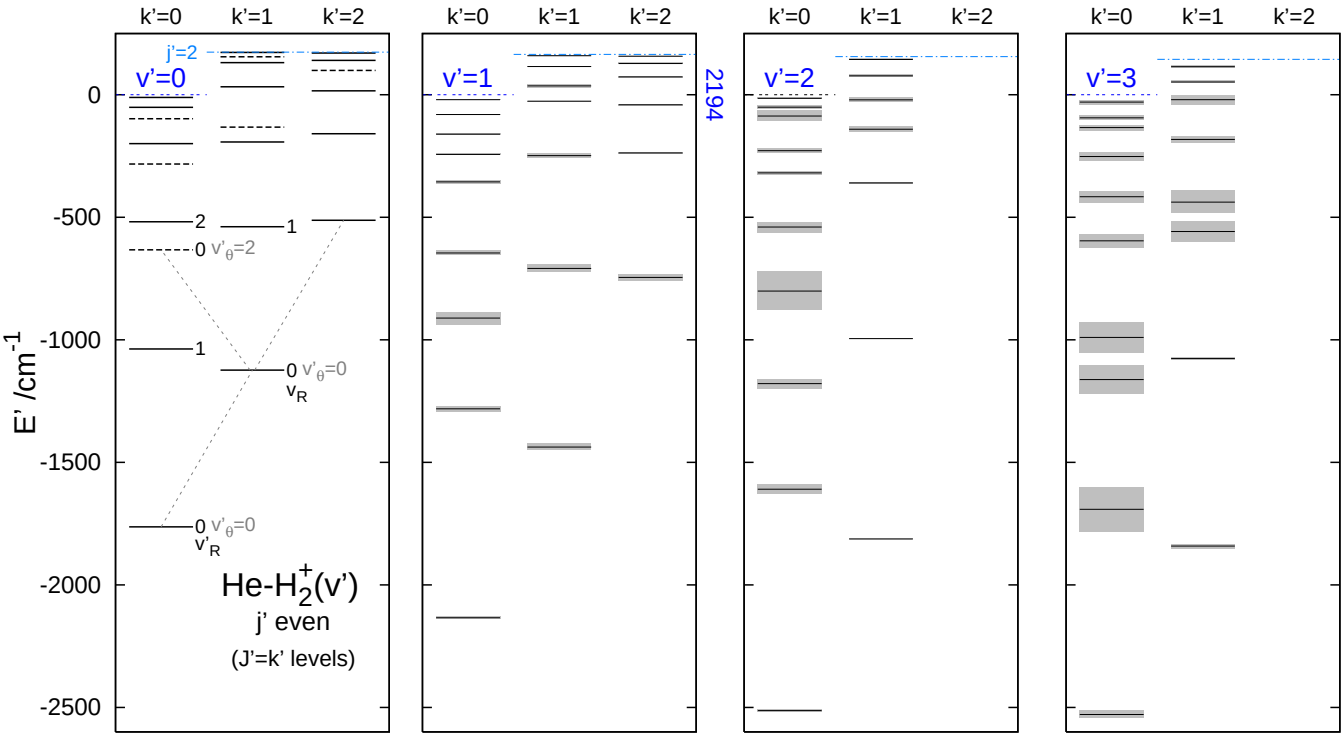

[(∗)] stands for the quantum numbers v'_θ (or b') and v'_R that characterize the atom-diatom bending and stretching motions in the states, see Table II in paper II and Table AV below.

The dotted gray lines connect the levels which form the pattern similar to that of circular harmonic oscillator with the vibrational quantum number $v'_\theta{+}k'$. The gray bars indicate the widths of the energy levels.

COMMENTS

(i) The name 'vibrational' means here the $J'{=}k'$ states. It is obviously not synonymous with 'vibrational predissociation' in the cases of quasi-bound states. The e-parity counterparts of the states shown between the $j'{=}0$ and $j'{=}2$ thresholds can decay also by rotational predissociation.

(ii) The structures of energy levels of the states of the He$-H_2^+$ complex associated with the $v'{=}1{-}2$ thresholds retain a similarity to the structure of the bound-state levels in the leftmost panel. The major difference is the considerable increase of the binding of the complex. If measured by the position of the lowest energy level relative to its respective v'-threshold, the binding increases by ca 380 cm^{-1} upon the $v'{=}0{\to}1$ and $1{\to}2$ excitations of the H_2^+ subunit (see Table AV). The analogous effect in the He^+-H_2 complex is about 7 times smaller (see Table CII in part C).

(iii) The binding energy of the He$-H_2^+(v'{=}1)$ complex is only by 59.5 cm^{-1} smaller than the $v'{=}0{\to}1$ excitation energy of free H_2^+ and the binding of He$-H_2^+(v'{=}2)$ is by nearly 450 cm^{-1} larger than the separation between the $v'{=}2$ and $v'{=}1$ thresholds, $\varepsilon'_{20}{-}\varepsilon'_{10}$. Because of these relations and the strength of the $r{-}\theta-R$ coupling in the potential V^X displayed in Fig. A1b, one can expect that vibrational predissociation is a very efficient mechanism of decay of the quasi-bound states of the complex. This is indeed observed, most clearly in Fig. A9.

(iv) Because of the limitations of the used CC-BF-diabatic approach (see Fig. A18), the information given here and in Table AV on the higher part of levels associated with the $v'{=}2$ threshold and on all levels associated with the $v'{=}3$ threshold is only qualitative.

TABLE AV: He$-H_2^+(I{=}0)$. Positions (E') and widths (Γ') of 'vibrational' states $k'{=}J'$ =0 and $k'{=}J'$ $=1^f, 2^f$ lying below the $v'{=}0{-}3\,j'$ thresholds for $j'{=}0$ and $j'{=}2$ for f-symmetry states. The positions ($\varepsilon'_{v'j'}$) of the thresholds are listed in the headings and in the bottom line (for $j'{=}2$). Deviations from exact values for H_2^+, Ref. 6, are shown in braces. All data are in cm^{-1}.

	$v'{=}0^a$ $\varepsilon'{=}0$		$v'{=}1^a$ $\varepsilon'{=}2194.4\,\{3.2\}$			$v'{=}2^a$ $\varepsilon'{=}4260.8\,\{5.7\}$			$v'{=}3^a$ $\varepsilon'{=}6175.9\,\{-20.1\}$		
k	$[v]^b$	$E'-\varepsilon'$	*[v]*^{c}	$E'-\varepsilon'$	Γ'	*[v]*^{c}	$E'-\varepsilon'$	Γ'	*[v]*^{c}	$E'-\varepsilon'$	Γ'
0	1	−1763.5	*1+*^{d}	−2134.9	8.2	*1+*	−2512.4	8.8	*1*	−2534.8	35.5
	2	−1037.2	*2*	−1282.2	19.9	*2*	−1612.9	36.9		−1692	182
	3	−632.4	^{e}	−911	50		−1176.2	17.3		−1162	117
	4	−518.1	*4*	−645.4	15.7		−801	157		−990	125
	5	−282.6	*5*	−354.9	13.5		−537.5	36.0		−596	54
	6	−199.2	*6*	−243.5	6.5		−315.6	12.5		−416	47
	7	−98.0	*7*	−160.7	7.4		−227.6	17.8		−251.9	33.2
	8	−51.1	*8*	−80.2	2.3		−86.8	43.0		−140.4	17.6
	9	−11.0	*9*	−19.9	1.5		−61.4	12.3		−92.9	19.3
							−14.4	3.8		−30.0	10.3
1^f	1	−1123.6	*1*	−1437.9	21.0	*1+*	−1812.5	0.7	*1+*	−1838.1	13.3
	2	−538.7	*2*	−701.8	25.7	*2*	−995.3	2.2	*2+*	−1076.5	9.9
	3	−192.7	*3*	−248.6	20.1	*3*	−359.6	4.7		−558	84
	4	−132.0					−140.8	21.2		−438	90
	5	32.4	*5*	−26.0	3.1		−20.8	13.3		−189	37
	6	131.5	*4*	36.4	13.0		77.0	13.3		−30	46
	7	155.0	(2,4)^f	115.6	1.1	(2,3)	144.1	5.2		52.1	9.8
	8	173.0	(2,5)	159.6	0.2					114.8	11.6
2^f	1	−511.8	*1*	−744.9	22.5						
	2	−158.6	*2*	−237.6	4.6						
	3	16.0	*3*	−40.5	4.2						
	4	99.7	*4*	73.0	3.6						
	5	140.7	*5*	127.4	7.1						
	6	170.2	*6*	157.6	2.2						
ε'		174.2		165.1			155.5			144.6	
		{0.0}		{0.0}			{−1.1}			{−3.0}	

[a] States listed in particular v' column are assigned the approximate quantum number $v'_r{=}v'$.

[b] The label of bound states of the complex introduced in Table I of paper I. It is an abbreviation of two vibrational quantum numbers v'_θ and v'_R assigned to the states in paper II, by performing the Natural Expansion Analysis of the bound-state functions.

[c] A crude assignment of resonance states, based on qualitative inspection of the sojourn-time maps $\rho_{\lambda'}(E'{\approx}E'_{\rm res}\,J'p';\overline{R};R,\theta)$ in the interaction region ($\overline{R}{=}4\mathring{A}$). The label *[v]*=$x$ means that the respective map $\rho_{\lambda'}(E'_{\rm res}J'p';\overline{R};R,\theta)$ shows a structure which resembles the structure in the probability distribution $\rho_{\lambda'}(E'^B J'p';R,\theta)$ of the bound state labeled with $[v]{=}x$ in Table II of paper II. There are misprints in the caption of this table. Instead of the second and third v_θ in the second line, the symbols v_R and v_r, respectively, should appear.

[d] The + sign means an overlapping with another resonance.

[e] Empty space in the *[v]* column means that no assignment of the resonance could be made in the way described in footnote *b*.

[f] (b', v'_R) where b' is the approximate quantum number assignable to states of atom-diatom complexes in which the rotation of the diatomic subunit changes adiabatically with the R-distance.

COMMENT

Because of the cases of substantial overlapping and incomplete identification of the resonances, the widths listed in the Table can not be taken as precise measures of the rate of vibrational predissociation of the He$-H_2^+$ complex. A crude estimate of this rate can be inferred, however: $\Gamma'/\hbar \sim 10^{12}{-}10^{13}$ s^{-1}.

SOME DETAILS

on

DYNAMICS

of

RCT

PROPENSITY RULES

POPULATIONS of PRODUCT STATES

Fig. A13. J'=0−2 **resonances in He+H_2^+ channel**
accessed in radiative transitions
from quasi-bound states of $He^+-H_2(v=0)$

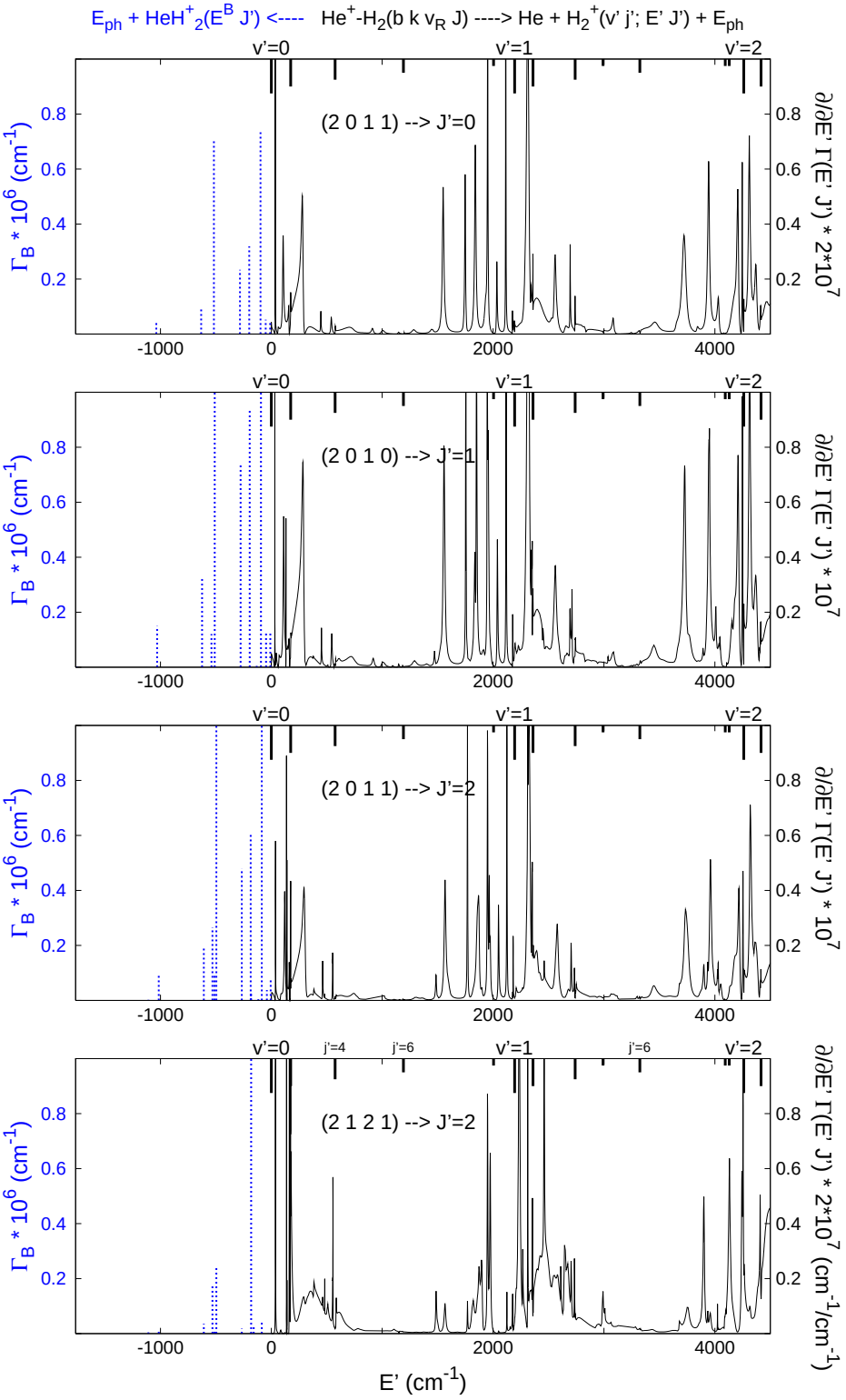

The resonances are displayed in the black parts of the panels (by the sharp peaks; the broader features above the v'=0, 1, 2 thresholds are mostly due to transitions to continuum states of He+H_2^+). The blue lines show bound J' states of the HeH_2^+ ion which are populated in the radiative association (RA) reaction from the indicated initial quasi-bound states. The widths $\Gamma_B^{\rm RA}(J\to J')$ of the states have been obtained as intermediate results of the calculations reported in paper II. Some similarity can be noted between the structures of the blue lines and the black peaks below the v'=1 threshold.

COMMENTS

(i) The resonance structures in the radiative width functions $\frac{\partial}{\partial E'}\Gamma(E'\,J')$ are by far less rich than the structures displayed by the time-delay functions $q^{J'p'}_{\max}(E')$ which characterize the same X channel continua $(E'\,J')$, see Fig. A9. This should be attributed to:
a) the very small j- and λ-mixing in the initial quasi-bound states of the He^+-H_2 complex, see Fig. A4a,
b) the properties of the $A\rightarrow X$ electric dipole transition vector used in the calculations. This quantity enters the calculations through the following matrix elements [cf. Eqs. (33)-(35) and (41)-(42) in paper I]

$$\left[{}_{\rm BF}\mathbf{d}^{J'p'\,J^e}(R)\right]_{v'j'\lambda',vj\lambda} \;=\; \delta_{\lambda,\lambda'}\;(-1)^{J'+\lambda}[(2J'+1)]^{1/2}\begin{pmatrix} J' & 1 & J \\ -\lambda & 0 & \lambda\end{pmatrix}\left[\mathbf{d}^{\lambda}(R)\right]_{v'j',vj} \qquad \text{(A11)}$$

$$\text{with} \qquad \left[\mathbf{d}^{\lambda}(R)\right]_{v'j',vj} \;=\; \sum_{L=0,2}\langle v'j'|D_{L\Lambda=0}(r,R)|vj\rangle_r\, g^{\lambda}_L(j',j)\,, \qquad \text{(A12)}$$

where $\langle v'j'|D_{L\Lambda=0}(r,R)|vj\rangle_r$ for L=0, 2 are the functions presented in Fig. A1c and $g^{\lambda}_L(j,j')$ denotes the Gaunt integral $\langle Y_{j\,\lambda}|\,Y_{L\,0}|Y_{j'\,\lambda}\rangle\times\sqrt{\frac{4\pi}{2L+1}}$.
The following propensity rules result from a) and b) for $(b\,k\,v_R\,J)\rightarrow(E'_{\rm res}\,k'\,J')$ transitions

$$\Delta k{=}0, \qquad \text{and} \qquad \Delta j{=}0\,. \qquad \text{(A13)}$$

The elements $\left[{}_{\rm BF}\mathbf{d}^{J'p'\,J^e}(R)\right]_{v'j'\lambda,vj\lambda}$ with $j'{=}j{\pm}2$ are definitely smaller than the $j'{=}j$ elements because of the relative strength of the radial functions $\langle\; D_{L\,0}(r,R)\;\rangle_r$ for L=2 and L=0. As shown in Fig. A1c, the L=2 function takes from $\sim$2 to $\sim$10 times smaller values than the L=0 function at $2{\leq}R{\leq}4\mathring{A}$, i.e. in the range of R- coordinate of the most probable simultaneous stay of the reactant and product systems, compare Fig. A5 with Figs. A6 and A10.

(ii) Because of the Δk=0 rule the bottom panel of Fig. A13 displays mostly k'=1 resonances while the other panels display k'=0 resonances. $\Delta k{\neq}0$ transitions can attain, however, appreciable strengths if there are large admixtures of $\lambda'{\neq}k'$ components in final states. The peak near E'=500 cm^{-1} in the bottom panel is an example of strong Δk=1 transition; the involved quasi-bound state of $He-H_2^+$ is nominally a k'=2 state but its λ'=1 component is only slightly weaker than λ'=2.

(iii) The meaning of the Δj=0 rule may seem unclear in view of the fact that there is usually a considerable j'-mixing in states of the $He+H_2^+$ system. Most safely it can be interpreted as a tendency among transitions from a given reactant state $(b\,k\,v_R\,J)$ to select the regions of the product energy E' which are characterized by relatively large values (sharp peaks) of the sojourn-time $\rho_{j'}(E'\,J';\overline{R})$ with $j'{=}b$. In this meaning, the rule certainly applies to resonance-resonance transitions explaining in particular the lack of peaks near the j'=6 thresholds in Fig. A13 (compare with the bottom panel of Fig. A10a).

The Δj=0 tendency also occurs in resonance-free transitions which dominate among transitions from high J resonances. However, the sojourn-time analysis of the final states in the flat continuum regions is by far less informative, see Fig. A13a.

A wide selection of examples of the Δj=0 propensity in the RCT reaction is provided in Figs. A14 and A15.

Fig. A13a. J'^e=17 **continuum states of He+H_2^+**
accessed in radiative transitions
from quasi-bound states of $He^+-H_2(v=0)$

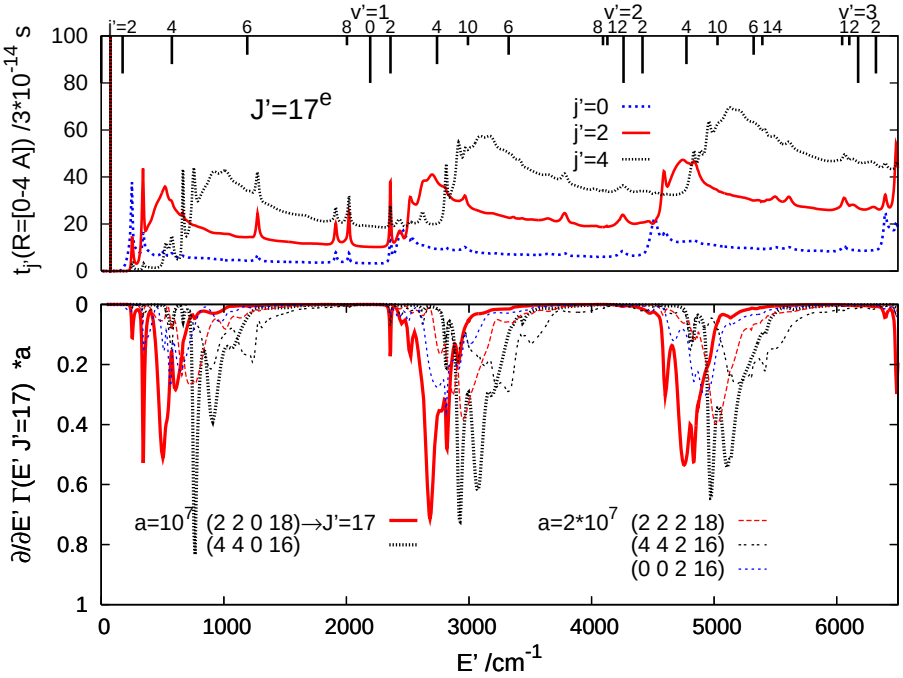

Upper: Sojourn-times $t_{j'}^{J'^e}(E';\overline{R})$ in the region $R{\leq}\overline{R}{=}4\mathring{A}$ of the He+H_2^+ system being in the partial state J'^e=17 with the H_2^+ subunit in state j' for j'=0, 2, 4 [see Eq. (A4)]. Lower: The width functions $\frac{\partial}{\partial E'}\Gamma(E'\,J'{=}17^e)$ of selected states $(b\,k\,v_R\,J{=}J'{\pm}1)$ of the complex $He^+-H_2(v=0)$.

COMMENTS

(i) The broad maxima in the functions $t_{j'}^{J'^e}(E';\overline{R})$ above the subsequent thresholds v'=0, 1, 2 signify the openings of the $(v'\,j')$ continua to radiative transitions from the reactant channel. The transitions take place at short R-distances. At these distances, the dynamics of the product system is strongly affected by the (sizeable for J'=17) centrifugal potential. Hence the openings (effective thresholds) occur at energies much higher than the respective asymptotic thresholds $\varepsilon'_{v'j'}$.

(ii) The positions of the effective thresholds $(v'\,j')$ for v'=0, 1, 2 displayed by the sojourn-time functions $t_{j'}^{J'^e}(E';\overline{R})$ for j'=2, 4 coincide quite well with the positions of the broad peaks in the functions $\frac{\partial}{\partial E'}\Gamma(E'\,J'{=}17^e)$ that describe radiative transitions $(b\,k\,v_R\,J{=}J'{\pm}1){\longrightarrow}(E'\,J'^e{=}17)$ from resonances with $b{=}k{=}j'$ and v_R=0.

(iii) It should be noted, however, that the resonances mentioned above, with $k{=}b$ and v_R=0, are the lowest ones (have the lowest energy $E_{\rm res}$) among those assigned with given values of b and J (see part C). Transitions from higher lying resonances, like the resonances with v_R=2 shown in the figure, produce features in the respective functions $\frac{\partial}{\partial E'}\Gamma$ which have maxima considerably shifted from the effective thresholds $(v'\,j')$ towards higher energies E'. These maxima do not have any visible counterparts in the functions $t_{j'}^{J'^e}(E';\overline{R})$.

Fig. A14. RCT from quasi-bound states* of $He^+-H_2(v{=}0)$

$$(b\,k\,v_R\,J\,p{=}1) := (n\,J)$$

into [He + $H_2^+(v',j')$]$(E'\,J')$

The width functions $\frac{\partial}{\partial E'}\Gamma_n^J(E'\,J')$ and the populations $P_{c'}(nJ;J')=\frac{\Gamma^J_{n,c'}(J')}{\Gamma^J_n(J')}$ ♯ for $c'=j',v'$

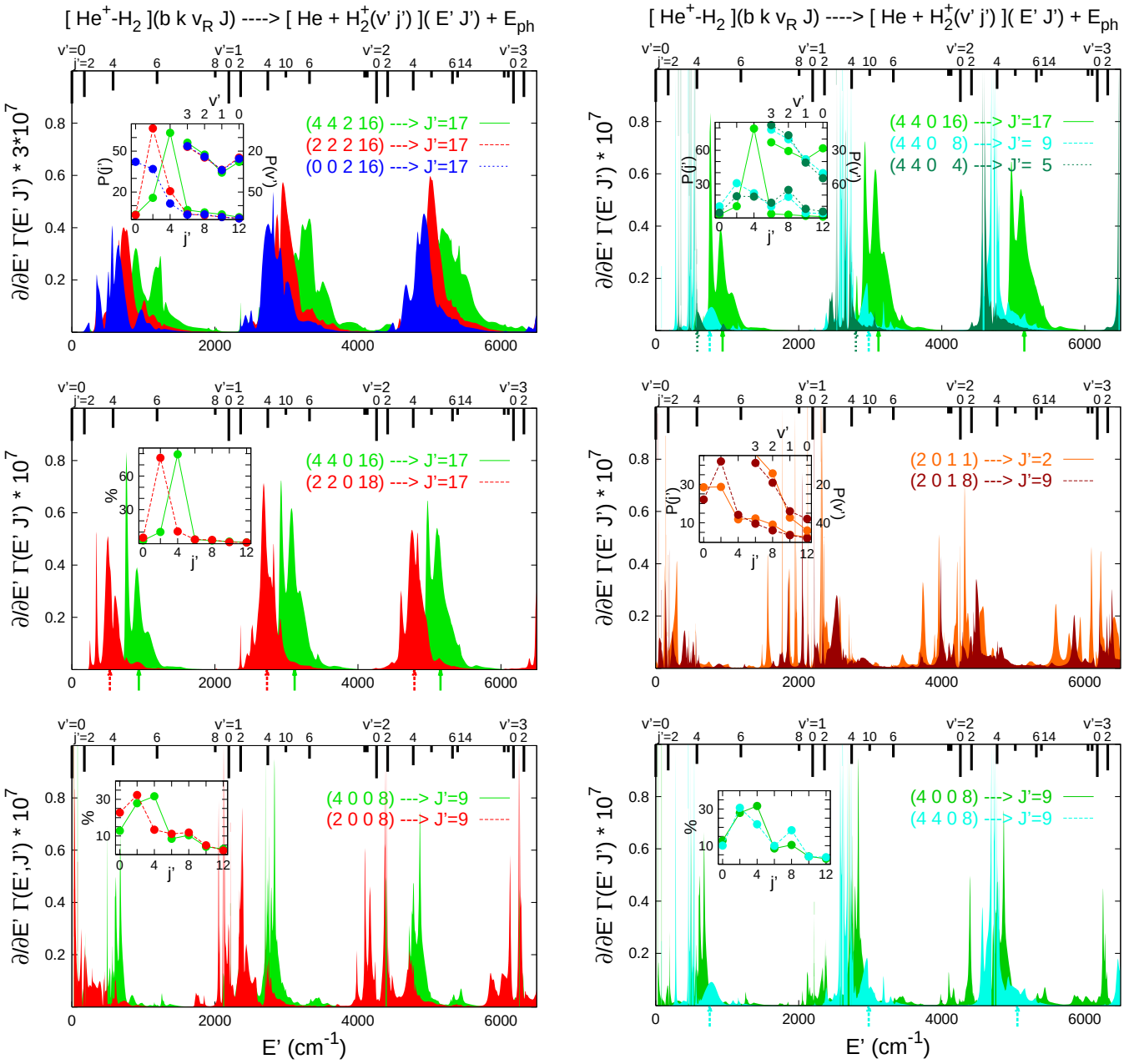

♯The populations are shown in the insets as $P_{c'}(nJ;J')\times 100\%$. The widths $\Gamma^J_{n,c'}(J')$ for $c'=j',v'$ were obtained as the integrals $\int_0^{E'_{\max}}\frac{\partial}{\partial E'}\Gamma^J_{n,c'}(E'J')\,dE'$ with $E'_{\max}$=7800 cm^{-1} and $\Gamma^J_n(J')=\sum_{c'}\Gamma^J_{n,c'}(J')$. The arrows in the bottom of the panels show the predictions of the 1-dim. model for the peaks in the resonance-free transitions $(b\,k{=}b\,v_R{=}0\,J\,p{=}1)\rightarrow(E'\,J'{=}J{\pm}1;j'{=}b\,\lambda'{=}k)$ presented in Figs. A2b and A2c.

*Transitions from b=4 states are shown here only for a better illustration of the propensity rules. The states lie much too high on the energy scale (see Table CII) to contribute to RCT at temperatures below 50 K.

COMMENTS

This figure should be analyzed together with the plots of the effective potentials in Fig. A2b and A2c. The following points merit more detailed comments:

(i) the correlations of the shapes of the width functions $\frac{\partial}{\partial E'}\Gamma^J_n(E'\,J')$ with the quantum numbers $(b\,k\,v_R\,J)$ of the quasi-bound states

1. The positions of the main peaks correlate with the positions of the $\varepsilon'_{v'\,j'=b}$ thresholds (best seen in the bottom panels) — the most explicit manifestation of the $\Delta j{=}0$ propensity.

2. With growing J, the peaks shift from their respective $\varepsilon'_{v'\,j'}$ thresholds towards higher energies E' and change their shapes; they become smoother and broader. The effect is best seen in the upper right panel; generally, for states with $k{=}b$. These states are localized within the effective potentials $W^J_{0\,j=b\,\lambda=j;\,0jj}(R)$ which have the deepest wells among those pertaining to a given $j{=}b$. The corresponding potentials $W'^{J'}_{v'\,j'=b\lambda'=j';\,v'j'j'}(R)$ are in turn the shallowest as compared to their $\lambda'{<}j'$ counterparts. With growing J', the shallow wells fill up most quickly. In other words, there is a range of J's where the $\lambda'{=}j'$ potentials are already purely repulsive whereas wells still remain in the $\lambda'{<}j'$ ones. For small values of J', the transition range [determined by the quasi-bound state function multiplied by $D_{L=0}(R)$, see Eq. (A11)] lies above the wells of the potentials $W'^{J'}_{v'bb;\,v'bb}(R)$ for $v'{=}0,1,2,3$. The transitions terminate mostly at resonances below the $\varepsilon'_{v'\,j'=b}$ thresholds. Transitions to free states above these thresholds produce only small features in the shapes. For medium size J's (here $J'{=}9$), some sharp peaks due to resonance-resonance transitions still appear but the resonance-free features become considerably bigger. For large J's (here $J'{=}17$), the shapes are almost entirely determined by resonance-free transitions. The following serves as evidence: the shifts of the centers of the broad peaks in the transitions $(b{=}2,4\,k{=}b\,v_R{=}0\,J{=}16,18){\to}J'{=}J{\pm}1$ from the $\varepsilon'_{v'=0-2\,j'=b}$ thresholds appear reasonably well predicted by the model which accounts only for the 'reflection' of the resonance functions from the single potentials $W'^{J'}_{v'bb;\,v'bb}(R)$.

3. Shapes pertaining to resonances with excited atom-diatom stretching mode, $v_R{>}0$, are characterized by generally broader peaks, as seen in the upper left panel. Qualitatively, this is also consistent with the reflection principle.

(ii) the correlations of the populations $P_{j'}(nJ;J')$ with the quantum numbers b, k, and J.

1. The maximum population is usually at $j'{=}b$. Exceptions from this rule may occur in cases of small J resonances when major parts of the peaks in the width functions lie below the $\varepsilon'_{v'\,j'=b}$ thresholds and resonance-free contributions are too small to outweigh them. The resonances $(4\,4\,0\,4)$, $(4\,4\,0\,8)$, and $(2\,0\,1\,1)$ shown in the figure belong to such cases.

2. The overall shapes of the functions $P_{j'}(nJ;J')$ depend on the number k. Peaks exceeding 50% occur at $j'{=}b$ values in the cases of $k{=}b{>}0$ resonances. Visibly broader are the peaks in the $k{=}0$ cases. The state $j'{=}2$ is populated with probability comparable to $j'{=}0$ in transitions from $b{=}0$ resonances (the example in the upper left panel). Relatively large is also the population of $j'{=}0$ state in transitions from $b{=}2\,k{=}0$ resonances. A good example here is $(2\,0\,1\,8){\to}J'{=}9$ in the right middle panel [nearly 80 % of the integrated width $\Gamma^J_n(J')$ comes from the regions of E' above the $\varepsilon'_{v'\,j'=2}$ thresholds but only 45% of this width is made by the width $\Gamma^J_{n,j'=2}(J')$].

For an explanation of the observed correlations with the k-number one should look at some off-diagonal elements of the matrices $\mathbf{W}'^{J'p'}(R)$ that describe the product system in the CC-BF-diabatic representation (see Fig. A2)

$$\begin{aligned}\left[\mathbf{W}'^{J'p'}(R)\right]_{v'j'\lambda,\,v''j''\lambda''} &= \delta_{v',v''}\delta_{j',j''}\,(\delta_{\lambda',\lambda''}+\delta_{\lambda'',\,\lambda'\pm1})\tfrac{\hbar^2}{2\mu R^2}\,C^{J'j'}_{\lambda',\lambda''} \\ &+ \delta_{\lambda',\lambda''}\left[\delta_{v',v''}\delta_{j',j'}\,\varepsilon'_{v'j'}+V^{\lambda'}_{v'j',\,v''j''}(R)\right]; \qquad \text{(A14)}\end{aligned}$$

$C^{J'j'}_{\lambda',\lambda'}=J'(J'+1)+j'(j'+1)-2\lambda'^2$, $C^{J'j'}_{\lambda',\lambda'\pm1}$ denote the Coriolis coupling coefficients, and the terms

$$V^{\lambda'}_{v'j',\,v''j''}(R)=\sum_L\langle v'j'|V^X_L(r,R)|v''j''\rangle_r\,g^{\lambda'}_L(j',j'') \qquad \text{(A15)}$$

[with the factors $g^{\lambda'}_L(j',j'')$ defined in Eq. (A11)] include the relevant rotational couplings. Because of the big strength of the radial factors $\langle v'j'|V^X_L(r,R)|v'j''\rangle_r$ for L=2, see Fig. A1a, it suffices to inspect only the role of the couplings $V^{\lambda'}_{v'j',\,v'j'+2}$.

As indicated by the form of the dipole matrix elements in Eq. (A11), the radiative transitions from the initial state $(b\,k\,v_R\,J)$ populate at short R-distances the components of the X-channel continuum functions $\left[{}_{\rm BF}\mathbf{F}^{(+)\,J'p'}(E';R)\,\mathbf{U}^{J'p'}\right]_{v'j'\lambda';\,v'_oj'_ol'_o}$, with λ'=k and j'=b, see Eq. (A3). The composite symbol $v'_{\rm o}\,j'_o\,l'_o$ designates states in the open scattering channels at the energy E'. The question about the population of different rotational states of H_2^+ in the RCT transitions translates into the question about how many of the open states other than the ones with $j'_{\rm o}$=b can have significant j'=$b\,\lambda'$=k components in the short R-range. The strongest rotational coupling $V^0_{v'\,0,v'\,2}$ induces relatively large j'=λ'=0 components in the functions that pertain to the open channel $j'_{\rm o}$=2. Overlapping of these components with the functions of the initial b=k=0 states can thus produce the population of $j'_{\rm o}$=2 states of H_2^+ which is nearly as large as the population of $j'_{\rm o}$=0 states produced by the overlapping with the large j'=λ'=0 components of the $j'_{\rm o}$ functions. The same coupling $V^0_{v'\,0,v'\,2}$ can create significant j'=2 λ'=0 components in the functions of $j'_{\rm o}$=0 channels and be thereby responsible for the enlarged population of the ground rotational states of H_2^+ in the transitions from b=2 k=0 resonances. Obviously, the rotational couplings are not able to induce large $j'\,\lambda'$=j' components in the functions of the open channels $j'_{\rm o}$=j'−2 which could form large overlap at short distances with the functions of b=k=2, 4 resonances. This is why the respective distributions $P(j'_o)$ are so strongly peaked at j'_o=b. (Note that the symbol j' in the labels and in the caption of Fig. A14 actually has the meaning of j'_o used in the present comment).

(iii) the correlation of the populations $P_{v'}(nJ;J')$ with the quantum number J (or J').
The populations show maxima at v'=0 in all $J'\leq$9 cases. In the high J' cases (J'=17), the maximum position shifts to v'=1, the values at v'=0 evidently diminish, and the values at v'=2 and v'=3 slightly increase. Added to that should be the observation that in every case shown in the figure the area of the peak in the width function near the v'=0 threshold is smaller than the areas of the peaks associated with the v'=1, 2 thresholds. This means that the excited v' states are preferentially populated at short R-distances by radiative transitions from the A-channel. The increased population of v'=0 states at large R-separations observed in low J' cases should be thus attributed to the presence of the strong ro-vibrational couplings in the X-channel (see Fig. A1b). Tests calculations with the matrix elements $\langle v'j'|V^X_{L>0}(r,R)|v''\neq v'j''\rangle$ set to zero confirmed this explanation: the maximum population appeared at v'=1 also in the low J' cases. For high J''s, the matrix $\mathbf{W}'^{J'p'}(R)$ in the coupled equations becomes dominated by the terms $\frac{\hbar^2}{2\mu R^2}\,C^{J'j'}_{\lambda',\lambda''}$. The ro-vibrational couplings become relatively weak and incapable of changing the states of the H_2^+ ions at the stage of their departure from He atoms.

Fig. A15. RCT from quasi-bound states of $He^+-H_2(v=0)$

A15a. into $He+H_2^+(v')$ channels **A15b. into $He+H_2^+(j')$ channels**

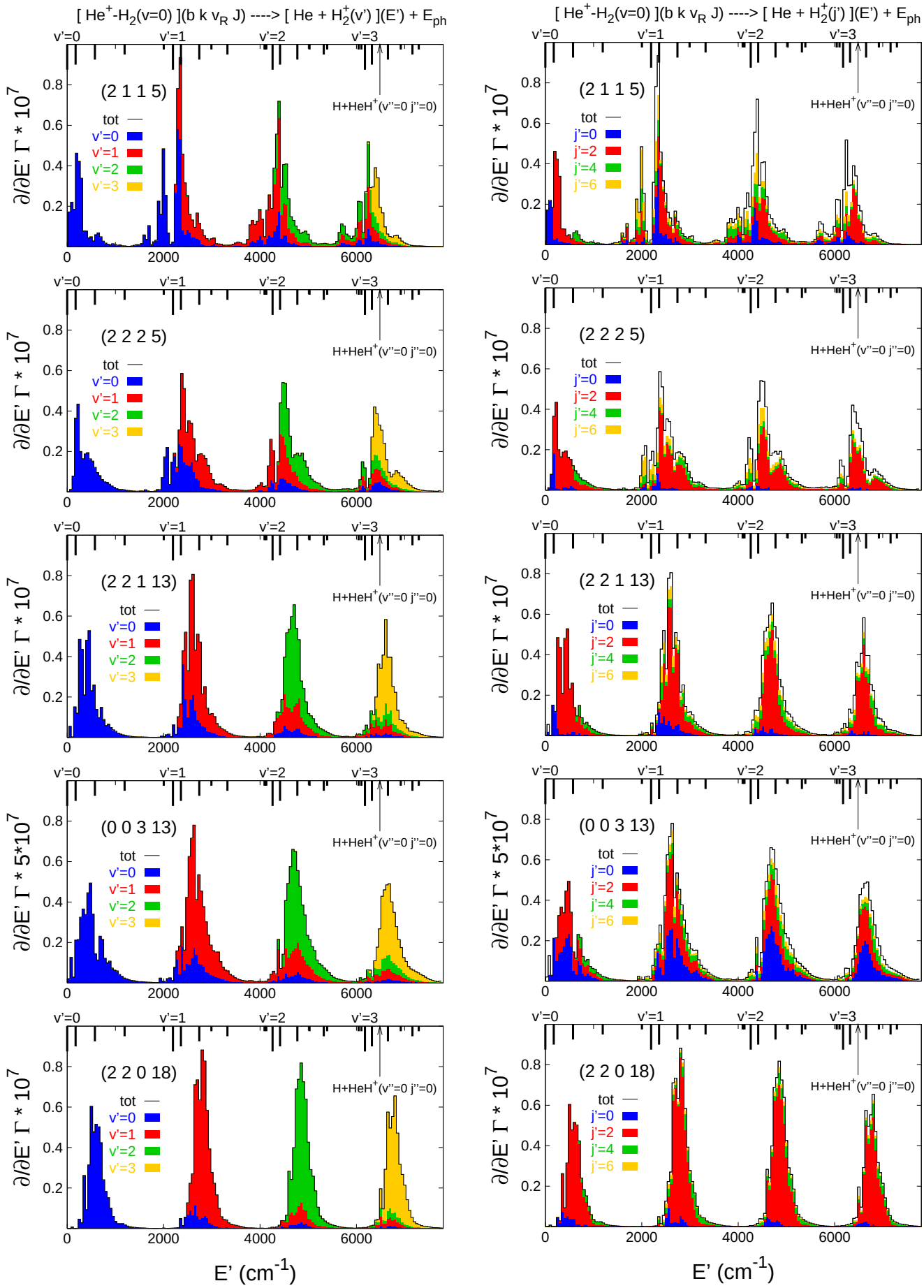

Fig. A15 continued

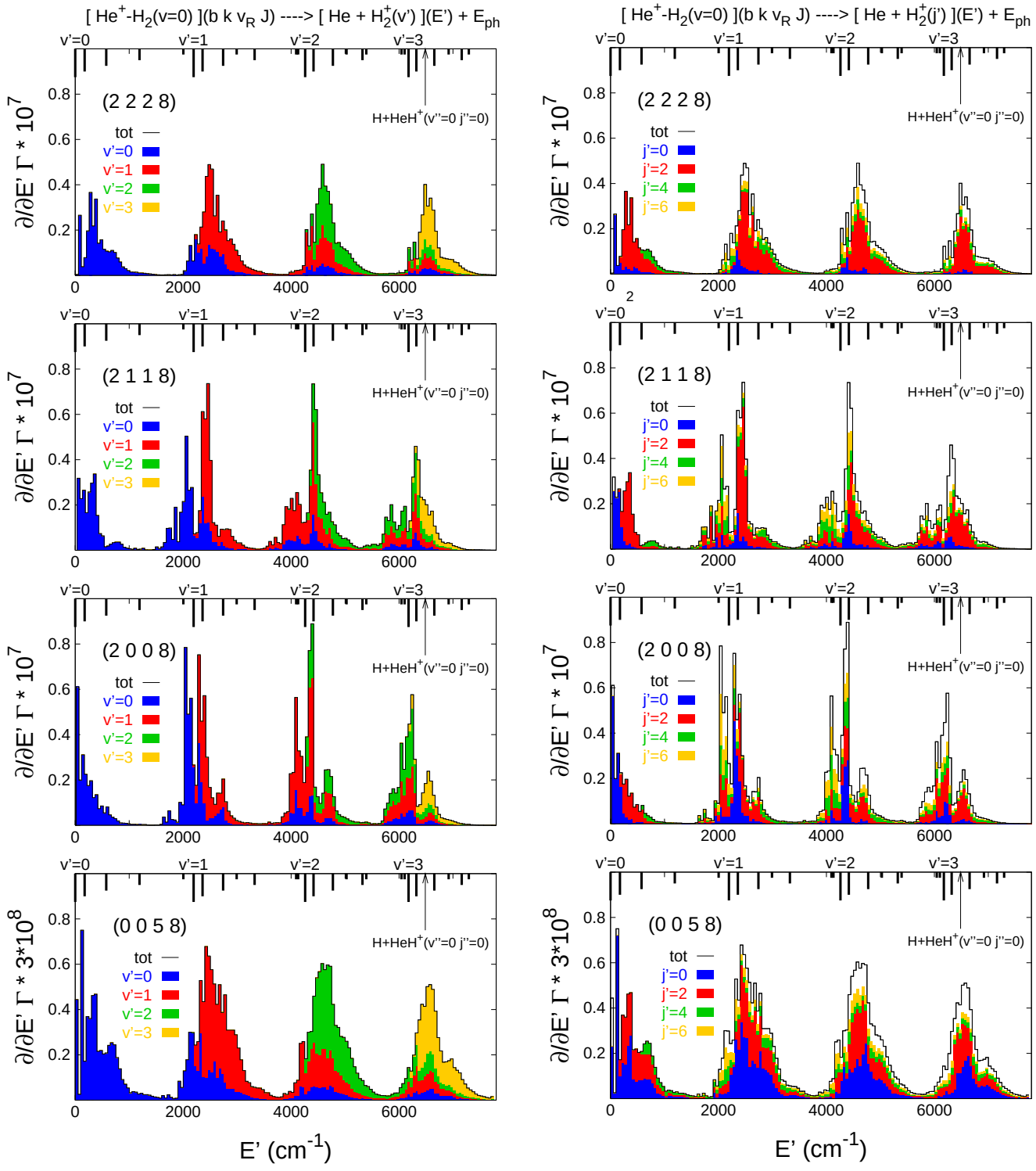

Plotted are the average values of $\frac{\partial}{\partial E'}\Gamma^{\rm RCT}(E')$ in the intervals $\Delta E'$=50 cm^{-1} and the resolutions into $\frac{\partial}{\partial E'}\Gamma^{\rm RCT}_{v'}$ and $\frac{\partial}{\partial E'}\Gamma^{\rm RCT}_{j'}$. Note that $\frac{\partial}{\partial E'}\Gamma^{\rm RCT}_{c'}(E')$=0 if c'=v', j' is a closed channel at E'. So, v' and j' have here the same meaning as the symbols v'_o and j'_o, respectively, used in Fig. A10c and in the comments to Fig. A14. The corresponding integrated widths $\Gamma^{\rm RCT}_{c'}$ are shown in Fig. A16 (as the ratios $\Gamma^{\rm RCT}_{c'}/\Gamma^{\rm RCT}$).

COMMENTS

(i) The propensity rules Δj=0 and Δk=0 show up here in that:

1. The positions of the peaks in the histograms for b=2 states correlate with positions of the $\varepsilon'_{v'\,j'=2}$ thresholds which is quite clear in all low J (=5, 8) cases. With increasing J the peaks shift towards higher energies E' which is (as explicitly demonstrated in Fig. A2b) a consequence of the enlarging centrifugal barriers in the product channel.

2. The partial widths $\frac{\partial}{\partial E'}\Gamma^{\rm RCT}_{j'}$ for transitions into j'=2 and j'=0 channels dominate in the resolutions of the widths $\frac{\partial}{\partial E'}\Gamma^{\rm RCT}(E')$ of b=2 and b=0 states, respectively.

3. The sizes of j'=2 and j'=0 components in the histograms for b=2 states clearly depend on the number k assigned to the states. The smallness of the widths $\frac{\partial}{\partial E'}\Gamma^{\rm RCT}_{j'=0}$ of k=2 states should be noted. The fact is in accord with the considerations presented in comment (ii.2) to Fig. A14.

(ii) The magnitude of the functions $\frac{\partial}{\partial E'}\Gamma^{\rm RCT}(E')$, and consequently the integrated widths $\Gamma^{\rm RCT}$, decrease with the growing number v_R of the states. [Note the change of the multiplying factors listed in the y-axis labels of the panels for states with v_R=3 and v_R=5]. This stems from the fact that the regions of the configuration space which are most likely occupied by the reactant system in states with higher and higher excited atom-diatom vibrations (see Fig. A5) become more and more distanced from the region where the $A{\rightarrow}X$ transition dipole function has appreciable values (see Fig. A1c).

(iii) The leftmost peaks are generally smaller than the peaks associated with higher v'-thresholds, especially with v'=1. This should be attributed to the relative magnitude of the matrix elements $\langle v{=}0|D_{L=0\,0}(R,r)|v'\rangle_r$ for v'=0 and v'>0 displayed in Fig. A1c.

(iv) The fact that the product states of energies E' in a range near the v'=1 threshold are the most strongly populated ones by the radiative transitions from the reactant channel at short R-distances does not necessarily mean the largest population of v'=1 state of the product ions H_2^+ at large separations from He atoms. This is demonstrated in the left panels of the figure by the resolutions of the width functions $\frac{\partial}{\partial E'}\Gamma^{\rm RCT}(E')$ into the partial widths $\frac{\partial}{\partial E'}\Gamma^{\rm RCT}_{v'}(E')$. The population of v'=0 state of the product ion (measured by the blue area) appears the largest in all cases shown except for those concerning high J states of the reactants. Parts of the blue areas within the v'=1 peaks of the width functions (and similarly parts of the red and green areas within the v'=2 and v'=3 peaks, respectively) are certainly due to inelastic $v'{\rightarrow}v'{-}1$ transitions in the X-channel mediated by the potential couplings which are displayed in Fig. A1b. For $J{\geq}13$, the state v'=1 becomes more populated than v'=0 (see Fig. A16). As already indicated in the comments to Fig. A14, this shift in the populations of vibrational states of H_2^+ is quite likely caused by the sizeable centrifugal potentials in the product channel (the potentials shield the region of small R-distances where the inelasticity occurs). In addition to the numerical tests mentioned in comment (iii) to Fig. A14, an argument in favor of this explanation can be found in the plots of the sojourn-time components $t^{J'}_{j'=2}(E', v'_o; \overline{R})$ in Fig. A10c. Namely, the comparison of v'_o=1 and v'_o=0 components in the insets of the panels for J'=8 and J'=17 shows that the two components have comparable sizes in the J'=8 case and the v'_o=1 component is clearly larger in the J'=17 case.

Fig. A16. Populations* of v' and j' states of H_2^+ in RCT reaction from various states of reactants

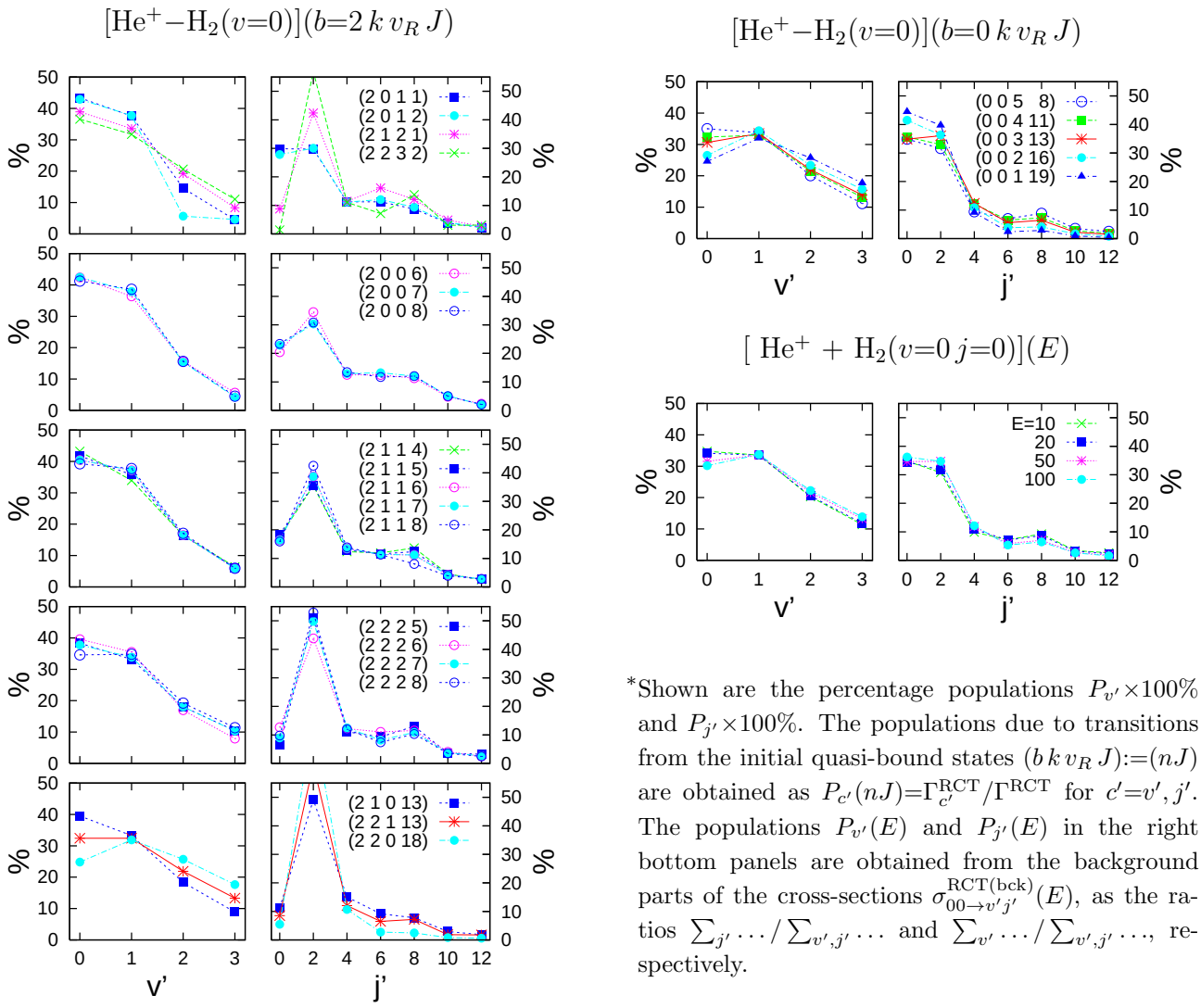

*Shown are the percentage populations $P_{v'}\times 100\%$ and $P_{j'}\times 100\%$. The populations due to transitions from the initial quasi-bound states $(b\,k\,v_R\,J)$:=(nJ) are obtained as $P_{c'}(nJ)=\Gamma^{\rm RCT}_{c'}/\Gamma^{\rm RCT}$ for $c'=v', j'$. The populations $P_{v'}(E)$ and $P_{j'}(E)$ in the right bottom panels are obtained from the background parts of the cross-sections $\sigma^{\rm RCT(bck)}_{00\to v'j'}(E)$, as the ratios $\sum_{j'}\ldots/\sum_{v',j'}\ldots$ and $\sum_{v'}\ldots/\sum_{v',j'}\ldots$, respectively.

COMMENTS

The plots summarize the features of the width functions $\frac{\partial}{\partial E'}\Gamma^{\rm RCT}_{c'}(E')$ for $c'=j', v'$ exhibited in the preceding figure and the information on the outcome of transitions from individual partial (J) continuum states presented in the next figure (A16a).

(i) The populations of v' states of the product ion show little sensitivity to the character of the initial state of the reactants, free or resonance state, shape $(b=0)$ or Feshbach $(b=2)$ resonance. Visible is only the correlation with the J number; when it grows, the excited v' states become more populated.

(ii) There is a clear distinction between the populations of j' states in the cases of the initial $b=2$ resonances on the one hand and the cases of the initial $b=0$ resonances and continuum states on the other hand. A (pronounced) peak at $j'=2$ appears in (almost) all $b=2$ cases. Together with the finding that $b=2$ resonances prevail in the dynamics of the RCT reaction in the subthermal range, this leads to the conclusion: the H_2^+ ions produced in the reaction are mostly in the excited rotational state $j'=2$.

Fig. A16a. Populations of v' and j' states of H_2^+ in RCT from continuum states of reactants

[$He^+ + H_2(v{=}0\, j{=}0)](E, J)$

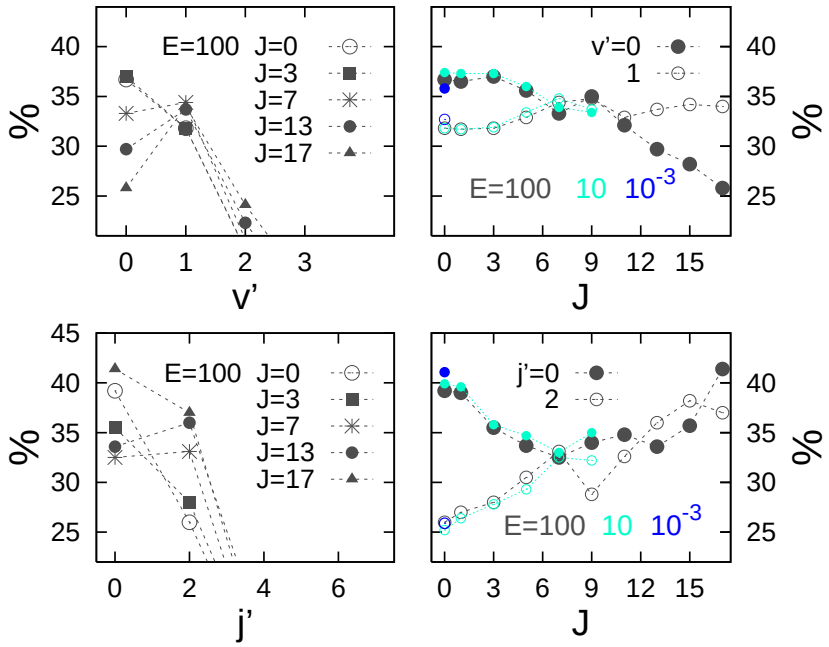

Populations $P_{v'}(E, J)$ (upper panels) and $P_{j'}(E, J)$ obtained from the partial cross-sections $\sigma^{\mathrm{RCT(bck)}}_{00\to v'j'}(E, J)$ as the ratios $\sum_{j'} \ldots / \sum_{v',j'} \ldots$ and $\sum_{v'} \ldots / \sum_{v',j'} \ldots$, respectively [the definition equivalent to Eq. (42) in the paper]. At E=100 cm^{-1}, the total cross-section $\sigma^{\mathrm{RCT(bck)}}_{00}(E)$ and its parts $\sigma^{\mathrm{RCT(bck)}}_{00\to c'}(E)$ for $c'{=}v', j'$ [used in the definition of the populations $P_{c'}(E)$ plotted in Fig. A16] are built of twenty partial cross-sections, for $J{=}0, \ldots, 19$, with maximal contribution made by $J{=}18$. At E=10 cm^{-1}, the $J{=}0{-}11$ partial cross-sections contribute, maximally the $J{=}9$ one. Only $J{=}0$ is important at $E{=}10^{-3}$ cm^{-1} [ultra-cold range].

COMMENTS

(i) The populations $P_{v'}(E, J)$ and $P_{j'}(E, J)$ are practically independent of the energy E in the entire range shown (near coincidence of black, green, and blue symbols in the right panels).

(ii) The J dependence of the populations $P_{v'=0}$ and $P_{v'=1}$ displayed in the upper right panel is analogous to that observed in transitions from quasi-bound state, see comment (iii) to Fig. A14.

(iii) The plots of the populations $P_{j'=0}$ and $P_{j'=2}$ as functions of J in the bottom right panel display a new fact. Namely, the $\Delta j{=}0$ propensity does occur in transitions from continuum states of the reactants, despite the counteracting inelastic transitions in the product channel, but only when the value of J is very low ($\leq$3). When J and $J'{=}J{\pm}1$, J grow, the depopulation of the $j'{=}0$ state by the inelastic transitions which stem from anisotropy of the potential V^X becomes enhanced (though not directly) by Coriolis couplings. For high J's, the shielding role of the centrifugal potentials comes into play [comments (iii) to Fig. A14 and (iv) to A15]. Only the largest $L{=}2$ anisotropy term of V^X remains important. Consequently, the higher j' states ($>$4) become much less involved in the dynamics. Instead of diminishing further, the value of $P_{j'=0}$ tends to grow with J above the $J{=}7$ value and stays comparable with $P_{j'=2}$.

ACCURACY ESTIMATIONS
of
THE STATE-TO-STATE DESCRIPTION

CONTINUED (SEE FIG. A0):

THE CC-BF-DIABATIC APPROACH
to
DYNAMICS ON THE X-STATE PES

Fig. A17. Coriolis-coupling-reducing (CCr) approximation*

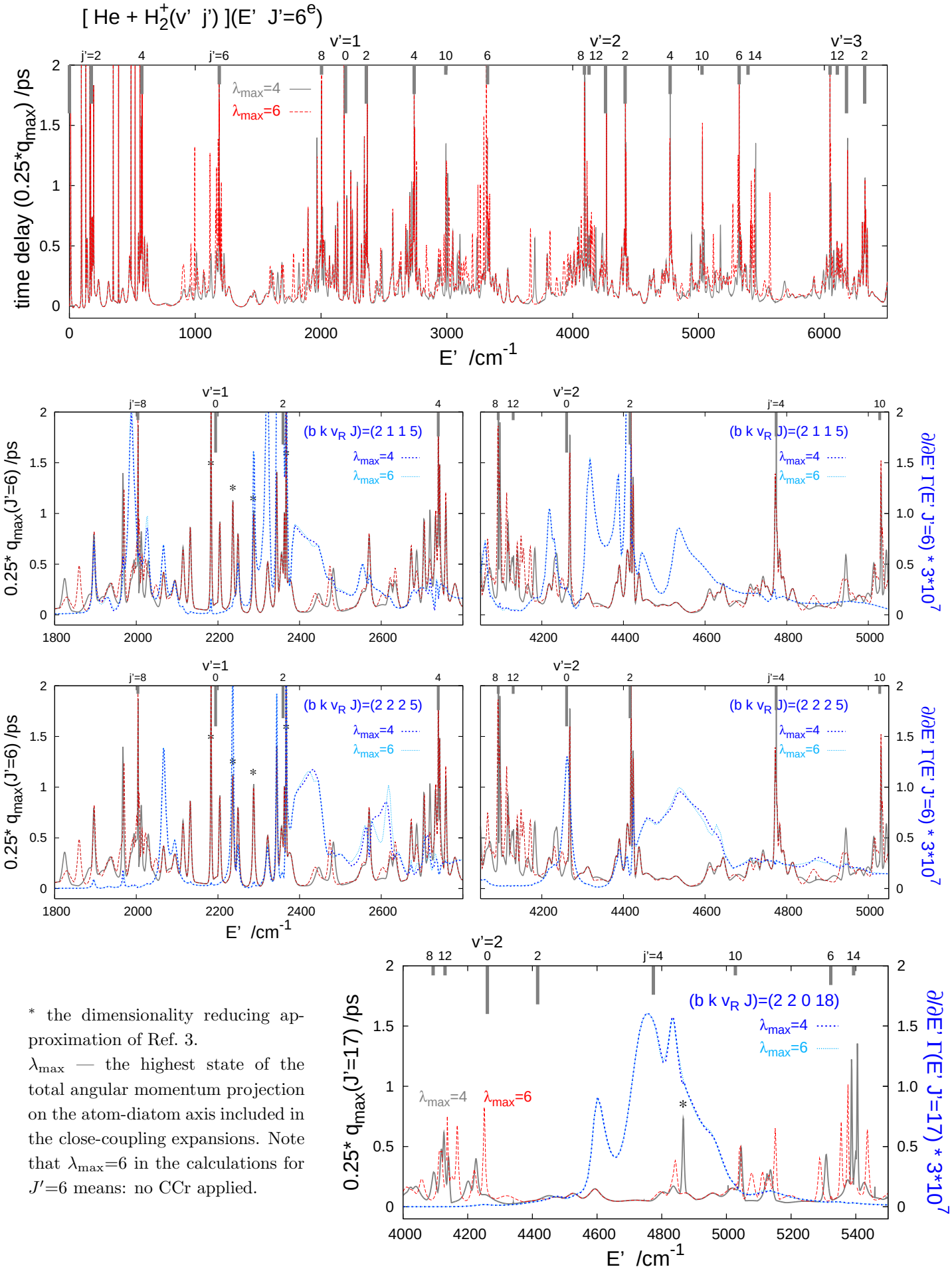

* the dimensionality reducing approximation of Ref. 3.

λ_{max} — the highest state of the total angular momentum projection on the atom-diatom axis included in the close-coupling expansions. Note that λ_{max}=6 in the calculations for J'=6 means: no CCr applied.

COMMENTS

(i) The CCr approximation was exploited in the calculations of the present paper in exactly the same way as described and exploited in the radiative association calculations of papers I and II. This means in particular that the restriction $\lambda'_{\rm max}$=4 was imposed in the construction of the CC-BF-diabatic representation of the partial scattering states of the He+H_2^+ system within the entire (large) energy range which is important in the RCT reaction (strictly, in the RCT_{nr} reaction, see Fig. A18). In the previous papers, the validity of the approximation in application to only low energy states ($E'\leq$300 cm^{-1}) was documented. A demonstration of how it works at much higher energies is thus requisite. Two aspects of the CCr approximation are illustrated in the figure:

1. the accuracy in the determination of resonances in the He+H_2^+ system (gray versus red lines),

2. the impact on the accuracy of the radiative widths $\frac{\partial}{\partial E'}\Gamma^{\rm RCT}$ of the low-energy quasi-bound states of the He^+-H_2 complex (blue versus light-blue lines).

(ii) As far as its original purpose is concerned, the CCr approximation works well; it does not affect the values, the positions, and the heights of the peaks in the time-delay functions $q^{J'}_{\rm max}(E')$ in the regions of energy E' near the j'=0 and j'=2 thresholds, where the states ($E'\,J'$) of the He+H_2^+ system have large admixtures of j'=0 or/and j'=2 components. These are the most essential components in the radiative transitions from b=2, 0 states of He^+-H_2, see Eq. (A11). Therefore the transition amplitudes could be expected to have little sensitivity to the removal from the final state functions of the λ' components that pertain to j'>4. Indeed, the determined widths $\Gamma^{\rm RCT}$ appear almost unaffected by this approximation.

(iii) The two lower left panels of the figure together with the sojourn-time maps in Fig. A11a provide yet another, probably the most explicit illustration of the Δk=0 propensity rule in the resonance–resonance transitions in the RCT reaction. Among the four resonances marked with the asterisks, there is a resonance of k'=0 character which is not populated by the transitions from the two ($b\,k$>0 $v_R\,J$) states of He^+-H_2 shown, a resonance of k'=1 character which is populated in the transitions from the k=1 state but not from the k=2 state, a k'=2 resonance populated from the k=2 state only, and a resonance of unspecified character (strong λ'-mixing) which is reached from both states.

(iv) The broad blue peaks appearing in the width functions $\frac{\partial}{\partial E'}\Gamma(E'\,J')$ above the j'=2 thresholds are due to resonance–free transitions. In the high J case shown in the lowest panel, concerning the (2 2 0 J=18) resonance, the peak appears considerably shifted from its respective (v'=2 j'=2) threshold. The shift is consistent with the position indicated in Fig. A2b (by the yellow arrow in the middle panel) as the result of 'reflection' of the resonance function from the effective potential $W^{\prime J'^e=17}_{v'=2\,j'=2\,\lambda'=2;\,v'\,j'\,\lambda'}(R)$.

Fig. A18. Convergence with the number of $(v'j')$ channels

Width functions

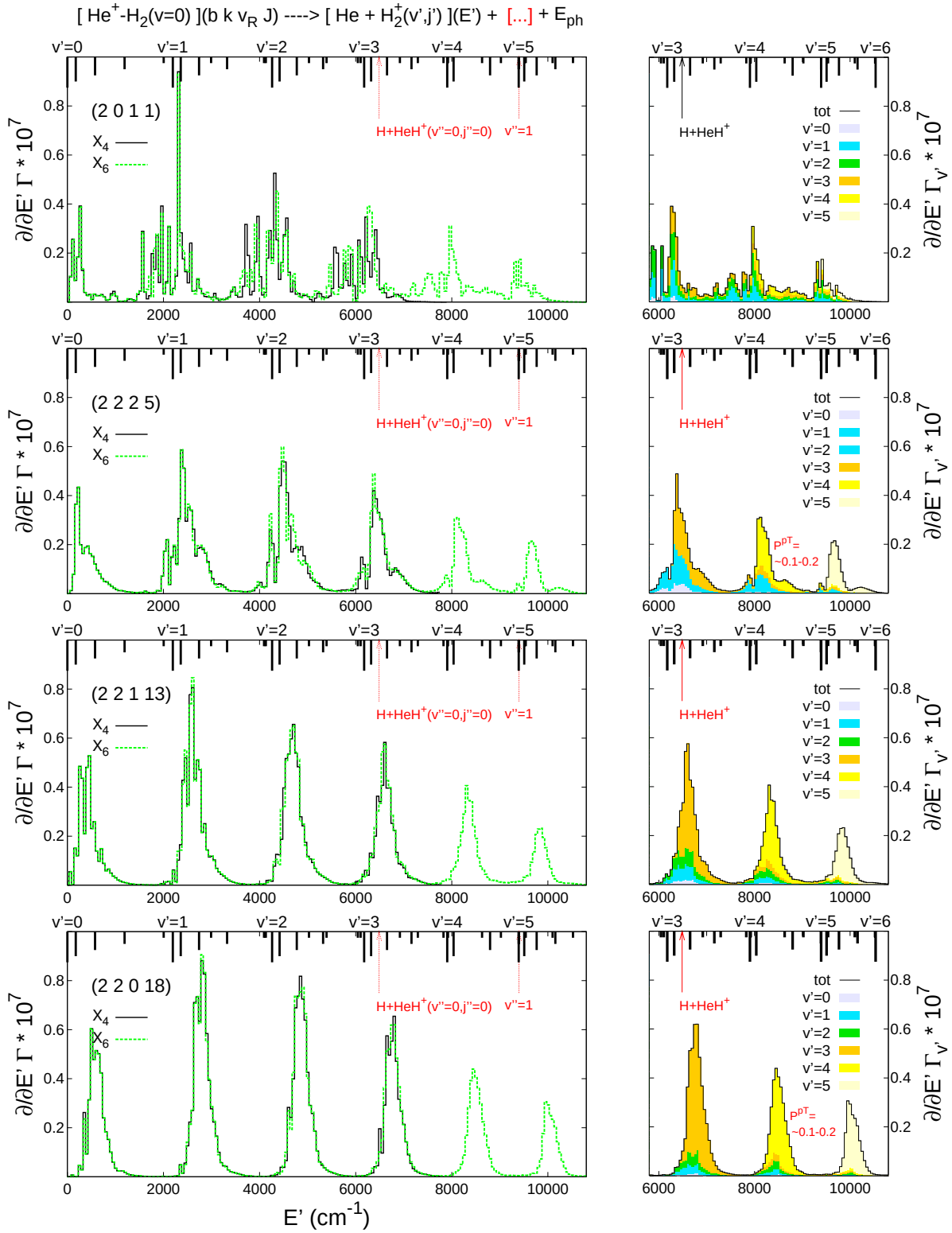

Left: Radiative widths of selected quasi-bound states in the A channel as functions of energy in the X channel. Comparison of results obtained with two bases to describe the continuum states in the X channel, both built of ro-vibrational (v', j') states of H_2^+. (The subscripts in the symbols of the bases indicate the number of included v' states).

Basis X_4 — includes 32 (v', j') functions, with v'=0−3 and j'=0, 2, 4, . . . , 14; leads to maximally N=136 coupled states (v', j', λ') since the CCr approximation limiting the values of λ' to $\lambda'_{\max}$=4 is applied.

Basis X_6 — includes 47 (v', j') functions, with v'=0−4, j'=0−14, and v'=5, j'=0−12, giving maximally N'=199 coupled states (v', j', λ').

Up to N'_o=86 states become open in the range of E'<6487 cm^{-1} (i.e. below the v''=0 j''=0 threshold).

Right: Resolutions $\frac{\partial}{\partial E'}\Gamma = \sum_{v'} \frac{\partial}{\partial E'}\Gamma_{v'}$ referred to in the estimation of the iRaT contribution at the end of this file.

COMMENTS

(i) The structures of the width functions $\frac{\partial}{\partial E'}\Gamma(E')$ [and the similar structures in the rates $\frac{\partial}{\partial E}\frac{\partial}{\partial E'}R(EJ;E'J')$ as functions of E'] testify to the fact that the RCT reaction proceeds via resonances and continuum states in the X channel which are grouped around the subsequent vibrational thresholds He+$H_2^+(v'\,j'{=}0)$.

The basis X_4, used in the main state-to-state calculations of the paper, can accurately describe the continuum and resonance states of the He+H_2^+ system which are associated with the three lowest thresholds, $v'{=}0{-}2$. The states around $v'{=}3$ threshold cannot be fully adequately represented by this (and any other) basis because the opening of the HeH^++H channel is disregarded by the X-state PES used in the calculations. Actually, the inspection of accuracy of the different parts of the potential V^X in Figs. A0b-d indicates that the positions and the overall sizes of the $v'{=}3$ peaks in the determined width (rate) functions are correct. These peaks effectively account for both allowed reaction paths the formation of the H_2^+ ions (RCT) and the indirect formation of the HeH^+ ions (iRaT). Obviously, accurate resolutions into the RCT and iRaT parts are not possible in the present study. Crude estimations of the iRaT contributions to the radiative widths and to other characteristics determined with the basis X_4 are given in Fig. A19.

(ii) The width functions obtained with the basis X_6 are an illustration to the widths $\Gamma^{\rm RCT..}$ listed in Table I of the paper. These widths are about 25−28% larger than the widths $\Gamma^{\rm RCT_{nr}}$. The sizes of the peaks near the $v'{=}4$ and $v'{=}5$ thresholds may be slightly affected (probably lowered) by the inaccuracy of the potential V^X. The main factors determining the sizes, i.e. the squared overlaps $|\langle v'|v{=}0\rangle|^2$, are demonstrated in Fig. A0d to depart slightly from the exact values for $v'{>}4$. Still, these peaks clearly show that convergence with respect to the covered range of the energy E' has not been achieved. Extension of the range up to ∼18000 cm^{-1}, by inclusion into the basis of v' states up to $v'{=}11$, would be necessary in order to account for ∼95% of fully convergent results, as revealed in the paper with the help of the $X_{N_{v'}}$-projected version of the optical potential model (Figs. 12 and 10b).

(iii) Fully convergent and accurate (i.e. insensitive to the large r-deficiency of the potential V^X shown in Fig. A0b) are the widths $\Gamma^{\rm RCT+RA+iRaT}$ yielded by the 'complete' version of the optical model. The peaks in the width functions associated with the $v'{\geq}4$ thresholds are implicitly summarized in the width difference $\Gamma^{\rm RCT+RA+iRaT}-\Gamma^{\rm RCT_{nr}}-\Gamma^{\rm RA}:=\Gamma^{\rm RCT+iRaT}_{\to X\setminus X_4}$. The contribution $\Gamma^{\rm iRaT}_{\to X\setminus X_4}$ is likely to be substantially larger than $\Gamma^{\rm iRaT}_{\to X_4}$ estimated in Fig. A19. See the considerations at the end of this file (A19a).

Fig. A18a. Convergence with the number of $(v'j')$ channels

Populations of v' and j' states of H_2^+

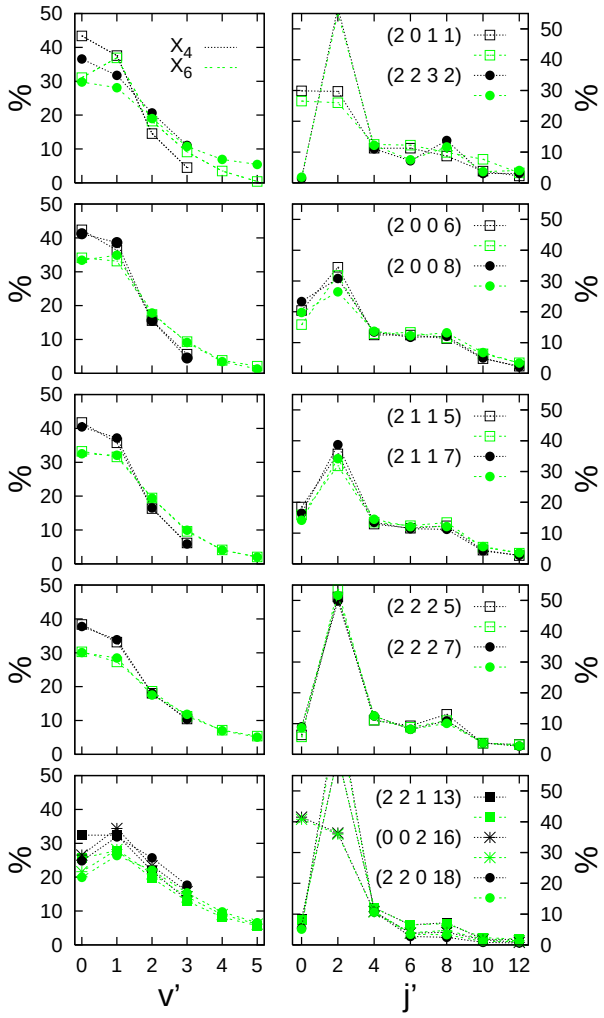

COMMENT

The comparison of green and black symbols in the figure suggests that all the transitions to the X-channel continuum states in the high energy region (E'>7800 cm^{-1}) that can possibly contribute to the RCT will not change qualitatively the populations of vibrational and rotational states of the product ion H_2^+ which result from transitions to the nonreactive range (obtained with the X_4 basis and discussed in Figs. A14-A16).

Fig. A19. Estimation of iRaT in transitions to $X_4(:=X_{\rm nr})$

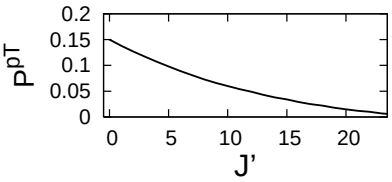

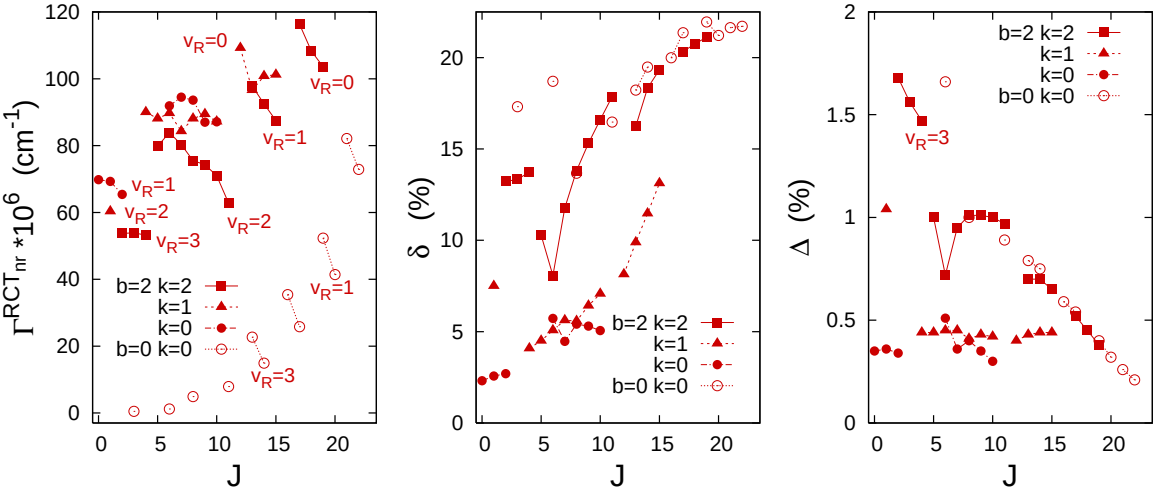

Transitions from resonances; $\mathcal{R}\longrightarrow X_4\,,\quad \mathcal{R}{:=}(b\,k\,v_R\,J)\,,\quad E'_{\rm max}(X_4){=}7800\ {\rm cm}^{-1}$

$$\Gamma^{\rm iRaT}_{\rightarrow X_4}\approx\sum_{J'=|J-1|}^{J+1}P^{\rm pT}(J')\int_{6487}^{7800}\frac{\partial}{\partial E'}\Gamma(J,J')\,dE'\approx P^{\rm pT}(J){\times}\delta(\mathcal{R}){\times}\Gamma^{\rm RCT_{nr}}:=\Delta(\mathcal{R}){\times}\Gamma^{\rm RCT_{nr}}$$

where $\Gamma^{\rm RCT_{nr}}{=}\sum_{J'}\int_0^{7800}\frac{\partial}{\partial E'}\Gamma(J,J')\,dE'$. The function $P^{\rm pT}(J')$ is based on inspection of the probabilities $P^{J'}_{v'}(E')$ of the pT reaction for $v'{=}3$, $J'{=}0{-}30$ and $E'{\in}[0.95,1.1]$ eV plotted in Fig. 5 of Ref. 16.

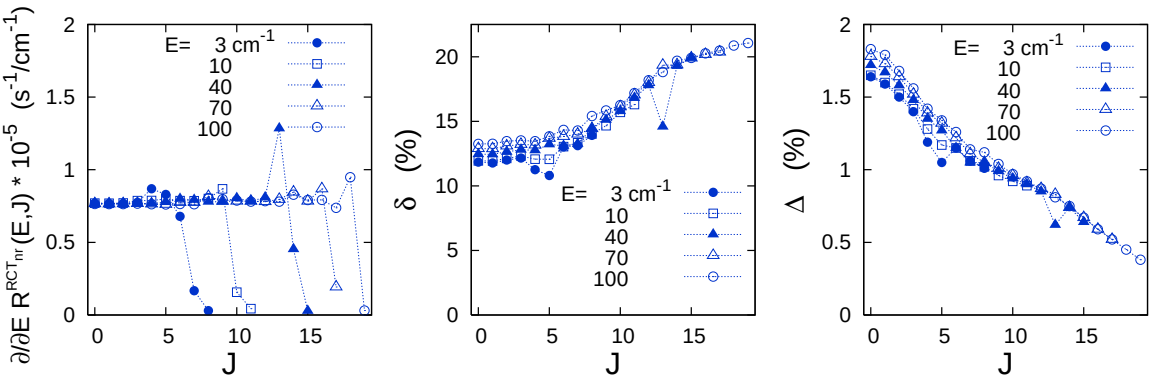

Transitions from continuum states; $(E,J)\longrightarrow X_4$

$$\frac{\partial}{\partial E}R^{\rm iRaT}_{\rightarrow X_4}(E,J)\approx\Delta(E,J){\times}\frac{\partial}{\partial E}R^{\rm RCT_{nr}(bck)}(E,J)$$

where $\Delta(E,J){=}P^{\rm pT}(J){\times}\delta(E,J)$ and $\delta{=}\int_{6487}^{7800}\frac{\partial^2}{\partial E\partial E'}R(EJ;E')\,dE'{\times}\big[\int_0^{7800}\ldots\big]^{-1}$.

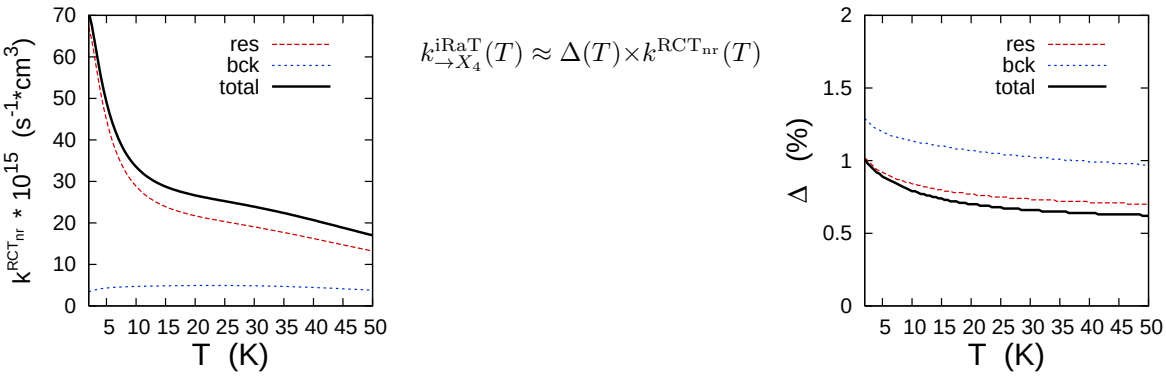

$$k^{\rm iRaT}_{\rightarrow X_4}(T)\approx\Delta(T){\times}k^{\rm RCT_{nr}}(T)$$

As a crude estimation of the iRaT contribution to the radiative width determined with the basis X_4, denoted in the paper as $\Gamma^{\mathrm{RCT_{nr}}}$, one may take the quantity

$$\Gamma^{\mathrm{iRaT}}_{\to X_4}=P^{\mathrm{pT}}\times\int\limits_{6487}^{7800}\frac{\partial}{\partial E'}\Gamma(E')\,dE'$$

in which P^{pT} denotes an average probability of the proton transfer (pT) reaction $\mathrm{He}+\mathrm{H}_2^+(v'=0-3)\longrightarrow \mathrm{HeH}^+ + \mathrm{H}$ in the energy range extending up to ∼0.15 eV above the reaction threshold ε''_{00}=6487 cm^{-1}. According to the information available in the literature, Refs. 14–17, the pT probabilities are quite small for v'=0 and v'=1 initial states (Figs. 2 and 5 in Ref. 16). The partial pT reaction probabilities $P^{J'}_{v'}(E')$ for v'=2, 3 and $E'-\varepsilon''_{00}\in[0, 0.15]$ eV are shown to be of the size of 0.1−0.2 when J' is low but rapidly decrease when J' gets larger. Since the plots of the width functions $\frac{\partial}{\partial E'}\Gamma_{v'}(E')$ in Fig. A15 show that the state v'=3 is mostly populated by the radiative transitions ending in the energy range $6487<E'\leq 7800$ cm^{-1}, the value of P^{pT} should roughly reflect the behavior of $P^{J'}_{v'=3}$. Thus, it seems reasonable to assume that this value depends on the number $J(=J', J'\pm 1)$ of the resonance and decreases from 0.15 to 0 when J' increases from 0 to 30 (as shown in the small panel next to the title of the present figure). The resulting 'true' values of the widths $\Gamma^{\mathrm{RCT_{nr}}}$ are

$$\Gamma^{\mathrm{RCT_{nr}}}_{\mathrm{true}}:=\Gamma^{\mathrm{RCT_{nr}}}-\Gamma^{\mathrm{iRaT}}_{\to X_4}=(1-\Delta)\Gamma^{\mathrm{RCT_{nr}}}\,,$$

where $\Delta=P^{\mathrm{pT}}(J)\times\delta$ and δ is the ratio of the integrals $\int\limits_{6487}^{7800}\frac{\partial}{\partial E'}\Gamma(E')\,dE'$ to $\int\limits_{0}^{7800}\ldots dE'$. The corrections Δ for all resonances listed in Table I of the paper, together with the uncorrected widths $\Gamma^{\mathrm{RCT_{nr}}}$ and the ratios δ, are shown in the the three panels of the upper row of the figure. The corrections are small, below 1% in the majority of cases.

In the same fashion one may correct the values of the rates $\frac{\partial}{\partial E}R^{\mathrm{RCT_{nr}(bck)}}(E, J)$ which characterize transitions from continuum states of the reactants to the product states of energy $E'\in[0, 7800]$ cm^{-1}. The corrected functions

$$\frac{\partial}{\partial E}R^{\mathrm{RCT_{nr}(bck)}}_{\mathrm{true}}(E, J):=\Big[\frac{\partial}{\partial E}R^{\mathrm{RCT_{nr}(bck)}}-\frac{\partial}{\partial E}R^{\mathrm{iRaT}}_{\to X_4}\Big](E, J)$$

for J=0−19 and E<150 cm^{-1} are smaller maximally by ∼2%. The respective corrections $\Delta(E, J)$ are shown in the middle right panel.

Obviously, the impact of the above corrections on the temperature averaged rate of the $\mathrm{RCT_{nr}}$ reaction is similarly small (≃1%), as demonstrated in the bottom panels of Fig. A19.

Thus, one may conclude:

the approximate treatment of the $\mathrm{He}+\mathrm{H}_2^+$ continuum states in the vicinity of the threshold for the proton transfer reaction does not practically affect the results presented in the paper with the label $\mathrm{RCT_{nr}}$: they describe the 'true' RCT (formation of the H_2^+ ions) though not exhaustively.

Fig. A19a. Estimation of iRaT
in transitions to $X\backslash X_4$

The reasoning is analogous to that presented above for transitions to the X_4 subspace. In cases of the initial quasi-bound states,

$$\Gamma^{\rm iRaT}_{\rightarrow X\backslash X_4} \approx P^{\rm pT}_{X_6\backslash X_4} \int\limits_{E'_{\rm max}(X_4)}^{E'_{\rm max}(X_6)} \frac{\partial}{\partial E'}\Gamma\, dE' \quad + \quad P^{\rm pT}_{X\backslash X_6} \int\limits_{E'_{\rm max}(X_6)}^{E'_{\rm max}} \frac{\partial}{\partial E'}\Gamma\, dE'$$

$$:= \left[P^{\rm pT}_{X_6\backslash X_4}\ \delta_{X_6\backslash X_4} + P^{\rm pT}_{X\backslash X_6}\ \delta_{X\backslash X_6}\right] \times \int\limits_{E'_{\rm max}(X_4)}^{E'_{\rm max}} \frac{\partial}{\partial E'}\Gamma\, dE'$$

$$:= \overline{P^{\rm pT}} \times \Gamma^{\rm RCT+iRaT}_{\rightarrow X\backslash X_4}, \qquad \text{(A16)}$$

where $P^{\rm pT}_{X_6\backslash X_4}$ denotes an average probability for the pT reaction at total energies in the $X_6\backslash X_4$ subspace, i.e. at $E'\in[7800, 11000]$ cm^{-1}, the symbol $P^{\rm pT}_{X\backslash X_6}$ denotes the probability at $11000<E'<\sim 21400$ cm^{-1}, the δ's are defined by equality with the second line, and $\overline{P^{\rm pT}}$ — with the third line. $\Gamma^{\rm RCT+iRaT}_{\rightarrow X\backslash X_4}$ denotes the integral over the energy in the entire 'reactive' (let us call it so) subspace $X\backslash X_4$. It is obtained from the quantities determined in the paper as

$$\Gamma^{\rm RCT+iRaT}_{\rightarrow X\backslash X_4} \approx \Gamma^{\rm trad} - \Gamma^{\rm RCT_{nr}} - \Gamma^{\rm RA} \approx \Gamma^{\rm trad} - \Gamma_{(\rightarrow X_4)}\,. \qquad \text{(A17)}$$

The widths $\Gamma^{\rm trad}$ and $\Gamma_{(\rightarrow X_4)}$ come from the optical potential model; the integrals over the respective ranges of E' are only implicitly (approximately) represented by them; hence the symbol '$\approx$' is used here. Similarly, the relative populations of the parts $X_6\backslash X_4$ and $X\backslash X_6$ of the 'reactive' subspace by the radiative transitions from the A channel can be inferred from Fig. 12 of the paper as

$$\delta_{X_6\backslash X_4} \approx \frac{\Gamma_{(\rightarrow X_6)} - \Gamma_{(\rightarrow X_4)}}{\Gamma^{\rm trad} - \Gamma_{(\rightarrow X_4)}} \approx 0.5 \qquad \text{and} \qquad \delta_{X\backslash X_6} \approx 0.5\,. \qquad \text{(A18)}$$

For an estimation of the probability $P^{\rm pT}_{X_6\backslash X_4}$, it is requisite to summarize first what can be inferred from the resolutions of the width functions shown in the right panels of Fig. A18, namely:
(i) the energy E' which is transferred to the system H_2^++He in the radiative transitions from the A channel goes preferably into vibrational excitation of H_2^+. [The peaks above the v'=4 and v'=5 thresholds are mostly yellow and light yellow, respectively].
(ii) the translational (collision) energy in the product system is relatively small, no larger than one half of the distance between the v'=5 and v'=4 thresholds, i.e. $0<E'-\varepsilon'_{v'}<\sim 0.1$ eV.
This helps in properly adapting the available information on the pT reaction. The recent quantum scattering study of the reaction $H_2^+(v'=2,4,6,j'=1)$+He$\longrightarrow$HeH$^+$+H, reported in Ref. 17, is particularly useful here. From the plots of the partial reaction probabilities $P^{J'}_{v'}$ for v'=4 and J'=0−20 as functions of collision energy in the range 0.1 – 2.5 eV presented in Fig. 4 of that paper one may infer that $P^{\rm pT}_{X_6\backslash X_4}$ should be $\sim$0.1−0.2.

Transitions to the subspace $X\backslash X_6$ are not explicitly investigated in this study. However, it seems likely that properties of the product states yielded by these transitions are similar to those found for $A{\rightarrow}X_6\backslash X_4$. This means that the H_2^+ subunit appears in higher and higher excited v' state so that the energy of translational motion of He relative to H_2^+ does not substantially exceed 0.1–0.2 eV. If this is true the probability $P^{\rm pT}_{X\backslash X_6}$ may be taken as $\sim$0.2$-$0.4. The supporting literature information is:
(i) the plots of the partial reaction probabilities $P^{J'}_{v'}$ for v'=6 and J'=0$-$20 as function of collision energy given in Fig. 5 in Ref. 17, and
(ii) the plots of the cross-section for the pT reaction as function of v' given in Fig. 3 of Ref. 18; they suggest that the partial probabilities $P^{J'}_{v'}$ do not grow further with increasing v' when v' becomes larger than 6$-$7.
Taken together, the above estimations give

$$\overline{P^{\rm pT}} \approx 0.15{-}0.3\,. \tag{A19}$$

Practically nothing would change if the estimations were made for transitions from continuum states. It suffices to recall the fact stated in the discussion of Fig. 12: the population of states in $X\backslash X_4$ expressed in terms of the rates $\frac{\partial}{\partial E}R^{\rm bck}_{(\rightarrow X_{N'_v})}(E,J)$ and $\frac{\partial}{\partial E}R^{\rm trad(bck)}(E,J)$ are practically indistinguishable from those expressed in terms of the widths $\Gamma_{(\rightarrow X_{N'_v})}$ and $\Gamma^{\rm trad}$. One would get

$$\frac{\partial}{\partial E}R^{\rm iRaT}_{\rightarrow X\backslash X_4}(E,J) \approx \overline{P^{\rm pT}}\times\Big[\frac{\partial}{\partial E}R^{\rm trad(bck)}-\frac{\partial}{\partial E}R^{\rm bck}_{(\rightarrow X_4)}\Big](E,J)\,. \tag{A20}$$

Therefore, upon summation/averaging over all possible initial states one gets the simple approximations to the cross-section $\sigma^{\rm iRaT}$ and to the rate constant $k^{\rm iRaT}$ that are used in the paper, in Eq. (49), in footnotes to Tables II and III, and in Fig. 13 and 17. A graphical presentation is given in the figure below.

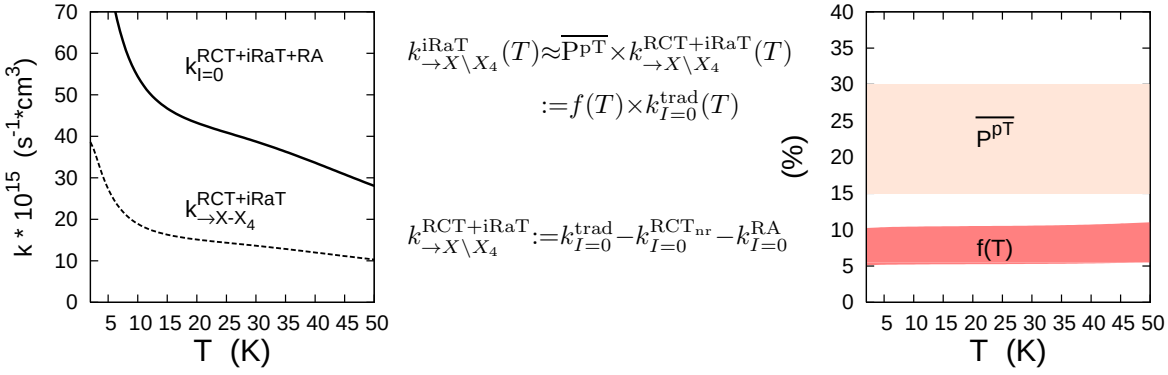

Note that the estimate $k^{\sim{\rm iRaT}}(T)$ shown in Fig. 17 of the paper is obtained as $k^{\sim{\rm iRaT}}(T){\approx}f(T){\times}k^{\rm trad}_{I=0+1}(T)$, i.e. the additional assumption is made that the I=1 contribution to the iRaT is also the fraction f of the rate function $k^{\rm trad}_{I=1}$. Adequacy of this extrapolation is almost inconsequential since in the conditions of thermal equilibrium the values of $k^{\rm trad}_{I=1}(T)$ at temperatures T<40 K are small.

When the radiative reactions take place in gas mixtures of the He^+ ions with 'normal' hydrogen, the respective rate constant functions ${}_{\rm n}k^{\rm rad}(T)$ for rad=RCT+RA+iRaT and rad=RA are determined, in ∼67% and ∼50%, respectively, in collisions with ortho-hydrogen, see Table BXI in Ref. 21. [Precisely, the statement is true for temperatures above 10 K].
Since individual transition rates from states of the He^++$H_2(I{=}1)$ system to the X-channel continuum states are not calculated in the present study, information on the shapes of the width functions $(\frac{\partial}{\partial E'}\Gamma)$ of $b{=}3,1$ resonances, on the populations of the particular subspaces X_4, X_6, $X\backslash X_4$, etc, is not explicitly available. However, these characteristics should not differ much from those for He^++$H_2(I{=}0)$; peaks in the emission spectra will be shifted by about 160–170 cm^{-1} towards higher energies since they will correlate with the $v', j'{=}3$ rather than with the $v', j'{=}2$ limits (the $\Delta j{=}0$ propensity rule). Since somewhat larger parts of the $v'{=}3$ peaks will extend above the threshold for the pT reaction the role of the iRaT in transitions to the X_4 subspace may be a little bigger than (∼1%) estimated above. Still, for the entire iRaT contribution to the RCT+iRaT+RA reaction in the mixtures with 'normal' hydrogen, the estimate ${}_{\rm n}k^{\sim{\rm iRaT}}(T){\approx}f(T){\times}{}_{\rm n}k^{\rm trad}(T)$ should remain reasonable. The corresponding estimate of the RCT contribution — ${}_{\rm n}k^{\sim{\rm RCT}}(T){\approx}[1{-}f(T)]\,{}_{\rm n}k^{\rm trad}(T){-}\,{}_{\rm n}k^{\rm RA}(T)$ — gives: ${}_{\rm n}k^{\sim{\rm RCT}}/{}_{\rm n}k^{\rm trad}{\approx}$87–93%. Obviously, ${}_{\rm n}k^{\rm trad}(T)$ is the function shown in the last column of Table III and in Fig. 16b with solid violet line. Values of ${}_{\rm n}k^{\rm RA}(T)$ can be found in Table BXI (Ref. 21). The estimate ${}_{\rm n}k^{\sim{\rm RCT}}(T)$ for $T{\in}[10,40]$ K is shown (by the light violet strip) in Fig. 16b of the paper and mentioned in the comparison with the experiment data of Ref. 19.

The X-channel continuum states are populated by radiative transitions from the A channel in the configuration region lying deeply inside the $He{+}H_2^+$ valley of the potential $V^X(r,R,\theta)$ (see Fig. A0). This concerns also the states populated in the 'reactive' energy range. The probability $\overline{P^{\rm pT}}$ used here in the estimation of the iRaT may be viewed as giving the fraction of all these high energy states which would extend, loosely speaking, into the HeH^++ H valley if the artificial wall did not forbid that. So, $\overline{P^{\rm pT}}{\approx}$0.15–0.30 approximately reflects the size of one of the final-state interaction effects which is the proton transfer forming the HeH^+ ions. Of interest is a comparison with other effects of the same kind — the inelastic transitions following the radiative $A{\rightarrow}X_4$ transitions and changing the populations of v' and j' states of the H_2^+ ion. The size of these changes is exhibited in Fig. B5e of Ref. 21: the populations of $v'{=}0$ and $v'{=}3$ state enlarge and diminish, respectively, by factors close to 2, the populations of $v'{=}2$ and $j'{=}2$ states diminish by ∼70% and ∼60%, respectively. Concluding, in the entire $A{\rightarrow}X$ radiative reaction scheme the inelastic transitions in the X channel play by far a bigger role than the rearrangement transitions.

Obviously, all the estimations of the iRaT contributions presented here and in Fig. A19 are rather crude. Functions from rearrangement scattering calculations (using an appropriate surface V^X) for continuum states of the He^++H_2 system in the energy range extending up to the $v'{=}11$ threshold (and perhaps even higher) would be necessary to verify these estimations, i.e. to evaluate separately the widths $\Gamma^{\rm RCT}$ and $\Gamma^{\rm iRaT}$, the rates $\frac{\partial}{\partial E}R^{\rm RCT(bck)}(E,J)$ and $\frac{\partial}{\partial E}R^{\rm iRaT(bck)}(E,J)$ and, eventually, the rate constants $k^{\rm RCT}(T)$ and $k^{\rm iRaT}(T)$. An attractive idea to exploit in such calculations, if they will appear necessary in the future, is the optical potential for chemical reactions proposed by Neuhauser and Baer[20]. It would require only a minor modification of the Hamiltonian H^X used in the present state-to-state calculations.

[1] W. P. Kraemer, V.Špirko, and O. Bludsky, Chem. Phys. **276**, 225 (2002).
[2] M. Šindelka, V. Špirko, and W. P. Kraemer, Theor. Chem. Acc. **110**, 170 (2003).
[3] F. Mrugała, V. Špirko, and W. P. Kraemer, J. Chem. Phys. **118**, 10547 (2003) (paper I).
[4] L. Wolniewicz, J. Chem. Phys. **99**, 1851 (1993).
[5] L. Wolniewicz and T. Orlikowski, Mol. Phys. **74**, 103 (1991).
[6] R. E. Moss, Mol. Phys. **80**, 1541 (1993).
[7] F. Mrugała and W. P. Kraemer, J. Chem. Phys. **122**, 224321 (2005) (paper II).
[8] M. S. Child, *Semiclassical Mechanics with Molecular Applications*, (Claredon, 1991), chaps. 5, 9.
[9] R. Schinke, *Photodissociation Dynamics*, (Cambridge, 1993), chap. 4.
[10] F. T. Smith, Phys. Rev. **118**, 349 (1960).
[11] W. Jaworski and D. M. Wardlaw, Phys. Rev. **A45**, 292 (1992).
[12] F. Mrugała and R. Moszynski, J. Chem. Phys. **109**, 10823 (1998).
[13] F. Mrugała, Int. Rev. Phys. Chem. **12**, 1 (1993).
[14] J. D. Kress, R. B. Walker, and E. F. Hayes, J. Chem. Phys. **93**, 8085 (1990).
[15] B. Lepetit and J. M. Launay, J. Chem. Phys. **95**, 5159 (1991).
[16] B. Maiti, C. Kalyanaraman, A. N. Panda, and N. Sathyamurthy, J. Chem. Phys. **117**, 9719 (2002).
[17] Tian-Shu Chu, Rui-Feng Lu, Ke-Li Han, X.-N Tang, H.-F. Xu, and C. Y. Ng, J. Chem. Phys. **122**, 244322 (2005).
[18] X. N. Tang, H. Xu, T. Zhang, Y. Hou, C. Chang, C. Y. Ng, Y. Chiu, R. A. Dressler, and D. J. Levandier, J. Chem. Phys. **122**, 164301 (2005).
[19] M.M. Schauer, S.R. Jefferts, S.E. Barlow, and G.H. Dunn, J. Chem. Phys. **91**, 4593 (1989).
[20] D. Neuhauser and M. Baer, J. Chem. Phys. **92**, 3419 (1990); D. Neuhauser, M. Baer, and D. J. Kouri, J. Chem. Phys. **93**, 2499 (1990).
[21] part B of this material: file Hep+HH_RCT_optpot.pdf.

B. SUPPLEMENTARY MATERIAL — PART B

OPTICAL POTENTIAL MODELS
of
RADIATIVE REACTIONS
in
$He^+ + H_2$

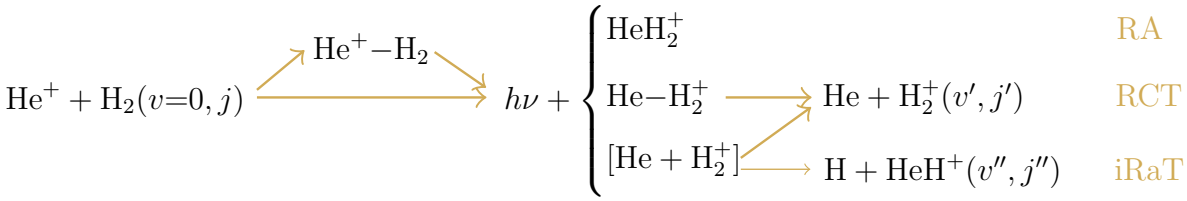

Fig. B1. $He^+ + H_2 \longrightarrow \{He + H_2^+ , HeH_2^+ , HeH^+ + H\}$

Calculations within the 1-dimensional optical potential model*

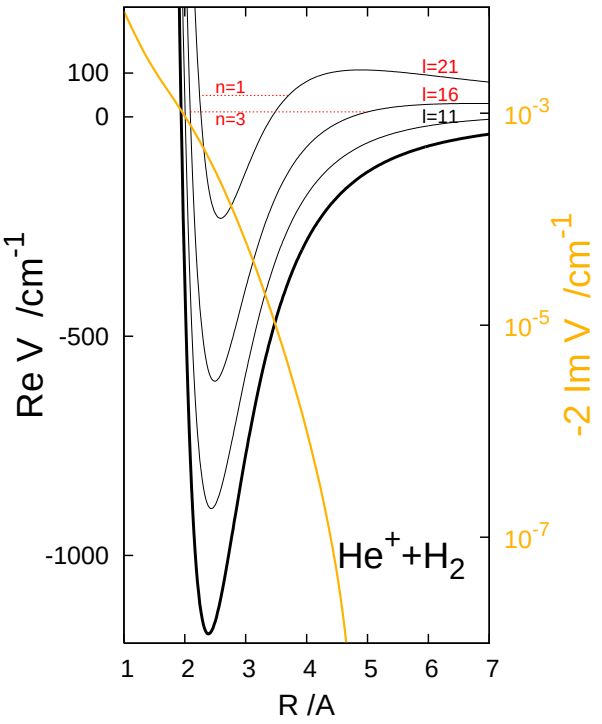

Fig. B1a. The complex potential used:

$$\mathrm{Re}\, V(R) = V^A(r{=}\overline{r}, R, \theta{=}\overline{\theta}) - V^A(r{=}\overline{r}, R{\to}\infty, \theta{=}\overline{\theta})$$

with $\overline{r}$=0.748 Å and $\overline{\theta}=\frac{\pi}{2}$ (the values at the minimum of the A-state PES),

$$-2\,\mathrm{Im}\, V(R) = \tfrac{4}{3\hbar^3 c^3}\,[\Delta V(R)]^3\,[d(R)]^2$$

$$\text{with} \quad \Delta V(R) = V^A(\overline{r}, R, \overline{\theta}) - V^X(\overline{r}, R, \overline{\theta})\,,$$

$\Delta V(R{\to}\infty)$=73476 cm^{-1}, and $d(R){=}d_Z^{\mathrm{BF}}(r{=}\overline{r}, R, \theta{=}\overline{\theta})$ (see Fig. A1 in Ref. 1).

The thin black lines represent the effective potentials $\mathrm{Re}\, V(R){+}\frac{\hbar^2}{2\mu}\frac{l(l+1)}{R^2}$ for selected values of the angular momentum quantum number l. Shown are also the energies of two resonances supported by the effective potentials. n denotes the vibrational quantum number.

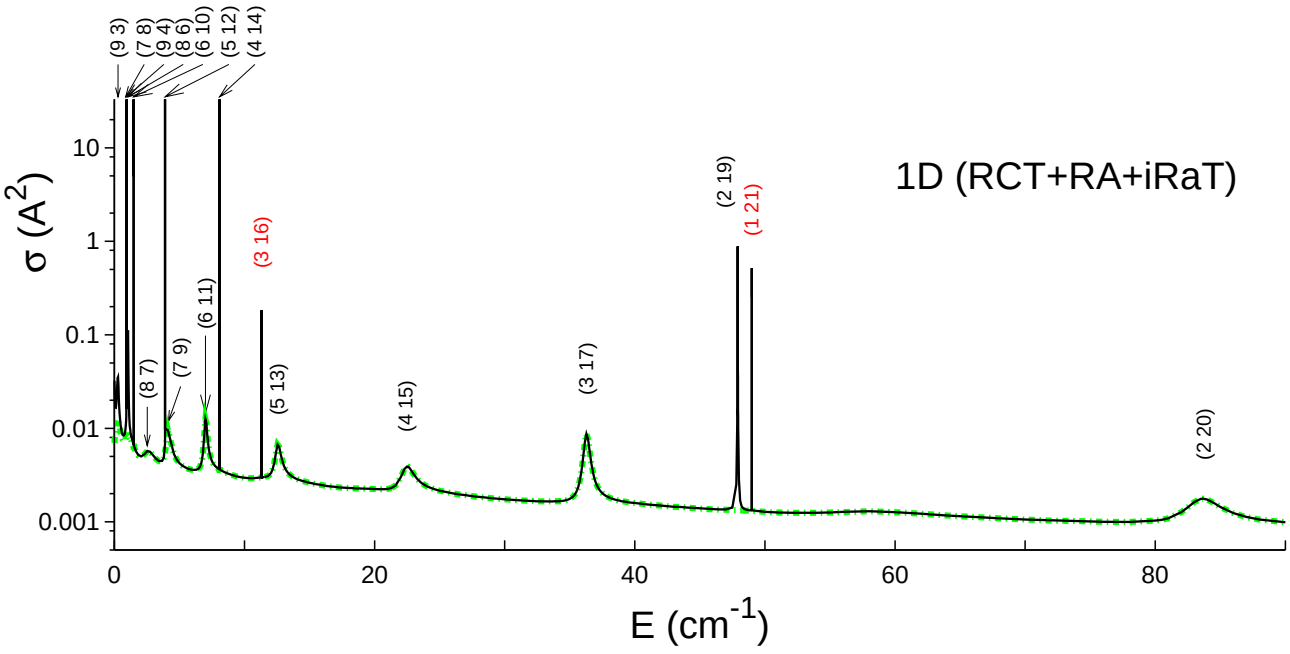

Fig. B1b. The total radiative cross-section $\sigma^{\mathrm{RCT+iRaT+RA}}{:=}\sigma^{\mathrm{rad}}$ as function of collision energy E. The line on the green background represents the contribution $\sigma^{\mathrm{rad}}_{\mathrm{bck}}(E){=}\frac{\hbar^2\pi}{2\mu E}\sum_{l=0}^{23}(2l{+}1)P_l(E)$ with $P_l{=}1{-}|S_l|^2$ and S_l denoting the partial S-matrix in the optical potential. The black peaks represent sharp resonance contributions evaluated using the approximation $P_l^{\mathrm{res}}(E){\approx}\Gamma^{\mathrm{rad}}\Gamma[(E{-}E^{\mathrm{res}})^2{+}(\Gamma^{\mathrm{tot}}/2)^2]^{-1}$ with $\Gamma^{\mathrm{tot}}{=}\Gamma^{\mathrm{rad}}{+}\Gamma$ (the parameters E^{res}, Γ, and Γ^{rad} of these resonances are listed in Table BI). The labels of the peaks are the numbers $(n\,l)$.

* Refs. 2-3

TABLE BI: The 1-dim. optical potential model of radiative reactions in $He^+ + H_2$ collisions. Parameters of selected resonances, the positions E^{res}, the tunneling widths Γ, and the radiative widths Γ^{rad} (all in cm^{-1}). Also shown are the probabilities of radiative decay of the resonances, $P_l^{res}:=1-|S_l(E=E^{res})|^2$, where S_l is the partial scattering matrix in the optical potential. In the last two columns are the values of P^{res} and Γ^{rad} from calculations using the distorted-wave (DW) approximation to account for the imaginary part of the optical potential.

n	l	$E^{res\,a}$	Γ^a	$\Gamma^{rad\,b}$	$\Gamma^{tot\,c}$	P^{res}	P^{res}_{DW}	$\Gamma^{rad\ d}_{DW}$
7	8	0.936	2.58 (−5)	5.9 (−6)	3.17 (−5)	0.611	0.929 (+0)	6.0 (−6)
8	6	1.045	4.95 (−2)	2.6 (−6)	4.95 (−2)	0.209 (−3)	0.211 (−3)	2.6 (−6)
5	12	3.892	1.80 (−6)	13.2 (−6)	1.50 (−5)	0.420	0.296 (+2)	13.3 (−6)
4	14	8.089	3.09 (−6)	22.7 (−6)	2.58 (−5)	0.420	0.295 (+2)	22.8 (−6)
3	16	11.316	1.63 (−8)	41.5 (−6)	4.16 (−5)	0.157 (−2)	0.102 (+5)	41.5 (−6)
2	18	8.145	1.84(−16)	71.5 (−6)	7.08 (−5)	0.105(−10)		70.9 (−6)
2	19	47.907	7.68 (−3)	53.4 (−6)	7.73 (−3)	0.274 (−1)	0.278 (−1)	53.4 (−6)
1	21	48.989	3.50 (−7)	93.2 (−6)	9.36 (−5)	0.149 (−1)	0.107 (+4)	93.3 (−6)
1	22	104.414	6.79 (−2)	71.2 (−6)	6.80 (−2)	0.418 (−2)	0.419 (−2)	71.2 (−6)
0	23	33.632	2.11(−16)	142.4 (−6)	1.43 (−4)	0.593(−11)		142.6 (−6)

[a]Determined by applying the Siegert quantization method[4] to the radial equation for l-th partial wave with the imaginary part of the potential set to zero.

[b]Determined as $P^{res}\times(\Gamma^{tot})^2/(4\Gamma)$. The background of the Lorentzian profile in $P(E)=1-|S(E)|^2$ is negligible if the resonance is sharp, $\Gamma\ll 0.1$ cm^{-1}.

[c]Obtained by applying the Siegert quantization method to the radial equations with the full complex potential.

[d]Obtained as $P^{res}_{DW}\times\Gamma/4$ or, in the $(n\,l)=(2\,18)$, $(0\,23)$ cases, as $-2\int|\Psi^B(R)|^2\,\mathrm{Im}\,V(R)\,dR$, where $\Psi^B(R)$ denotes a bound state function approximating the scattering function in the potential $\mathrm{Re}\,V(R)$ at $E\approx E^{res}$.

COMMENTS

(i) In the exact (Siegert quantization) calculations within the optical potential approach, the two ways of decay of resonances, by tunneling and by spontaneous emission, are treated on the same footing. One can thus explicitly see how small the role of the resonances termed sharp (having very small dissociative width Γ) in the RCT and RA reactions is. The probabilities P_l^{res} inform about that; multiplied by $(2l+1)$ they determine the heights of the peaks in the cross-section $\sigma^{rad}(E)$. In the cases of the two sharpest resonances in the table, $(n\,l)=(2\,18)$ and $(0\,23)$, the probabilities P^{res} are seen to be practically zero. These resonances do not produce any peak in the cross-section in Fig. B1b despite the fact that their radiative widths are larger than the radiative widths of most other resonances.

(ii) The numbers in the last two columns also serve a pedagogical purpose. They show that correct values of the radiative widths of the sharp resonances are obtainable when the imaginary part of the potential is treated as perturbation (DW approximation), but the values of P^{res}_{DW} are too big by a factor very close to $(\Gamma^{tot}/\Gamma)^2$. Thus, it is possible to restore the correct values of the probabilities P^{res} without leaving the DW approximation by means of the simple operation

$$P_{DW}(E\approx E^{res})\approx\Gamma^{rad}_{DW}\Gamma[(E-E^{res})^2+(\Gamma/2)^2]^{-1}\longrightarrow\ldots\Gamma^{rad}_{DW}+\Gamma\ldots$$

which essentially is what was termed "the implicit optical potential approach" in Ref. 5. As described in Sec. IIE of the paper, this approach was rather extensively exploited in the calculations of the study, to account for sharp resonances in the initial as well as in the final channel of the RCT reaction.

An illustration of the sharp resonance problem within the 3D optical potential model is given in Table BV.

Fig. B2. $He^+ + H_2 \longrightarrow \{He + H_2^+ , HeH_2^+ , HeH^+ + H\}$

THE 3-DIMENSIONAL OPTICAL POTENTIAL MODEL

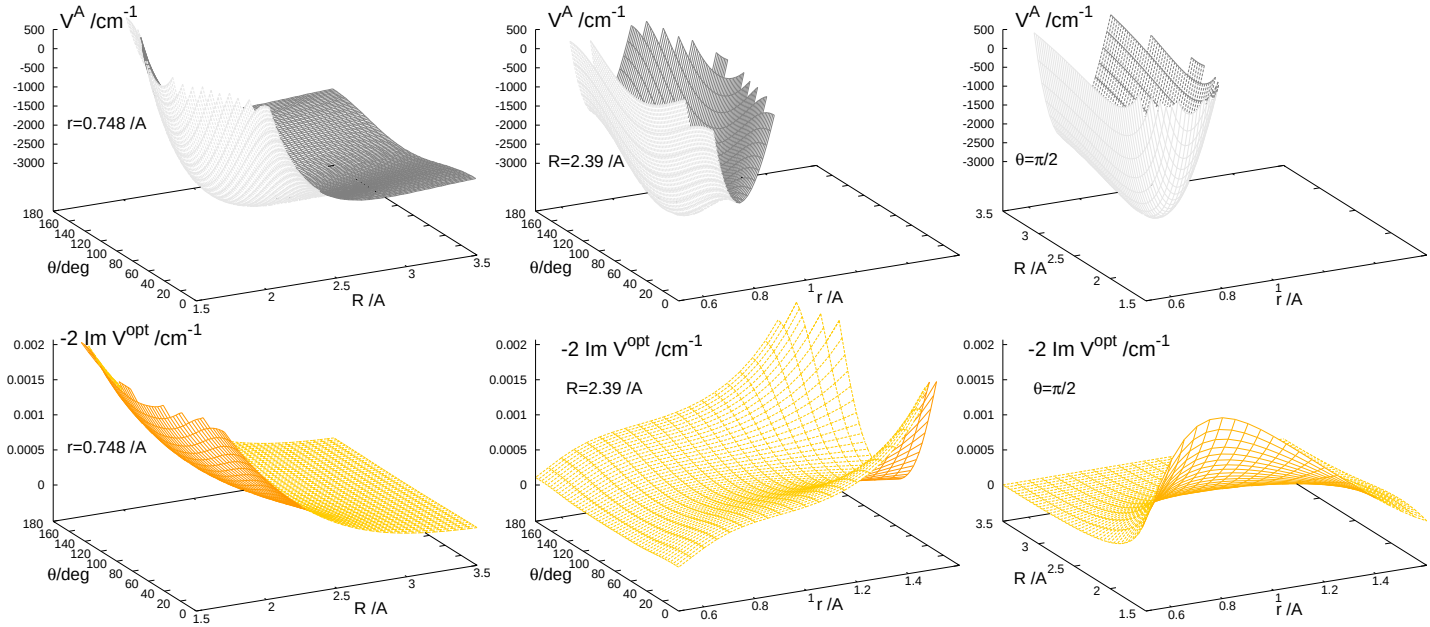

Fig. B2a. The PES of the first excited electronic state of HeH_2^+. The three cuts of the surface are at the values $r{=}r^A_{\rm min}$, $R{=}R^A_{\rm min}$, and $\theta{=}\theta^A_{\rm min}$, respectively, which are the coordinates of the minimum of $V^A(r,R,\theta)$ at -3351 cm^{-1}. Zero of energy is at the $He^+ + H_2(v{=}0,j{=}0)$ threshold, which is 2177 cm^{-1} above the limit $V^A(r,R{\to}\infty)$.
Lower: The optical potential surface for $A{\to}X$ transitions: $-2\,{\rm Im}V^{\rm opt}(r,R,\theta) = \frac{4}{3c^3\hbar^3}\,\mathbf{d}^2(r,R,\theta)\,[\Delta V(r,R,\theta)]^3$, where $\mathbf{d}^2{=}[d_Z^{\rm BF}(A{\to}X)]^2$ and $\Delta V(r,R,\theta){=}V^A(r,R,\theta){-}V^A(r,R{\to}\infty){-}V^X(r,R,\theta){+}\Delta E$ with $\Delta E{=}74507$ cm^{-1}.

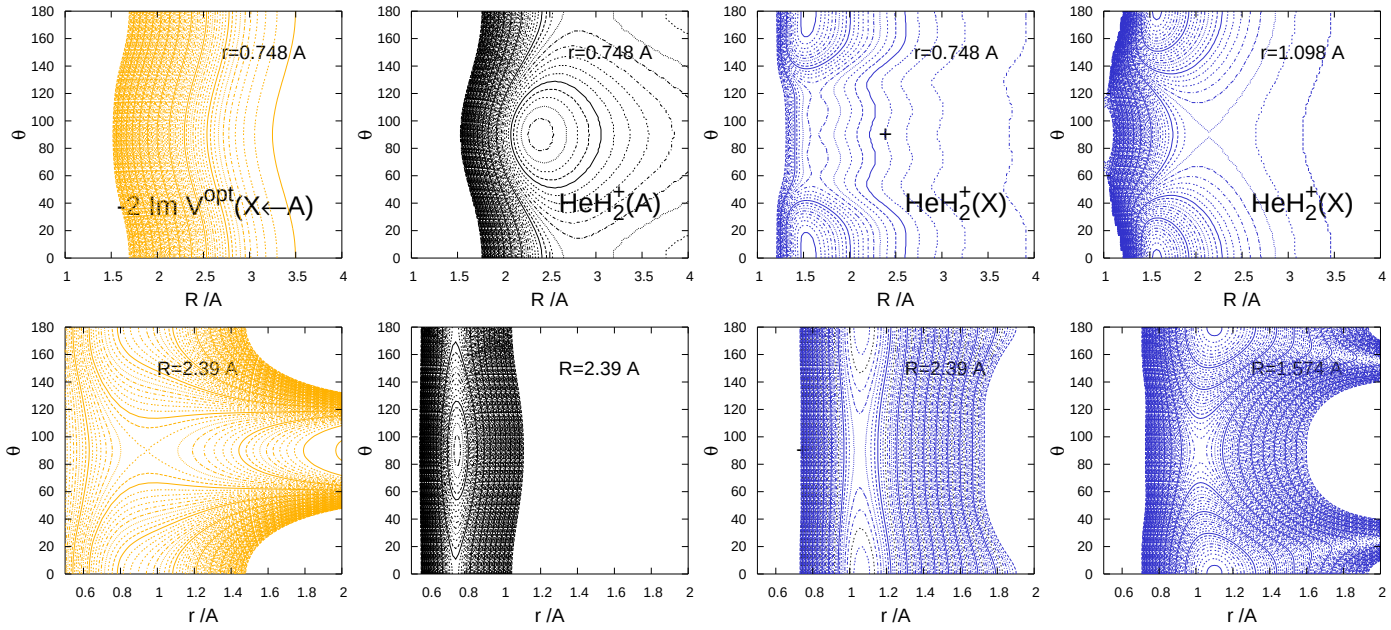

Fig. B2b. Contour plots of 2D cuts of the surface $-2{\rm Im}V^{\rm opt}(r,R,\theta)$ at $r{=}r^A_{\rm min}$ and $R{=}R^A_{\rm min}$ compared to cuts of the surfaces $V^A(r,R,\theta)$ and $V^X(r,R,\theta)$. The contours of $-2{\rm Im}V^{\rm opt}$ are drawn in step of $2{\times}10^{-5}$ cm^{-1} and cover the range of $0-2{\times}10^{-3}$ cm^{-1}. The contours of V^A and V^X are drawn in step of 100 cm^{-1} and cover the ranges $[-3300, 6000]$ (zero at $He^+ + H_2(v{=}0,j{=}0)$) and $[-3800, 6000]$ cm^{-1} (zero at $He + H_2^+(v{=}0,j{=}0)$), respectively. The crosses in the third column cuts show the endpoint of vertical transition from the minimum of V^A, called the Franck-Condon point, $E'_{\rm FC}{=}5300$ cm^{-1}. The cuts in the rightmost column are through the minimum of $V^X(r,R,\theta)$.

The anisotropy of the surface $-2{\rm Im}V^{\rm opt}(r,R,\theta)$ at r's near $r^A_{\rm min}$ is rather weak. The R dependence of the surface is in turn strong and has a substantial impact on rates of the $A{\to}X$ transitions from low energy states in the A channel (see Fig. B5).

Fig. B3. 1D versus 3D optical potential* and state-to-state approaches

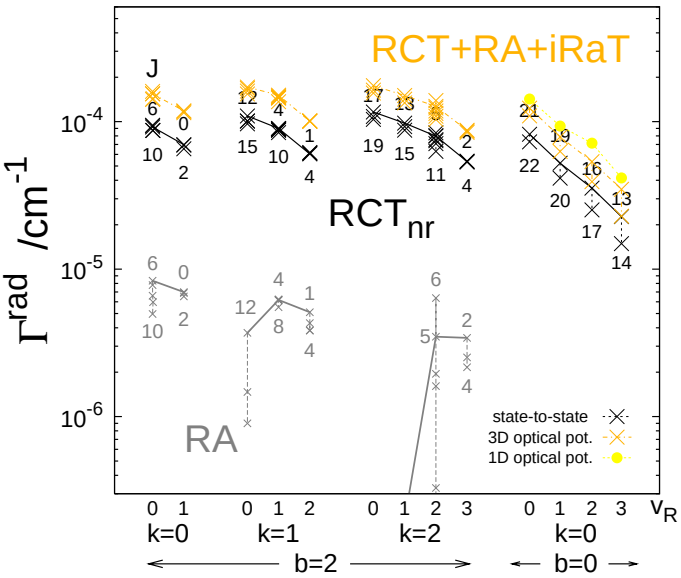

Fig. B3a. Radiative widths of resonances.
The gray, black and dark-yellow crosses represent, respectively, the widths $\Gamma^{\rm RA}$, $\Gamma^{\rm RCT_{nr}}$, and $\Gamma^{\rm RCT+RA+iRaT}$ of the $(b\,k\,v_R\,J)$ resonances listed in Table I of the paper. The yellow dots are the widths $\Gamma^{\rm rad}$ of the $(n\,l)$=(0 23), (1 21), (2 18), (3 16) resonances from Table BI. They are drawn at the v_R=n positions.

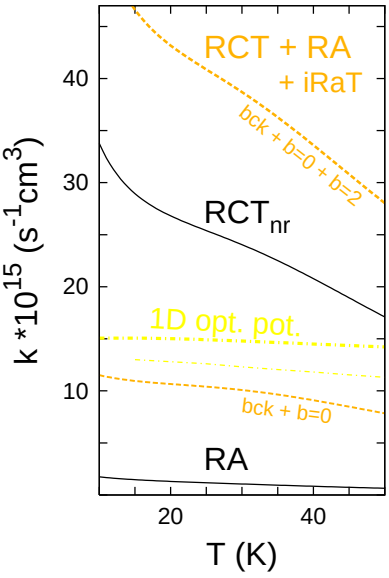

Fig. B3b. Rate constant as function of temperature.
The unlabeled yellow line represents results of the 1D optical potential model of Ref. 3. 1D models do not account for b=2 resonance contribution. 'bck' stands for 'background'.

COMMENT

The resonances in the 1D complex potential are counterparts of the shape resonances $(b$=0 k=0 $v_R\,J)$ of the He^++H_2 system on its full-dimensional PES. Obviously, one-to-one correspondence could not be established with the present simple construction of $\mathrm{Re}\,V(R)$. Nevertheless, it is worth noting that the magnitude of the radiative widths of the resonances in the 1D complex potential, the growth of these widths with decreasing vibrational number n, agree reasonably with the magnitude and the dependence on the number v_R of the radiative widths of shape resonances in the 'exact' potential. Perhaps somewhat better agreement would be achieved if the potentials $\mathrm{Re}\,V(R)$ and $-2\mathrm{Im}\,V(R)$ were constructed as averages of the 3D surfaces $V^A(r,R,\theta)$ and ${}^{\rm opt}V(r,R,\theta)$ in the basis function $\Phi^{JM}_{vj\lambda}(\mathbf{r},\widehat{\mathbf{R}})$ with J=M=j=λ=0 and v=0 [see Sec. III and IV in the paper]. However, irrespective of details of construction of the complex potential the 1D model of dynamics is evidently insufficient for simulation of radiative quenching in systems like He^++H_2 in which Feshbach resonances play a dominant role.

*the complete version described in Sec. IVA of the paper

A SIMPLIFIED $X_{Nv'}$ PROJECTED VERSION of THE 3-DIMENSIONAL OPTICAL POTENTIAL MODEL

In the version of the model used in the calculations of the paper to simulate the radiative transitions from ($[E, E+dE]Jp=1$, $v=0\, j=0$) states in the A channel to the subspace $X_{N_{v'}}$ of the X channel, the skew-hermitian matrices $-\frac{\imath}{2}\,{}^{\rm opt}_{X_{N'_v}}\mathbf{W}^{J^e}(R)$ that were added to the Hamiltonian matrices $\mathbf{H}^{J^e}(R)=-\frac{\hbar^2}{2\mu}\mathbf{I}\frac{d^2}{dR^2}+\mathbf{W}^{J^e}(R)$ had the following form

$$ {}^{\rm opt}_{X_{N_{v'}}}\mathbf{W}^{J^e}(R) \;=\; \sum_{J'=|J-1|}^{J+1} {}^{\rm opt}_{X_{N_{v'}}}\mathbf{W}^{J'p'\,J^e}(R)\,, \tag{B1} $$

$$ \text{where}\qquad {}^{\rm opt}_{X_{N_{v'}}}\mathbf{W}^{J'p'\,J^e}(R) \;=\; \frac{4}{3c^3\hbar^3}\left[\mathbf{d}^{J'p'\,J^e}(R)\right]^\dagger\left[\Delta\mathbf{V}^{J'p'}(R)\right]^3\mathbf{d}^{J'p'\,J^e}(R)\,, \tag{B2} $$

$$ \Delta\mathbf{V}^{J'p'}(R) \;=\; \Delta E\mathbf{I} + \langle\Phi'^{\,J'M'p'}|V^A|\Phi'^{\,J'M'p'}\rangle_{\mathbf{r},\hat{\mathbf{R}}} - \mathbf{W}'^{\,J'p'}(R)\,; \tag{B3} $$

(all symbols are defined in the paper). As documented in Tables I and III and in Figs. 10 and 12 of the paper, this version of the $X_{N_{v'}}$ projected optical potential is capable of reproducing the state-to-state results for the rate function $k^{\rm RCT_{nr}+RA}(T)$ at $T\in[2-50]$ K and for the radiative widths $\Gamma^{\rm RCT_{nr}+RA}$ of all involved A channel resonances (Feshbach and shape) with percentage deviations rarely exceeding 1%. Additional tests of the various terms of ${}^{\rm opt}_{X_{N_{v'}}}\mathbf{W}(R)^{J'p'\,J^e}$ defined in (B2)-(B3) revealed that the off-diagonal elements of $\Delta\mathbf{V}^{J'p'}(R)$ had practically no impact on the results and could safely be omitted. The J' dependent centrifugal terms in diag $\Delta\mathbf{V}^{J'p'}(R)$ play a role when $J'>10$. If these terms were omitted the widths of $J=20-22$ resonances would be larger by 3-4% and thereby less consistent with the state-to-state values. It is possible, however, to remove the J' dependency from ${}^{\rm opt}_{X_{N_{v'}}}\mathbf{W}^{J'p'\,J^e}(R)$ by using in the centrifugal terms of the factor $\Delta\mathbf{V}^{J'p'}(R)$ a common effective value of J' for all three $J\to J'=J\pm1, J$ transitions, eg. $J'^{\rm eff}=J-1$. Then, exploiting the factorization

$$ \left[\mathbf{d}^{J'p'\,J^e}(R)\right]_{v'j'\lambda';vj\lambda} \;=\; C(J1J',\lambda0\lambda')\,\left[\mathbf{d}'^{\lambda}(R)\right]_{v'j';vj}\,, \tag{B4} $$

$$ \text{where}\qquad \left[\mathbf{d}'^{\lambda}(R)\right]_{v'j';vj} \;=\; \sum_L{}'\langle v'j'|D_L(r,R)|vj\rangle_r\; g_L^\lambda(j',j)\,, \tag{B5} $$

one can perform the sum in Eq. (B1) analytically and obtain

$$ \left[{}^{\rm opt}_{X_{N_{v'}}}\tilde{\mathbf{W}}^J(R)\right]_{\tilde{v}\tilde{j}\tilde{\lambda};vj\lambda} \;=\; \frac{4}{3c^3\hbar^3}\,\delta_{\tilde{\lambda},\lambda}\sum_{v'=0}^{N_{v'}-1}\sum_{j'=0}^{j'_{\rm max}}\left[\mathbf{d}'^{\lambda}(R)\right]_{v'j';\tilde{v}\tilde{j}}\left[\Delta V^{J\lambda}_{v'j'}(R)\right]^3\left[\mathbf{d}'^{\lambda}(R)\right]_{v'j';vj} \tag{B6} $$

$$ \text{with}\qquad \Delta V^{J\lambda}_{v'j'}(R) \;=\; \Delta E - \varepsilon'_{v'j'} + \sum_L{}'\langle v'j'|V_L^A(r,R) - V_L^X(r,R)|v'j'\rangle_r\; g_L^\lambda(j',j') - \frac{J(J-1)+j'(j'+1)-2\lambda^2}{2\mu R^2}\,, $$

and $g_L^\lambda(j',j)=(-1)^L C(j'Lj,\lambda0\lambda)\,C(jLj',000)$.

Fig. B4. $He^+ + H_2 \longrightarrow \{He + H_2^+ , HeH_2^+\}$

Calculations within the X_4-projected 3D optical potential model

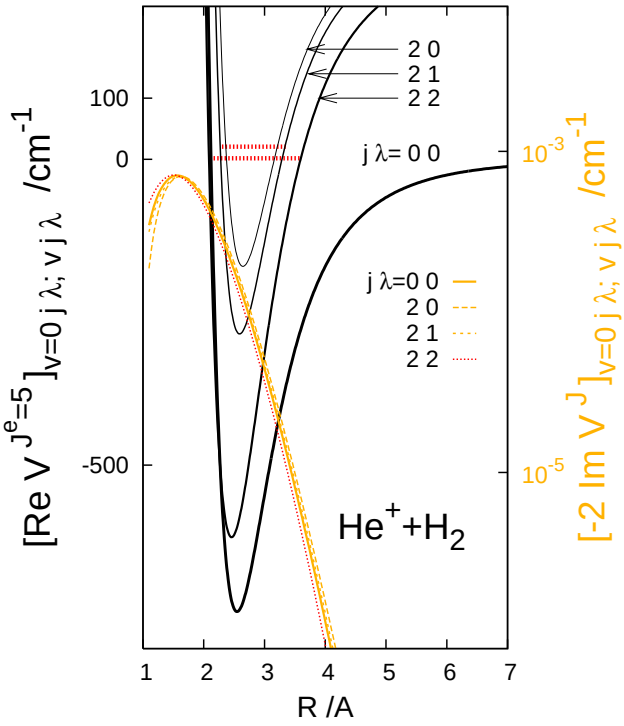

Fig. B4a. A comparison of diagonal elements of the molecular and optical potential matrices

$$\mathbf{W}^{J^e}(R) := \mathrm{Re}\mathbf{V}^{J^e}(R)\,, \quad {}^{\mathrm{opt}}_{X_4}\tilde{\mathbf{W}}^{J}(R) := -2\mathrm{Im}\mathbf{V}^{J}(R)$$

which correlate with the thresholds $H_2(v{=}0, j){+}He^+$ for $j{=}0$ and $j{=}2$. See Fig. A2 of Ref. 1 and Eq. (B6) for the definitions of $\mathbf{W}^{J^e}$ and ${}^{\mathrm{opt}}_{X_4}\tilde{\mathbf{W}}^{J}(R)$, respectively. The red lines drawn within the potentials $W^{J^e=5}_{022;022}(R)$ and $W^{J^e=5}_{021;021}(R)$ show the energies and the spatial extents of functions of the states $(b\,k\,v_R\,J^e){=}(2\,2\,2\,5)$ and $(2\,1\,1\,5)$, respectively.

The comparison shows that radiative transitions from the initial $(b\,k\,v_R\,J)$ quasi-bound states occur preferably in the regions of left turning points in the potentials $W^{J}_{0bk;0bk}(R)$. The repulsive wall region of $W^{J}_{000;000}(R)$ is decisive in transitions from free states.

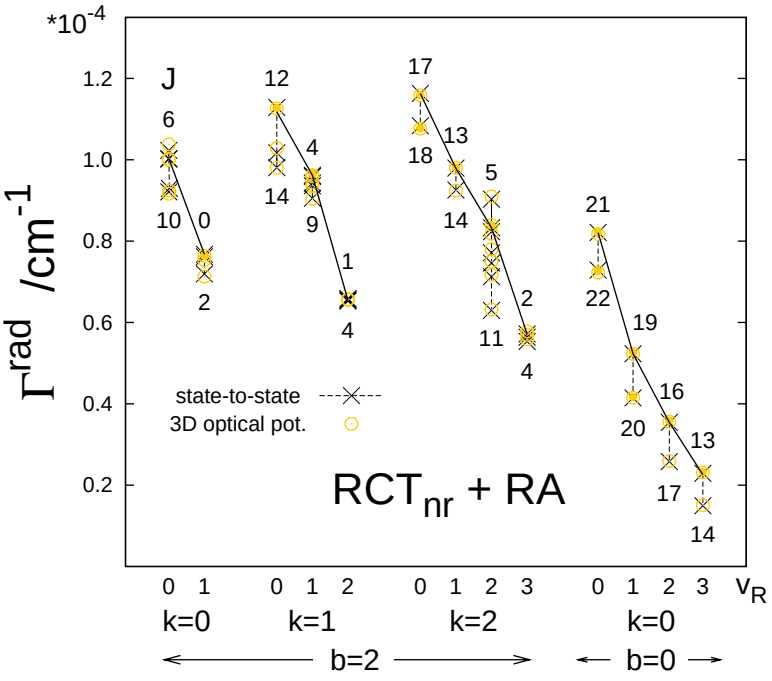

3D optical potential
versus
state-to-state approach

Fig. B4b. Radiative widths of resonances.

The open circles represent the results listed in Table I of the paper, obtained from the optical potential ${}^{\mathrm{opt}}_{X_4}\mathbf{W}^{J^e}$ of Eq. (B1)-(B3). The yellow dots denote results from the simplified version of this potential defined here in Eq. (B6).

The simplified version of the X_4-projected optical potential is seen to be as good as the one used in the paper.

COMMENT

Because of its ability to account for the existence of rotationally predissociating states in the reactant channel, the 3D optical potential model is certainly superior to the 1D model. The accuracy of the X_4-projected version of the 3D model which is documented here in the calculations of the rates of radiative processes in the low temperature H_2 + He^+ gas mixture may certainly be exploited in the analysis of the state-to-state results obtained for this system (see Fig. B5).

Fig. B5. X_4-projected 3D optical potential model

as an aid in the analysis of state-to-state results

Correlations of transition rates with properties of initial state functions

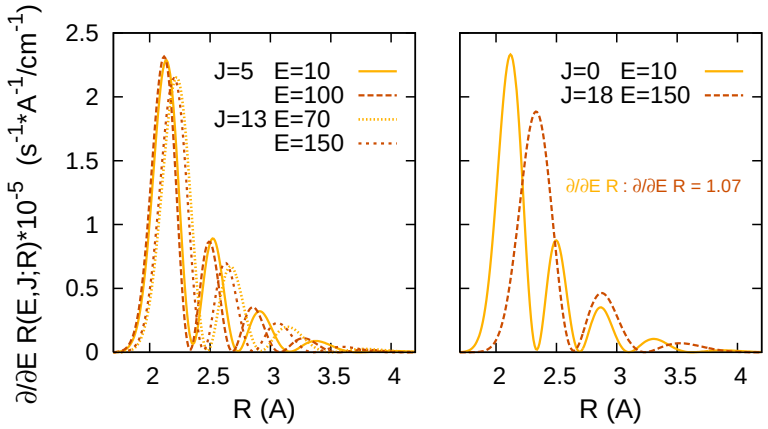

Fig. B5a. R-dependent rates of transitions from selected continuum states (E, J) of $He^+ + H_2(v{=}0)$ obtained as $\frac{\partial}{\partial E} R_{(\to X_4)}(EJ^e; R) = \frac{1}{\hbar}[\mathbf{F}^{(+)J^e}(E;R)]^\dagger \, {}^{\rm opt}_{X_4}\tilde{\mathbf{W}}^{J^e}(R)\, \mathbf{F}^{(+)J^e}(E;R)\,.$

The integrated rates $\frac{\partial}{\partial E} R_{(\to X_4)}(EJ^e)$ are approximations to state-to-state values of $\frac{\partial}{\partial E} R^{\rm RCT_{nr}} + \frac{\partial}{\partial E} R^{\rm RA}$; deviations ~2%.

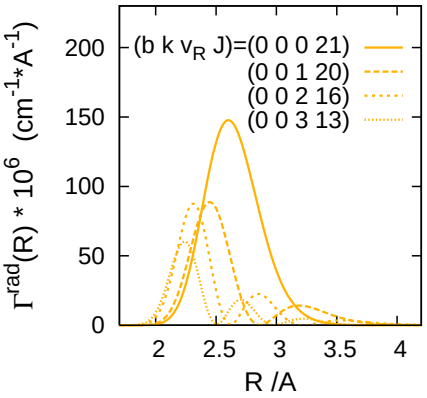

Fig. B5b. R-dependent widths of selected quasi-bound states $(b\,k\,v_R\,J^e){=}(n, J^e)$ of $He^+{-}H_2(v{=}0)$ obtained as

$$\Gamma^{J^e}_{n\,(\to X_4)}(R) = [\mathbf{F}^{B\,J^e}_n(R)]^T \; {}^{\rm opt}_{X_4}\tilde{\mathbf{W}}^{J^e}(R)\; \mathbf{F}^{B\,J^e}_n(R)\,.$$

The integrated widths $\Gamma^{\rm rad}{:=}\Gamma^{J^e}_{n\,(\to X_4)}$ are approximations to the state-to-state values of $\Gamma^{\rm RCT_{nr}}{+}\Gamma^{\rm RA}$; deviations $\lesssim$1%, see Table I in the paper.

In the bottom row: $F_{02k}{:=}c * [\mathbf{F}^B]_{v=0\,j=2\,\lambda=k}$ where c is a factor (close to 1) chosen to give $\langle F_{02k}|F_{02k}\rangle{=}1$.

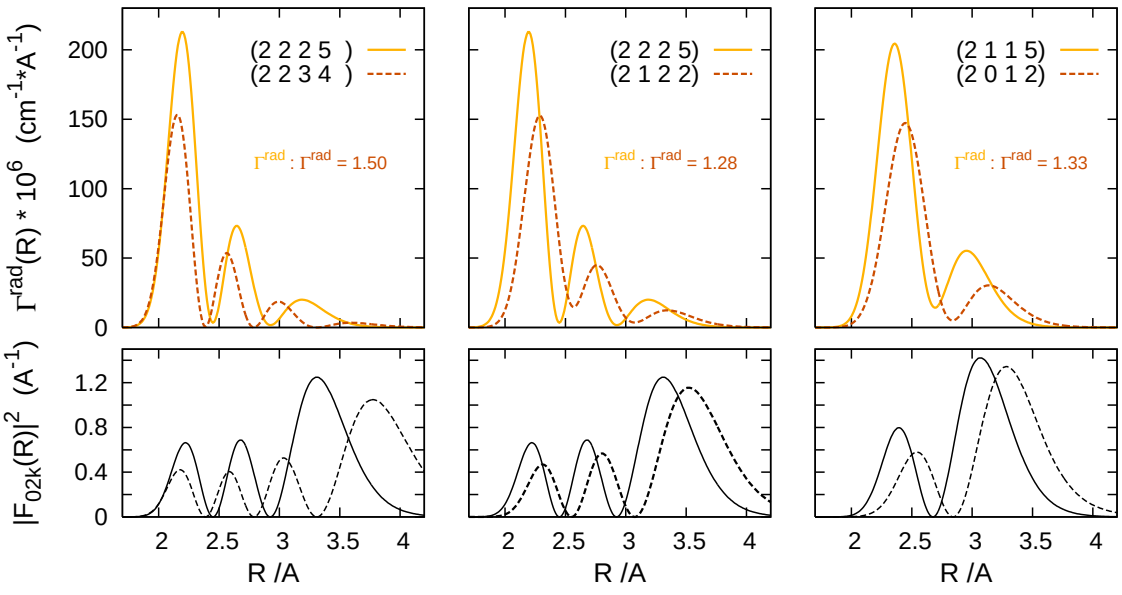

COMMENTS

(i) Because of the monotone dependence of the optical potential on the R coordinate, see Fig. B4a, the oscillations in the functions $\frac{\partial}{\partial E}R(\ ;R)$ and $\Gamma^{\rm rad}(R)$ come from the initial state functions. The rapid decrease of the optical potential, by a factor of $\sim$500 between R=2 and R=4 $\mathring{A}$, dampens the oscillations.

(ii) Radial functions of continuum states for a given J change very little with the energy E in the small range considered, $[10, 150]$ cm^{-1}, specifically, in its subrange above the top of the centrifugal barrier in the potential $W^J_{000;000}(R)$. The transition region near the turning point remains almost constant. This is why the rate functions behave as demonstrated in the left panel of Fig. B5a.

(iii) With growing J, the functions of continuum states become shifted towards larger R's where they are exposed to a larger damping by the optical potential. However, since the largest amplitudes of the functions stay near the turning points the impact of the shift on the integrated rates $\frac{\partial}{\partial E}R(E,J)$ is relatively small, as demonstrated in the right panel of Fig. B5a.

(iv) In contrast to the small sensitivity of the rate functions to changes of energy of continuum states, the correlations of the radiative widths of quasi-bound states with the vibrational numbers v_R and v_θ=$b-k$ are noticeable$^{(*)}$ in Table I of the paper, in Figs. B3 and B4b. An inspection of Fig. B5b together with Fig. B4a helps to rationalize these correlations.

(iv)' Functions of quasi-bound states trapped by the barrier in the effective potential $W^J_{000;000}(R)$ change their shapes when the number v_R grows; their largest amplitudes appear at R's closer and closer to the barrier position, i.e. in the region where the optical potential is already small and vanishes rapidly. This gives the decrease of the widths of b=0 states with growing v_R (upper panel of Fig. B5b). Similarly, the decrease of the widths of a given b=2 k state with growing v_R (lower left panels) can be explained by the changing shapes of the related bound state functions in the potential $W^J_{0bk;0kb}(R)$.

(iv)" A decrease of the radiative widths of $b\,k$ states with growing $b-k$ is seen in Fig. B4b when one compares the cases (2 2 0 17), (2 1 0 12) , and (2 0 0 6). The effect would be larger if cases with the same J number could be compared$^{(*)}$. The origin of this correlation should be attributed to the relative configuration of the wells in the potentials $W^J_{0bk;0bk}(R)$ for k diminishing from b to 0. See Fig. 2 in the paper. Comparing vibrational functions in these potentials characterized by the same v_R (examples in the middle and right panels of Fig. B5b) one easily realizes that the function in the shallower potential (smaller k) should be more suppressed by the optical potential since its maximal amplitude occurs at larger R's.

$^{(*)}$clear expositions of the correlations in a larger set of the widths $\Gamma^{\rm RCT+RA+iRaT}$ of bound and quasi-bound states of the $He^+-para H_2$ and $He^+-ortho H_2$ complexes are given in Figs.B7b and B8.

X_4-projected 3D optical potential model as an aid in the analysis of state-to-state results

Populations of v' and j' states

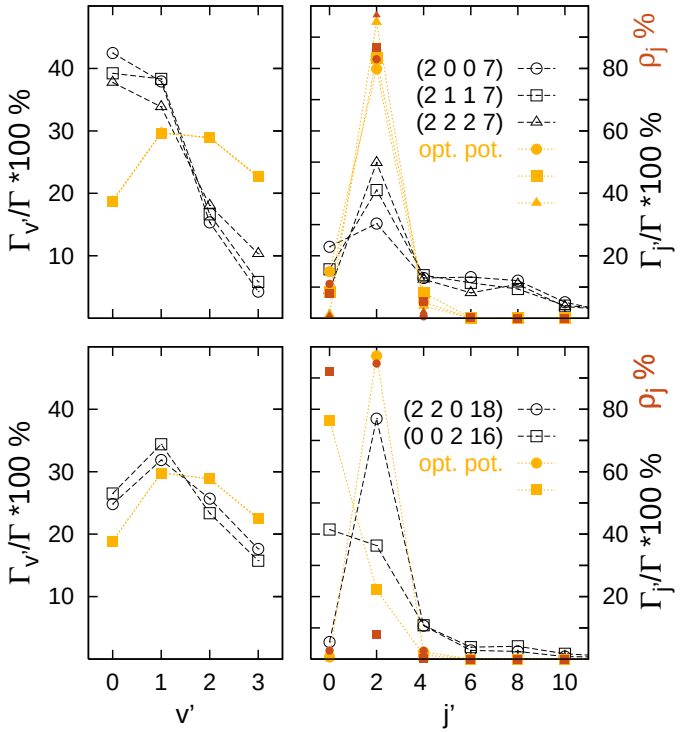

Fig. B5c. Populations of v' and j' states of H_2^+ due to transitions from $(b\,k\,v_R\,J^e)=(n,J^e)$ states of He^+-H_2.

The black symbols are the 'true' populations of the RCT_{nr} reaction products obtained from the state-to-state approach, see Fig. A15 in Ref. 1. The yellow symbols represent the ratios $\Gamma^{J^e\mathrm{rad}}_{n,c'}/\Gamma^{J^e\mathrm{rad}}:={}^{\mathrm{opt}}P_{c'}$ for $c'=v',j'$, where the width $\Gamma^{J^e\mathrm{rad}}$ is obtained by evaluation of the formula $\langle \mathbf{F}^{B\,J^e}_n | \,{}^{\mathrm{opt}}_{X_4}\tilde{\mathbf{W}}^J\, | \mathbf{F}^{B\,J^e}_n\rangle$, see Eq. (38) in the paper, and the quantities $\Gamma^{J^e\mathrm{rad}}_{n,c'}$ result from the resolutions ${}^{\mathrm{opt}}_{X_4}\tilde{\mathbf{W}}^J=\sum_{c'}{}^{\mathrm{opt}}_{X_4}\tilde{\mathbf{W}}^J_{c'}$ for $c'=v',j'$, see Eq. (B6).

The brown symbols represent j-mixing in the functions of the initial states, see Fig. A4 in part A.

COMMENTS

(i) ${}^{\mathrm{opt}}P_{v'}$ and ${}^{\mathrm{opt}}P_{j'}$ describe the populations of v' and j' states of the H_2^+ ions at short separations from the He atoms which result from transitions to the energy range of the H_2^++He system including the continuum part (the same as the state-to-state results, 0-7800 cm^{-1}) and also bound state energies. Actually, transitions to bound states (the RA process) constitute only a small fraction in the radiative decay of the resonances shown in the upper panels and practically do not occur in the decay of the high J resonances shown in the bottom panels (compare the respective values of Γ^{RA} and $\Gamma^{\mathrm{RCT_{nr}}}$ in Table I of the paper).

(ii) The populations ${}^{\mathrm{opt}}P_{j'}$ differ only slightly from the populations of j-states (j-mixing) in the functions of the He^+-H_2 complex. This follows from the properties of the transition dipole moment involved ($\Delta j=0$ propensity, see the discussion below Fig. A12 in part A).

(iii) The populations ${}^{\mathrm{opt}}P_{v'}$ in turn differ dramatically from v-mixing in the initial states (which is small: $\rho_{v=0}\gtrsim 90\%$ in all cases). They rather reflect the overlapping between vibrational functions of H_2 and H_2^+, see Fig. 12b in the paper and Fig. A1d in part A. This is precisely the effect predicted by Hopper in Ref. 6.

(iv) By construction, the optical potential model does not account for dynamics in the H_2^++He system, for the internal energy transfer. Thus, the differences between the yellow symbols in the figure and their black counterparts display, quite adequately, how much the vibrational and rotational inelasticity in the product channel contributes to the final populations of vibrational and rotational states of the H_2^+ ions at large separations from the He atoms. The picture is fully consistent with the considerations presented on this matter in part A, below Fig. A14.

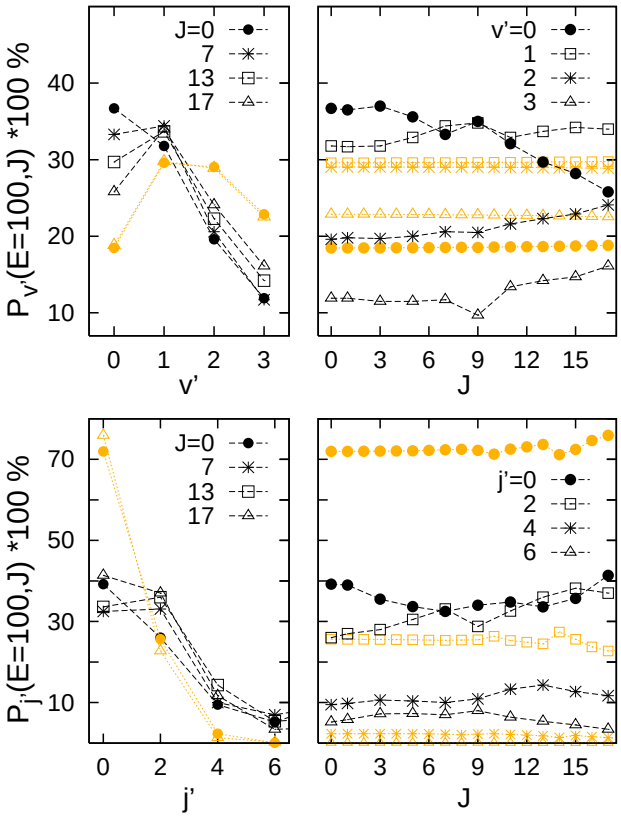

Fig. B5d. Populations $P_{c'}(E,J)$ of $c'{=}v'$ and $c'{=}j'$ states of H_2^+ due to transitions from continuum (E,J) states of $He^+{-}H_2$.

The black symbols are the 'true' populations in RCT_{nr} [state-to-state results, see Eq. (42) in the paper]. The yellow symbols represent quantities obtained in the same way as the ratios ${}^{opt}P_{c'}(n,J^e)$ in Fig. B5c except the matrix elements of the optical potential between continuum state functions are used, $\langle \mathbf{F}^{(+)J^e}(E)|\,{}^{opt}_{X_{N_{v'}}}\tilde{\mathbf{W}}^J\,|\mathbf{F}^{(+)J^e}(E)\rangle$.

The J dependence of the populations (examples in Figs. 4, 6, and 18 of the paper) is summarized here. Documented is the fact (black versus yellow curves in the right panels) that the dependence is actually established in the product channel, by rotational couplings (potential anisotropy) acting together with Coriolis couplings and centrifugal distortions.

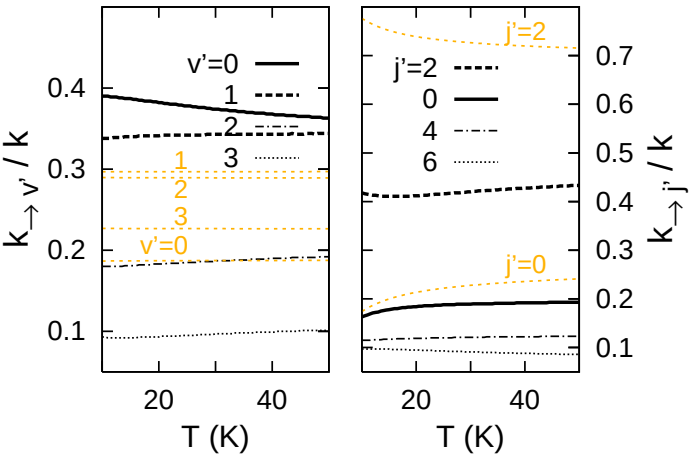

Fig. B5e. Temperature averaged populations of v' and j' states of the product ion of the RCT_{nr} reaction

compared to the short-range populations of the states obtained from the X_4-projected 3D optical potential model (yellow lines) which disregards the v' and j' changing transitions in the product channel.

CONCLUSIONS

- The population of vibrational states of the H_2^+ ions produced in the RCT reaction at temperatures 10-40 K would be qualitatively different and nearly consistent with Hopper's prediction[6] (maximum at $v'{=}2$ state) if vibrational (vibro-rotational) inelasticity of motion in the final channel of the reaction were neglected.

- The population of rotational states would be quantitatively different, more strongly peaked at $j'{=}2$ state, and thereby even more inconsistent with Hopper's prediction (maximum at $j'{=}0$) if rotational inelasticity in the product channel were neglected.

Fig. B6. $He^+ + H_2 \longrightarrow \{He + H_2^+ , HeH_2^+ , HeH^+ + H\}$

Application of the 'complete' 3D optical potential model

Fig. B6a. Radiative quenching of He^+ ions in collisions with $H_2(v{=}0, j{=}0)$ molecules, RCT+RA+iRaT(:=trad), in cold range(*)

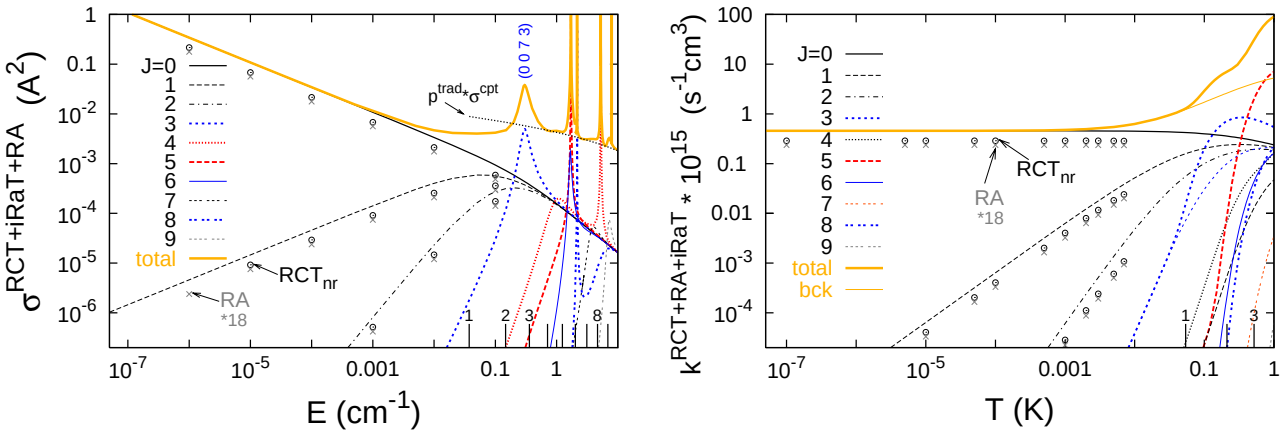

A demonstration of Wigner's threshold laws:

- in partial cross-sections (left panel),

$$\sigma_{00}^{\rm rad}(E,J) := \frac{\hbar^2\pi}{2\mu} E^{-1} \left[2\pi\hbar \frac{\partial}{\partial E} R_{00}^{\rm rad}(E,J)\right] \underset{E \ll E_{\rm cbr}^J}{\sim} \frac{\hbar^2\pi}{2\mu}\, \mathcal{C}_J^{\rm rad}\, E^{J-\frac{1}{2}}$$

  for rad=trad, $\mathrm{RCT_{nr}}$, RA, where $E_{\rm cbr}^J$ denotes the height of the centrifugal barrier in the effective potential $W_{000;000}^{J^e}(R)$. The values of $E_{\rm cbr}^J$ for $J{=}1, ..., 9$ are shown by the sticks in the lower right corner(*). All determined coefficients $\mathcal{C}_J^{\rm rad}$ (for rad=$\mathrm{RCT_{nr}}$, RA — in the state-to-state approach) are listed in table below.

- in partial rate constants (right panel),

$$k_{00}^{\rm rad}(T,J) := \int dE\, P^0(E,T)\, \frac{\partial}{\partial E} R_{00}^{\rm rad}(E,J) \underset{k_{\rm B}T \ll E_{\rm cbr}^J}{\sim} \mathcal{K}_J^{\rm rad}\, (k_{\rm B}T)^J$$

  with $\mathcal{K}_J^{\rm rad} = \frac{\hbar^2\pi}{\mu^{3/2}} \frac{(2J+1)!!}{2^{J+1/2}}\, \mathcal{C}_J^{\rm rad}$. The sticks in the lower right corner show the temperatures $E_{\rm cbr}^J/k_{\rm B}$.

At $T{<}1$ mK, the total rates $k_{00}^{\rm rad}(T) = \sum_J (2J{+}1)\, k_{00}^{\rm rad}(T,J)$ are practically determined by $J{=}0$ partial rates, which are: $\mathcal{K}_0^{\rm rad} = 4.56{\times}10^{-16}$, $2.88{\times}10^{-16}$, and $1.3{\times}10^{-17}$ $\mathrm{s^{-1}cm^3}$ for rad=trad, $\mathrm{RCT_{nr}}$, and RA, respectively.

J	$\mathcal{C}_J^{\rm RA}$ ♭	$\mathcal{C}_J^{\rm RCT_{nr}}$ ♭	$\mathcal{C}_J^{\rm trad}$ ♭	J	$\mathcal{C}_J^{\rm trad}$ ♭	J	$\mathcal{C}_J^{\rm trad}$ ♭
0	2.49 (−7)	5.45 (−6)	8.65 (−6)	3	1.44 (−4)	6	7.2 (−9)
1	3.34 (−6)	7.40 (−5)	1.16 (−4)	4	4.14 (−6)	7	9.7 (−11)
2	1.88 (−5)	4.14 (−4)	6.55 (−4)	5	2.28 (−6)	8	1.5 (−12)

♭ in units of $E^{-(J+1/2)}$ and E in $\mathrm{cm^{-1}}$.

(*) The value of $E_{\rm cbr}^{J=1} = 0.037$ $\mathrm{cm^{-1}}$ is taken as a rough limit of 'cold' energy range. Energies from ∼0.05 up to ∼200 $\mathrm{cm^{-1}}$ are named 'subthermal'.

B6b. RCT+RA+iRaT in cold $He^+ + H_2(v{=}0, j{=}1)$ collisions

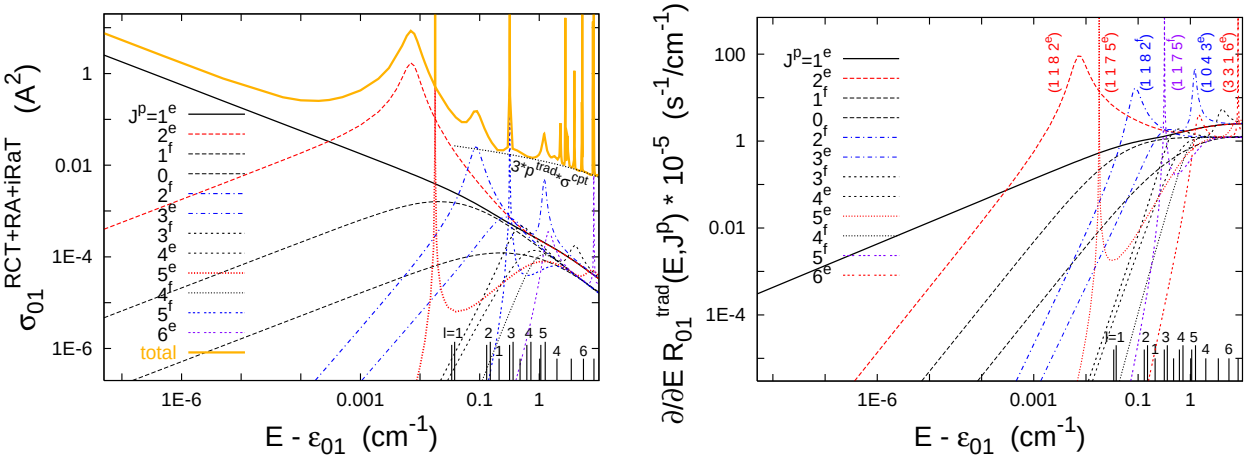

Wigner's laws in partial cross-sections and reaction probabilities $[2\pi\hbar\frac{\partial}{\partial E}R^{\rm rad}_{0j}(E,J)]$ near $j{=}1$ threshold:
$\sigma^{\rm trad}_{01}(E,J^p) := \frac{\hbar^3\pi^2}{\mu(E-\varepsilon_{01})}\frac{\partial}{\partial E}R^{\rm trad}_{01}(E,J^p) \underset{E\ll E^{J^p l_{\rm min}}_{\rm cbr}}{\sim} \frac{\hbar^2\pi}{2\mu}\mathcal{C}^{\rm trad}_{J^p l_{\rm min}}(E-\varepsilon_{01})^{l_{\rm min}-\frac{1}{2}}$ with $l_{\rm min}{=}J^e{-}1$ or J^f for $J{\geq}1$ and $l_{\rm min}{=}1$ for $J{=}0$. Values of several determined coefficients $\mathcal{C}^{\rm trad}_{J^p l_{\rm min}}$ are listed in Table below. The sticks in the corners of the panels show the heights $E^{J^p l}_{\rm cbr}{-}\varepsilon_{01}$ of the centrifugal barriers in the adiabatic potentials $e^{J^p}_{v=0\,j=1\,l}(R)$ obtained by diagonalizing the matrices $\mathbf{W}^{J^p}(R) := \{W^{J^p}_{vj\lambda;\tilde{v}\tilde{j}\tilde{\lambda}}(R)$ for $v,\tilde{v}{=}0,3$, $j,\tilde{j}{=}1{-}13$, and $\lambda,\tilde{\lambda}{=}\frac{1-p}{2},\ldots\min(j,J,4)\}$. The three different heights of the sticks are to differentiate between barriers in the potentials with $l{=}J^e{-}1$ (the highest sticks), $l{=}J^e{+}1$ (the lowest), and $l{=}J^f$.

Wigner's laws in partial rate constants ${}_{\rm o}k^{\rm trad}_{01}(T,J^p)$ describing the RCT+RA+iRaT in gas mixtures with pure ortho-H_2

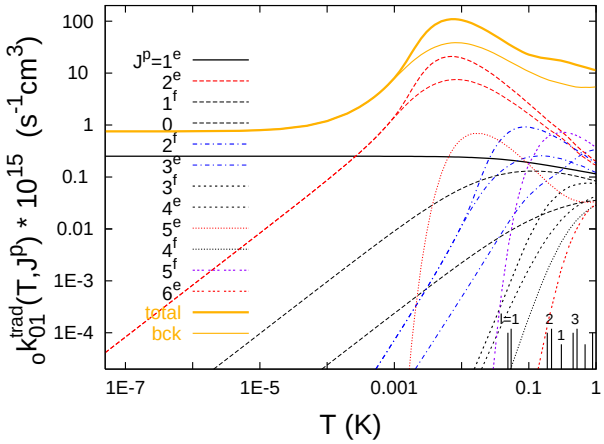

${}_{\rm o}k^{\rm rad}_{01}(T,J^p) := \int_{\varepsilon_{01}} dE\,{}_{\rm o}P(E,T)\frac{\partial}{\partial E}R^{\rm trad}_{01}(E,J^p) \underset{k_{\rm B}T\ll E^{J^p l_{\rm min}}_{\rm cbr}-\varepsilon_{01}}{\sim} \frac{1}{3}\mathcal{K}^{\rm trad}_{J^p l_{\rm min}}(k_{\rm B}T)^{l_{\rm min}}$,
where ${}_{\rm o}P(E,T){=}P^1(T)\frac{Z(T)}{3Z_1(T)}$ (see Table BX) and $\mathcal{K}^{\rm trad}_{J^p l_{\rm min}} = \frac{\hbar^2\pi}{\mu^{3/2}}\frac{(2l_{\rm min}+1)!!}{2^{l_{\rm min}+1/2}}\mathcal{C}^{\rm trad}_{J^p l_{\rm min}}$.

At $T{<}0.01$ mK, the total rate ${}_{\rm o}k^{\rm trad}_{01}(T){=}\sum_J\sum_p(2J{+}1)\,{}_{\rm o}k^{\rm trad}_{01}(T,J^p)$ is practically determined by $J^p{=}1^e$ partial rate:

$${}_{\rm o}k^{\rm trad}_{01}(T) \approx \mathcal{K}^{\rm trad}_{1^e 0} = 7.54{\times}10^{-16}\ {\rm s}^{-1}{\rm cm}^3.$$

$l_{\rm min}$	J^p	$\mathcal{C}^{\rm trad}_{J^p l_{\rm min}}$ ♭	$l_{\rm min}$	J^p	$\mathcal{C}^{\rm trad}_{J^p l_{\rm min}}$ ♭	$l_{\rm min}$	J^p	$\mathcal{C}^{\rm trad}_{J^p l_{\rm min}}$ ♭	$l_{\rm min}$	J^p	$\mathcal{C}^{\rm trad}_{J^p l_{\rm min}}$ ♭	$l_{\rm min}$	J^p	$\mathcal{C}^{\rm trad}_{J^p l_{\rm min}}$ ♭
0	1^e	1.43 (−5)	1	2^e	4.5 (−2)	2	1^f	2.2 (−3)	3	3^f	6.9 (−5)	4	5^e	2.1 (−2)
				1^f	5.3 (−4)		3^e	1.5 (−4)		4^e	3.7 (−5)		4^f	1.3 (−5)
				0	1.3 (−5)									

♭ in units of $E^{-(l_{\rm min}+1/2)}$ and E in $\rm cm^{-1}$.

Fig. B7. Applications of the 3D optical potential model in sub- and thermal ranges

B7a. RCT+RA+iRaT in transitions from continuum states of $He^+ + H_2(v{=}0, j)$ for $j{=}0, 1$

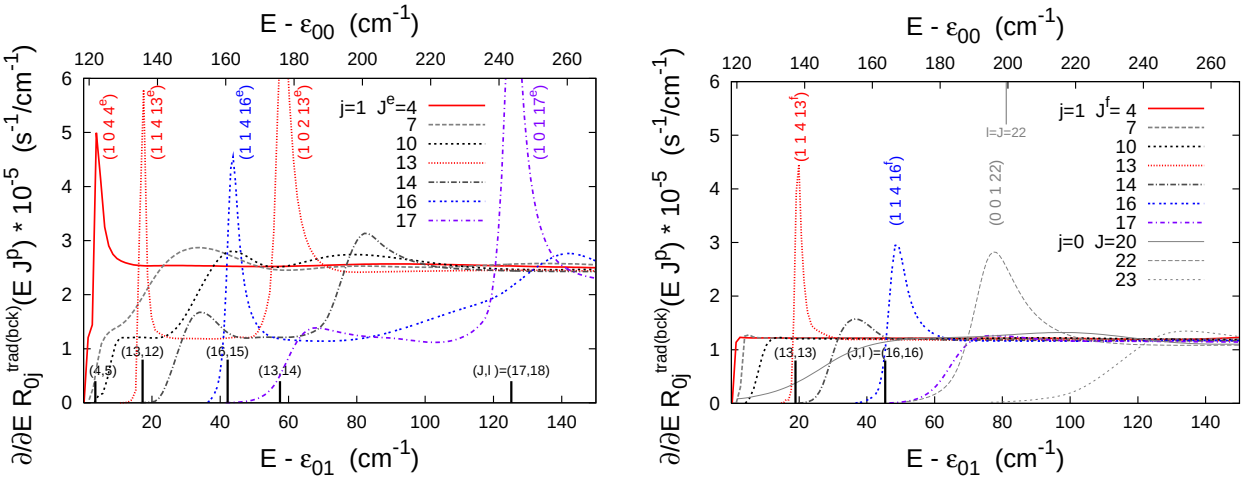

Rates $\frac{\partial}{\partial E} R_{0j}^{\rm trad(bck)}(EJp)$ for $j{=}1, 0$ and selected J's as functions of collision energy $(E{-}\varepsilon_{0j})$. Apart from the broad resonance peaks the functions behave consistently with the capture model, i.e.,

$$2\pi\hbar \frac{\partial}{\partial E} R_{0j}^{\rm trad(bck)}(EJp) \approx \sum_{\lambda=(1-p)/2}^{\min(j,J)} \Theta(E{-}E_{\rm cbr}^{Jpjl(\lambda)}{-}\varepsilon_{0j})\, p^{\rm trad}\,,$$

where $l(\lambda){:=}J{+}j{+}\frac{1-p}{2}{-}2\lambda$ for $p{=}{\pm}1$.

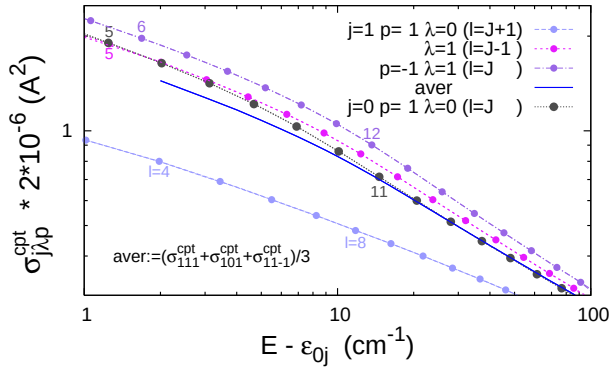

Three capture cross-sections $\sigma_{j\lambda p}^{\rm cpt}$ can be introduced to describe the result of summation over the Jp contributions to the cross-section $\sigma_{0\,j=1}^{\rm trad(bck)}(E)$,

$$\sigma_{01}^{\rm trad(bck)}(E) \;=\; \frac{\hbar^3\pi^2}{\mu(E{-}\varepsilon_{01})} \sum_{p,J} (2J{+}1) \frac{\partial}{\partial E} R_{01}^{\rm trad(bck)}(EJp)$$

$$\approx\; p^{\rm trad} \Big[\sum_{\lambda=0}^{1} \sigma_{1\lambda\,1}^{\rm cpt} {+} \sigma_{11\,-1}^{\rm cpt} \Big](E{-}\varepsilon_{01})\,.$$

However, their sum, $\sum\limits_{\lambda=0}^{1} \sigma_{1\lambda\,1}^{\rm cpt}{+}\sigma_{11\,-1}^{\rm cpt}$, is close to $3{\times}\sigma_{0\,01}^{\rm cpt}$. The resulting approximation

$$\sigma_{01}^{\rm trad(bck)}(E) \approx 3\, p^{\rm trad} \sigma^{\rm cpt}(E{-}\varepsilon_{01}) \quad \text{with} \quad \sigma^{\rm cpt}{:=}\sigma_{0\,01}^{\rm cpt}$$

is used in the top left panel of Fig. B6b and in Fig. 15 of the paper.

B7b. Total radiative widths of quasi-bound states of $He^+-H_2(v{=}0)$, $(b\,k\,v_R\,J\,p)$, in the energy range up to $j{=}2$ threshold

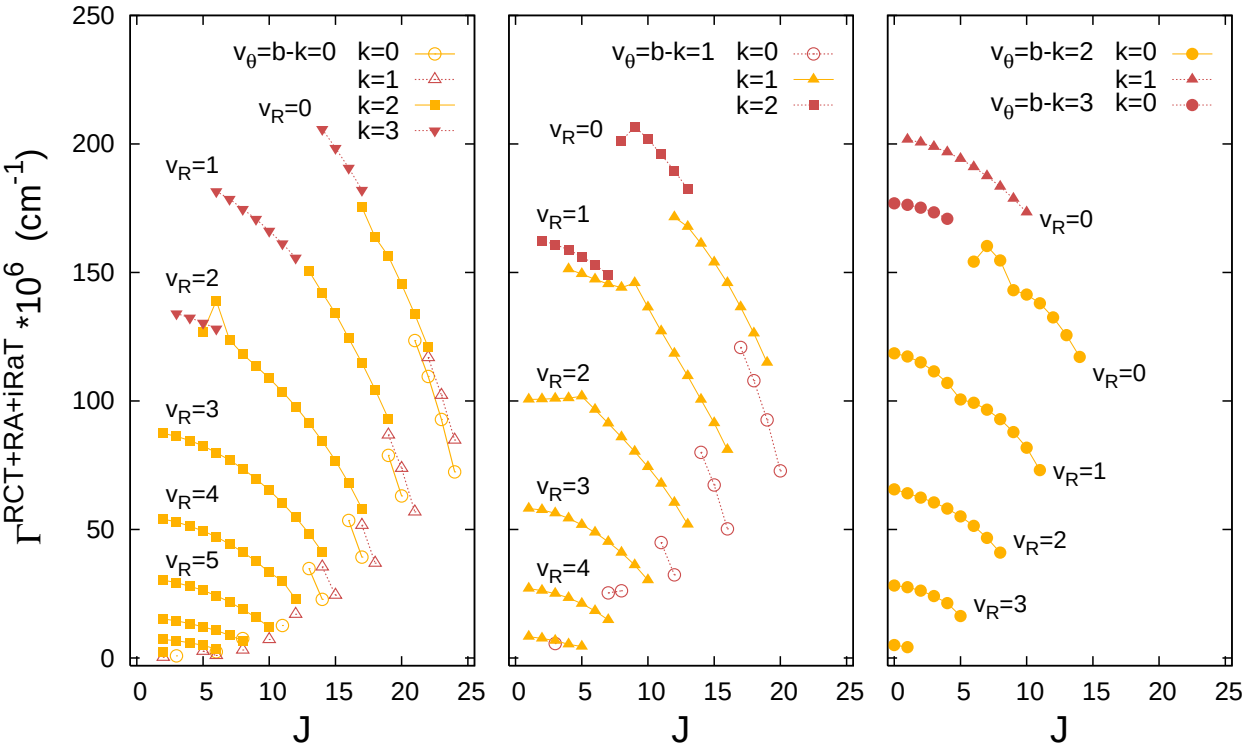

The open symbols are for $b{=}0,1$ states (shape resonances). The f parity states are not shown here. The largest $(f-e)/e$ differences in the radiative widths, for $k{=}1$ states, are of the size of -12%, see Tables BIII-IV.

Energies$^{(*)}$ of the states

$b{=}2$

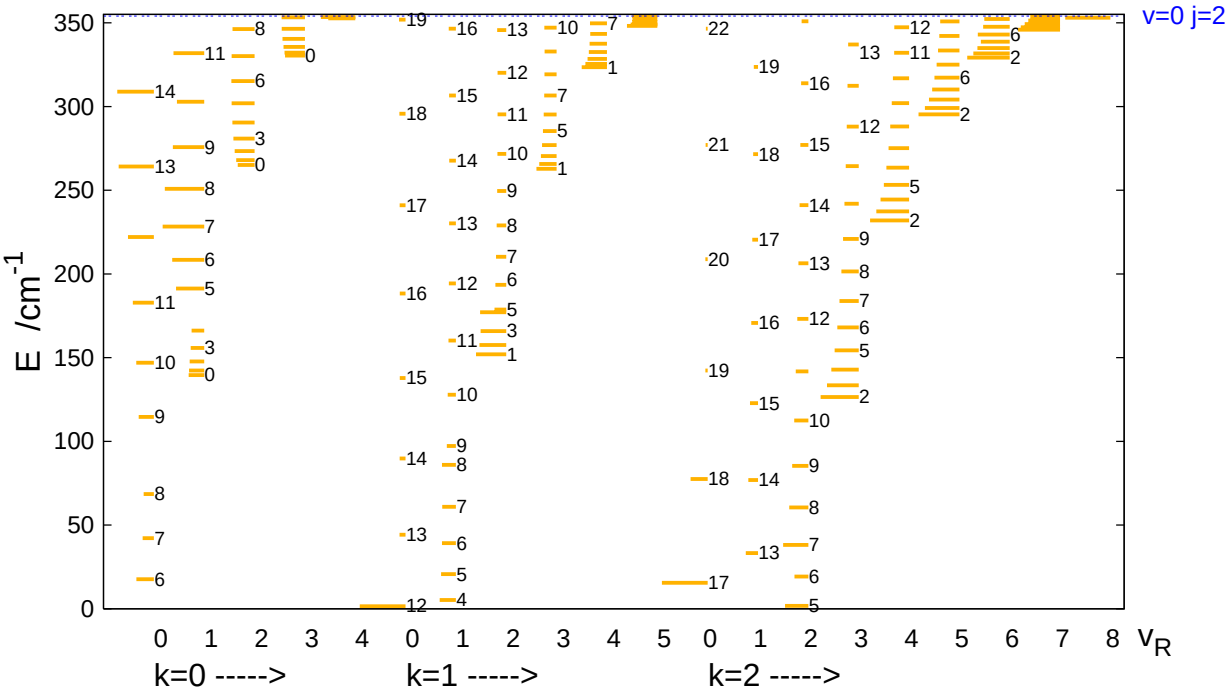

$^{(*)}$ Determined together with the dissociative widths Γ in the life-time matrix approach, see Refs. 7 and 8.

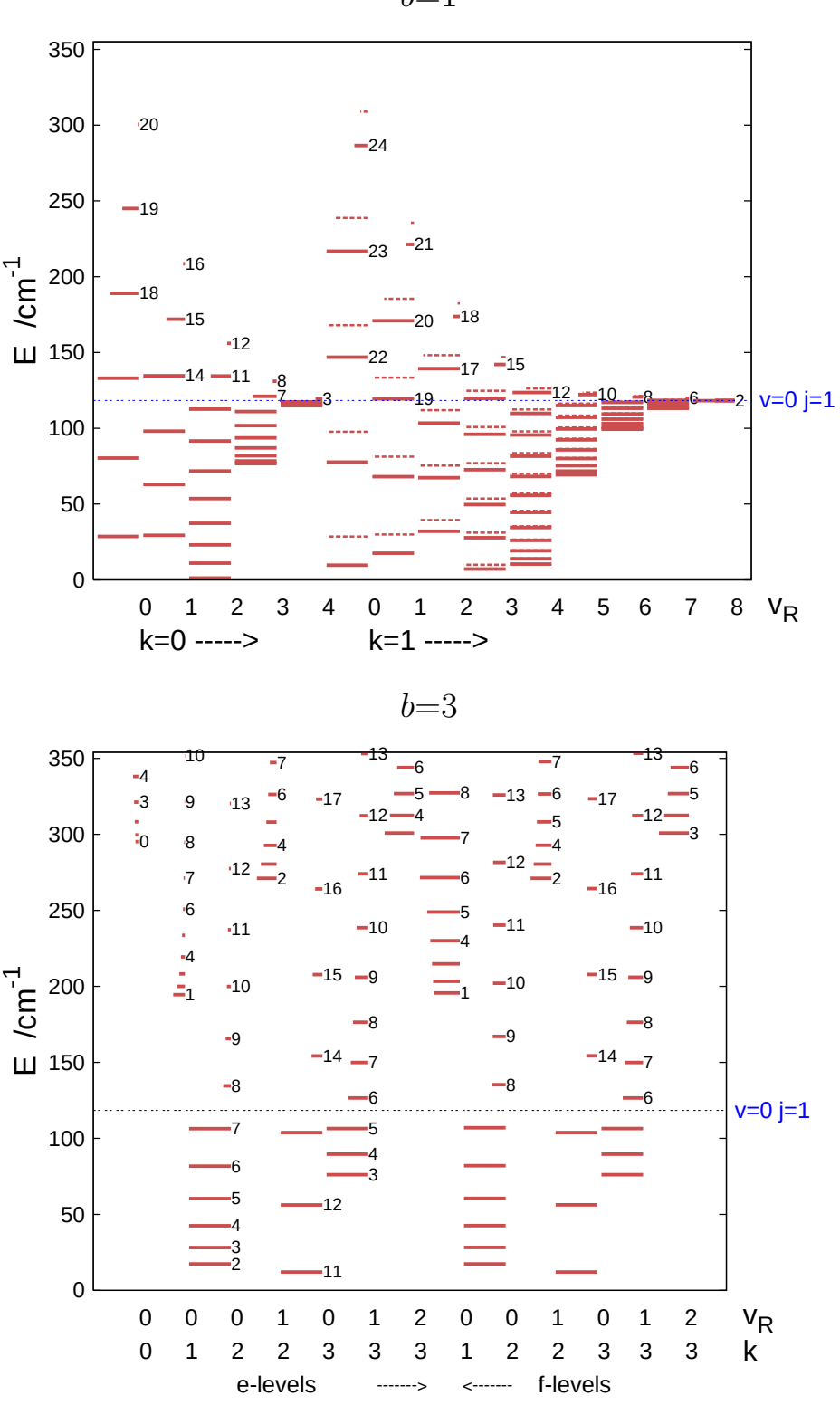

The numbers next to the lines are the values of J. The dashed lines in the b=1 panel represent f-levels. The lengths of all lines in the b=2 panel and of lines above the j=1 threshold in the b=1, 3 panels represent $-\log_{10}\Gamma$ if $10^{-5}\leq\Gamma<1$ cm^{-1}. Levels of widths $\Gamma>1$ cm^{-1} are not shown. Levels of widths $\Gamma<10^{-5}$ cm^{-1} are shown as bound states, i.e. with lines of the same length as the levels below the j=1 threshold.
Note, the correlations of Γ's with the numbers J, k, and v_θ are qualitatively different than the correlations of $\Gamma^{\rm trad}$'s. See also Figs. C3b, C3c, and C4b in Part C.
Energies of b=0 states are not shown here. They are listed in Table I of the paper and in Table BVI.

This figure and Tables BII-V complete Table I of the paper with information on all (14+44+165+81) quasi-bound (b=0 + 1 + 2 + 3) states of the He^++H_2 system which was used to generate the resonance parts of the cross-sections $\sigma_{0j}^{\rm RCT+RA+iRaT}(E)$ and of the rate constants $k_{0j}^{\rm RCT+RA+iRaT}(T)$ for j=0, 1 presented in Figs. 13-16 and in Table III.

TABLE BII: $He^+-H_2(I{=}0)$. Energies E (in cm^{-1}), dissociative widths Γ (in cm^{-1}), and total radiative widths[a] $\Gamma^{\rm trad}{:=}\Gamma^{\rm RCT+iRaT+RA}$ (in 10^{-6} cm^{-1}) of all rotationally predissociating $b{=}2\,k\,v_R\,J\,p{=}1$ states below $v{=}0\,j{=}2$ threshold.

	$b{=}2\ k{=}2$				$b{=}2\ k{=}1$				$b{=}2\ k{=}0$			
J	v_R	E	Γ	$\Gamma^{\rm trad}$ [$\Gamma^{\rm RA}$]	v_R	E	Γ	$\Gamma^{\rm trad}$ [$\Gamma^{\rm RA}$]	v_R	E	Γ	$\Gamma^{\rm trad}$ [$\Gamma^{\rm RA}$]
17	0	15.52	3. (−15)	175.4 [0.05]								
18		77.55	1.3 (−2)	163.7 [0.02]								
19		142.32	5.6 (−1)	156.3 [0.00]								
20		208.83	5.6 (−1)	145.4 [0.00]								
21		277.02	6.1 (−1)	133.7 [0.00]								
22		346.48	6.4 (−1)	120.8 [0.00]								
12					0	1.54	1. (−16)	171.5 [3.70]				
13	1	33.26	4.7 (−2)	150.5 [0.20]		44.23	2.2 (−1)	167.8 [2.03]				
14		76.92	8.9 (−2)	142.1 [0.10]		89.75	2.2 (−1)	161.2 [1.99]				
15		122.83	1.3 (−1)	134.0 [0.00]		137.85	2.3 (−1)	153.9 [0.32]				
16		170.77	1.8 (−1)	124.4 [0.00]		188.35	2.3 (−1)	145.9 [0.28]				
17		220.45	2.4 (−1)	114.8 [0.00]		241.04	2.2 (−1)	136.5 [0.16]				
18		271.56	3.0 (−1)	104.4 [0.00]		295.67	2.1 (−1)	126.3 [0.11]				
19		323.64	3.5 (−1)	93.1 [0.00]		351.91	1.9 (−1)	114.9 [0.16]				
4					1	5.25	1.7 (−2)	151.3 [6.18]				
5	2	1.68	2.9 (−3)	126.9 [3.48]		20.66	2.4 (−2)	149.4 [6.13]				
6		19.23	3.1 (−2)	139.0 [6.36]		39.18	3.0 (−2)	147.3 [6.22]	0	17.64	1.2 (−2)	154.2 [8.34]
7		38.12	1.8 (−3)	123.8 [1.95]		60.89	3.2 (−2)	145.5 [6.23]		42.19	5.8 (−2)	160.3 [7.79]
8		60.50	8.4 (−3)	118.2 [1.61]		85.95	3.0 (−2)	144.1 [5.52]		68.53	7.7 (−2)	154.7 [6.60]
9		85.34	1.7 (−2)	113.6 [0.33]		97.22	1.0 (−1)	145.9 [5.10]		114.62	2.1 (−2)	143.1 [5.97]
10		112.47	2.8 (−2)	108.8 [0.27]		127.83	1.3 (−1)	136.4 [1.47]		146.96	1.2 (−2)	141.4 [4.96]
11		141.80	4.3 (−2)	103.6 [0.13]		160.21	1.5 (−1)	127.1 [1.27]		182.88	5.1 (−3)	138.0 [4.87]
12		173.16	6.1 (−2)	97.8 [0.09]		194.36	1.7 (−1)	118.4 [0.83]		222.07	1.5 (−3)	132.5 [3.69]
13		206.34	8.4 (−2)	91.4 [0.04]		230.23	1.8 (−1)	109.7 [0.52]		264.18	1.5 (−4)	125.6 [1.50]
14		241.08	1.1 (−1)	84.4 [0.05]		267.72	1.8 (−1)	100.5 [0.62]		308.85	9.9 (−5)	117.1 [1.47]
15		277.06	1.4 (−1)	76.8 [0.01]		306.59	1.8 (−1)	91.4 [0.18]				
16		313.87	1.6 (−1)	68.0 [0.01]		346.48	1.7 (−1)	81.0 [0.16]				
17		350.94	1.8 (−1)	58.1 [0.01]								
0									1	139.57	2.0 (−2)	118.5 [6.98]
1					2	152.04	5.0 (−4)	100.6 [5.10]		142.33	2.2 (−2)	117.3 [6.89]
2	3	126.46	6.9 (−5)	87.4 [3.42]		157.54	1.2 (−3)	100.7 [3.84]		147.76	2.6 (−2)	115.0 [6.53]
3		133.51	3.4 (−4)	86.2 [2.52]		165.88	1.6 (−3)	100.9 [3.83]		155.78	3.3 (−2)	111.5 [5.97]
4		142.84	1.0 (−3)	84.6 [2.16]		177.12	1.4 (−3)	101.1 [4.30]		166.15	4.2 (−2)	107.0 [5.38]
5		154.38	2.3 (−3)	82.5 [1.92]		178.77	5.2 (−2)	101.8 [4.61]		191.32	8.5 (−4)	100.6 [4.41]
6		168.07	4.6 (−3)	79.9 [1.78]		193.52	6.4 (−2)	96.6 [3.94]		208.43	3.2 (−4)	99.3 [4.56]
7		183.81	8.0 (−3)	77.0 [0.96]		210.29	7.7 (−2)	91.3 [2.77]		228.32	2.9 (−5)	96.6 [3.86]
8		201.47	1.3 (−2)	73.6 [0.88]		229.00	8.8 (−2)	85.9 [1.84]		250.84	5.0 (−5)	92.9 [3.65]
9		220.91	1.9 (−2)	69.7 [0.22]		249.52	9.9 (−2)	80.3 [1.40]		275.78	3.8 (−4)	87.9 [2.88]
10		241.98	2.8 (−2)	65.3 [0.18]		271.71	1.1 (−1)	74.3 [0.56]		302.90	1.0 (−3)	81.8 [2.56]
11		264.44	3.8 (−2)	60.3 [0.09]		295.35	1.1 (−1)	67.8 [0.57]		331.87	4.4 (−4)	73.1 [2.19]
12		288.03	4.9 (−2)	54.7 [0.07]		320.14	1.1 (−1)	60.4 [0.54]				
13		312.40	6.1 (−2)	48.4 [0.03]		345.68	1.0 (−1)	51.9 [0.30]				
14		337.09	7.0 (−2)	41.2 [0.03]								

TABLE BII: continued

0									2	265.09	1.4 (−2)	65.6 [2.98]
1					3	262.78	6.1 (−3)	58.1 [2.49]		268.02	1.0 (−2)	64.1 [2.87]
2	4	232.00	5.5 (−5)	54.0 [2.05]		265.69	1.2 (−2)	57.6 [1.91]		273.36	6.8 (−3)	62.4 [2.72]
3		237.38	2.7 (−4)	52.9 [1.49]		270.44	1.9 (−2)	56.3 [1.76]		280.87	4.9 (−3)	60.5 [2.66]
4		244.48	7.8 (−4)	51.3 [1.24]		277.01	2.6 (−2)	54.3 [1.73]		290.43	3.8 (−3)	58.1 [2.60]
5		253.21	1.8 (−3)	49.4 [1.05]		285.32	3.2 (−2)	51.8 [1.55]		301.94	3.2 (−3)	55.1 [2.27]
6		263.47	3.4 (−3)	47.1 [0.96]		295.23	3.9 (−2)	48.8 [1.44]		315.24	3.0 (−3)	51.4 [2.09]
7		275.15	5.7 (−3)	44.3 [0.52]		306.60	4.4 (−2)	45.2 [1.15]		330.13	3.1 (−3)	46.7 [1.66]
8		288.08	8.9 (−3)	41.2 [0.46]		319.24	4.8 (−2)	41.0 [0.73]		346.28	4.0 (−3)	41.0 [1.35]
9		302.06	1.3 (−2)	37.6 [0.12]		332.86	4.9 (−2)	36.1 [0.58]				
10		316.85	1.7 (−2)	33.3 [0.09]		347.11	4.6 (−2)	30.3 [0.27]				
11		332.11	2.3 (−2)	29.9 [0.12]								
12		347.34	2.5 (−2)	22.9 [0.05]								
0									3	330.42	6.7 (−3)	28.2
1					4	323.51	1.7 (−3)	27.0		332.20	5.8 (−3)	27.5
2	5	295.34	3.5 (−5)	30.3 [1.13]		325.46	4.4 (−3)	26.2		335.60	4.6 (−3)	26.2
3		299.16	1.7 (−4)	29.3 [0.79]		328.47	7.5 (−3)	25.0		340.44	3.6 (−3)	24.1
4		304.14	4.8 (−4)	27.9 [0.64]		332.53	1.0 (−2)	23.4		346.46	2.9 (−3)	21.3
5		310.21	1.1 (−3)	26.3 [0.53]		337.55	1.3 (−2)	21.1		353.27	2.8 (−3)	16.3
6		317.23	1.9 (−3)	24.2 [0.47]		343.37	1.5 (−2)	18.3				
7		325.05	3.2 (−3)	21.8 [0.24]		349.71	1.4 (−2)	14.8				
8		333.46	4.7 (−3)	18.9 [0.21]								
9		342.18	6.3 (−3)	15.8 [0.05]								
10		350.82	8.2 (−3)	12.0 [0.04]								
0									4	352.70	1.1 (−3)	5.0
1					5	348.15	4.9 (−4)	8.3		353.44	1.7 (−4)	4.2
2	6	329.24	2.3 (−5)	15.2		349.05	1.2 (−3)	7.6				
3		331.72	1.1 (−4)	14.4		350.41	1.9 (−3)	6.7				
4		334.92	3.0 (−4)	13.4		352.16	1.9 (−3)	5.3				
5		338.73	6.9 (−4)	12.1		354.15	1.8 (−3)	4.4				
6		343.02	3.3 (−4)	10.7								
7		347.62	1.2 (−3)	8.8								
8		352.26	1.7 (−3)	6.7								
2	7	345.87	2.6 (−5)	7.2								
3		347.36	5.1 (−5)	6.7								
4		349.24	1.4 (−4)	5.9								
5		351.37	3.3 (−4)	4.9								
6		353.58	5.6 (−4)	3.5								
2	8	353.07	1.1 (−5)	2.3								

[a]The quantities were determined using the procedure described below Eq.(B7)-(B12). The parts $\Gamma^{\rm RA}$ of the radiative widths, shown in parentheses, are results of the state-to-state approach of Ref. 7.

TABLE BIII: $He^+-H_2(I=1)$. Energies E (in cm^{-1}) and radiative widths $\Gamma^{trad}:=\Gamma^{RCT+iRaT+RA}$ (in 10^{-6} cm^{-1}) of $b=1\,k\,v_R\,J\,p$ states in the range $\varepsilon_{v=0,j=1}<E<350$ cm^{-1} ♮. Tunneling widths Γ are given in cm^{-1}. Also shown are selected states from the range $0<E<\varepsilon_{v=0,j=1}$ ♯.

		$b=1\ k=1$						$b=1\ k=0$			
		$p=1$ (e)			$p=-1$						
J	v_R	E	Γ	Γ^{trad}	$E-E(e)$	Γ	$\Gamma^{trad}-\Gamma^{trad}(e)$	v_R	E	Γ	Γ^{trad}
22	0	146.90	∼0	116.9	21.12	0	−5.7				
23		216.83	4.5 (−6)	102.2	21.95	1.1 (−4)	−6.4				
24		286.55	2.2 (−2)	84.8	22.30	1.1 (−1)	−7.9				
17	1	17.57	0	108.1	12.33	0	−3.1	0	133.03	1. (−11)	120.8
18		68.06	0	98.1	13.22	0	−3.5		189.02	3.2 (−4)	107.9
19		119.43	∼0	86.8	13.98	0	−4.0		244.97	9.7 (−3)	92.6
20		170.96	8.0 (−6)	73.8	14.46	2.6 (−4)	−4.8		300.50	6.8 (−1)	72.8
21		221.34	1.1 (−1)	56.8	14.27	4.3 (−1)	−6.5				
14	2	32.06	0	79.3	7.35	0	−1.9	1	134.66	3.2 (−6)	79.9
15		67.41	0	71.3	8.01	0	−2.2		171.94	5.9 (−3)	67.3
16		103.41	0	62.3	8.56	0	−2.6		208.57	6.0 (−1)	50.2
17		139.34	3.9 (−7)	51.6	8.88	4.1 (−5)	−3.3				
18		173.80	1.6 (−1)	36.9	8.58	5.5 (−1)	−4.5				
11	3	49.69	0	55.8	3.89	0	−1.0	2	134.50	3.9 (−3)	44.9
12		72.63	0	50.1	4.37	0	−1.3		156.05	3.6 (−1)	32.3
13		96.04	0	45.7	4.76	0	3.3				
14		119.65	∼0	35.4	5.06	∼0	−1.9				
15		142.08	4.3 (−2)	24.4	4.91	2.1 (−1)	−3.0				
7	4	55.75	0	40.8	1.38	0	−0.7	3	121.11	1.3 (−3)	25.3
8		68.16	0	37.3	1.75	0	−0.6		131.04	3.5 (−1)	26.1
9		81.54	0	33.4	2.07	0	−0.6				
10		95.57	0	28.9	2.37	0	−0.8				
11		109.83	0	23.6	2.61	0	−1.0				
12		123.63	2.2 (−5)	17.0	2.67	5.4 (−4)	−1.4				
3	5	75.34	0	26.2	0.24	0	0.3	4	119.58	1.5 (−1)	5.6
4		80.06	0	24.6	0.39	0	−0.1				
5		85.77	0	22.8	0.57	0	−0.2				
6		92.34	0	20.8	0.76	0	−0.2				
7		99.56	0	18.6	0.96	0	−0.3				
8		107.25	0	15.2	1.15	0	−0.4				
9		115.01	0	11.7	1.29	0	−0.5				
10		122.24	5.4 (−3)	7.2	1.32	1.8 (−2)	−0.8				
8	6	120.64	5.1 (−2)	3.1	0.70	8.5 (−2)	0.1				
5	7	118.39	3.3 (−8)	2.6	0.30	7.0 (−4)	−0.1				
6		119.77	4.0 (−1)	1.0	0.39	4.7 (−1)	0.1				
1	8	118.17	0	1.1	0.03	0	0.0				
2		118.38	4.5 (−3)	0.15	0.08	4.0 (−2)	0.18				

♮ $\varepsilon_{v=0\,j=1}=118.37$ cm^{-1}. Only states with $\Gamma<1$ cm^{-1} are included.

♯ See Table BVIII for a complete list of $b=1$ states below the $v=0\,j=1$ threshold.

TABLE BIV: $He^+-H_2(I{=}1)$. Energies E (in cm^{-1}) and radiative widths $\Gamma^{trad}{:=}\Gamma^{RCT+iRaT+RA}$ (in 10^{-6} cm^{-1}) of $b{=}3\,k\,v_R\,J\,p$ states. All states in the range $0{<}E{<}350$ cm^{-1} are shown[♮].

		$b{=}3\ k{=}3$					$b{=}3\ k{=}2$				
		$p{=}1\ (e)$		$f-e$			$p{=}1\ (e)$		$f-e$		
J	v_R	E	Γ^{trad}	E	Γ^{trad}		v_R	E	Γ^{trad}	E	Γ^{trad}
11	0	12.04	224.8	0.03	0.1						
12		56.18	218.1	0.08	0.9						
13		103.79	210.1	0.05	−4.5						
14		154.25	205.8	0.04	0.3						
15		207.76	198.4	0.11	0.2						
16		264.15	190.7	0.16	−0.1						
17		323.21	182.1	0.24	0.0						
2							0	17.40	227.9	0.00	0.0
3	1	76.08	188.2	0.00	−0.3			28.20	226.6	0.02	0.0
4		89.61	186.7	0.00	0.0			42.55	224.6	0.06	0.0
5		106.47	184.4	0.00	0.0			60.41	222.1	0.15	0.1
6		126.59	181.6	0.00	0.1			81.71	218.9	0.30	0.2
7		149.94	178.6	0.00	0.0			106.40	214.5	0.57	0.5
8		176.44	174.7	0.01	0.2			134.55	201.1	0.78	10.3
9		206.01	170.8	0.01	0.1			165.64	206.8	1.41	0.0
10		238.58	166.2	0.03	0.1			199.97	201.9	2.10	−0.3
11		274.04	161.3	0.05	0.0			237.29	195.9	3.00	−0.2
12		312.28	155.7	0.10	0.2			277.47	189.6	4.15	−0.3
13		353.16		0.18				320.38	182.4	5.55	−0.4
2							1	271.14	162.4	0.00	0.0
3	2	300.91	134.0	0.00	0.0			280.44	160.9	0.02	0.0
4		312.48	132.4	0.00	0.0			292.77	158.8	0.07	0.1
5		326.87	130.4	0.00	0.0			308.07	156.2	0.17	0.1
6		344.04	128.1	0.01	0.0			326.29	153.0	0.34	0.1
7								347.31	149.2	0.60	0.0
		$b{=}3\ k{=}1$					$b{=}3\ k{=}0$				
0	0						0	295.26	176.9		
1		194.58	201.7	1.14	−0.1			299.64	176.3		
2		200.01	200.6	3.36	−0.1			308.33	175.2		
3		208.26	198.9	6.56	−0.2			321.23	173.4		
4		219.42	196.8	10.62	−0.4			338.18	170.9		
5		233.58	194.2	15.38	−0.7						
6		250.83	191.0	20.70	−1.1						
7		271.23	187.5	26.44	−1.7						
8		294.82	183.4	32.46	−2.5						
9		321.63	178.7	38.63	−3.3						
10		351.64	173.4								

[♮] Predissociation widths of states with $E{>}\varepsilon_{v=0\,j=1}$(=118.37 cm^{-1}) are given in Table CV of Ref. 8.

DETERMINATION OF RESONANCE PARAMETERS

within

THE 3-DIMENSIONAL OPTICAL POTENTIAL MODEL

The quantity analyzed is the radiative quenching probability from continuum states (EJp, vj) of the $He^+ + H_2$ system which is obtained from the scattering matrix $\mathbf{S}^{Jp}(E)$ in the Hamiltonian $\mathbf{U}^{Jp\,T}\,[\mathbf{H}^{Jp}(R) - \frac{i}{2}{}^{\rm opt}\mathbf{W}^{jp}(R)]\,\mathbf{U}^{Jp}$ (all symbols are as defined in Sec.III and IVA of the paper),

$$P_{vj}^{Jp}(E) = \sum_l \big[\mathbf{I} - \mathbf{S}^{Jp\,\dagger}(E)\,\mathbf{S}^{Jp}(E)\big]_{vjl;vjl}\,. \tag{B7}$$

In the vicinity of an isolated resonance $\mathcal{R}_n^{Jp}$, the function $P_{vj}^{Jp}(E)$ takes the form

$$P_{vj}^{Jp}(E) \approx B(E) + \frac{\Gamma_n^{Jp\,\rm trad}\;\Gamma_{n,vj}^{Jp}}{(E - E_n^{Jp\,\rm res})^2 + (\Gamma_n^{Jp\,\rm trad} + \Gamma_n^{Jp})^2/4} \tag{B8}$$

where $B(E)$ denotes a slowly varying background. It is assumed here in the form

$$B(E) \approx a + bE + cE^2\,.$$

Thus, there are six parameters of the resonance profile: a, b, c, $\Gamma^{\rm trad}$, Γ, and $E^{\rm res}$.

If the potential $-\frac{i}{2}{}^{\rm opt}\mathbf{W}^{jp}$ is treated in first order of perturbation theory, the following (distorted wave, DW) approximation to the probability P_{vj}^{Jp} arises

$${}^{\rm DW}P_{vj}^{Jp}(E) = 2\pi \sum_l \big[\mathbf{U}^{Jp\,T}\langle \mathbf{F}^{(+)\,Jp}(E)|{}^{\rm opt}\mathbf{W}^{Jp}|\mathbf{F}^{(+)\,Jp}(E)\rangle \mathbf{U}^{Jp}\big]_{vjl;vjl}\,, \tag{B9}$$

where $\mathbf{F}^{(+)\,Jp}(E;R)$ contains the scattering states of the Hamiltonian $\mathbf{H}^{Jp}(R)$. The respective resonance profile is

$${}^{\rm DW}P_{vj}^{Jp}(E) \approx {}^{\rm DW}B(E) + \frac{{}^{\rm DW}\Gamma_n^{Jp\,\rm trad}\;\;{}^{\rm DW}\Gamma_{n,vj}^{Jp}}{(E - {}^{\rm DW}E_n^{Jp\,\rm res})^2 + ({}^{\rm DW}\Gamma_n^{Jp})^2/4}\,. \tag{B10}$$

If a given $\mathcal{R}_n^{Jp}$ can be treated as an infinitely narrow resonance (INR), then

$${}^{\rm INR}P_{vj}^{Jp}(E) \approx B(E) + 2\pi\,\delta(E - E_n^{B_Q})\,\frac{{}^{\rm INR}\Gamma_n^{Jp\,\rm trad}\;\Gamma_{n,vj}^{Jp}}{{}^{\rm INR}\Gamma_n^{Jp\,\rm trad} + \Gamma_n^{Jp}} \tag{B11}$$

$$\text{with} \qquad {}^{\rm INR}\Gamma_n^{Jp\,\rm trad} = \langle \mathbf{F}_n^{B_Q\,Jp}|{}^{\rm opt}\mathbf{W}^{Jp}|\mathbf{F}_n^{B_Q\,Jp}\rangle\,, \tag{B12}$$

where $\mathbf{F}_n^{B_Q\,Jp}$ is a bound state function of the Hamiltonian $\mathbf{H}^{Jp}$ projected onto an appropriately chosen subspace Q (an indication of appropriateness is the energy $E_n^{B_Q}$ lying close to $E_n^{\rm res}$).

Based on these facts, the following three versions of the procedure for the determination of resonance parameters $E^{\rm res}$, Γ, and $\Gamma^{\rm trad}$ were exploited: [For simplicity, the indices J, p, n, v, and j are omitted hereafter.]

'exact' version

step 1. determination of the parameters $E^{\rm res}_{\rm SQ}$ and $\Gamma_{\rm SQ}$ by applying the Siegert quantization (SQ) method[4] to the Hamiltonian $\mathbf{H}(R)$. The implementation of the method is similar to that described in Ref. 9. The parameters are given here the subscript 'SQ' as they may slightly change in further steps.

step 2. application of the SQ method to the Hamiltonian $\mathbf{H}-\frac{i}{2}{}^{\rm opt}\mathbf{W}$. The resulting parameters are denoted as $E^{\rm res}_{\rm SQ1}$ and $\Gamma^{\rm tot}_{\rm SQ}$.

step 3. determination of the probabilities $P(E_i)$, Eq.(B7), at a grid of energies covering the interval $E^{\rm res}_{\rm SQ1}\pm 4\Gamma^{\rm tot}_{\rm SQ}$.

step 4. least squares fitting of the profile (B8) to the values of $P(E_i)$ for $i=1,\ldots,M$ (typically $M=17$). The values of $\Gamma^{\rm tot}_{\rm SQ}-\Gamma_{\rm SQ}$, $\Gamma_{\rm SQ}$, and $E^{\rm res}_{\rm SQ1}$ are used as initial guesses for the parameters of the profile $\Gamma^{\rm trad}$, Γ, and $E^{\rm res}$, respectively.

DW version

step 1. as in the 'exact' version

step 2. as in the 'exact' version

step 3. determination of the probabilities ${}^{\rm DW}P(E_i)$, Eq.(B9), at a grid of energy points covering the interval $E^{\rm res}_{\rm SQ}\pm 4\Gamma_{\rm SQ}$. The integral in Eq.(B9) was evaluated with the help of the log-derivative algorithm for free-free transition amplitudes[10,13], omitting the explicit determination of the function $\mathbf{F}^{(+)Jp}(E;R)$.

step 4. least squares fitting of the profile (B10) to the values of ${}^{\rm DW}P(E_i)$ for $i=1,\ldots,M$. In most cases the parameter ${}^{\rm DW}E^{\rm res}$ was fixed at the value of $E^{\rm res}_{\rm SQ}$.

INR version

step 1. determination of parameters $E^{\rm res}$ and Γ using the life-time matrix (LT) approach[11], implemented as described in Refs. 12,13. The values of $E^{\rm res}_{\rm LT}$ and $\Gamma_{\rm LT}$ agree with the values $E^{\rm res}_{\rm SQ}$ and $\Gamma_{\rm SQ}$, respectively, in at least three significant figures.

step 2. determination of the bound state function $\mathbf{F}^{BQ}$ of the Hamiltonian $\mathbf{H}(R)$ modified by adding an infinite wall at $R=R_\infty$. In most cases, the value $R_\infty=17\mathring{A}$ was used. The difference $|E^{BQ}-E^{\rm res}_{\rm LT}|$ was usually smaller than $\Gamma_{\rm LT}$ when $\Gamma_{\rm LT}\in[0.01,0.3]$ cm^{-1}.

step 3. evaluation of formula (B12) for $\Gamma^{\rm trad}$.

TABLE BV: Determination of parameters $E^{\rm res}$, Γ, and $\Gamma^{\rm trad}:=\Gamma^{\rm RCT+iRaT+RA}$ of quasi-bound states of the He^+-H_2 complex $(b\,k\,v_R\,J\,p)$ within the 3D optical potential model. A comparison of results obtained from three versions of the procedure: 'exact', DW (distorted-wave approximation), and INR (infinitely narrow resonance approximation). The parameters are given in cm^{-1}. The comparison is made in terms of relative percentage deviations $\delta x:=(^{\rm appr}x/^{\rm exct}x-1)\times 100\%$ for x=Γ, $\Gamma^{\rm trad}$ ♮.

State				'exact'				DW			INR
b	k	v_R	J^p	$E^{\rm res}$	Γ	$\Gamma^{\rm trad}\times 10^6$	$P^{\rm res\ a}$	$\delta\Gamma$	$\delta\Gamma^{\rm trad}$	$P^{\rm res\ b}$	$\delta\Gamma^{\rm trad}$
0	0	0	22^e	89.111	3.38 (−7)	109.46	1.226 (−2)	0.0	0.0	1296.700	0.0
0	0	1	19^e	50.693	2.26 (−6)	78.82	1.087 (−1)	0.0	−0.2	139.030	0.1
0	0	2	16^e	24.653	3.62 (−6)	53.55	2.366 (−1)	0.1	0.3	59.310	0.1
1	0	1	14^e	134.656	3.20 (−6)	79.94	1.482 (−1)	0.5	0.3	99.520	0.1
1	1	2	17^e	139.340	3.86 (−7)	51.64	2.945 (−2)	0.0	0.0	535.240	0.0
1	1	2	17^f	148.216	4.13 (−5)	48.37	9.938 (−1)	0.0	0.0	4.684	−0.1
2	2	3	2^e	126.465	6.89 (−5)	87.43	1.569 (−1)	−0.5	−0.3	5.081	0.0
2	2	3	3^e	133.510	3.41 (−4)	86.21	6.440 (−1)	0.0	0.0	1.010	0.0
3	3	2	3^e	300.906	2.87 (−4)	134.03	8.682 (−1)	0.0	0.0	1.869	0.0
2	1	1	4^e	5.279	1.72 (−2)	151.32	3.462 (−2)	0.3	0.0	0.035	−1.3
2	0	0	7^e	42.192	5.84 (−2)	160.34	1.093 (−2)	0.0	0.0	0.011	−0.8
2	2	1	13^e	33.265	4.65 (−2)	150.51	1.285 (−2)	0.0	0.0	0.013	−1.4
2	1	0	14^e	89.753	2.24 (−1)	161.24	2.877 (−3)	0.0	0.1	0.003	−3.3
3	1	0	2^e	200.007	1.11 (−1)	200.56	7.195 (−3)	0.0	0.0	0.007	−2.3

♮ Differences between values of $E^{\rm res}$ obtained from the 'exact' and DW versions were always $\ll 0.0001$ cm^{-1} and therefore are insignificant here.

[a] The height of the peak in $P(E)$ near $E^{\rm res}$.

[b] The value of $^{\rm DW}P(E^{\rm max})$ where $|E^{\rm max}-E^{\rm res}|<\Gamma$. The value is bigger than the corresponding value of $P^{\rm res}$ (in the eighth column) by the factor $(1+\Gamma^{\rm trad}/\Gamma)^2$. This is obviously the analog of the factor $(\Gamma^{\rm tot}/\Gamma)^2$ that appeared in the 1D model presented in Table BI.

COMMENTS

(i) The three groups of examples in the table illustrate the situations of $\Gamma\lll\Gamma^{\rm trad}$, $\Gamma\lesssim\Gamma^{\rm trad}$, and $\Gamma\ggg\Gamma^{\rm trad}$, respectively. In the first two situations, $^{\rm DW}P^{\rm res}>1$ which means a violation of unitarity by the DW approximation. However, no matter how strong the violation is, it does not impair the accuracy of the parameters, in particular of the $\Gamma^{\rm trad}$ parameter, determined according to the DW version of the procedure. The values of $|\delta\Gamma^{\rm trad}|$ rarely exceed 0.1%.

(ii) The INR version of the procedure is obviously much more convenient than the other two. However, the resulting values of $\Gamma^{\rm trad}$ may be in error by several per cent when the widths Γ are $\gtrsim 0.1$ cm^{-1}. Therefore application of the INR version to resonances with $\Gamma>0.1$ cm^{-1} was rather avoided in the study.

(iii) Obviously, the INR version can be adapted to the determination of the widths $\Gamma^{\rm trad}$ of bound states of the He^+-H_2 complex ($\Gamma=0$). Instead of the function $\mathbf{F}^{B_Q}$, function $\mathbf{F}^{B}$ of a given bound state of the (unprojected) Hamiltonian $\mathbf{H}$ should be determined at step 2 and inserted into formula (B12) at step 3. Results are presented in Fig. B8 and in Tables BVI-BIX.

Fig. B8. Applications of the 3D optical potential model

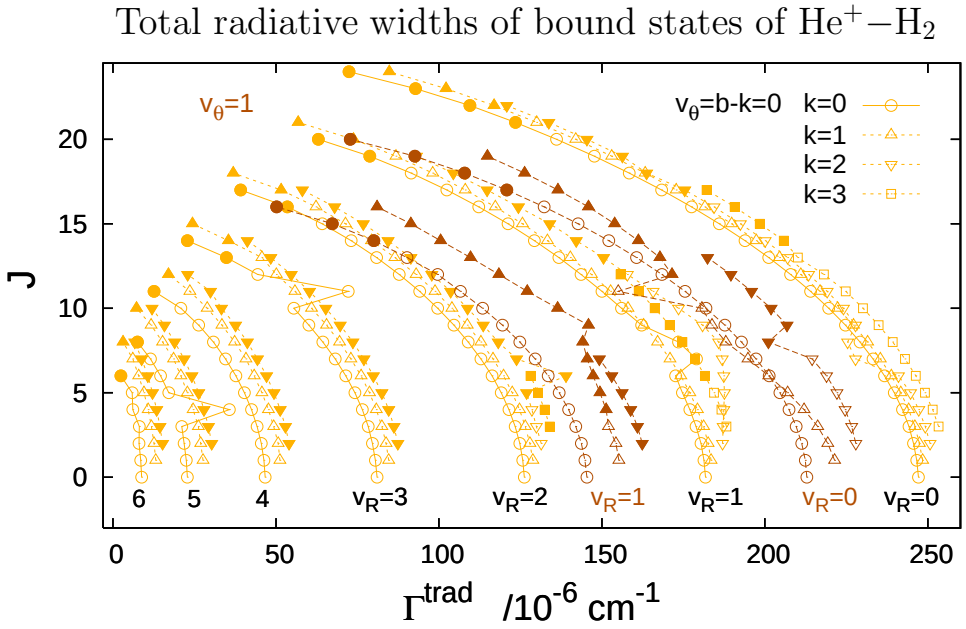

Fig. B8a. Radiative widths $\Gamma^{\rm trad}$=$\Gamma^{\rm RCT+RA+iRaT}$ of ro-vibrational states of the He^+-H_2(v=0) complex, $b\,k\,v_R\,J\,p$=1. The open symbols denote bound states, i.e. states of energies E<0 and E<118.37 cm^{-1} for b=0, 2 and b=1, 3, respectively, and the full symbols denote quasi-bound states of energies up to 354.03 cm^{-1} (the $\varepsilon_{v=0\,j=2}$ threshold). For clarity of the figure, some groups of states are omitted. All (603) bound states are listed in Tables BVI-BIX.

COMMENTS

(i) Fig. B8a, like Fig. B7b, exhibits strong correlations of the radiative widths $\Gamma^{\rm trad}$ with the vibrational (v_R and v_θ=b−k) and rotational (J, k) quantum numbers assigned to the states. The correlations are the same as those exhibited by the radiative widths $\Gamma_{(\to X_4)}$ in Fig. B4b and B5b. Thus, the analysis presented in the comments to these figures applies to the widths $\Gamma^{\rm trad}$, too.

(ii) The J dependence of the radiative widths can be approximated by the formula

$$\Gamma^{\rm rad}(J) \approx \Upsilon - \sum_{m=1}^{2} \gamma_m [J(J+1)-k^2]^m \,. \qquad \text{(B13)}$$

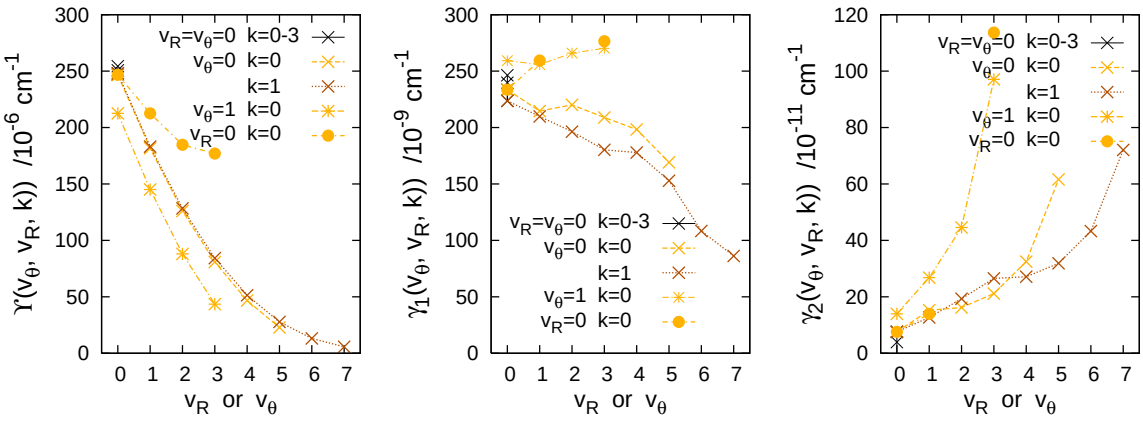

Fig. B8b. Parameters of formula (B13) fitted to values of $\Gamma^{\rm trad}$ of J levels in several groups (v_θ, v_R, k). Values evidently perturbed were excluded from the fit. The percentage deviation between the fitted and calculated values, averaged over levels in a given group, was usually below 1%.

The parameter Υ diminishes rapidly with growing v_R and less rapidly with growing v_θ (the residual dependence on k is very weak). The parameter γ_1 diminishes clearly with growing v_R and tends to grow slightly with the excitement of v_θ.

TABLE BVI: $He^+-H_2(I=0)$. Energies E (in cm^{-1}) and radiative widths $\Gamma^{trad}=\Gamma^{RCT+iRaT+RA}$ (in 10^{-6} cm^{-1}) of $b=0\,k=0\,v_R\,J\,p=1$ states. $E=0$ is at $v=0\,j=0$ threshold. Tunneling widths Γ (in cm^{-1}) are shown for $E>0$ states[a].

							$b=k=0$								
J	v_R	E	Γ	Γ^{trad}	v_R	E	Γ	Γ^{trad}	v_R	E	Γ	Γ^{trad}	v_R	E	Γ	Γ^{trad}
0	0	−817.03	0	247.1	1	−538.42	0	181.8	2	−326.28	0	126.2	3	−177.19	0	81.0
1		−813.06	0	246.6		−534.95	0	181.3		−323.36	0	125.7		−174.86	0	80.5
2		−805.13	0	245.6		−528.01	0	180.4		−317.52	0	124.8		−170.20	0	79.6
3		−793.26	0	244.2		−517.64	0	178.9		−308.79	0	123.4		−163.25	0	78.3
4		−777.48	0	242.2		−503.86	0	177.0		−297.22	0	121.5		−154.06	0	76.5
5		−757.80	0	239.7		−486.69	0	174.7		−282.85	0	119.1		−142.71	0	74.2
6		−734.28	0	236.7		−466.16	0	172.6		−265.74	0	116.3		−129.28	0	71.4
7		−706.96	0	233.2		−442.15	0	179.0		−245.99	0	112.9		−113.88	0	68.2
8		−675.90	0	229.2		−415.98	0	173.5		−223.68	0	109.0		−96.67	0	64.4
9		−641.18	0	224.7		−385.80	0	162.2		−198.95	0	104.6		−77.80	0	60.1
10		−602.85	0	219.6		−352.74	0	156.0		−171.93	0	99.6		−57.50	0	55.5
11		−561.03	0	214.0		−316.84	0	150.0		−142.81	0	94.1		−35.55	0	72.2
12		−515.79	0	207.9		−278.20	0	143.6		−111.78	0	87.8		−14.33	0	44.4
13		−467.27	0	201.2		−236.98	0	136.8		−79.12	0	80.9		7.96	1.2 (−7)	34.8
14		−415.58	0	193.9		−193.37	0	129.3		−45.16	0	73.1		29.00	2.7 (−1)	22.8
15		−360.87	0	186.0		−147.58	0	121.2		−10.35	0	64.2				
16		−303.30	0	177.5		−99.89	0	112.2		24.65	3.6 (−6)	53.5				
17		−243.06	0	168.3		−50.62	0	102.4		58.52	1.8 (−1)	39.2				
18		−180.36	0	158.4		−0.22	0	91.5								
19		−115.45	0	147.7		50.69	2.3 (−6)	78.8								
20		−48.63	0	136.1		101.02	4.5 (−2)	63.0								
21		19.72	∼0	123.5												
22		89.11	3.4 (−7)	109.5												
23		158.80	4.5 (−3)	92.8												
24		227.28	6.0 (−1)	72.4												
0	4	−83.21	0	46.7	5	−31.89	0	22.8	6	−9.11	0	8.8	7	−1.09	0	2.5
1		−81.48	0	46.3		−30.75	0	22.5		−8.46	0	8.5		−0.80	0	2.2
2		−78.03	0	45.5		−28.48	0	21.8		−7.20	0	8.0		−0.28	0	1.7
3		−72.93	0	44.2		−25.15	0	21.1		−5.38	0	8.1		0.32	9.7 (−2)	0.8
4		−66.22	0	42.5		−20.97	0	35.7		−3.15	0	6.1				
5		−58.01	0	40.3		−15.74	0	17.1		−0.66	0	5.9				
6		−48.43	0	37.7		−9.97	0	14.6		1.67	1.1 (−1)	2.4				
7		−37.64	0	34.5		−3.84	0	11.5								
8		−25.87	0	30.8		2.17	7.8 (−4)	7.5								
9		−13.43	0	26.3												
10		−0.78	0	20.8												
11		11.11	1.1 (−1)	12.6												

[a]The list of these shape resonances is limited to those with $\Gamma<1$ cm^{-1}.

TABLE BVII: $He^+-H_2(I{=}0)$. Energies E (in cm^{-1}) and radiative widths $\Gamma^{\rm trad}{=}\Gamma^{\rm RCT+iRaT+RA}$ (in 10^{-6} cm^{-1}) of $b{=}2\,k\,v_R\,J\,p$ states below $v{=}0\,j{=}2$ threshold[a]. $E{=}0$ is at $v{=}0\,j{=}0$.

	$b{=}2$ $k{=}2$					$b{=}2$ $k{=}1$					$b{=}2$ $k{=}0$		
		$p{=}1\,(e)$		$f-e$			$p{=}1\,(e)$		$f-e$				
J	v_R	E	$\Gamma^{\rm trad}$	E	$\Gamma^{\rm trad}$	v_R	E	$\Gamma^{\rm trad}$	E	$\Gamma^{\rm trad}$	v_R	E	$\Gamma^{\rm trad}$
2	0	−541.11	250.7	0.00	0.0								
3		−529.38	249.2	0.00	0.0								
4		−513.77	247.2	0.01	0.1								
5		−494.33	244.7	0.03	0.2								
6		−471.12	241.0	0.09	1.0								
7		−444.37	227.8	0.37	10.8								
8		−412.91	225.4	−0.35	9.3								
9		−378.71	227.8	−0.17	2.5								
10		−340.82	224.1	−0.10	1.3								
11		−299.44	219.1	−0.04	0.9								
12		−254.66	213.4	0.02	0.7								
13		−206.62	207.0	0.11	0.6								
14		−155.42	200.1	0.21	0.5								
15		−101.22	192.5	0.35	0.5								
16		−44.17	184.4	0.53	0.5								
17		15.52	175.4	0.78	0.6								
18		77.55	163.7	1.23	2.9								
19		142.32	156.3	1.25	0.1								
20		208.83	145.4	1.58	0.1								
21		277.02	133.7	1.96	0.0								
22		346.48	120.8	2.43	0.1								
0													
1						0	−264.34	221.4	0.30	0.0			
2	1	−253.93	187.0	0.04	0.8		−257.42	219.3	0.86	−0.9			
3		−243.46	187.2	0.24	5.1		−247.06	216.2	1.55	−5.3			
4		−229.54	187.4	−1.69	10.5		−233.31	212.0	4.66	−10.8			
5		−212.18	187.6	−1.71	0.2		−216.19	207.0	6.15	−0.6			
6		−191.42	187.4	−1.98	−5.9		−195.76	201.2	8.17	5.3			
7		−167.31	186.9	−2.44	−10.2		−172.08	194.8	10.64	9.4			
8		−139.90	185.8	−3.04	−13.7		−145.23	188.0	13.51	12.7			
9		−115.28	180.9	2.24	−13.6		−109.25	183.8	10.76	12.4			
10		−82.34	173.5	2.20	−11.3		−75.47	180.7	13.60	10.2			
11		−46.53	165.7	2.18	−9.0		−39.13	155.0	17.17	30.0			
12		−7.88	157.8	2.11	−7.0		1.54	171.5	19.57	6.9			
13		33.26	150.5	2.16	−6.2		44.23	167.8	22.97	3.2			
14		76.92	142.1	2.18	−4.9		89.75	161.2	26.42	1.8			
15		122.83	134.0	2.22	−4.4		137.85	153.9	29.97	0.4			
16		170.77	124.4	2.30	−3.1		188.35	145.9	33.60	−1.2			
17		220.45	114.8	2.40	−2.5		241.04	136.5	37.25	−2.2			
18		271.56	104.4	2.55	−1.9		295.67	126.3	40.87	−3.4			
19		323.64	93.1	2.74	−1.4		351.91	114.9					
0											0	−55.46	184.5
1						1	−22.48	155.2	0.21	−0.1		−51.89	183.8
2	2	−32.88	131.4	0.00	0.0		−16.30	154.3	0.63	−0.2		−44.76	182.5
3		−24.20	129.9	0.00	0.3		−7.06	152.0	1.24	0.4		−34.12	180.3
4		−12.66	128.5	0.01	−0.1		5.28	151.3	1.97	−1.1		−19.90	161.0
5		1.68	126.9	−0.02	−0.7		20.66	149.4	2.80	−1.9		−2.60	171.9
6		19.23	139.0	−0.47	−15.5		39.18	147.3	3.62	−3.1		17.64	154.2
7		38.12	123.8	0.42	−3.4		60.89	145.5	4.28	−5.1		42.19	160.3
8		60.50	118.2	0.42	−1.5		85.95	144.1	4.51	−8.1		68.53	154.7
9		85.34	113.6	0.49	−1.0		97.22	145.9	21.39	−14.9		114.62	143.1
10		112.47	108.8	0.60	−0.9		127.83	136.4	21.58	−10.9		146.96	141.4
11		141.80	103.6	0.72	−0.8		160.21	127.1	22.53	−7.9		182.88	138.0
12		173.16	97.8	0.86	−0.7		194.36	118.4	24.06	−6.1		222.07	132.5
13		206.34	91.4	1.02	−0.7		230.23	109.7	25.97	−5.2		264.18	125.6

14		241.08	84.4	1.19	−0.6		267.72	100.5	28.09	−4.6		308.85	117.1
15		277.06	76.8	1.38	−0.7		306.59	91.4	30.29	−5.2			
16		313.87	68.0	1.58	−0.5		346.48	81.0					
17		350.94	58.1	1.81	−0.4								
0											1	139.57	118.5
1						2	152.04	100.6	−0.04	−0.6		142.33	117.3
2	3	126.46	87.4	0.00	0.1		157.54	100.7	−0.18	−1.7		147.76	115.0
3		133.51	86.2	0.01	0.0		165.88	100.9	−0.51	−3.5		155.78	111.5
4		142.84	84.6	0.02	−0.1		177.12	101.1	−1.16	−5.8		166.15	107.0
5		154.38	82.5	0.03	0.0		178.77	101.8	10.31	−9.2		191.32	100.6
6		168.07	79.9	0.07	0.0		193.52	96.6	11.11	−7.2		208.43	99.3
7		183.81	77.0	0.11	−0.1		210.29	91.3	12.20	−5.7		228.32	96.6
8		201.47	73.6	0.17	−0.1		229.00	85.9	13.52	−4.7		250.84	92.9
9		220.91	69.7	0.25	−0.1		249.52	80.3	15.02	−4.2		275.78	87.9
10		241.98	65.3	0.34	−0.2		271.71	74.3	16.64	−3.9		302.90	81.8
11		264.44	60.3	0.46	−0.1		295.35	67.8	18.30	−4.1		331.87	73.1
12		288.03	54.7	0.59	−0.1		320.14	60.4	19.89	−4.4			
13		312.40	48.4	0.75	−0.1		345.68	51.9					
14		337.09	41.2	0.92	−0.1								
0											2	265.09	65.6
1						3	262.78	58.1	0.81	−1.0		268.02	64.1
2	4	232.00	54.0	0.00	0.0		265.69	57.6	1.94	−1.5		273.36	62.4
3		237.38	52.9	0.00	0.0		270.44	56.3	3.17	−1.7		280.87	60.5
4		244.48	51.3	0.01	0.1		277.01	54.3	4.48	−1.8		290.43	58.1
5		253.21	49.4	0.02	0.1		285.32	51.8	5.83	−1.8		301.94	55.1
6		263.47	47.1	0.05	0.0		295.23	48.8	7.22	−2.0		315.24	51.4
7		275.15	44.3	0.08	0.1		306.60	45.2	8.62	−2.1		330.13	46.7
8		288.08	41.2	0.13	0.0		319.24	41.0	9.97	−2.5		346.28	41.0
9		302.06	37.6	0.20	−0.1		332.86	36.1	11.29	−3.4			
10		316.85	33.3	0.28	0.0		347.11	30.3					
11		332.11	29.9	0.38	−1.4								
12		347.34	22.9	0.52	0.0								
0											3	330.42	28.2
1						4	323.51	27.0	0.41	−0.2		332.20	27.5
2	5	295.34	30.3	30.3	0.00		325.46	26.2	1.13	−0.3		335.60	26.2
3		299.16	29.3	29.3	0.00		328.47	25.0	2.03	−0.6		340.44	24.1
4		304.14	27.9	27.9	0.01		332.53	23.4	3.03	−1.0		346.46	21.3
5		310.21	26.3	26.3	0.02		337.55	21.1	4.03	−1.2		353.27	16.3
6		317.23	24.2	24.2	0.04		343.37	18.3	4.94	−1.7			
7		325.05	21.8	21.8	0.08		349.71	14.8					
8		333.46	18.9	18.9	0.13								
9		342.18	15.8	15.8	0.13								
10		350.82	12.0	12.0	0.23								
0											4	352.70	5.0
1						5	348.15	8.3	0.27	−0.1		353.44	4.2
2	6	329.24	15.2	0.00	0.0		349.05	7.6	0.73	−0.2			
3		331.72	14.4	0.00	0.0		350.41	6.7	1.26	−0.5			
4		334.92	13.4	0.00	0.1		352.16	5.3	1.74	−1.0			
5		338.73	12.1	0.02	0.0		354.15	4.4					
6		343.02	10.7	0.04	−0.1								
7		347.62	8.8	0.08	0.0								
8		352.26	6.7	0.13	0.0								
2	7	345.87	7.2	0.00	0.0								
3		347.36	6.7	0.00	0.0								
4		349.24	5.9	0.02	0.0								
5		351.37	4.9	0.04	0.0								
6		353.58	3.5	0.10	0.1								
2	8	353.07	2.3	0.01	0.0								

[a]The p=1 states above E=0 are quasi-bound. They are listed here again to display the effect of parity on the radiative widths.

TABLE BVIII: $He^+-H_2(I=1)$. Energies E (in cm^{-1}) and radiative widths $\Gamma^{trad}=\Gamma^{RCT+iRaT+RA}$ (in 10^{-6} cm^{-1}) of $b=1\,k\,v_R\,J\,p$ states below $v=0\,j=1$ threshold (at 118.37 cm^{-1}).

	b=1 k=1					b=1 k=0		
		p=1 (e)		p=−1				
J	v_R	E	Γ^{trad}	$E-E(e)$	$\Gamma^{trad}-\Gamma^{trad}(e)$	v_R	E	Γ^{trad}
1	0	−744.80	248.4	0.11	0.0			
2		−737.01	247.4	0.34	−0.1			
3		−725.35	246.0	0.68	−0.1			
4		−709.82	244.1	1.13	−0.2			
5		−690.48	241.7	1.69	−0.3			
6		−667.34	238.8	2.35	−0.5			
7		−640.47	235.4	3.12	−0.6			
8		−609.91	231.5	3.97	−0.8			
9		−575.73	227.2	4.92	−1.0			
10		−537.99	222.3	5.96	−1.2			
11		−496.80	216.9	7.07	−1.5			
12		−452.22	211.0	8.25	−1.7			
13		−404.39	204.5	9.49	−2.0			
14		−353.40	197.4	10.78	−2.3			
15		−299.40	189.8	12.11	−2.7			
16		−242.54	181.6	13.47	−3.0			
17		−182.99	172.8	14.84	−3.4			
18		−120.94	163.3	16.21	−3.7			
19		−56.63	153.0	17.55	−4.1			
20		9.69	142.0	18.84	−4.6			
21		77.67	130.0	20.05	−5.1			
0						0	−390.45	212.9
1	1	−462.00	183.5	0.10	0.0		−386.76	212.4
2		−455.17	182.6	0.31	−0.1		−379.38	211.3
3		−444.96	181.2	0.61	−0.1		−368.34	209.6
4		−431.39	179.3	1.01	−0.2		−353.66	207.4
5		−414.50	177.0	1.51	−0.3		−335.38	204.6
6		−394.32	174.2	2.10	−0.5		−313.55	201.3
7		−370.93	170.9	2.77	−0.6		−288.22	197.3
8		−344.38	167.1	3.52	−0.8		−259.48	192.8
9		−314.77	162.8	4.35	−1.0		−227.39	187.7
10		−282.17	158.0	5.24	−1.2		−192.07	181.9
11		−246.71	152.7	6.19	−1.4		−153.60	175.5
12		−208.51	146.8	7.18	−1.6		−112.14	168.4
13		−167.71	140.3	8.21	−1.9		−67.82	160.6
14		−124.49	133.3	9.26	−2.2		−20.82	152.1
15		−79.03	125.6	10.31	−2.5		28.65	142.7
16		−31.58	117.3	11.34	−2.8		80.34	132.3
17		17.57	108.1	12.33	−3.1			
18		68.06	98.1	13.22	−3.5			

0						1	−168.09	145.4
1	2	−245.16	128.8	0.09	0.0		−164.95	144.8
2		−239.38	127.9	0.26	−0.1		−158.68	143.7
3		−230.76	126.5	0.52	−0.1		−149.31	142.0
4		−219.30	124.7	0.87	−0.2		−136.87	139.8
5		−205.08	122.5	1.28	−0.3		−121.42	136.9
6		−188.13	119.8	1.78	−0.4		−103.03	133.5
7		−168.55	116.6	2.34	−0.5		−81.77	129.5
8		−146.42	112.9	2.96	−0.7		−57.76	124.8
9		−121.85	108.7	3.64	−0.8		−31.12	119.5
10		−94.97	104.0	4.36	−1.0		−2.00	113.4
11		−65.93	98.8	5.10	−1.2		29.42	106.6
12		−34.92	93.0	5.86	−1.4		62.92	99.6
13		−2.17	86.5	6.62	−1.7		98.08	90.2
14		32.06	79.3	7.35	−1.9			
15		67.41	71.3	8.01	−2.2			
16		103.41	62.3	8.56	−2.6			
0						2	−13.62	88.2
1	3	−90.40	84.6	0.07	0.0		−11.13	87.6
2		−85.75	83.8	0.21	0.0		−6.17	86.5
3		−78.81	82.5	0.43	−0.1		1.23	84.8
4		−69.62	80.8	0.70	−0.2		11.01	82.5
5		−58.25	78.7	1.04	−0.2		23.07	79.6
6		−44.77	76.1	1.43	−0.3		37.33	76.0
7		−29.30	73.0	1.87	−0.4		53.61	71.5
8		−11.94	69.5	2.35	−0.6		71.81	66.6
9		7.14	65.5	2.86	−0.7		91.59	60.8
10		27.77	60.9	3.38	−0.9		112.66	53.7
11		49.69	55.8	3.89	−1.0			
12		72.63	50.1	4.37	−1.3			
13		96.04	45.7	4.76	3.3			
0						3	76.69	43.5
1	4	10.41	51.2	0.06	0.0		78.44	43.0
2		13.93	50.7	0.17	0.0		81.90	41.8
3		19.16	49.3	0.33	−0.1		87.01	40.1
4		26.05	47.7	0.54	−0.1		93.68	37.7
5		34.52	45.7	0.79	−0.2		101.76	34.5
6		44.46	43.3	1.08	−0.3		111.01	30.5
7		55.75	40.8	1.38	−0.7			
8		68.16	37.3	1.75	−0.6			
9		81.54	33.4	2.07	−0.6			
10		95.57	28.9	2.37	−0.8			
11		109.83	23.6	2.61	−1.0			
0						4	114.93	11.9
1	5	69.27	27.6	0.04	0.0		115.81	11.1
2		71.72	26.9	0.12	0.0		117.46	9.4
3		75.34	26.2	0.24	0.3			
4		80.06	24.6	0.39	−0.1			
5		85.77	22.8	0.57	−0.2			
6		92.34	20.8	0.76	−0.2			
7		99.56	18.6	0.96	−0.3			
8		107.25	15.2	1.15	−0.4			
9		115.01	11.7	1.29	−0.5			
1	6	99.36	13.1	0.03	0.0			
2		100.90	12.6	0.09	0.0			
3		103.15	11.8	0.17	0.0			
4		106.03	10.8	0.27	−0.1			
5		109.42	9.5	0.39	−0.1			
6		113.17	7.9	0.51	−0.1			
7		117.05	6.1	0.63	−0.2			
1	7	113.14	5.7	0.02	0.0			
2		114.02	5.3	0.07	0.0			
3		115.26	4.7	0.13	0.0			
4		116.78	3.9	0.21	0.0			
1	8	118.17	1.1	0.03	0.0			

TABLE BIX: $He^+-H_2(I{=}1)$. Energies E (in cm^{-1}) and radiative widths $\Gamma^{trad}{=}\Gamma^{RCT+iRaT+RA}$ (in 10^{-6} cm^{-1}) of $b{=}3\,k\,v_R\,J\,p$ states. All states below $v{=}0\,j{=}1$ threshold are shown.

		$b{=}3\ k{=}3$					$b{=}3\ k{=}2$				
		$p{=}1\ (e)$		$f-e$			$p{=}1\ (e)$		$f-e$		
J	v_R	E	Γ^{trad}	E	Γ^{trad}		v_R	E	Γ^{trad}	E	Γ^{trad}
3	0	−214.54	253.3	0.00	0.0						
4		−199.15	251.5	0.00	0.0						
5		−179.97	249.1	0.00	0.0						
6		−157.03	246.3	0.00	0.0						
7		−130.38	243.0	0.00	0.0						
8		−100.08	239.2	0.00	0.0						
9		−66.19	234.9	0.01	0.0						
10		−28.79	230.1	0.01	0.0						
11		12.04	224.8	0.03	0.1						
12		56.18	218.1	0.08	0.9						
13		103.79	210.1	0.05	−4.5						
2							0	17.40	227.9	0.00	0.0
3	1	76.08	188.2	0.00	−0.3			28.20	226.6	0.02	0.0
4		89.61	186.7	0.00	0.0			42.55	224.6	0.06	0.0
5		106.47	184.4	0.00	0.0			60.41	222.1	0.15	0.1
6								81.71	218.9	0.30	0.2
7								106.40	214.5	0.57	0.5

Fig. B9. Some details on rate constant of RCT+RA+iRaT

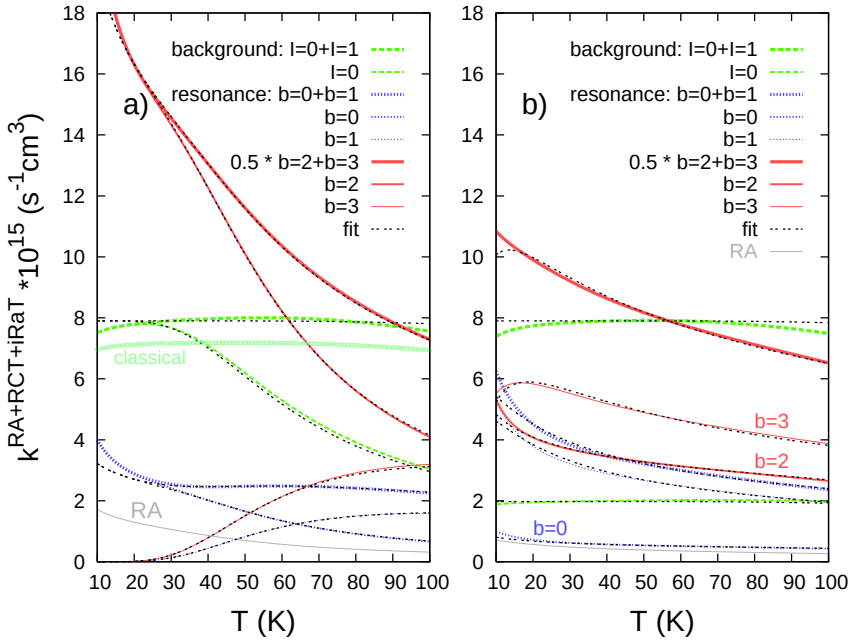

Fig. B9a. Rate constant $k^{\mathrm{RCT+RA+iRaT}}(:=k^{\mathrm{trad}})$ in temperature range 10−100 K (population of ortho- and para-H_2 in gas mixture appropriate for thermal equilibrium). Completion of Fig. 16b of the paper with analytical fits to various parts; formulas in Table BXa.
Note that the parts contributed by transitions from b=2 and b=3 resonances (red lines) are multiplied by a factor of 0.5 in the figure.

Comparison of the classical results used in Fig. 16b to represent the contribution of transitions from reactant continuum states with the background part of the function $k^{\mathrm{trad}}(T)$.
The values of $k^{\mathrm{trad(bck)}}$ are by ∼10% higher than the classical results. It is assumed that this difference represents the contributions of the broad shape resonances which were included into the background in the calculations of $k^{\mathrm{trad(bck)}}$.

Fig. B9b. Same as in Fig. B9a but for reactions in He^++H_2 gas mixtures with fixed 3:1 ('normal') population of ortho- and para-H_2. The respective rate constant functions are denoted by ${}_{\mathrm{n}}k^{\mathrm{rad}}$. Appropriately modified formulas of the analytical fit are given in Table BXb.

Fig. B9d. Comparison of resonance parts of the rate constant functions $k^{\mathrm{trad}}(T)$ and ${}_{\mathrm{n}}k^{\mathrm{trad}}(T)$ in the range 10–100 K. Crude analytical representations of these parts used in the discussion of the paper. The crosses and stars show values of $k^{\mathrm{trad(res)}}$ and ${}_{\mathrm{n}}k^{\mathrm{trad(res)}}$, respectively, obtained from test calculations in which energies of all resonances were shifted down by 5.5 cm^{-1}. These tests are referred to in the discussion of possible impact of a slight inaccuracy of the A-state PES (of its lowest part) on the size of the resonance contributions.

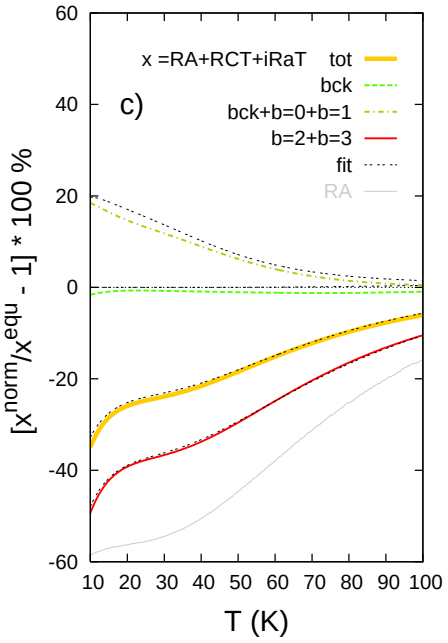

Fig. B9c. Rate constant function $k^{\mathrm{trad}}(T)$, total and various its parts, for the radiative reactions in the mixtures with 'normal' hydrogen compared to the respective functions for mixtures with 'equilibrium' hydrogen. See Table BXI.

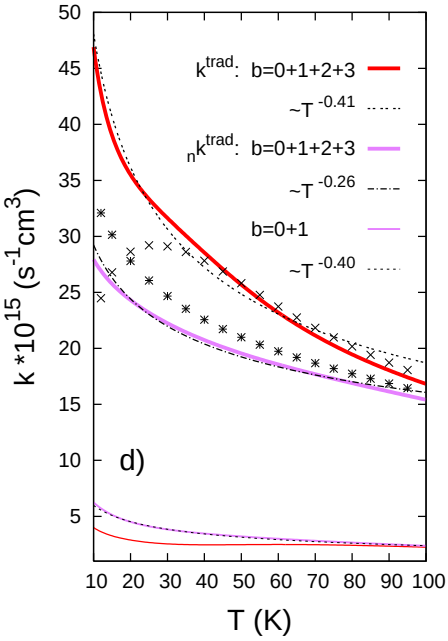

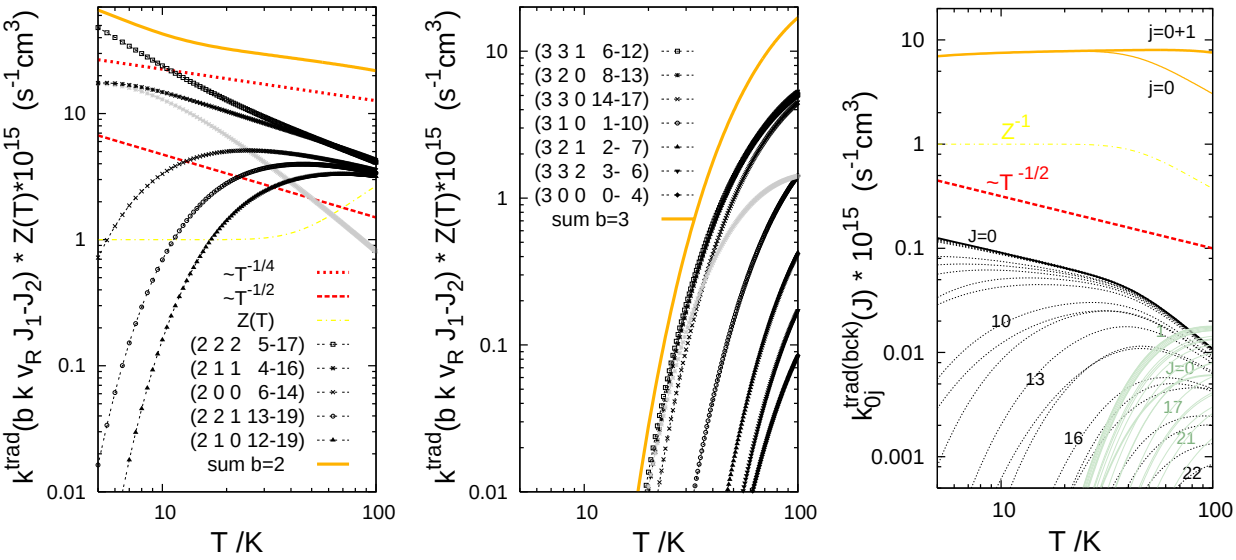

Fig. B9e. Details on temperature dependence of various parts of the rate constant $k^{\mathrm{RCT+RA+iRaT}}$. Thermal equilibrium assumed.

Left: Resonance part of k_{00}^{trad}.
The contribution of individual resonance $\mathcal{R}_n^J$ scales like $T^{-3/2}/Z(T)$ at $T \gg E_n^{J\,\mathrm{res}}/k_{\mathrm{B}}$ (gray line). The contribution of a group of resonances of energies $E_n^{J\,\mathrm{res}} \approx E_n + B_n J(J+1)$ for $J=J_1,\ldots,J_2$ scales like $T^{-1/2}/Z(T)$ at $T \gg E_n^{J_1\,\mathrm{res}}/k_{\mathrm{B}}$. The temperature dependence of the contribution summarized over different groups $n:=(b\,k\,v_R)$ becomes close to $T^{-1/4}/Z(T)$.

Middle: Resonance part of k_{01}^{trad}.
Here $E^{\mathrm{res}}/k_{\mathrm{B}} > T$ for all b=3 and b=1 resonances. Contribution of individual resonance (gray line) scales like $T^{-3/2}\exp(-E^{\mathrm{res}}/k_{\mathrm{B}}T)/Z(T)$. Correspondingly, the contribution of a group of resonances b=3 $k\,v_R$ $J=J_1-J_2$ scales like $T^{-1/2}\exp(-\widetilde{E}/k_{\mathrm{B}}T)/Z(T)$, where $\widetilde{E}$ is a parameter correlating with the lowest energy in the group $E^{J_1\,\mathrm{res}}$, usually $\widetilde{E} < E^{J_1\,\mathrm{res}}$.

Right: Partial (J) contributions to the backgrounds of $k_{I=0}^{\mathrm{trad}}(\approx k_{00}^{\mathrm{trad}})$ and $k_{I=1}^{\mathrm{trad}}(\approx k_{01}^{\mathrm{trad}})$.
The partial rate constants $k_{00}^{\mathrm{trad(bck)}}(T,J)$ decrease like $T^{-1/2}/Z(T)$ at temperatures $T \gg E_{\mathrm{cbr}}^J/k_{\mathrm{B}}$.

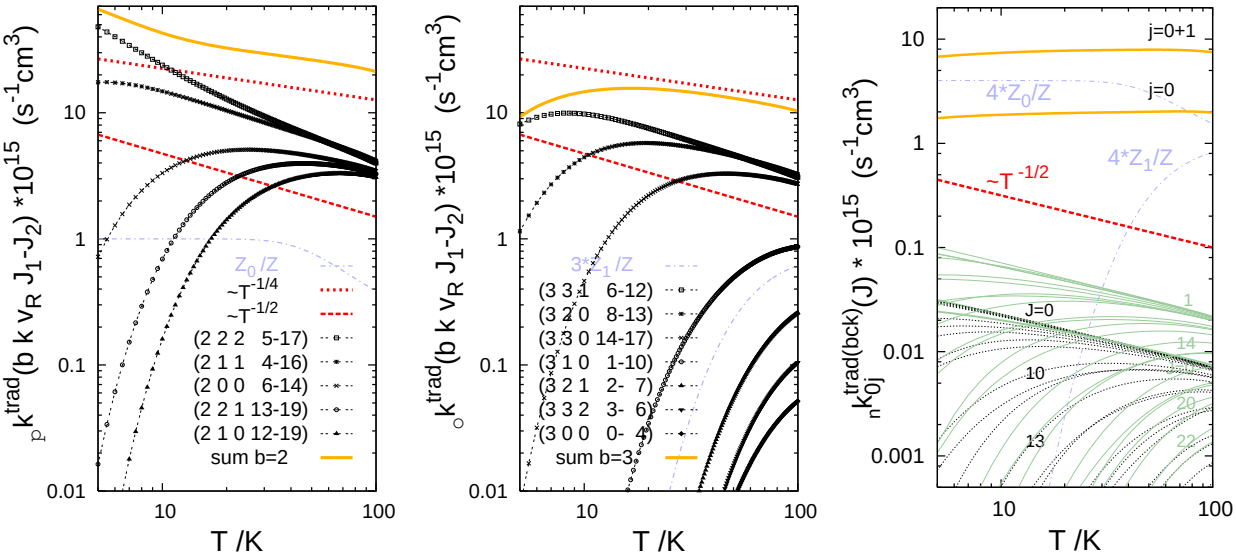

Fig. B9f. Same as in Fig. B9e for 'normal' hydrogen in the gas mixture, ${}_{\mathrm{n}}k^{\mathrm{trad}} = \frac{1}{4}\,{}_{\mathrm{p}}k^{\mathrm{trad}} + \frac{3}{4}\,{}_{\mathrm{o}}k^{\mathrm{trad}}$ with ${}_{\mathrm{p}}k^{\mathrm{trad}} = k_{I=0}^{\mathrm{trad}} \times \frac{Z}{Z_0}$ and ${}_{\mathrm{o}}k^{\mathrm{trad}} = k_{I=1}^{\mathrm{trad}} \times \frac{Z}{3Z_1}$, where $Z = Z_0 + 3Z_1$, see Table BX.

TABLE BX: Analytical representation of temperature dependence of $k^{\mathrm{RCT+RA+iRaT}}$ in the range 10−100 K

a) thermal equilibrium

$k_{I=0}^{\mathrm{RCT+RA+iRaT}}(T)$ [♭]				$k_{I=1}^{\mathrm{RCT+RA+iRaT}}(T)$ [♭]			
background	resonance (b=0, 2)			background	resonance (b=1, 3)		
$B/Z(T)$ [†]	$CT^{-\alpha}/Z(T)$			$9B\exp(-\frac{170.31}{T})/Z(T)$	$DT^{-1/2}\exp(-\beta/T)/Z(T)$		
B=7.9 [♮]	b	C [§]	α		b	D [♯]	β
	0	5.74	0.251		1	243.1	173.6
	2	67.5	0.242		3	1005.5	179.6

[♭] $k_{I=0}\approx k_{v=0\,j=0}$ since $\exp(-\varepsilon_{0\,2}/k_{\mathrm{B}}T)\approx 6\times10^{-3}$ at T=100 K and $k_{I=1}\approx k_{01}$.
[†] $Z(T)=1+9\exp(-170.31/T)+5\exp(-509.37/T)+21\exp(-1014.1/T)$. T in K. See Eq. (8) of the paper.
[♮] in unit of 10^{-15} s^{-1}cm^3. [§] in unit of 10^{-15} s^{-1}cm^{3}K$^{\alpha}$. [♯] in unit of 10^{-15} s^{-1}cm^{3}K$^{1/2}$.

b) fixed 3:1 ('normal') population of ortho- and para-H_2 in the gas mixture

${}_{\mathrm{n}}k_{I=0}^{\mathrm{RCT+RA+iRaT}}(T)=\frac{1}{4}\,{}_{\mathrm{p}}k^{\mathrm{trad}}(T)$		${}_{\mathrm{n}}k_{I=1}^{\mathrm{RCT+RA+iRaT}}(T)=\frac{3}{4}\,{}_{\mathrm{o}}k^{\mathrm{trad}}(T)$	
background	resonance (b=0, 2)	background	resonance (b=1, 3)
$B/4Z_0(T)$ [‡]	$CT^{-\alpha}/4Z_0(T)$	$9B\exp(-\frac{170.31}{T})/4Z_1(T)$ [‡]	$DT^{-1/2}\exp(-\beta/T)/4Z_1(T)$

[‡] $Z_0(T)=1+5\exp(-509.37/T)$ and $Z_1(T)=3\exp(-170.31/T)+7\exp(-1014.1/T)$.

COMMENT

As demonstrated in Fig. 16 of the paper, the rate constant function $k^{\mathrm{trad}}(T)$ changes when the way of thermal averaging is adapted to gas mixtures with 'normal' hydrogen. In panels b) to d) of the present figure, it is shown how the various parts of the rate constant function behave upon the adaptation in the range 10–100 K. The background part is seen to hardly change at all. This is attributed to the fact that the dependence of the cross-sections $\sigma_{0\,j}^{\mathrm{trad(bck)}}$ for j=0, 1 on the kinetic energy $E-\varepsilon_{0\,j}:=e$ is well-described by the capture model (see Fig. B7a) or, more specifically, that the averaged cross-sections $\frac{1}{2j+1}\sigma_{0\,j}^{\mathrm{trad(bck)}}(e)$ are almost independent of j, see Eq. (53). In turn the resonance parts of ${}_{\mathrm{n}}k^{\mathrm{trad}}(T)$ substantially differ from the respective resonance parts of $k^{\mathrm{trad}}(T)$. Unlike the backgrounds of the cross-sections, the resonance parts $\sigma_{0\,0}^{\mathrm{trad(res)}}(e)$ and $\frac{1}{3}\sigma_{0\,1}^{\mathrm{trad(res)}}(e)$ differ between each other, mainly because the positions of resonances b=3 relative to the threshold $\varepsilon_{0\,1}$ are quite different from the positions of resonances b=2 relative to $\varepsilon_{0\,0}$ (see Tables BII and BIV). The resonances b=3 lie on average higher. Therefore the b=3 contribution to the rate constant of the reaction with pure ortho-H_2 (the curve 'sum b=3' in the middle panel of Fig. B9f) is smaller than the b=2 contribution to the rate of the reaction with pure para-H_2 (the curve 'sum b=2' in the left panel), about 6 times at T=10 K and about 2 times at T>20 K. The values of the total rate constant for the 'normal' mixture, ${}_{\mathrm{n}}k^{\mathrm{trad}}(T)$, are smaller than the 'equilibrium values', $k^{\mathrm{trad}}(T)$, by 35% at T=10 K, 18% at 50 K, and only by 6% at 100 K. The total Feshbach resonance contribution (b=2+3) to the function ${}_{\mathrm{n}}k^{\mathrm{trad}}(T)$ at temperatures 10–100 K is 61–57% whereas the contribution made by these resonances at equilibrium ranges from 79 to 60%. Except for very low temperatures (shown in Fig. 16a), the shape resonances b=0, 1 are less important than the Feshbach resonances because of possessing smaller radiative widths Γ^{trad} or much too small dissociative widths Γ (see Tables I and BIII). It should nevertheless be noted that contribution of these resonances to ${}_{\mathrm{n}}k^{\mathrm{trad}}(T)$ is somewhat larger than to $k^{\mathrm{trad}}(T)$: 18 vs 7% at T=10 K, 12 vs 7% at 50 K, and 10 vs 9% at 100 K (see Table BXI).

TABLE BXI: Rate constants $k^{\rm rad}(T)$ (in 10^{-15} s^{-1}cm^3) for reactions RCT+RA+iRAT(:=trad) and RA in gas mixtures of He^+ ions with 'normal' (**n**) and 'equilibrium' (**e**) hydrogen at selected temperatures in the range 5−100 K. Resolution of the rate constant $k^{\rm trad}$ into contributions of transitions from continuum (bck), shape (b=0+1), and Feshbach (b=2+3) resonance states of He^++H_2 reactants. Percentage involvement of states of He^++H_2(I=1) pairs in the particular contributions compared to populations of I=1 states in the 'normal' and 'equilibrium' H_2 $^\diamondsuit$.

	$k^{\rm RCT+RA+iRaT}$		$k^{\rm trad}_{I=0+1}$			$\frac{I=1}{I=0+1}\times 100\%$			$\frac{k^{\rm trad}_{I=1}}{k^{\rm trad}_{I=0+1}}$	$\diamondsuit$	$k^{\rm RA}$		$k^{\rm RA(bck)}_{I=0+1}$	$\frac{k^{\rm RA}_{I=1}}{k^{\rm RA}_{I=0+1}}$
T	I=0+1	I=1	bck	b=0+1	b=2+3	bck	$\frac{b=1}{b=0+1}$	$\frac{b=3}{b=2+3}$	×100%		I=0+1	I=1		×100%
n														
5	39.1	19.3	6.9	8.6	23.5	75	82	30	49	*75*	0.90	0.31	0.37	34
7	37.3	21.0	7.2	7.4	22.7	75	83	41	56		0.80	0.29	0.34	37
10	35.4	21.8	7.5	6.2	21.7	75	84	51	62		0.71	0.28	0.31	40
15	33.5	21.8	7.7	5.1	20.7	75	84	57	65		0.63	0.26	0.28	42
20	32.1	21.3	7.8	4.5	19.8	75	84	59	66		0.57	0.24	0.26	43
25	31.0	20.7	7.8	4.1	19.1	75	84	60	67		0.52	0.23	0.24	43
30	30.1	20.1	7.8	3.8	18.4	75	84	60	67		0.48	0.21	0.22	44
35	29.3	19.6	7.9	3.6	17.8	75	84	60	67		0.45	0.20	0.21	44
40	28.6	19.2	7.9	3.5	17.3	75	84	60	67		0.43	0.19	0.21	45
45	28.0	18.7	7.9	3.3	16.8	75	83	60	67		0.41	0.18	0.20	45
50	27.5	18.4	7.9	3.2	16.3	75	83	60	67		0.39	0.18	0.19	46
55	27.0	18.0	7.9	3.1	15.9	75	83	60	67		0.37	0.17	0.19	46
60	26.5	17.7	7.9	3.0	15.6	74	83	60	67		0.35	0.17	0.18	47
65	26.0	17.3	7.9	2.9	15.2	74	83	60	67		0.34	0.16	0.17	47
70	25.6	17.0	7.9	2.8	14.9	74	83	60	67		0.33	0.16	0.17	48
75	25.1	16.7	7.8	2.7	14.6	74	82	59	67		0.32	0.15	0.17	48
80	24.7	16.4	7.8	2.7	14.2	74	82	59	66		0.30	0.15	0.16	48
85	24.2	16.1	7.7	2.6	13.9	74	82	59	66		0.29	0.14	0.16	48
90	23.8	15.8	7.6	2.5	13.6	74	82	59	66		0.28	0.14	0.15	49
95	23.3	15.5	7.6	2.4	13.3	74	82	59	66		0.28	0.14	0.15	49
100	22.9	15.2	7.5	2.4	13.0	74	82	59	66		0.27	0.13	0.14	49
e														
5	79.3	0.0	7.0	6.0	66.3	0	0	0	0	*0*	2.39	0.00	0.31	0
7	65.3	0.0	7.3	4.9	53.1	0	0	0	0	*0*	2.03	0.00	0.28	0
10	54.4	0.0	7.5	4.0	42.9	0	0	0	0	*0*	1.73	0.00	0.25	0
15	46.7	0.0	7.7	3.3	35.8	0	0	0	0	*0*	1.46	0.00	0.22	0
20	43.3	0.1	7.8	2.9	32.6	0	0	0	0	*0*	1.30	0.00	0.21	0
25	41.2	0.3	7.9	2.7	30.7	1	2	0	1	*1*	1.17	0.00	0.20	0
30	39.5	0.8	7.9	2.5	29.1	3	5	2	2	*3*	1.06	0.01	0.19	1
35	38.0	1.7	7.9	2.5	27.6	6	11	3	4	*6*	0.96	0.02	0.19	2
40	36.5	2.9	8.0	2.5	26.1	11	18	6	8	*11*	0.86	0.03	0.19	3
45	35.1	4.2	8.0	2.5	24.6	17	26	9	12	*17*	0.78	0.04	0.19	5
50	33.7	5.6	8.0	2.5	23.2	23	33	13	17	*23*	0.70	0.05	0.18	8
55	32.4	6.9	8.0	2.5	21.9	28	40	17	21	*29*	0.63	0.07	0.18	10
60	31.2	8.1	8.0	2.5	20.7	34	46	21	26	*34*	0.57	0.08	0.17	13
65	30.1	9.1	8.0	2.5	19.6	39	51	24	30	*40*	0.52	0.08	0.17	16
70	29.1	10.0	8.0	2.5	18.7	43	55	28	34	*44*	0.48	0.09	0.17	19
75	28.2	10.7	7.9	2.4	17.8	47	59	31	38	*48*	0.44	0.10	0.16	22
80	27.3	11.3	7.9	2.4	17.0	50	62	34	41	*51*	0.41	0.10	0.16	25
85	26.5	11.7	7.8	2.4	16.3	53	65	37	44	*55*	0.38	0.10	0.16	27
90	25.8	12.1	7.7	2.3	15.7	56	67	39	47	*57*	0.36	0.11	0.15	30
95	25.1	12.3	7.6	2.3	15.1	58	69	42	49	*59*	0.34	0.11	0.15	32
100	24.4	12.5	7.6	2.2	14.6	60	71	44	51	*61*	0.32	0.11	0.14	34

$\diamondsuit$ the population of I=1 states: 75% in the 'normal' and $3Z_1(T)/Z(T)\times 100\%$ in the 'equilibrium' hydrogen.

COMMENT

The percentage contributions of collisions of the He^+ ions with the ortho-H_2 in the gas mixture to the rate constants of the radiative reactions, shown by the ratios $k^{\rm rad}_{I=1}/k^{\rm rad}_{I=0+1}$ for rad=trad and rad=RA, are generally smaller than the population of the ortho-states in the hydrogen gas used in the mixture, no matter whether it is 'normal' or determined by the thermal equilibrium at a given temperature T. This is also an effect of the complex formation in the collisions (compare the data in columns seventh to eleventh).

---

[1] part A of this material: file Hep+HH_RCT_state2state.pdf.

[2] J. S. Cohen and J. N. Bardsley, Phys. Rev. **A18**, 1004 (1978); J. N. Bardsley, J. S. Cohen, and J. M. Wadehra, Phys. Rev. **A19**, 2129 (1979).

[3] M. Kimura and N. F. Lane, Phys. Rev. **A44**, 259 (1991) and references therein.

[4] A. F. J. Siegert, Phys. Rev. **56**, 750 (1939); O. Atabek and R. Lefebvre, Phys. Rev. **A22**, 1817 (1980); R. Lefebvre, J. Chem. Phys. **92**, 2869 (1990).

[5] F. H. Mies, J. Chem. Phys. **51**, 787 (1969).

[6] D. G. Hopper, J. Chem. Phys. **73**, 3289 (1980).

[7] F. Mrugała and W. P. Kraemer, J. Chem. Phys. **122**, 224321 (2005).

[8] part C of this material: file HepHH_prediss.pdf.

[9] F. Mrugała, J. Chem. Phys. **129**, 064314 (2008).

[10] F. Mrugała, J. Comput. Phys. **58**, 113 (1985).

[11] F. T. Smith, Phys. Rev. **118**, 349 (1960).

[12] F. Mrugała and R. Moszynski, J. Chem. Phys. **109**, 10823 (1998).

[13] F. Mrugała, Int. Rev. Phys. Chem. **12**, 1 (1993).

[1] part A of this material: file Hep+HH_RCT_state2state.pdf
[2] F. Mrugała and W. P. Kraemer, J. Chem. Phys. **122**, 224321 (2005) (paper II).
[3] C. C. Chuang, S. N. Tsang, W. Klemperer, and H. C. Chang, J. chem. Phys. **109**, 8836 (1998).
[4] F. Mrugała, V. Špirko, and W. P. Kraemer, J. Chem. Phys. **118**, 10547 (2003) (paper I).
[5] C. D. Thompson, C. Emmeluth, B. L. J. Poad, G. H. Weddle, and E. J. Bieske, J. Chem. Phys. **125**, 044310 (2006).
[6] U. Fano, Phys. Rev. **124**, 1866 (1961).
[7] F. H. Mies, Phys. Rev. **175**, 164 (1968).
[8] F. Mrugała, J. Chem. Phys. **129**, 064314 (2008).
[9] S. L. Holmgren, M. Waldman and W. Klemperer, J. Chem. Phys.**67**, 4414 (1977); L. Tao and M. H. Alexander, J. Chem. Phys. **127**, 114301 (2007) and references therein.
[10] F. Mrugała, Int. Rev. Phys. Chem. **12**, 1 (1993).
[11] O. I. Tolstikhin, S. Watanabe, and M. Matsuzawa, J. Phys. **B29**, L389 (1996); F. D. Colavecchia, F. Mrugała, G. A. Parker, and R. T Pack, J. Chem. Phys. **118**, 10387 (2003); F. Mrugała, 2004, unpublished.

C. SUPPLEMENTARY MATERIAL — PART C

$He^+–H_2$ COMPLEX

PREDISSOCIATION

VIBRATIONAL
versus
ROTATIONAL PREDISSOCIATION
below
the v=1 j=4 threshold

Fig. C1. $He^+-H_2(I=0)$ complex

$v=0-1$ $b=0-4$ k v_R $J=8^e$ levels

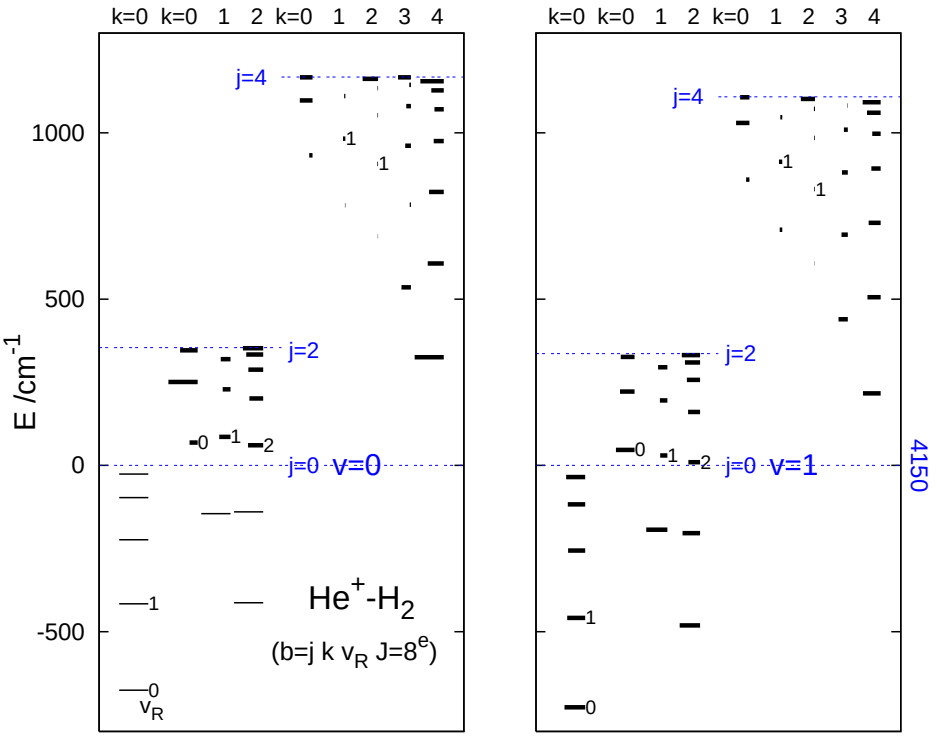

Complete assignment of all peaks plotted in Fig. A7 of Ref. 1 (except for the ones associated with the $j=6$ threshold). Additionally, the widths of the energy levels are indicated by the lengths of the thick lines. Specifically, the lengths are proportional to $|\log_{10}\Gamma|$ if $\Gamma>10^{-4}$ cm^{-1}. The two longest thick lines represent widths smaller than 10^{-4} cm^{-1}, see Table CI. The thin lines represent bound states energies. Their counterparts in the right panel are vibrationally predissociating states.

COMMENT

The structure of ro-vibrational energy levels of the He^+-H_2 complex is essentially the same as the structure revealed by van der Waals complexes belonging to the class of medium anisotropy of atom-diatom interaction, best exemplified by the Ar-HF complex. The fact has already been stressed in Ref. 2 (paper II). Considering here a larger part of the spectrum and the widths of the levels, one can note a major qualitative difference between He^+-H_2 and Ar-HF. The difference concerns the relative efficiency of rotational and vibrational predissociation.

It is a well-established fact[3] that stability of the Ar-HF complex against vibrational predissociation is much greater than its stability against rotational predissociation; the respective level widths differ by several orders of magnitude. No such disproportion occurs between the widths of vibrationally and rotationally predissociating states of He^+-H_2 (see Table CII). The fact should be attributed to the stronger (by about 10 times) binding of He^+-H_2 and to the relatively large separation of rotational levels in H_2.

TABLE CI: $He^+-H_2(I=0)$. Positions[a] (E) and widths[a] (Γ) of $b=j\,k\,v_R$ J=8 p=1 levels below the $v=0-1\,j=0-4$. The positions (ε_{vj}) of the thresholds[b] are listed in the headings. The positions of the levels are given relative to the respective $v\,j=0$ threshold. All data are in cm^{-1}.

	v=0							
	j=0 (ε=0)		j=2 (ε=354.03)					
	k=0		k=0		k=1		k=2	
v_R	E	Γ	E	Γ	E	Γ	E	Γ
0	−675.90	0	68.54	7.7 (−2)	−145.23	0	−412.91	0
1	−415.98	0	250.84	5.2 (−5)	85.99	3.0 (−2)	−139.90	0
2	−223.68	0	346.28	4.0 (−3)	229.00	8.8 (−2)	60.54	8.3 (−3)
3	−96.67	0			319.24	4.8 (−2)	201.47	1.3 (−2)
4	−25.87	0					288.08	8.9 (−3)
5							333.46	4.7 (−3)
6							352.26	1.7 (−3)
	v=1							
	j=0 (ε=4149.97)		j=2 (ε=336.11+4149.97)					
0	−727.52	1.4 (−3)	46.50	2.9 (−3)	−193.45	1.3 (−3)	−481.33	1.6 (−3)
1	−458.72	3.4 (−3)	221.91	1.0 (−2)	29.98	1.1 (−1)	−203.71	3.8 (−3)
2	−256.17	4.3 (−3)	326.09	1.3 (−2)	195.62	9.7 (−2)	9.64	2.4 (−2)
3	−117.03	4.0 (−3)			295.10	5.5 (−2)	160.88	2.2 (−2)
4	−35.25	2.5 (−3)					257.20	1.5 (−2)
5							309.44	8.4 (−3)
6							331.75	3.0 (−3)

	v=0 j=4 (ε=1167.63)									
	k=0		k=1		k=2		k=3		k=4	
v_R	E	Γ	E	Γ	E	Γ	E	Γ	E	Γ
0	932.48	3.6(−1)	782.21	1.1	689.02	9.0(−1)	535.48	4.9(−2)	325.49	5.3(−9)
1	1097.27	1.8(−2)	982.53	2.1	906.68	1.3	783.89	6.7(−1)	607.15	6.3(−3)
2	1166.74	1.9(−2)	1110.43	1.4	1052.69	1.3	961.41	1.7(−1)	822.24	9.6(−3)
3					1134.30	7.9(−1)	1080.52	2.2(−1)	975.47	4.0(−2)
4					1162.25	7.4(−3)	1144.21	5.7(−1)	1070.83	5.3(−2)
5							1167.06	1.7(−2)	1127.54	1.9(−2)
6									1155.25	6.0(−4)
	v=1 j=4 (ε=1108.40 + 4149.97)									
0	859.50	3.5(−1)	708.75	2.2	607.53	8.9(−1)	439.50	5.2(−2)	216.79	3.7(−3)
1	1029.99	1.5(−2)	913.02	2.7	831.08	1.3	693.82	1.3(−1)	505.51	1.6(−2)
2	1106.79	5.4(−2)	1046.97	1.8	984.67	1.3	880.79	1.6(−1)	729.35	2.2(−2)
3					1072.15	7.0(−1)	1009.62	2.8(−1)	892.67	5.4(−2)
4					1102.13	1.1(−2)	1082.23	8.8(−1)	997.24	6.9(−2)
5									1060.62	1.3(−2)
6									1092.15	3.3(−3)

[a] Results of convergent calculations within the CC-BF-diabatic approach of Ref. 4 (paper I).
The basis built of 28 ro-vibrational functions of H_2, for v=0−3 and j=0, 2 ... 12, was used. The Coriolis-coupling-reducing parameter $\lambda_{\max}$ was equal to b+2 giving maximally N=148 $v\,\mathrm{J}\,\lambda$ basis states.

[b] The values of ε_{vj} are as they result from the PES of the A-state of $HeHH^+$ and from the use of atomic masses in the calculations. In comparison with the accurate data for H_2, these values are too low by 0.34, 0.72, 11.20, 11.75, and 13.00 cm^{-1} for (v,j)=(0,2), (0,4), (1,0), (1,2), and (1,4), respectively. The deviations from the accurate values would be 0.15, 0.55, 10.13, 10.51, and 11.36 cm^{-1}, respectively, if the proton mass were used in the calculations.

TABLE CII: $He^+-H_2(I=0)$. Positions (E) and widths (Γ) of 'vibrational' levels (b=$j\,k\,v_R$ J=k p) below the v=0−1 j=0−4 thresholds. The positions are relative to the respective $v\,j$=0 threshold. The positions of j>0 thresholds are shown in lines marked with ε. All data are in cm^{-1}.

			v=0 (ε=0)				v=1 (ε=4149.97)			
			p=1		p=−1		p=1		p=−1	
j	k	v_R	E	Γ^a	$E-E(p{=}1)$	Γ^a	E	Γ^b	$E-E(p{=}1)$	Γ^b
0	0	0	−817.03	0			−868.92	1.9 (−3)		
		1	−538.42	0			−582.69	4.5 (−3)		
		2	−326.28	0			−360.90	6.3 (−3)		
		3	−177.19	0			−200.83	6.3 (−3)		
		4	−83.21	0			−96.51	4.7 (−3)		
		5	−31.89	0			−37.89	2.7 (−3)		
		6	−9.11	0			−11.64	1.1 (−3)		
2	2	0	−541.11	0	0.00	0	−609.49	2.1 (−3)	0.00	2.1 (−3)
		1	−253.93	0	0.04	0	−315.65	5.2 (−3)	0.01	5.3 (−3)
		2	−32.88	0	0.00	0	−85.81	7.9 (−3)	0.00	7.9 (−3)
		3	126.47	6.9 (−5)	0.00	0	83.25	8.3 (−3)	0.00	8.2 (−3)
		4	232.00	5.5 (−5)	0.00	0	198.09	6.7 (−3)	0.00	6.6 (−3)
		5	295.34	3.5 (−5)	0.00	0	268.54	4.4 (−3)	0.00	4.4 (−3)
		6	329.24	2.3 (−5)	0.00	0	306.62	2.4 (−3)	0.00	2.4 (−3)
		7	345.87	2.6 (−5)	0.00	0	325.42	1.2 (−3)	0.00	1.2 (−3)
		8	353.07	1.1 (−5)	0.01	0	334.18	5.3 (−4)	0.00	5.3 (−4)
	1	0	−264.34	0	0.30	0	−316.59	1.2 (−3)	0.28	1.3 (−3)
		1	−22.48	0	0.21	0	−68.26	6.9 (−3)	0.12	7.0 (−3)
		2	152.04	5.0 (−4)	−0.04	0	116.51	2.1 (−2)	−1.60	7.0 (−3)
		3	262.78	6.1 (−3)	0.81	0	235.42	9.9 (−3)	0.47	5.4 (−3)
		4	323.51	1.7 (−3)	0.41	0	302.64	4.7 (−3)	0.34	3.0 (−3)
		5	348.15	4.9 (−4)	0.27	0	329.49	1.5 (−3)	0.25	9.1 (−4)
	0	0	−55.46	0			−87.11	1.4 (−3)		
		1	139.57	2.1 (−2)			111.93	4.8 (−2)		
		2	265.09	1.5 (−2)			243.69	3.7 (−2)		
		3	330.42	6.7 (−3)			313.46	1.8 (−2)		
		4	352.70	1.1 (−3)			334.94	2.4 (−3)		
ε			354.03				336.11			

TABLE CII: continued

4	4	0	228.21	8.8 (−9)	0.00	0	118.97	4.4 (−3)	0.00	4.4 (−3)
		1	521.80	1.8 (−4)	0.00	1.7 (−4)	419.19	1.0 (−2)	0.00	1.0 (−2)
		2	749.69	2.5 (−4)	0.00	2.5 (−4)	655.27	1.4 (−2)	0.00	1.4 (−2)
		3	915.95	4.9 (−4)	0.00	4.2 (−4)	830.75	1.5 (−2)	0.00	1.5 (−2)
		4	1027.03	4.9 (−3)	0.01	3.2 (−3)	951.22	1.3 (−2)	0.00	1.3 (−2)
		5	1096.96	7.7 (−4)	0.00	1.2 (−4)	1027.78	8.3 (−3)	0.00	8.3 (−3)
		6	1135.54	2.2 (−3)	0.00	1.3 (−5)	1070.78	4.7 (−3)	0.00	4.7 (−3)
		7	1155.48	8.5 (−6)	0.00	< 1 (−14)	1093.10	2.7 (−3)	0.00	2.5 (−3)
	3	0	430.69	2.1 (−3)	0.00	2.0 (−3)	334.04	2.3 (−3)	0.00	2.0 (−3)
		1	692.82	4.1 (−3)	0.00	3.7 (−3)	602.39	1.1 (−2)	0.00	1.1 (−2)
		2	888.01	4.8 (−3)	0.00	4.5 (−3)	805.66	1.5 (−2)	0.00	1.4 (−2)
		3	1021.11	5.4 (−3)	0.00	4.7 (−3)	947.59	1.5 (−2)	0.00	1.4 (−2)
		4	1102.19	3.1 (−2)	0.03	9.3 (−3)	1036.43	3.8 (−2)	0.05	2.0 (−2)
		5	1143.35	9.6 (−3)	0.13	5.1 (−3)	1081.48	1.3 (−2)	−0.24	6.2 (−3)
		6	1161.50	1.7 (−2)	−0.05	2.1 (−4)	1100.95	1.7 (−3)	0.03	1.6 (−3)
	2	0	590.19	2.0 (−2)	0.06	1.5 (−2)	506.20	1.8 (−2)	0.04	1.3 (−2)
		1	823.97	3.3 (−2)	0.06	2.5 (−2)	745.28	3.0 (−2)	0.04	2.3 (−2)
		2	989.09	3.5 (−2)	0.06	2.7 (−2)	917.62	3.3 (−2)	0.04	2.6 (−2)
		3	1091.88	2.7 (−1)	0.04	2.2 (−2)	1027.65	5.7 (−2)	0.07	2.2 (−2)
		4	1145.00	4.4 (−2)	0.15	1.8 (−2)	1085.16	4.8 (−2)	0.16	1.8 (−2)
		5	1164.99	9.5 (−2)	−0.73	1.1 (−3)	1104.14	3.1 (−3)	0.75	1.2 (−3)
	1	0	696.32	4.3 (−1)	3.94	1.1 (−1)	623.57	3.9 (−1)	3.32	7.5 (−2)
		1	908.82	6.2 (−1)	3.34	1.7 (−1)	840.15	5.4 (−1)	2.79	1.2 (−1)
		2	1050.41	5.7 (−1)	2.82	1.5 (−1)	987.41	5.1 (−1)	2.37	1.0 (−1)
		3	1129.82	4.0 (−1)	2.24	8.5 (−2)	1071.46	3.7 (−1)	1.92	6.0 (−2)
		4	1162.74	1.9 (−1)	1.43	2.5 (−2)	1104.57	1.8 (−1)	1.23	1.4 (−2)
	0	0	746.45	2.8			680.59	3.1		
		1	949.35	3.6			886.93	3.9		
		2	1078.67	2.8			1020.34	2.9		
		3	1145.78	1.4			1089.54	1.4		
ε			1167.63				1108.40			

[a] All $\Gamma>0$ widths in the column are due to rotational predissociation.

[b] The red numbers in the column are the widths due to pure vibrational predissociation. The black numbers pertain to states which can predissociate both vibrationally and rotationally.

COMMENTS

(i) Tables CII and CIII (below) present further information on the energy levels structure of the complex compared to that given in Fig. 3 and Table IV of paper II.

(ii) One can note in the v=0 parts of the tables that there is a strong correlation of the widths due to pure rotational predissociation with the quantum number k. Among the states assigned with the same number b and different k's, $k=\frac{1-p}{2},\ldots,b$, the $k=b=J$ state possesses the smallest width, of the order of $\sim 5\times10^{-5}$ cm^{-1} for b=2 and $\sim10^{-4}$ cm^{-4} for b=4. The widths of the corresponding $b\,k=J=0$ states are larger by two orders of magnitude for b=2 and by four orders for b=4.

(iii) An inspection of the widths in the v=1 parts of the tables reveals that vibrational predissociation (VP) is the leading mechanism of decay of the states v_r=1 $b\,k\,v_R\,J=k$ with $k\geq2$, $\frac{\hbar}{\Gamma_{\rm VP}}\approx1$ ns, and is only slightly slower than the rotational predissociation (RP) of the b=2 $k=J=0$ states, $\frac{\hbar}{\Gamma_{\rm RP}}\approx0.5$ ns.

(iv) The total widths due to vibrational predissociation do not show much dependence on the numbers b and k of the states. However, the partial widths Γ_j, describing the decay into the open channels $H_2(v=0,j)$+He^+, correlate with these numbers very strongly, see Fig. C2.

TABLE CIII: $He^+-H_2(I=1)$. Positions (E) and widths (Γ) of 'vibrational' levels (b=$j\,k\,v_R$ J=k p) below the v=0−1 j=1−3 thresholds. The positions are relative to the respective $v\,j$=0 threshold. The positions of j>0 thresholds are shown in lines marked with ε. All data are in cm^{-1}.

			v=0 (ε=0)				v=1 (ε=4149.97)			
			p=1		p=−1		p=1		p=−1	
j	k	v_R	E	Γ^a	$E-E(p{=}1)$	Γ^a	E	Γ^b	$E-E(p{=}1)$	Γ^b
1	1	0	−744.80	0	0.11	0	−801.41	3.0 (−3)	0.11	3.0 (−3)
		1	−462.00	0	0.10	0	−511.55	5.7 (−3)	0.10	5.7 (−3)
		2	−245.16	0	0.09	0	−285.75	7.4 (−3)	0.09	7.4 (−3)
		3	−90.40	0	0.07	0	−120.87	7.3 (−3)	0.07	7.3 (−3)
		4	10.41	0	0.06	0	−10.46	5.7 (−3)	0.06	5.7 (−3)
		5	69.27	0	0.04	0	55.48	3.6 (−3)	0.04	3.6 (−3)
		6	99.36	0	0.03	0	89.46	1.8 (−3)	0.03	1.8 (−3)
		7	113.14	0	0.02	0	105.19	8.4 (−4)	0.02	8.4 (−4)
		8	118.17	0	0.03	0				
	0	0	−390.45	0			−429.40	1.3 (−3)	0.00	1.3 (−3)
		1	−168.09	0			−199.88	2.9 (−3)	0.00	2.9 (−3)
		2	−13.62	0			−35.25	3.3 (−3)	0.00	3.3 (−3)
		3	76.69	0			65.42	2.4 (−3)	0.00	2.4 (−3)
		4	114.93	0			108.95	7.0 (−4)	0.00	7.0 (−4)
ε			118.37				112.38			
3	3	0	−214.54	0	0.00	0	−300.63	2.7 (−3)	0.00	2.7 (−3)
		1	76.08	0	0.01	0	−3.28	6.7 (−3)	0.00	6.7 (−3)
		2	300.91	2.9 (−4)	0.00	2.5 (−3)	229.96	1.0 (−2)	0.00	1.0 (−2)
		3	466.08	1.4 (−2)	0.03	6.9 (−2)	402.09	1.1 (−2)	0.00	1.0 (−2)
		4	572.86	2.1 (−2)	0.05	1.5 (−4)	520.51	8.6 (−3)	0.00	8.5 (−3)
		5	639.50	2.3 (−5)	0.00	1.3 (−4)	594.22	5.8 (−3)	0.00	5.8 (−3)
		6	676.00	1.4 (−5)	0.00	1.3 (−4)	635.07	3.2 (−3)	0.00	3.2 (−3)
		7	694.50	6.6 (−5)	0.00	5.3 (−4)	666.08	7.9 (−4)	0.00	7.7 (−4)
	2	0	17.40	0	0.00	0	−54.48	2.2 (−3)	0.00	2.2 (−3)
		1	271.14	4.3 (−3)	0.00	3.1 (−2)	205.54	9.0 (−3)	0.00	7.9 (−3)
		2	457.69	5.1 (−3)	0.01	3.2 (−2)	400.43	1.1 (−2)	0.01	9.6 (−3)
		3	582.03	7.3 (−3)	0.04	2.9 (−2)	533.90	1.4 (−2)	0.07	7.8 (−3)
		4	653.47	2.4 (−2)	0.34	5.9 (−3)	612.87	8.5 (−3)	0.09	5.7 (−3)
		5	689.24	4.3 (−3)	−0.03	4.9 (−3)	651.59	2.6 (−3)	0.11	2.5 (−3)
		6	702.19	5.9 (−5)	0.05	2.1 (−1)	665.70	8.4 (−4)	0.04	8.3 (−4)
	1	0	194.58	3.9 (−2)	1.14	7.3 (−3)	138.12	2.9 (−2)	0.96	2.2 (−3)
		1	414.31	5.4 (−2)	0.99	1.6 (−2)	362.77	3.9 (−2)	0.81	3.8 (−3)
		2	564.83	5.1 (−2)	0.84	1.8 (−2)	520.28	3.6 (−2)	0.68	4.0 (−3)
		3	653.30	4.0 (−2)	0.65	1.3 (−2)	615.36	2.6 (−2)	0.51	2.7 (−3)
		4	694.13	2.7 (−2)	0.38	5.2 (−3)	658.86	1.5 (−2)	0.20	9.6 (−4)
3	0	0	295.26	3.5 (−1)			252.33	1.1 (−1)		
		1	492.21	4.1 (−1)			452.03	1.2 (−1)		
		2	617.33	3.0 (−1)			581.39	8.2 (−2)		
		3	682.11	1.4 (−1)			648.63	3.7 (−2)		
		4	704.10	2.5 (−2)			668.75	3.8 (−2)		
ε			704.83				669.12			

[a] All Γ>0 widths in the column are due to rotational predissociation.
[b] The red numbers in the column are widths due to pure vibrational predissociation.

Fig. C2. He^+-H_2

Vibrationally predissociating states below v=1 threshold

Populations of decay channels $H_2(v{=}0, j)$ + He^+

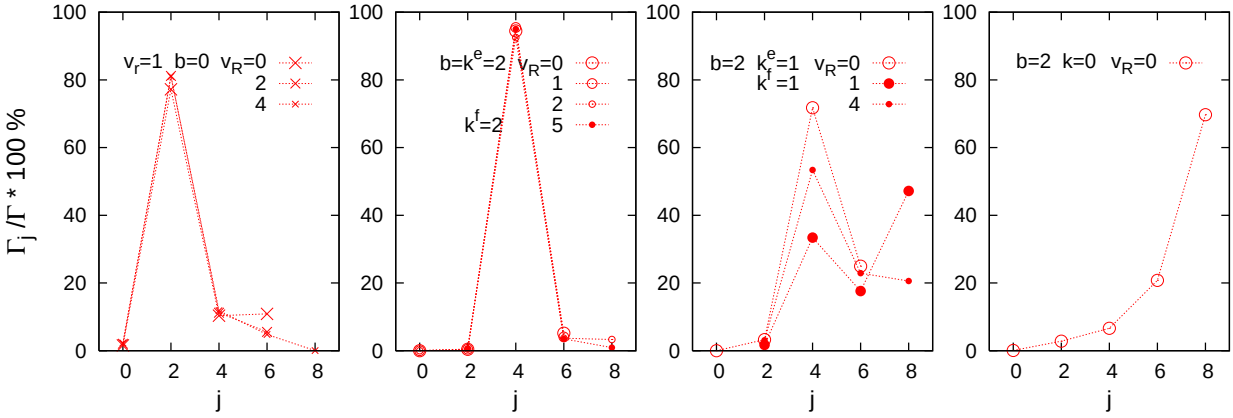

Fig. C2a. Populations Γ_j/Γ due to vibrational predissociation of the states $v_r{=}1\, b{=}0, 2\, k{=}0{-}b\, v_R\, J{=}k\, p$ for selected values of v_R. The energies and the total dissociative widths of the states $\Gamma{=}\sum_j \Gamma_j$ are in the last four columns of Table CII.

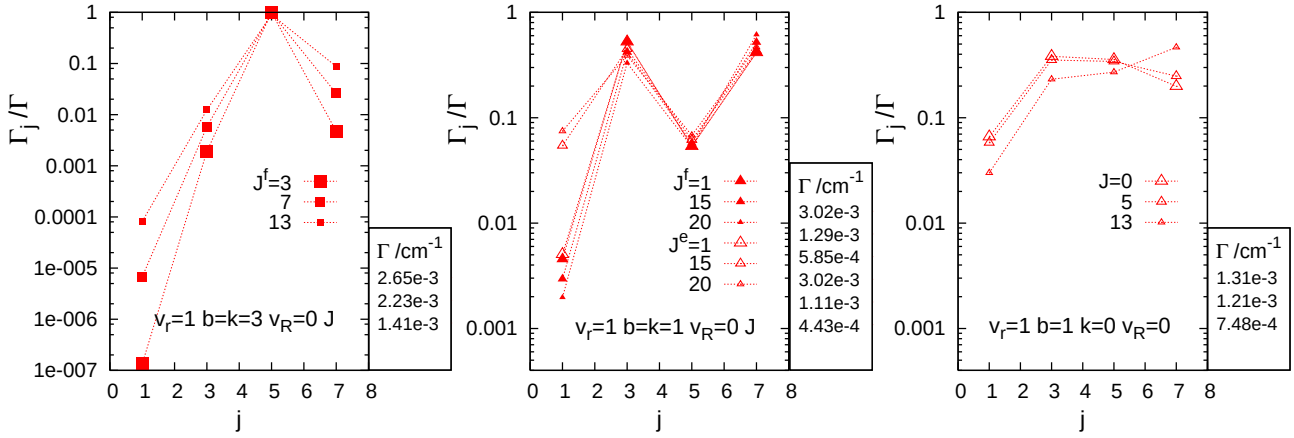

Fig. C2b. Populations Γ_j/Γ due to vibrational predissociation of the states $v_r{=}1\, b{=}1, 3\, k{=}0{-}b\, v_R{=}0\, J\, p$ for selected values of J. The total widths Γ are for J's listed in the legends. Note that the widths diminish with growing J. The energy splitting of the $J^f{=}20$ and $J^e{=}20$ states shown in the middle panel is as large as 19.0 cm^{-1} whereas the widths Γ of these states differ as little as $1.42{\times}10^{-4}$ cm^{-1}.

COMMENTS

(i) There is a strong $b{-}j{=}2$ propensity in the decay of the $b{=}k$ states (having T-shape geometry). With growing quantum number $v_\theta{=}b{-}k$, i.e. with increasing departure from the T-shape geometry, the propensity weakens; the populations tend to become peaked at the highest open channel.

(ii) Effects of (e,f) parity of the states on the vibrational predissociation widths are very small.

(iii) The properties of vibrational predissociation of the He^+-H_2 complex illustrated here are expected to be qualitatively the same as properties of complexes formed by the H_2 (D_2) molecules with other atomic cations. The Li^+-D_2 complex in particularly interesting since its infrared spectrum has recently been measured[5] and a lower bound for the vibrational predissociation lifetime of $v_r{=}1$ states has been provided.

ROTATIONAL PREDISSOCIATION
below
the j=2 and j=3 thresholds

Fig. C3. $He^+-H_2(I=0)$

Rotationally predissociating states below $v=0\ j=2$ threshold

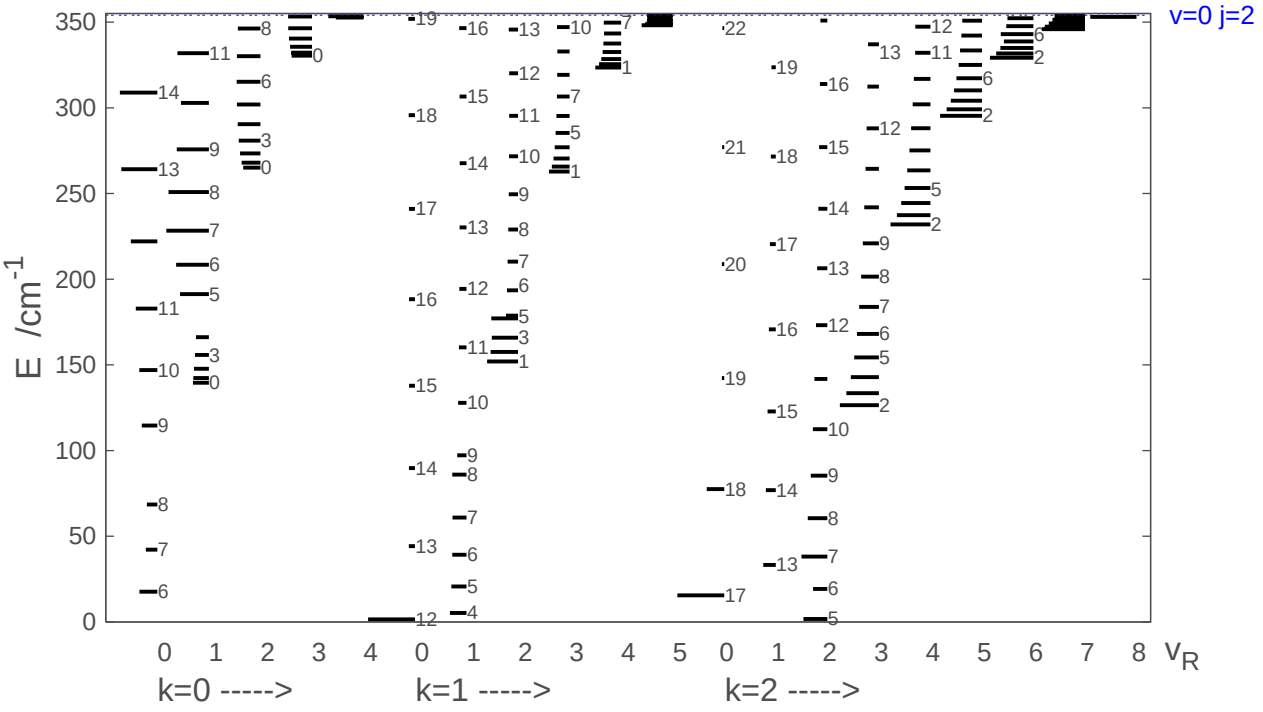

Fig. C3a. The structure of energy levels and their widths (the lengths of the lines show $-\log_{10}\Gamma$). The assignment of the levels with the quantum numbers k, v_R, and J (the numbers next to the lines). See Table CIV.

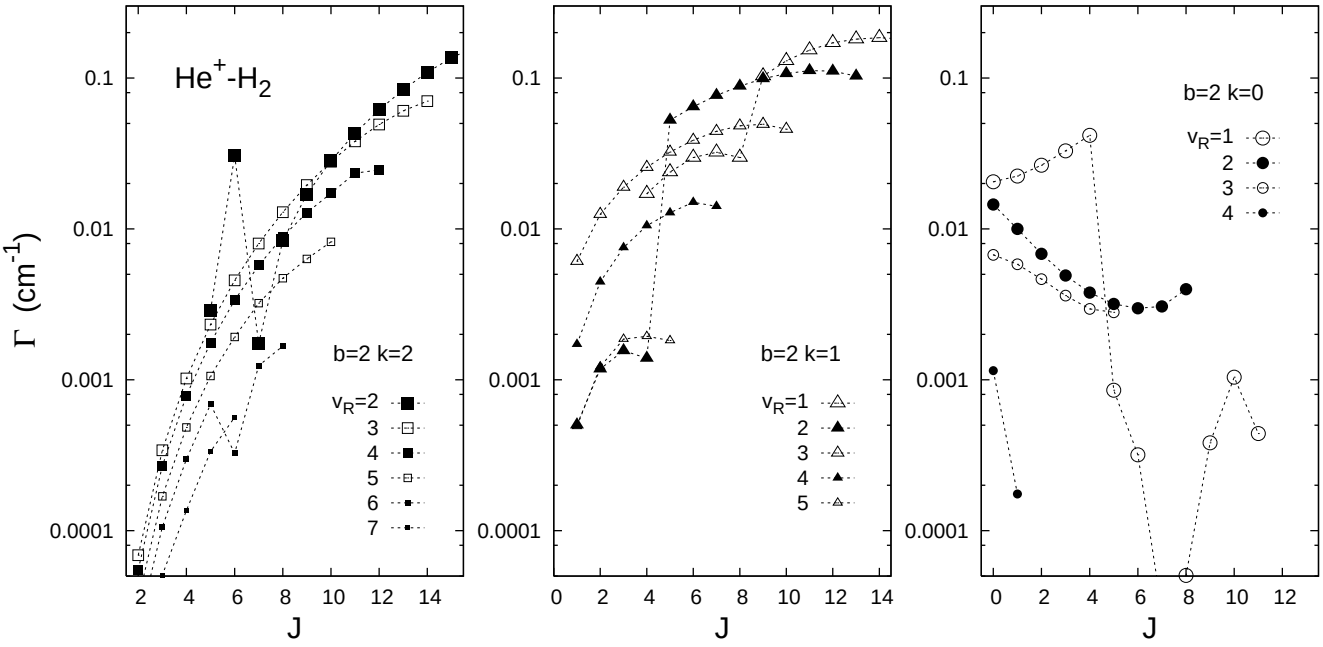

Fig. C3b. The widths of the states: correlations with the quantum number v_R, $v_\theta=b-k$, k, and J.

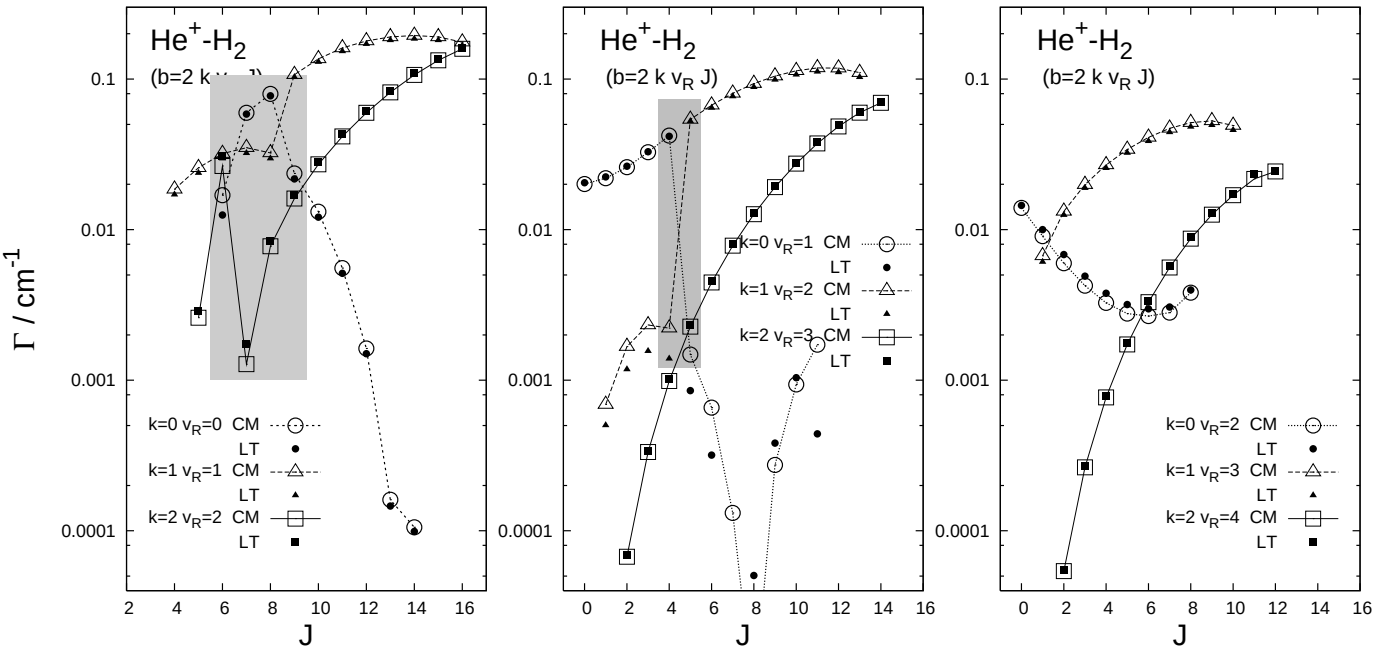

Fig. C3c. The widths of the states: 'exact' (**L**ife-**T**ime matrix) and perturbative (bound-continuum **C**onfiguration **M**ixing†) results.

† The theory of Fano[6,7] applied to the Hamiltonian in the CC-SF-adiabatic representation defined in Fig. A2d of part A (see also Fig. C5 and Table CVI).

COMMENTS

(i) Fig. C3a and Table CIV provide further information on the predissociating states of the He^+-H_2 complex compared to that given in Fig. 4 and Table VI of paper II. All b=2 states with Γ<1 cm^{-1} in the energy range of 0 – 354.0 cm^{-1} are shown. There are six $k\,v_R$ groups of the states which lie entirely above 300 cm^{-1}.

(ii) Figs. C3b and C3c expose the correlations of the predissociation widths with the quantum numbers assigned to the states.

- The dependence on the number J differs qualitatively between k>0 and k=0 states. The growth with J testifies to the dominance of Coriolis interaction in the predissociation of k>0 states. The overall tendency of the widths of k=0 states to decline with growing J indicates that potential anisotropy is an important factor in the decay of these states. [The nonadiabatic coupling which is mostly responsible for these widths within the CC-SF-adiabatic representation (see the red curves in Fig. C5, does not grow with J).]

- The widths diminish with increasing v_R but grow with v_θ=$b-k$ increasing from 0 to $b-1$.

(iii) The disturbances in the behavior of k=0 and k=1 curves in Fig. C3c give evidence of a strong interplay between the two sources of bound-continuum configuration mixing in the complex: the anisotropy of the A-state PES and the Coriolis interaction. An insight into these disturbances, into pathways of decay of the quasi-bound states, can be gained if an appropriate perturbation scheme is applied[8].

(iv) The consistency of the CM and LT results demonstrated in Fig. C3c and in Table CVI proves that the perturbative resonance theory of Fano, when implemented within the CC-SF-adiabatic representation of the respective Hamiltonian, can adequately describe many cases of rotational predissociation in atom-diatom complexes even if the anisotropy of involved interactions is not weak (but it is intermediate).

TABLE CIV: $He^+-H_2(I{=}0)$. Energies[a] (E) and widths[a] (Γ) of rotationally predissociating states below the $v{=}0\,j{=}2$ threshold, $b{=}2\,k\,v_R\,J\,p{=}1$. All data are in cm^{-1}.

	$k=2$			$k=1$			$k=0$		
J	v_R	E	Γ	v_R	E	Γ	v_R	E	Γ
17	0	15.53	3. (−15)[b]						
18		77.55	1.3 (−2)						
19		142.32	5.6 (−1)						
20		208.83	5.6 (−1)						
21		277.02	6.1 (−1)						
22		346.48	6.4 (−1)						
12				0	1.54	1. (−16)[b]			
13	1	33.26	4.7 (−2)		44.23	2.2 (−1)			
14		76.92	8.9 (−2)		89.75	2.2 (−1)			
15		122.83	1.3 (−1)		137.85	2.3 (−1)			
16		170.77	1.8 (−1)		188.35	2.3 (−1)			
17		220.45	2.4 (−1)		241.04	2.2 (−1)			
18		271.56	3.0 (−1)		295.67	2.1 (−1)			
19		323.64	3.5 (−1)		351.91	1.9 (−1)			
4				1	5.28	1.7 (−2)			
5	2	1.72	2.9 (−3)		20.69	2.4 (−2)			
6		19.26	3.1 (−2)		39.21	3.0 (−2)	0	17.64	1.2 (−2)
7		38.16	1.7 (−3)		60.92	3.2 (−2)[c]		42.19	5.8 (−2)[c]
8		60.54	8.3 (−3)		85.99	3.0 (−2)[c]		68.53	7.7 (−2)[c]
9		85.34	1.7 (−2)		97.22	1.0 (−1)[c]		114.62	2.1 (−2)[c]
10		112.47	2.8 (−2)		127.83	1.3 (−1)		146.96	1.2 (−2)
11		141.80	4.3 (−2)		160.21	1.5 (−1)		182.88	5.1 (−3)
12		173.16	6.1 (−2)		194.36	1.7 (−1)		222.07	1.5 (−3)
13		206.34	8.4 (−2)		230.23	1.8 (−1)		264.18	1.5 (−4)
14		241.08	1.1 (−1)		267.72	1.8 (−1)		308.85	9.9 (−5)
15		277.06	1.4 (−1)		306.59	1.8 (−1)			
16		313.87	1.6 (−1)		346.48	1.7 (−1)			
17		350.94	1.8 (−1)						
0							1	139.57	2.0 (−2)
1				2	152.04	5.0 (−4)		142.33	2.2 (−2)
2	3	126.46	6.9 (−5)		157.54	1.2 (−3)		147.76	2.6 (−2)
3		133.51	3.4 (−4)		165.88	1.6 (−3)		155.78	3.3 (−2)
4		142.84	1.0 (−3)		177.12	1.4 (−3)[c]		166.15	4.2 (−2)[c]
5		154.38	2.3 (−3)		178.77	5.2 (−2)[c]		191.32	8.5 (−4)[c]
6		168.07	4.6 (−3)		193.52	6.4 (−2)[c]		208.43	3.2 (−4)[c]
7		183.81	8.0 (−3)		210.29	7.7 (−2)		228.32	2.9 (−5)
8		201.47	1.3 (−2)		229.00	8.8 (−2)		250.84	5.0 (−5)
9		220.91	1.9 (−2)		249.52	9.9 (−2)		275.78	3.8 (−4)
10		241.98	2.8 (−2)		271.71	1.1 (−1)		302.90	1.0 (−3)
11		264.44	3.8 (−2)		295.35	1.1 (−1)		331.87	4.4 (−4)
12		288.03	4.9 (−2)		320.14	1.1 (−1)			
13		312.40	6.1 (−2)		345.68	1.0 (−1)			
14		337.09	7.0 (−2)						

TABLE CIV: continued

0							2	265.09	1.4 (−2)
1				3	262.78	6.1 (−3)		268.02	1.0 (−2)
2	4	232.00	5.5 (−5)		265.69	1.2 (−2)		273.36	6.8 (−3)
3		237.38	2.7 (−4)		270.44	1.9 (−2)		280.87	4.9 (−3)
4		244.48	7.8 (−4)		277.01	2.6 (−2)		290.43	3.8 (−3)
5		253.21	1.8 (−3)		285.32	3.2 (−2)		301.94	3.2 (−3)
6		263.47	3.4 (−3)		295.23	3.9 (−2)		315.24	3.0 (−3)
7		275.15	5.7 (−3)		306.60	4.4 (−2)		330.13	3.1 (−3)
8		288.08	8.9 (−3)		319.24	4.8 (−2)		346.28	4.0 (−3)
9		302.06	1.3 (−2)		332.86	4.9 (−2)			
10		316.85	1.7 (−2)		347.11	4.6 (−2)			
11		332.11	2.3 (−2)						
12		347.34	2.5 (−2)						
0							3	330.42	6.7 (−3)
1				4	323.51	1.7 (−3)		332.20	5.8 (−3)
2	5	295.34	3.5 (−5)		325.46	4.4 (−3)		335.60	4.6 (−3)
3		299.16	1.7 (−4)		328.47	7.5 (−3)		340.44	3.6 (−3)
4		304.14	4.8 (−4)		332.53	1.0 (−2)		346.46	2.9 (−3)
5		310.21	1.1 (−3)		337.55	1.3 (−2)		353.27	2.8 (−3)
6		317.23	1.9 (−3)		343.37	1.5 (−2)			
7		325.05	3.2 (−3)		349.71	1.4 (−2)			
8		333.46	4.7 (−3)						
9		342.18	6.3 (−3)						
10		350.82	8.2 (−3)						
0							4	352.70	1.1 (−3)
1				5	348.15	4.9 (−4)		353.44	1.7 (−4)
2	6	329.24	2.3 (−5)		349.05	1.2 (−3)			
3		331.72	1.1 (−4)		350.41	1.9 (−3)			
4		334.92	3.0 (−4)		352.16	1.9 (−3)			
5		338.73	6.9 (−4)		354.15	1.8 (−3)			
6		343.02	3.3 (−4)						
7		347.62	1.2 (−3)						
8		352.26	1.7 (−3)						
2	7	345.87	2.6 (−5)						
3		347.36	5.1 (−5)						
4		349.24	1.4 (−4)						
5		351.37	3.3 (−4)						
6		353.58	5.6 (−4)						
2	8	353.07	1.1 (−5)						

[a]Results of the life-time matrix calculations performed within the CC-BF-diabatic approach using maximally N=96 coupled $v\,j\,\lambda$ states, for v=0 − 3, j=0, 2, . . . , 12, and λ's limited to $\lambda_{\max}$=3.

[b]The predissociation of these states is inhibited by large centrifugal barriers.

[c]The assignment of the states with the number k was aided by the perturbative calculations of the energies and widths. See the shadowed areas in Fig. C3c.

Fig. C4. $He^+-H_2(I=1)$

Rotationally predissociating states associated with the $v=0\, j=3$ threshold

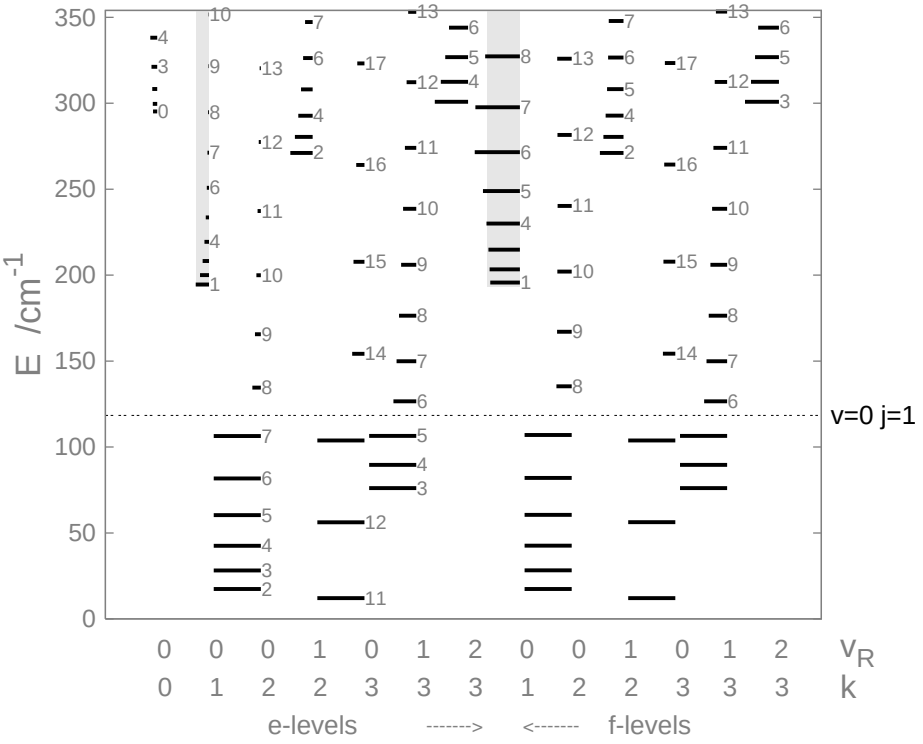

Fig. C4a. The structure of energy levels. The lengths of the lines above the $j=1$ threshold represent $-\log_{10}\Gamma$. See Table CV.

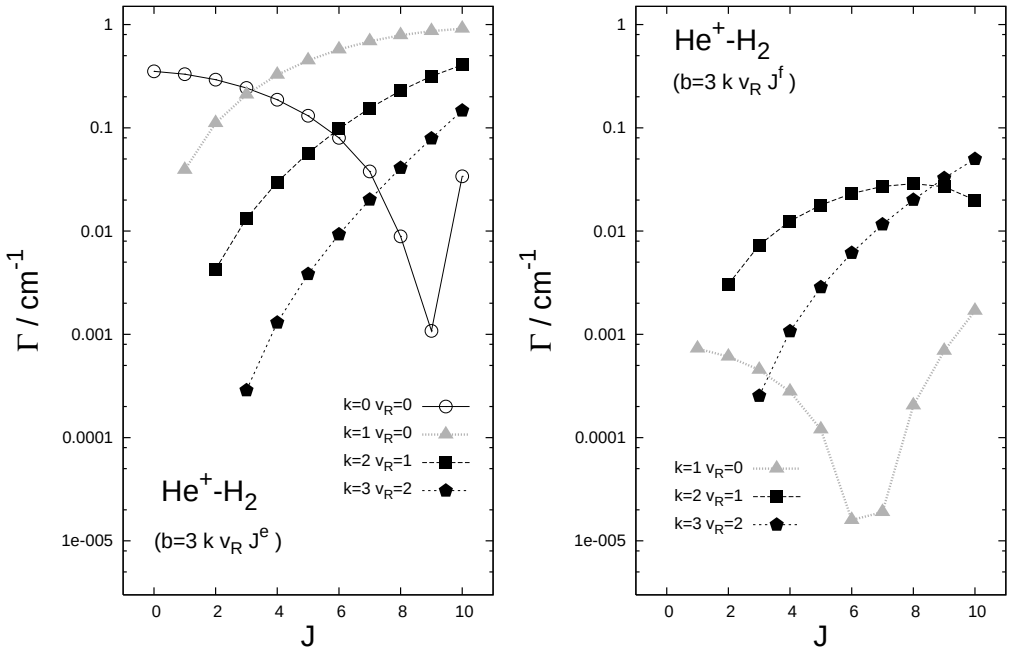

Fig. C4b. The widths of levels in selected $k\, v_R$ ladders shown in Fig. C4a. The e- and f-parity levels are in the left and right panels, respectively.

The gray strips in Fig. C4a and the gray symbols in Fig. C4b indicate the strongest parity effects on the level positions and widths; they concern the levels in the $k=1$ ladders. The shifts between the corresponding f and e levels grow quickly with J. The widths of f levels are smaller by at least two orders of magnitude and display different, non-monotonic, dependence on the number J.

TABLE CV: $He^+-H_2(I=1)$. Energies[a] and widths[a] of $b=3\,k\,v_R\,J\,p$ states. All states in the range $0-350$ cm^{-1} and selected higher states are shown. $E=0$ is at the $v=0\,j=0$ threshold. All data are in cm^{-1}.

		$k=1$					$k=0$				
		$p=1$		$p=-1$			$p=1$		$p=-1$		
J	v_R	E	Γ	$E-E(p=1)$	Γ	v_R	E	Γ	$E-E(p=1)$	Γ	
0	0					0	295.26	3.5 (−1)			
1		194.58	3.9 (−2)	1.14	7.3 (−4)		299.64	3.3 (−1)			
2		200.01	1.1 (−1)	3.36	6.1 (−4)		308.33	2.9 (−1)			
3		208.26	2.1 (−1)	6.56	4.5 (−4)		321.23	2.4 (−1)			
4		219.42	3.3 (−1)	10.62	2.8 (−4)		338.18	1.9 (−1)			
5		233.58	4.5 (−1)	15.38	1.2 (−4)		359.01	1.3 (−1)			
6		250.83	5.7 (−1)	20.70	1.6 (−5)		383.54	8.0 (−2)			
7		271.23	6.9 (−1)	26.44	1.9 (−5)		411.56	3.8 (−2)			
8		294.82	7.9 (−1)	32.46	2.1 (−4)		442.85	8.9 (−3)			
9		321.63	8.6 (−1)	38.63	6.9 (−4)		477.11	1.1 (−3)			
10		351.64	9.1 (−1)	44.77	1.7 (−3)						
		$k=3$					$k=2$				
11	0	12.04	0[b]	0.03	0						
12		56.18	0	0.08	0						
13		103.79	0	0.05	0						
14		154.25	5.0 (−2)	0.04	4.8 (−2)						
15		207.76	7.0 (−2)	0.11	5.5 (−2)						
16		264.15	1.3 (−1)	0.16	6.6 (−2)						
17		323.21	1.7 (−1)	0.24	7.8 (−2)						
2						0	17.40	0	0.00	0	
3	1	76.08	0	0.00	0		28.20	0	0.02	0	
4		89.61	0	0.00	0		42.55	0	0.06	0	
5		106.47	0	0.00	0		60.41	0	0.15	0	
6		126.59	3.7 (−3)	0.00	3.6 (−3)		81.71	0	0.30	0	
7		149.94	8.2 (−3)	0.00	6.5 (−3)		106.40	0	0.57	0	
8		176.44	1.5 (−2)	0.01	1.1 (−2)		134.55	1.3 (−1)	0.78	2.4 (−2)	
9		206.01	2.5 (−2)	0.01	1.7 (−2)		165.64	2.4 (−1)	1.41	2.7 (−2)	
10		238.58	4.0 (−2)	0.03	2.5 (−2)		199.97	3.4 (−1)	2.10	3.0 (−2)	
11		274.04	6.2 (−2)	0.05	3.5 (−2)		237.29	4.6 (−1)	3.00	3.1 (−2)	
12		312.28	9.3 (−2)	0.10	4.8 (−2)		277.47	6.0 (−1)	4.15	3.1 (−2)	
13		353.16	1.4 (−1)	0.18	6.3 (−2)		320.38	7.6 (−1)	5.55	2.9 (−2)	
2						1	271.14	4.3 (−3)	0.00	3.1 (−3)	
3	2	300.91	2.9 (−4)	0.00	2.5 (−4)		280.44	1.3 (−2)	0.02	7.3 (−3)	
4		312.48	1.3 (−3)	0.00	1.1 (−3)		292.77	3.0 (−2)	0.07	1.3 (−2)	
5		326.87	3.8 (−3)	0.00	2.9 (−3)		308.07	5.7 (−2)	0.17	1.8 (−2)	
6		344.04	9.3 (−3)	0.01	6.2 (−3)		326.29	9.8 (−2)	0.34	2.3 (−2)	
7		363.92	2.0 (−2)	0.02	1.2 (−2)		347.31	1.6 (−1)	0.60	2.7 (−2)	
8		386.46	4.1 (−2)	0.06	2.0 (−2)		371.02	2.3 (−1)	0.98	2.9 (−2)	
9		411.58	7.9 (−2)	0.16	3.3 (−2)		397.30	3.2 (−1)	1.51	2.7 (−2)	
10		439.21	1.5 (−1)	0.40	5.0 (−2)		425.95	4.1 (−1)	2.17	2.0 (−2)	

[a]Results of the life-time matrix calculations performed within the CC-BF-diabatic approach using maximally $N=124$ coupled $v\,j\,\lambda$ states, for $v=0-3$, $j=1,3,\ldots,13$, and λ's limited to $\lambda_{\max}=4$.

[b]States below the threshold $\varepsilon_{v=0\,j=1}=118.37$ cm^{-1} are bound in the approach.

Fig. C5. Perturbative calculations on rotational predissociation of He^+-H_2. Hamiltonian matrix in the CC-SF-adiabatic representation

$$ {}_{\rm a}\mathbf{H}^{Jp}(R) = -\frac{\hbar^2}{2\mu}\left[\mathbf{I}\frac{d^2}{dR^2} + 2\mathbf{A}^{Jp}(R)\frac{d}{dR} + \mathbf{B}^{Jp}(R)\right] + \mathbf{e}^{Jp}(R) $$

P- and Q-subspaces

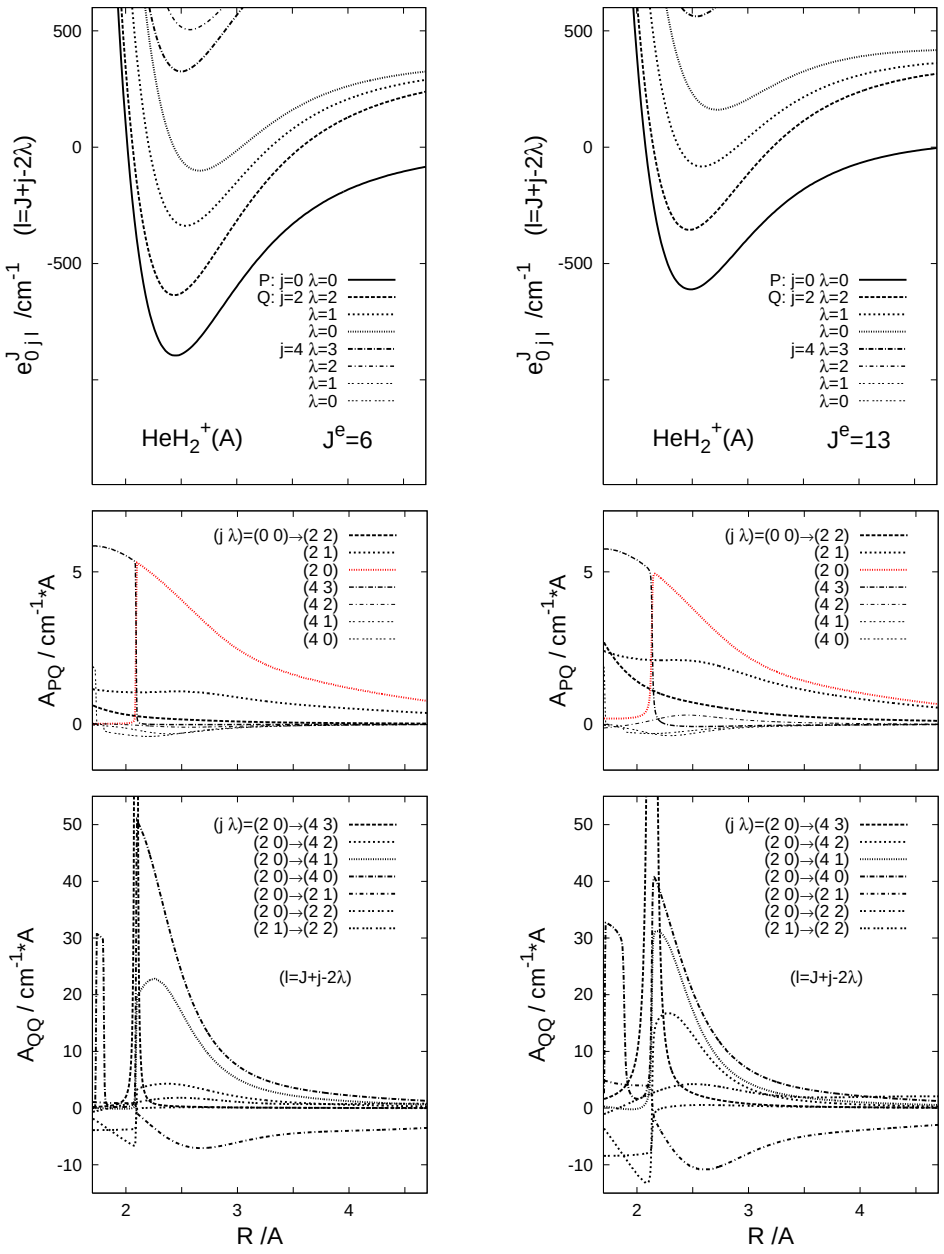

The complete model space was spanned by N=96 diabatic basis functions which were used in the LT calculations (see footnote a to Table CIV). The adiabatic basis resulting from diagonalization of the $N\times N$ matrix $\mathbf{W}^{J^e}(R)$ was contracted to M=8 states, so that the respective block of the Hamiltonian matrix ${}_{\rm a}\mathbf{H}^{J^e}(R)$ included the adiabatic potentials $e^{J^e}_{\bar{v}\bar{j}\bar{l}}(R)$ which correlate asymptotically with the thresholds $\varepsilon_{v=0\,j}$ for j=0, 2, 4. Consequently, the open (P) and the closed (Q)-channel subspaces included M_P=1 and M_Q=7 states, respectively. The potentials in the P- and Q-subspaces for two values of J are shown in the two upper panels. The three $\bar{j}$=2 potentials in the Q-subspace, with $\bar{l}$=J−2, J, and J+2, support the predissociating b=2 states with k=2, 1, and 0, respectively. The (larger, first-derivative) nonadiabatic couplings between the P- and Q-subspaces are plotted in the middle panels. Selected couplings in the Q-subspaces are shown in the bottom panels. However, neither the A- nor the B-couplings were explicitly needed in the calculations because Smooth Variable Discretization methods were exploited (see footnote b to Table CVI).

Fig. C5a. Energies and widths of $v{=}0\, b{=}2\, k\, v_R\, J^e$ states of $He^+{-}H_2$. Perturbative (CM) versus 'exact' (LT) results

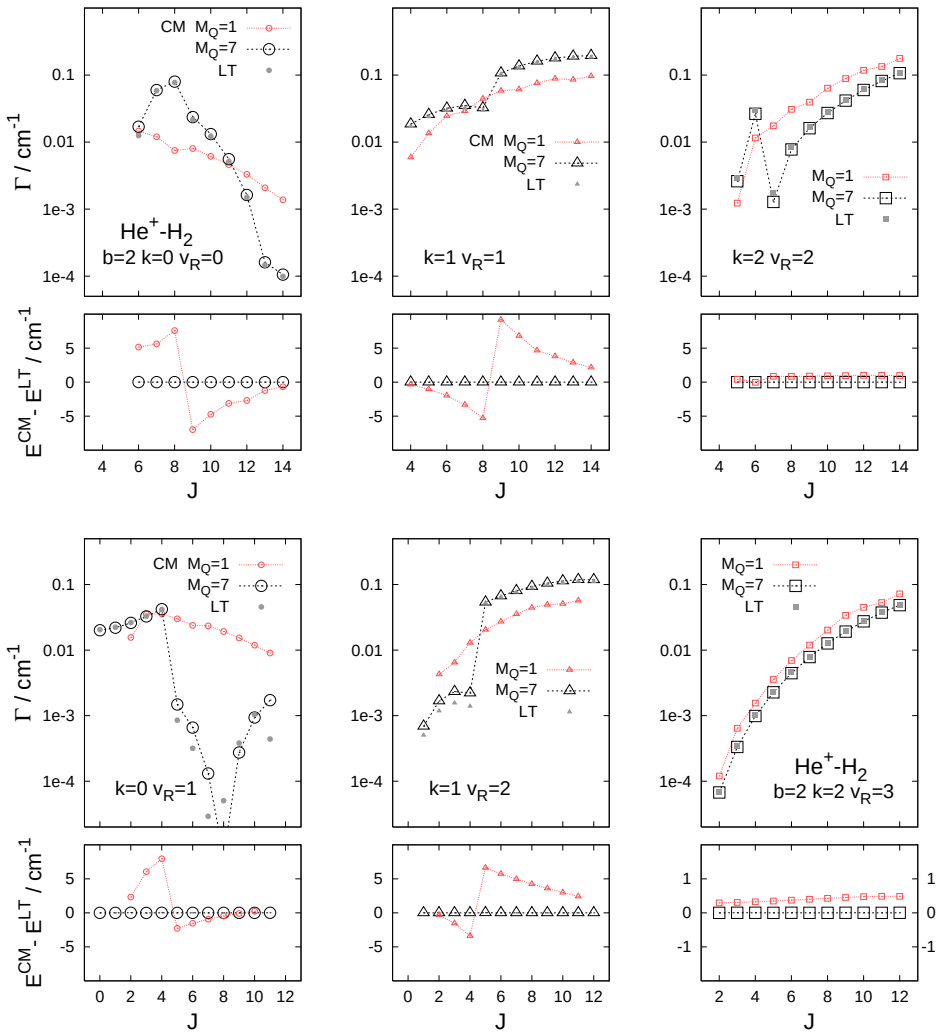

The CM results shown with the black and red symbols differ in the choices of the Q-subspaces. $M_Q{=}7$ means the choice described in Fig. C5. $M_Q{=}1$ means that only one adiabatic basis state $\bar{v}\,\bar{j}\,\bar{l}$ was included into the Q-subspace when evaluating the CM formulas for the predissociating state $v{=}0\, b{=}2\, k\, v_R\, J^e$, namely, the state with $\bar{v}{=}0$, $\bar{j}{=}b$, and $\bar{l}{=}J{+}b{-}2k$.

COMMENTS

(i) The comparison of the two sets of the CM results (for $M_Q{=}1$ and $M_Q{=}7$) with the LT results reveals the following facts on the pathways of decay of the states:

- the $b{=}k{=}2$ states, supported by the lowest closed-channel potentials $\bar{j}{=}2\,\bar{l}{=}J{-}2$, decay rather directly to the P-subspace.

- the $b{=}2\, k{=}0$ states, supported by the $\bar{j}{=}2\,\bar{l}{=}J{+}2$ potentials, decay indirectly, via mixing with other states in the closed-channel subspace, mostly with the $\bar{l}{=}J$ and $\bar{l}{=}J{-}2$ states. Indeed, the CM calculations disregarding this mixing, with $M_Q{=}1$, fail to reproduce the complex dependence of the widths of these states on the number J, as shown in the leftmost panels of the figure.

(ii) The present perturbative treatment of resonances may be viewed as an extension of the popular adiabatic-bender model[9].

TABLE CVI: $He^+-H_2(I=0)$. Perturbative (CM) versus 'exact' (LT) results for energies and widths of rotationally predissociating states below $v=0\,j=2$ threshold, $b=2\,k\,v_R\,J\,p=1$. For each state shown are: $E^{(0)}$ — the energy of related bound state in the Q-subspace[a], $\Delta E^{(0)}=E^{(0)}-E^{\rm LT}$, $\Delta E=E^{\rm CM}-E^{\rm LT}$ (both Δ's in cm^{-1}), and $\delta\Gamma=(\Gamma^{\rm CM}/\Gamma^{\rm LT}-1)\times100\%$ [b]. The values of $\Gamma^{\rm LT}$ can be found in Table CIV.

	$k=2$					$k=1$					$k=0$				
J	v_R	$E^{(0)}$	$\Delta E^{(0)}$	ΔE	$\delta\Gamma$	v_R	$E^{(0)}$	$\Delta E^{(0)}$	ΔE	$\delta\Gamma$	v_R	$E^{(0)}$	$\Delta E^{(0)}$	ΔE	$\delta\Gamma$
17	0	15.549	0.023	0.004	0.0										
18		77.809	0.258	0.008	0.6										
19		142.327	0.002	0.001	−0.4										
20		208.835	0.009	0.003	−0.3										
21		277.013	−0.006	−0.003	−0.3										
22		346.465	−0.019	−0.004	−0.3										
12						0	1.247	−0.292	0.006	0.0					
13	1	33.244	−0.019	0.005	−9.0		43.992	−0.240	0.002	3.4					
14		76.909	−0.015	0.004	−5.3		89.476	−0.277	0.002	3.7					
15		122.828	−0.004	0.003	−3.5		137.549	−0.302	0.003	3.6					
16		170.773	0.006	0.002	−2.5		188.031	−0.322	0.003	3.7					
17		220.468	0.014	0.003	−2.0		240.712	−0.333	0.003	3.3					
18		271.575	0.018	0.002	−1.4		295.335	−0.336	0.003	3.1					
19		323.658	0.019	0.003	−1.0		351.580	−0.330	0.000	-0.2					
4						1	5.188	−0.091	0.004	8.5					
5	2	1.708	−0.008	0.000	−9.3		20.552	−0.137	0.004	8.2					
6		19.147	−0.117	−0.013	−13.5		39.021	−0.189	0.004	7.7	0	17.419	−0.219	0.018	35.6
7		38.153	−0.010	0.002	−26.6		60.678	−0.244	0.005	8.8		41.902	−0.290	0.001	2.1
8		60.543	0.001	0.001	−7.2		85.687	−0.299	0.005	8.9		68.272	−0.265	0.001	3.0
9		85.343	0.005	0.002	−4.8		96.973	−0.244	0.001	3.9		114.283	−0.339	0.005	8.9
10		112.478	0.006	0.002	−4.1		127.581	−0.247	0.002	4.7		146.611	−0.349	0.005	8.7
11		141.812	0.007	0.002	−3.3		159.941	−0.271	0.003	5.2		182.547	−0.334	0.004	8.3
12		173.174	0.011	0.003	−2.8		194.054	−0.303	0.003	4.7		221.768	−0.306	0.003	8.4
13		206.353	0.013	0.002	−2.5		229.901	−0.332	0.005	5.4		263.909	−0.270	0.003	10.1
14		241.094	0.015	0.002	−2.2		267.366	−0.355	0.004	5.3		308.613	−0.233	0.002	6.5
15		277.077	0.014	−0.001	−2.0		306.224	−0.366	0.004	5.2					
16		313.889	0.015	−0.002	−1.2		346.121	−0.362	0.004	5.3					
17		350.952	0.014	−0.002	−1.2										
0											1	138.890	−0.685	0.002	−2.0
1						2	152.007	−0.030	0.001	37.3		141.675	−0.651	0.005	−2.0
2	3	126.466	0.001	0.001	−2.2		157.443	−0.095	−0.001	41.8		147.176	−0.587	0.009	−1.5
3		133.512	0.002	0.002	−2.3		165.688	−0.188	−0.002	49.3		155.263	−0.522	−0.016	−0.7
4		142.838	0.002	0.001	−3.1		176.834	−0.292	0.000	59.4		165.756	−0.392	0.009	1.1
5		154.384	0.002	0.001	−2.1		178.474	−0.299	0.007	2.7		190.939	−0.386	0.001	73.6
6		168.073	0.003	0.002	−2.3		193.279	−0.237	0.004	3.9		207.981	−0.447	0.004	106.9
7		183.809	0.003	0.001	−2.0		210.082	−0.205	0.003	4.9		227.848	−0.472	0.006	351.2
8		201.474	0.004	0.001	−1.9		228.799	−0.197	0.002	5.5		250.368	−0.470	0.005	−85.7
9		220.925	0.006	0.002	−1.7		249.322	−0.202	0.003	5.8		275.332	−0.446	0.006	−28.3
10		241.987	0.007	0.002	−1.7		271.498	−0.216	0.003	6.1		302.489	−0.408	0.005	−9.9
11		264.447	0.008	0.001	−1.7		295.121	−0.228	0.003	5.9		331.519	−0.352	0.009	291.1
12		288.036	0.010	0.002	−1.4		319.904	−0.235	0.004	6.5					
13		312.410	0.009	0.000	−1.3		345.444	−0.232	0.003	7.1					
14		337.098	0.008	−0.001	−1.1										

TABLE CV: continued

0											2	264.544	−0.547	0.003	−3.8
1						3	262.719	−0.058	0.007	9.9		267.540	−0.484	−0.001	−9.5
2	4	232.000	0.001	0.001	−2.0		265.608	−0.080	0.005	5.9		272.906	−0.455	0.002	−12.4
3		237.385	0.001	0.001	−1.9		270.357	−0.084	0.004	5.3		280.426	−0.443	0.004	−13.6
4		244.480	0.001	0.001	−2.1		276.928	−0.084	0.002	5.1		290.002	−0.431	0.005	−13.6
5		253.209	0.000	0.000	−1.8		285.231	−0.085	0.002	5.5		301.528	−0.412	0.005	−12.9
6		263.475	0.003	0.002	−2.1		295.144	−0.088	0.002	6.0		314.857	−0.386	0.005	−10.5
7		275.151	0.003	0.002	−2.0		306.511	−0.094	0.002	6.2		329.783	−0.348	0.005	−8.2
8		288.082	0.004	0.002	−1.8		319.136	−0.100	0.002	6.5		345.978	−0.300	0.004	−4.2
9		302.067	0.004	0.002	−1.8		332.758	−0.105	0.002	6.8					
10		316.855	0.003	0.000	−1.6		347.009	−0.103	0.002	7.4					
11		332.109	−0.003	−0.005	−7.3										
12		347.344	0.004	0.001	−1.0										
0											3	330.143	−0.277	0.003	−4.3
1						4	323.505	−0.006	0.000	5.3		331.932	−0.265	0.003	−5.0
2	5	295.339	0.001	0.001	−1.7		325.444	−0.014	0.001	5.2		335.359	−0.246	0.004	−5.9
3		299.156	0.000	0.000	−1.8		328.450	−0.020	0.001	5.3		340.216	−0.224	0.003	−6.2
4		304.144	0.000	0.000	−1.8		332.505	−0.025	0.001	5.3		346.264	−0.196	0.004	−5.8
5		310.211	0.001	0.001	−2.1		337.520	−0.028	0.001	6.2		353.124	−0.150	0.004	18.6
6		317.235	0.001	0.000	−1.8		343.337	−0.029	0.001	6.5					
7		325.054	0.001	0.000	−1.0		349.678	−0.030	0.001	7.1					
8		333.462	0.001	0.000	−1.1										
9		342.181	0.001	0.000	−1.0										
10		350.818	0.001	0.000	−0.8										
0											4	352.644	−0.052	0.000	0.8
1						5	348.147	−0.002	0.000	5.4					
2	6	329.244	0.000	0.000	−0.9		349.043	−0.004	0.000	5.2					
3		331.724	0.000	0.000	−1.4		350.403	−0.004	0.000	6.1					
4		334.921	0.000	0.000	−1.2		352.153	−0.004	0.000	14.8					
5		338.735	0.001	0.001	−1.1		354.142	−0.008	0.002	−55.1					
6		343.024	0.000	0.000	−19.0										
7		347.621	0.000	0.000	−1.9										
8		352.259	0.000	0.000	−1.3										

[a]including $M_{\rm Q}$=7 adiabatic states; see the caption of Fig. C5.

[b]The bound states of ${}_{\rm a}\mathbf{H}^{J^e}_{QQ}(R)$ were determined and the formulas for the resonance widths $\Gamma^{\rm CM}$ and the energy shifts $E^{\rm CM}-E^{(0)}$ were evaluated with the help of the quasi-diabatic versions of the log-derivative algorithms[10] adapted to the Smooth-Variable-Discretization approach[11].

[1] part A of this material: file Hep+HH_RCT_state2state.pdf
[2] F. Mrugała and W. P. Kraemer, J. Chem. Phys. **122**, 224321 (2005) (paper II).
[3] C. C. Chuang, S. N. Tsang, W. Klemperer, and H. C. Chang, J. chem. Phys. **109**, 8836 (1998).
[4] F. Mrugała, V. Špirko, and W. P. Kraemer, J. Chem. Phys. **118**, 10547 (2003) (paper I).
[5] C. D. Thompson, C. Emmeluth, B. L. J. Poad, G. H. Weddle, and E. J. Bieske, J. Chem. Phys. **125**, 044310 (2006).
[6] U. Fano, Phys. Rev. **124**, 1866 (1961).
[7] F. H. Mies, Phys. Rev. **175**, 164 (1968).
[8] F. Mrugała, J. Chem. Phys. **129**, 064314 (2008).
[9] S. L. Holmgren, M. Waldman and W. Klemperer, J. Chem. Phys.**67**, 4414 (1977); L. Tao and M. H. Alexander, J. Chem. Phys. **127**, 114301 (2007) and references therein.
[10] F. Mrugała, Int. Rev. Phys. Chem. **12**, 1 (1993).
[11] O. I. Tolstikhin, S. Watanabe, and M. Matsuzawa, J. Phys. **B29**, L389 (1996); F. D. Colavecchia, F. Mrugała, G. A. Parker, and R. T Pack, J. Chem. Phys. **118**, 10387 (2003); F. Mrugała, 2004, unpublished.